

**A Thesis Submitted for the Degree of PhD at the University of Warwick**

**Permanent WRAP URL:**

<http://wrap.warwick.ac.uk/88398>

**Copyright and reuse:**

This thesis is made available online and is protected by original copyright.

Please scroll down to view the document itself.

Please refer to the repository record for this item for information to help you to cite it.

Our policy information is available from the repository home page.

For more information, please contact the WRAP Team at: [wrap@warwick.ac.uk](mailto:wrap@warwick.ac.uk)

# Electrodes for Top-Illuminated Organic

## Photovoltaic Devices

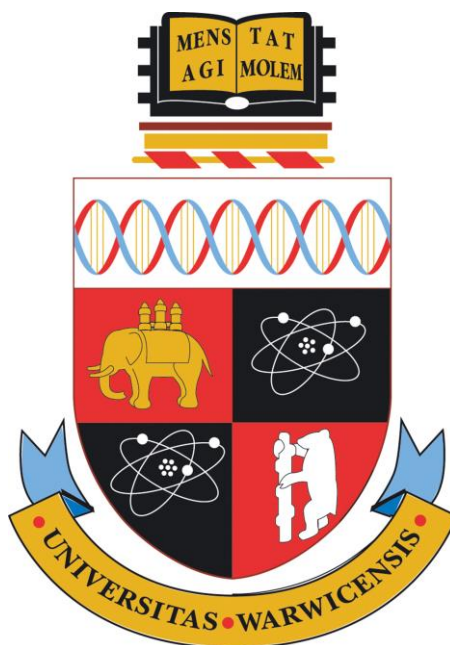
by

**Martin Stuart Tyler**

A thesis submitted for the degree of

**Doctor of Philosophy**

The University of Warwick



Supervised by Dr. Ross A. Hatton

Department of Chemistry

University of Warwick

**July 2016**

---

## Abstract

The work in this thesis focuses on the development of electrodes for top-illuminated organic photovoltaics (OPVs) and studies how their complex interactions with other layers affect the device. The development of a novel substrate electrode based on an Al | Cu bilayer capped with an ultra-thin Al layer is initially shown. This electrode offers the rare combination of high reflectivity, a very low work function of  $\sim 3.2$  eV, and high stability towards oxidation. Photoelectron spectroscopy studies shows that an Al capping layer of  $\sim 1$  nm in thickness is sufficient to block oxidation of the underlying Cu, which is remarkable given that the self-limiting oxide thickness for bulk Al is  $\geq 2$  nm. This promising substrate electrode is used to elucidate a new design rule for top-illuminated bulk-heterojunction OPVs. It is shown that for OPVs utilising high performance donor-type organic semiconductors in conjunction with a low work function electron extracting electrode, a barrier to hole-extraction spontaneously forms at the donor | electron-extracting electrode interface, blocking unwanted hole-extraction and negating the need for a hole-blocking layer, which simplifies the device architecture. This electrode design rule is underpinned by studies of the interfacial energetics with five widely used solution processed organic semiconductors as well as device based investigations. A novel organo-molybdenum oxide bronze is also developed which combines the function of wide band-gap interlayer for efficient hole-extraction with the role of a metal electrode seed layer, enabling the fabrication of highly transparent, low-sheet-resistance silver window electrodes for top-illuminated OPVs. Additionally, preliminary results relating to the fabrication of a model nano-structured reflective electrode are shown. This is designed to investigate the extent to

which absorption of light can be enhanced in a top-illuminated OPVs by texturing the reflective substrate electrode.

---

# Table of Contents

Abstract.....	ii
Table of Contents .....	iv
Acknowledgements .....	viii
List of Publications .....	ix
Symbols and Abbreviations .....	x
Chapter 1. Introduction .....	1
1.1 Context .....	1
1.2 Organic Photovoltaics .....	3
1.3 Organic Semiconductors .....	5
1.4 Energy Alignment at Electrode-Organic Semiconductor Interfaces.....	9
1.5 Principles of OPV Operation .....	14
1.6 <i>JV</i> Device Characteristics .....	18
1.7 OPV Processing Techniques.....	21
1.8 OPV Materials .....	22
1.9 Interfacial Layers for Charge Extraction in OPVs .....	28
1.10 Transition Metal Oxides as Interfacial layers .....	32
1.11 Top-Illuminated OPV Device Architectures.....	34
Chapter 2. Experimental Techniques .....	43
2.1 Thin Film Fabrication Techniques .....	43
2.1.1 Substrate Preparation.....	43
2.1.2 Molecular Monolayer Deposition .....	44
2.1.3 Vacuum Evaporation Deposition.....	46
2.1.4 Spin Coating .....	48
2.2 OPV Device fabrication.....	49
2.2.1 Metal electrode deposition .....	50
2.2.2 Charge extraction layer deposition .....	52
2.2.3 Photoactive layer deposition .....	53
2.2.4 OPV Device Layout.....	54

---

2.3 OPV testing .....	55
2.3.1 OPV Current Density vs Voltage Analysis .....	55
2.3.2 OPV External Quantum Efficiency Analysis.....	56
2.4 Characterisation Techniques .....	58
2.4.1 X-ray photoelectron spectroscopy and Auger electron spectroscopy.....	58
2.4.2 Ultraviolet photoelectron spectroscopy.....	61
2.4.3 Kelvin Probe .....	63
2.4.4 Atomic Force Microscopy .....	66
2.4.5 Scanning Electron Microscopy .....	68
2.4.6 Sheet Resistance.....	69
2.4.7 Absorption/ Reflection spectroscopy .....	70
2.4.8 Contact Angle Measurements.....	71
2.4.9 Optical Simulations .....	72
Chapter 3. A Silver-Free, Reflective Substrate Electrode for Electron Extraction in Top-Illuminated Organic Photovoltaics .....	73
3.1 Summary.....	73
3.2 Introduction.....	74
3.3 Experimental.....	76
3.4 Results and Discussion .....	77
3.5 Conclusion .....	99
Chapter 4. Elucidating an Electrode Design Rule for High Performance Top-Illuminated Organic Photovoltaics.....	100
4.1 Summary.....	100
4.2 Introduction.....	101
4.3 Experimental.....	103
4.4 Results & discussion.....	104
4.5 Conclusions .....	118
Chapter 5. High Performance Silver Window Electrodes for Top-Illuminated Organic Photovoltaics Using an Organo-Molybdenum Oxide Bronze Interlayer .....	119
5.1 Summary.....	119
5.2 Introduction.....	120
5.3 Experimental.....	123

---

5.4 Results & Discussion.....	124
5.4.1 $H_yMoO_{3-x}$ synthesis .....	124
5.4.2 $H_yMoO_{3-x}$ characterisation .....	132
5.4.3 Ag Window Electrode Characterisation.....	143
5.4.4 Device Studies .....	154
5.4.5 Substitution of Ag with Cu .....	164
5.5 Conclusions .....	169
Chapter 6. A Nano-Structured Reflective Electrode for Top-Illuminated Organic Photovoltaics.....	171
6.1 Summary.....	171
6.2 Introduction .....	171
6.3 Experimental.....	173
6.4 Results and Discussion .....	174
6.5 Conclusions .....	179
Chapter 7.Future Outlook.....	180
References .....	182

## Declaration

The work presented in this thesis has been conducted at the Department of Chemistry at The University of Warwick except the X-ray photoelectron spectroscopy, Ultra-violet photoelectron spectroscopy, scanning electron microscopy, and X-ray diffraction measurements, which were carried out in the Department of Physics. XPS/UPS data collection and analysis assistance was provided by Dr Marc Walker. Assistance with X-ray diffraction data collection and analysis was provided by Dr. David Walker. All data collection was performed by me apart from that mentioned above. Parts of the work have been published in scientific journals and presented at the conferences MC11 (Jul 2013), MC12 (Jul 2015), and Next Generation Materials for Solar Photovoltaics (Jan 2016)

## Acknowledgements

I would like to first and foremost thank my supervisor Dr. Ross Hatton for his guidance and support throughout my PhD. He has been a great source of inspiration and I am truly grateful to have had the opportunity to work in his group and have him as a supervisor.

Additionally I would like to thank my excellent colleagues in the Hatton Group throughout the years; Helena Stec, Oliver Hutter, Kenny Marshall, Dinesha Dabera, Jessica Pereira, Jaemin Lee, and Silvia Varagnolo. No matter how long or brief it has been a pleasure to work alongside them all.

I would also like to thank Professor Tim Jones, Professor Julie Macpherson, Professor Patrick Unwin, and their research groups for allowing me access to the various instrumentation in their laboratories. From the Department of Physics I would also like to thank Dr. Marc Walker for the collection of the XPS/UPS data within this thesis as well as for his expertise in helping to unravel its secrets.

Lastly I would like to thank my family whose constant support I can rely on no matter what, and the wonderful Sarah Keane for always putting a smile on my face.

---

## List of Publications

### Publications:

- *A Silver-Free, Reflective Substrate Electrode for Electron Extraction in Top-Illuminated Organic Photovoltaics*, Martin S. Tyler, Oliver S. Hutter, Marc Walker, and Ross A. Hatton, *ChemPhysChem.* **2015**, DOI: 10.1002/cphc.201402880
- *An Electrode Design Rule for High Performance Top-Illuminated Organic Photovoltaics* Martin S. Tyler, Immad M. Nadeem, Ross A. Hatton, *Mater. Horiz.* **2016**, DOI:10.1039/C6MH00124F
- *High-Performance Silver Window Electrodes for Top-Illuminated Organic Photovoltaics Using an Organo-Molybdenum Oxide Bronze Interlayers* Martin S. Tyler, Marc Walker, Ross A. Hatton, *ACS Appl. Mater. Interfaces*, **2016**, DOI:10.1021/acsami.6b02647

---

## Symbols and Abbreviations

Abs	absorption
AES	auger electron spectroscopy
AFM	atomic force microscopy
AM	air mass
APTMS	3-aminopropyltrimethoxysilane
$A_s$	electron affinity
B.E	binding energy
BCP	bathocuproine
BHJ	bulk-heterojunction
$C$	capacitance
CB	conduction band
CB	Chlorobenzene
CIGS	copper-indium-gallium-selenide
CTL	charge transport layer
$D$	diffusion coefficient
D-A	donor-acceptor
DCB	1,2-dichlorobenzene
DIO	1,8-diiodooctane
DMD	dielectric metal dielectric
$E_f$	Fermi level
$E_g$	band-gap
EQE	external quantum efficiency
$FF$	fill factor

---

HBL	hole blocking layer
HOMO	highest occupied molecular orbital
HOPG	highly-ordered-pyrolitic-graphite
HRXPS	x-ray photoelectron spectroscopy
HTL	hole transport layer
$I_p$	ionisation potential
IPCE	incident photon to current quantum efficiency
ITO	indium tin oxide
$J_{MP}$	current at maximum power
$J_{sc}$	short circuit current density
$JV$	current density vs voltage
K.E	kinetic energy
$k_B$	Boltzmann constant
$L_D$	exciton diffusion length
LUMO	lowest unoccupied molecular orbital
MO	molecular orbital
MPA	3-mercaptopropionic acid
MPTMS	3-mercaptopropyltrimethoxysilane
OPV	organic photovoltaic
P3HT	poly(3-hexylthiophene)
PBDTTT-EFT	poly[4,8-bis(5-(2-ethylhexyl)thiophen-2-yl)benzo[1,2-b;4,5-b']dithiophene-2,6-diyl-alt-(4-(2-ethylhexyl)-3-fluorothieno[3,4-b]thiophene-)-2-carboxylate-2-6-diyl]
PC <sub>61</sub> BM	[6,6]-phenyl C <sub>61</sub> butyric acid methyl ester
PC <sub>71</sub> BM	[6,6]-phenyl-C <sub>71</sub> -butyric acid methyl ester

PCDTBT	poly[N-90-heptade- canyl-2,7-carbazole-alt-5,5-(40,70-di-2-thienyl-20,10,30-benzothia- diazole)]
<i>PCE</i>	power conversion efficiency
<i>P<sub>inc</sub></i>	total incident power
<i>P<sub>MP</sub></i>	maximum power point
PTB7	polythieno[3,4-b]-thiophene-co-benzodithiophene
PV	photovoltaic
<i>Q</i>	charge on parallel plate capacitor
QCM	quartz crystal microbalance
rpm	rotations per minute
<i>R<sub>RMS</sub></i>	root-mean –squared roughness
<i>R<sub>series</sub></i>	series resistance
<i>R<sub>sheet</sub></i>	sheet resistance
<i>R<sub>shunt</sub></i>	shunt resistance
SEM	scanning electron microscopy
TMO	transition metal oxide
UPS	ultra violet electron spectroscopy
UV	ultraviolet
<i>V</i>	voltage
VB	valence band
<i>V<sub>CPD</sub></i>	contact potential difference
VdP	van der Pauw
VL	vacuum level
<i>V<sub>L∞</sub></i>	vacuum level at infinity
<i>V<sub>Ls</sub></i>	vacuum level at the surface

$V_{MP}$	voltage at maximum power
$V_{oc}$	open circuit voltage
XPS	x-ray photoelectron spectroscopy
$\Phi$	work function
$\chi$	surface potential
$\mu$	chemical potential
$\rho(x)$	space charge density distribution
$\varepsilon_F^{vac}$	energy difference between Fermi level and vacuum level
$\varepsilon_r$	relative permittivity
$\lambda$	wavelength
$\tau$	exciton lifetime

---

# Chapter 1.

## Introduction

### 1.1 Context

One of the greatest challenges to modern society is the production of energy in both a reliable and environmentally sustainable way. Currently energy produced from burning fossil fuels dominates the power sector, with a total share of power generation of 68%,<sup>1</sup> although unfortunately this inevitably goes hand-in-hand with the production of CO<sub>2</sub>.<sup>2</sup> There have been numerous studies showing that this large scale CO<sub>2</sub> production has led to, and will continue to result in, significant global warming<sup>3</sup> giving rise to climate change which risks food security, extreme weather events, and a loss in biodiversity. Additionally, other pollutants from burning fossil fuels have been shown to have adverse human health effects<sup>4</sup> and more direct environmental damage due to extraction processes.<sup>5</sup> At the Paris Climate Change Conference (COP21) in December 2015 the global community agreed to limit the rise in global temperature to an increase of  $\leq 2^{\circ}\text{C}$  that of pre-industrial levels, with each country setting targets to reduce CO<sub>2</sub> emissions.<sup>6</sup> A recent study by McGlade *et al.*<sup>7</sup> has concluded that roughly two-thirds of the remaining fossil fuels in the earth's crust will have to remain unused if there is to be a 50% chance of keeping global warming to the  $\leq 2^{\circ}\text{C}$  limit.

Environmental considerations aside, humanity's demand for energy has been predicted to rapidly increase with a doubling of the current demand by 2050.<sup>8</sup> It has been estimated by Smalley<sup>9</sup> that in the near future, based on an estimated global population of 10 billion people,  $60 \times 10^{12}$  watts of power will be required per day in order to provide a developed world standard of living for all. Whilst there are still significant reserves of oil and gas they are declining and it is clear that these cannot last

---

indefinitely.<sup>10</sup> Additionally, increasingly environmentally damaging and hazardous procedures must be used to extract what remains which leads to increased costs of energy production. There is therefore a clear need for the widespread implementation of existing clean and renewable means of energy production, and the development of new ones. Solar energy can produce both heat and electricity and so will play a large part in helping to address our future energy needs. Additionally it is the most abundant source of energy, since more energy arrives from the sun on the earth's surface every hour than is used by all of mankind in one year.<sup>11</sup>

Another key consideration is the need for nation states to have energy security.<sup>12</sup> Whilst most of the current energy supply is generated by burning fossil fuels, relatively few countries have large enough reserves of fossil fuel deposits to be self-sufficient, and so many nations are heavily dependent on other countries for their energy supply. This, in turn, leads to uncertainties and vulnerabilities in the energy supply many of which are out of the control of the buyer. For instance, energy prices can be changed quickly through manipulation of the supplies and/or due to deliberate damage to infrastructure and facilities. Solar energy production can provide an almost universal means to produce energy and, in conjunction with other energy sources, provide a high degree of energy security. Solar energy can also provide access to energy for the approximately 2 billion people in the world today who currently live off grid and so require a power supply at the point use.<sup>13</sup>

## 1.2 Organic Photovoltaics

Currently the solar photovoltaic (PV) market is dominated by highly crystalline silicon PVs. Crystalline Si has a high electron and hole mobility and absorbs over a broad range of the solar spectrum.<sup>14</sup> Si PVs were invented in 1954 at the Bell Labs in New Jersey,<sup>15</sup> and since then intensive research and development has culminated in today's high power conversion efficiency of ~25% for non-concentrator single crystal Si solar cells. However, Si PVs have a number of drawbacks which can limit the range of applications for which they are useful, particularly for certain building integration and transportation applications, including their opacity, rigidity, and relatively high weight. Additionally, Si has an indirect band-gap of 1.1 eV, which does not absorb long wavelength light efficiently, and only becomes a direct band-gap semiconductor for photons with energy  $\geq 3.4$  eV, which corresponds to only a small fraction of the useful solar spectrum, as shown in Figure 1.1. This limits the maximum achievable power conversion efficiency and requires that a relatively large thickness of Si (typically 150-300  $\mu\text{m}$ )<sup>16</sup> is needed to efficiently absorb the incident sunlight.

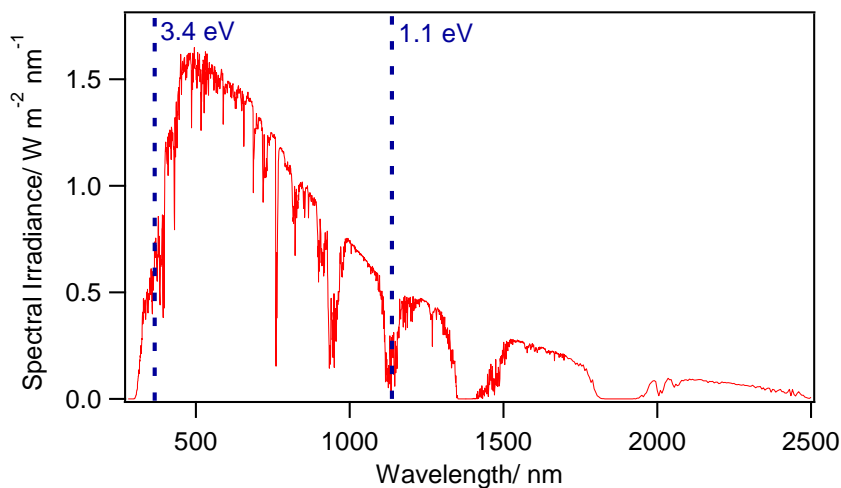


**Figure 1.1:** American Society for Testing Materials (G173-03) reference spectra of the spectral irradiance from the sun with air mass (AM) 1.5 attenuation by the atmosphere.

---

Alternative classes of PVs based on much thinner films of direct band-gap inorganic semiconductors, collectively known as second generation PVs, are based on materials such as amorphous Si, III-V semiconductors (e.g. GaAs or InP), II-VI semiconductors (eg CdS or CdTe), and copper-indium-gallium-selenide (CIGS). These semiconductors offer smaller and more direct band-gaps than crystalline Si, and so a much thinner semiconducting layer can be used which imparts a higher degree of mechanical flexibility and reduced material cost. However, second generation PV still require vacuum and high temperature processing and so use a relatively large amount of energy in their production. One emerging third generation PV technology uses thin films of organic semiconductors as the basis of the photoactive layer and are generically known as organic photovoltaics (OPV). Despite having a lower theoretical maximum power conversion efficiency (*PCE*) than Si PV, OPVs offer some important advantages. These include being much more light weight and flexible, which allows for easier integration into a range of applications for which crystalline Si is simply not practical, faster roll-to-roll manufacture, and the possibility of semi-transparency and colour tunability. The increased versatility of OPVs creates new market opportunities in such areas as wearable electronics and transportation. Since OPVs are also amenable to solution processing at low temperature the manufacturing costs are potentially low due to compatibility with high speed roll-to-roll printing methods.<sup>17</sup>

Modern OPVs are based on a heterojunction of donor and acceptor type organic semiconductors, which is a concept first proposed by Tang in 1986 using thermally evaporated phthalocyanine and perylene derivatives, devices which had a *PCE* of 0.95%.<sup>18</sup> Since then great strides have been made in *PCE* due to the introduction of novel photoactive low band-gap materials, the addition of charge-extraction layers, energy level optimisation of the various components, changes to the architecture of the

device to improve light harvesting, and a better understanding of the device physics. The potential of conjugated polymers to serve as part of the heterojunction in place of small molecule organic semiconductors was shown in 1992 when efficient electron transfer was observed between poly(3-hexylthiophene) and buckminsterfullerene<sup>19</sup>, and in a separate paper between poly[2-methoxy,5-(2'-ethyl-hexyloxy)-p-phenyl-ene vinylene] and buckminsterfullerene<sup>20</sup>. These reports were followed in 1995 by an important improvement in device architecture, in which the electron donor and electron acceptor type organic semiconductors are intermixed to form a complex interpenetrating network of donor and acceptor phases as opposed to a simple bilayer structure which has become known as a bulk-heterojunction (BHJ).<sup>21</sup> Cumulatively these advances have led to the current record *PCE* for laboratory scale OPVs of 11.5%.<sup>22</sup> This is comparable to other emerging third generation PVs such as dye-sensitized cells, 11.9%,<sup>23,24</sup> and quantum dot cells, 11.6%,<sup>25,26</sup> although perovskite PVs have shown greater efficiencies of 22.1%.<sup>27</sup> However due to unanswered stability questions<sup>28</sup> and safety concerns, due to the lead based nature of perovskite PVs, OPVs remain a viable technology.<sup>25</sup> For instance when integrated in transport, damage to the PV is likely and could lead to materials leaching out of the device which, for lead based compounds, is a major environmental and health concern.<sup>29</sup>

### 1.3 Organic Semiconductors

A large degree of the theory discussed in the upcoming sections is taken from references<sup>30,31</sup>. Organic semiconductors offer a number of potential advantages over conventional semiconductors such as Si and GaAs, particularly for use in PVs. These include a relatively low materials cost, low-temperature and high-speed thin film deposition, mechanical flexibility, and the possibility of colour tuning. Organic

---

semiconductors are based on highly conjugated  $sp^2$  hybridised carbon molecules and can be divided into one of two categories: polymeric organic semiconductors, which can conduct charges efficiently along their length, or small molecule organic semiconductors which offer the advantage of a very well-defined optical and electronic properties. In both cases the molecules used are extensively conjugated which ensures that the frontier orbitals are accessible for the injection/extraction of charge carriers. However, transport of free charge carriers in organic semiconductor films is ultimately limited by the process of intermolecular transport, since charge carriers must hop between adjacent molecules. Common polymeric semiconductors include polythiophenes, poly-phenylene-vinylenes, polyfluorenes, and polycarbazoles. Widely used small molecule organic semiconductors are usually variants of fullerenes, phthalocyanines, perylenes or acenes (e.g. pentacene).

The strong optical absorption exhibited by most organic semiconductors stems from the delocalized  $\pi$ -bonding which makes up the conjugated bonds in the molecules. In this bonding configuration the carbon atoms form three  $\sigma$  bonds by hybridization of one s and two p atomic orbitals to form  $sp^2$  orbitals, with the remaining p orbital contributing to the delocalized  $\pi$  bonded network which allows charges to move along the length of the molecule.

The electronic structure of an organic solid can be described using conventional molecular orbital (MO) theory since the properties of the bulk are dominated by those of the molecule. A schematic MO diagram for an organic semiconductor is shown in Figure 1.2(a). Deep potential energy wells for the core atomic orbitals of the individual atoms are depicted as well as MO orbitals at shallower potentials. For an electron to escape from the molecule it requires enough energy to reach the vacuum level (VL), which is a distance just outside the molecule where the electron is at rest. The most

weakly bound occupied MO is known as the highest occupied MO (HOMO) and immediately above this is the lowest unoccupied MO (LUMO). The energy required to remove an electron from the HOMO to the VL is the ionisation potential ( $I_p$ ), and the energy dissipated when an electron moves from the VL to the LUMO is the electron affinity ( $A_s$ ).

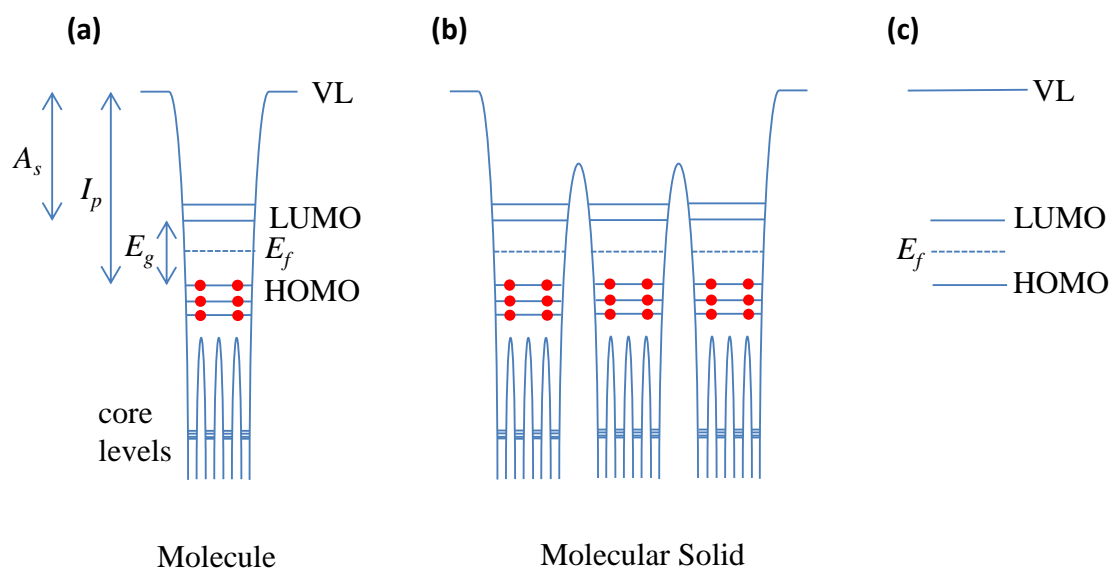


**Figure 1.2:** Schematic molecular orbital diagrams of (a) an organic (molecular) semiconductor, (b) a molecular solid, and (c) the simplified frontier orbitals of a molecular solid.

When brought together there are only weak Van-der-Waals attractive interactions between molecules such that in general the HOMO and LUMO states remain localised on the individual molecules (Figure 1.2(b)) rather than forming extended states between molecules, as in a crystalline inorganic semiconductor. The HOMO and LUMO in an organic semiconductor are equivalent to the sum valence band (VB) and conduction band (CB) in a conventional semiconductor, although due to the persistence of the

---

molecular state they are most accurately described as the HOMO and LUMO. When depicting the molecular orbitals the electronic structure of an organic semiconductor is simplified as in Figure 1.2(c) because only the frontier orbitals are involved in charge transport. The energy level at which the probability of occupancy of an electron state is 0.5 is called the Fermi level ( $E_f$ ) and is an important energy level in the context of the science of the electrode | semiconductor interface, as discussed in more detail later in this chapter. One of the key characteristics of an organic semiconductor for PV applications is the energy difference between the HOMO and LUMO, which is equivalent to that between the VB and CB in conventional inorganic semiconductors and so is widely described as the band-gap ( $E_g$ ). For PV applications  $E_g$  must be chosen to enable absorption of as much of the solar spectrum as possible. For organic semiconductors the electronic structure depends on the chemical structure of the molecule, and therefore  $E_g$  can be engineered to optimise the absorption over the target wavelength range.

In organic semiconductors the excitation of an electron across  $E_g$  results in the formation of a quasi-particle called a Frenkel exciton rather than a free electron and a hole as in the case of crystalline inorganic semiconductors. A Frenkel exciton comprises an electron in the LUMO and hole in the HOMO of the same molecule that are coulombically bound to each other. Excitons are a feature of organic semiconductors because the photo-excited electron and hole are highly localised on an individual molecule or segment of a polymer chain, and due to the small dielectric constant in organic materials of 2-4 which means there is little shielding of the attractive electrostatic interaction between the electron and hole. Frenkel excitons have typically binding energies of 0.3-0.5 eV, an order of magnitude larger than the loosely bound Mott-Wannier excitons found in crystalline inorganic semiconductors. They are also

highly mobile, diffusing between many thousands of molecules before relaxing to the ground state as shown in Figure 1.3. A second class of exciton that is of relevance to OPVs is the charge transfer exciton, where the electron and hole are coulombically bound, but reside on separate molecules. Charge transfer excitations typically have a lower binding energy than Frenkel excitons of the order of  $\sim 0.1$  eV.<sup>32</sup>

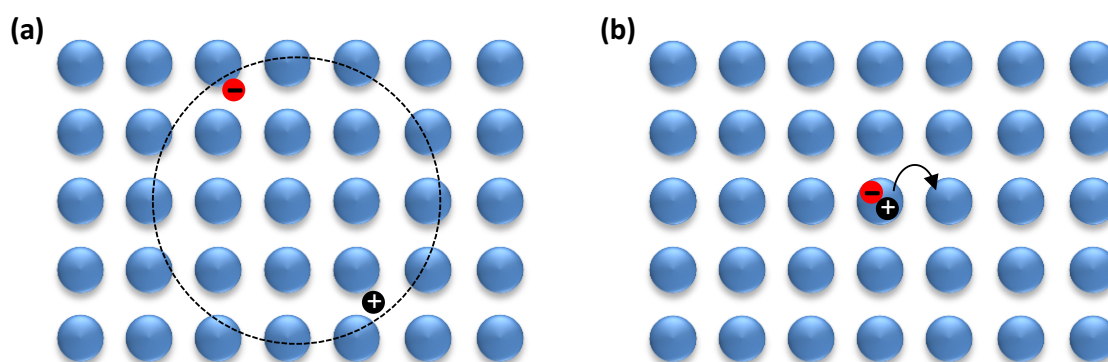


**Figure 1.3:** Interaction ranges and exciton movement for (a) Mott-Weiner and (b) Frenkel excitons

#### 1.4 Energy Alignment at Electrode-Organic Semiconductor Interfaces

The Fermi-Dirac distribution function (Equation 1.1) describes the probability,  $f(E)$ , that any given energy state is occupied at temperature  $T$ ;

$$f(E) = \frac{1}{e^{(E-E_f)/k_B T} + 1} \quad \text{Equation 1.1}$$

where  $E$  is the energy of the electron and  $E_f$  is the Fermi level. It is clear from Equation 1.1 that when the energy is equal to  $E_f$  the probability of finding an electron is 0.5. The energy required to take an electron from  $E_f$  to the VL is called the work function ( $\Phi$ ) which has two components:

$$\Phi = \mu + \chi \quad \text{Equation 1.2}$$

$\mu$  is the bulk chemical potential and is the energy required to remove an electron from the  $E_f$  to a point infinitely far from the solid.  $\chi$  is the surface potential contribution to  $\Phi$  which results from the dipole layer that exists at the surface of all solids due to the spilling of the electron cloud into the vacuum. The dipole layer increases the potential energy of an electron as it passes from the solid into the vacuum and is larger at the surface of metals than semiconductors due to the higher free electron density in metals. In the region just outside the surface the variation in potential energy with distance from the surface is negligible and so the electron is considered to be at rest. This region of unchanging potential extends several micrometres into the vacuum and corresponds to the vacuum level at the surface (VL<sub>s</sub>). As the electron moves beyond this near surface region the potential energy falls away with distance, until at an infinite distance from surface it reaches VL<sub>∞</sub>, as depicted in Figure 1.4.

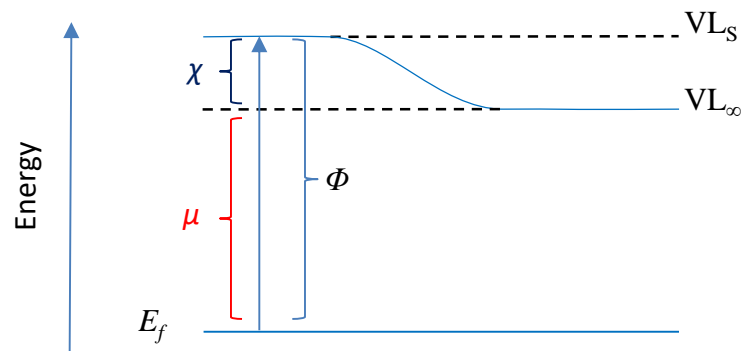


**Figure 1.4:** Energy level diagram showing the contributions to  $\Phi$  made by the chemical potential ( $\mu$ ) and surface ( $\chi$ ) potential.

VL<sub>s</sub> is the energy level of relevance for the definition of  $\Phi$ ,  $A_s$ , and  $I_p$ , and is described simply as the VL throughout this thesis.  $\chi$  depends on the arrangements of atoms at the

---

material surface as well as the nature of the bonds between atoms, since denser structures give rise to a larger  $\chi$  and therefore a larger  $\Phi$ . This is shown by Strayer *et al.* for a W surface such that the  $\Phi$  changes from 4.47 eV for a (111) surface to 5.25 eV for (110).<sup>33</sup>

When organic molecules are adsorbed on a metal surface a decrease in  $\Phi$  is most often observed due to suppression of the native surface dipole layer, brought about by the repulsive columbic interaction between the electron density on the organic molecule and the electron cloud spilling into the vacuum from the metal surface. This repulsive interaction leads to electron density being pushed back into the metal and so decreases the size of the surface dipole. Consequently, it is known as the ‘*push-back*’ effect and causes a decrease in  $\Phi$  due to a decrease in  $\chi$ . This effect can lead to a reduction in the measured  $\Phi$  of samples in the laboratory environment as compared to that of the pristine surface, due to unintentional physisorption of low mass hydrocarbons, siloxanes, or solvent molecules from the atmosphere.

The  $\Phi$  of a material can also be tuned by modification of  $\mu$  by doping with an excess of either negative (*n*-type) or positive (*p*-type) charge carriers, which moves the position of  $E_f$  in  $E_g$  and so alters the chemical potential contribution to  $\Phi$ . In an intrinsic (organic) semiconductor (i.e. with no doping)  $E_f$  is located in the middle of the band-gap. If *n*-doped, the excess of electrons results in the  $E_f$  being shifted towards the LUMO, whereas *p*-doping moves the  $E_f$  closer towards the HOMO. In both cases doping leads to an increase in the conductivity of the material due to an increase in the free carrier density as for a conventional inorganic semiconductor.

When an electrode and organic semiconductor, or two organic semiconductors, are brought into contact with each other, an abrupt shift in the VL can occur due to the

formation of a dipole layer at the interface, or modification of the dipole layer that exists at one or both solid surfaces. This interfacial dipole layer can form for a number of reasons, including charge transfer, chemical reaction between the surfaces and/or a redistribution of the electron cloud (such as the push-back effect). It should be noted that the VL at interfaces between materials is a hypothetical concept but serves well as a concept to understand energy level diagrams at solid interfaces. The effect of dipole layer formation (or modification of the interfacial dipole) on the relative position of the energy levels in each material is illustrated in Figure 1.5.

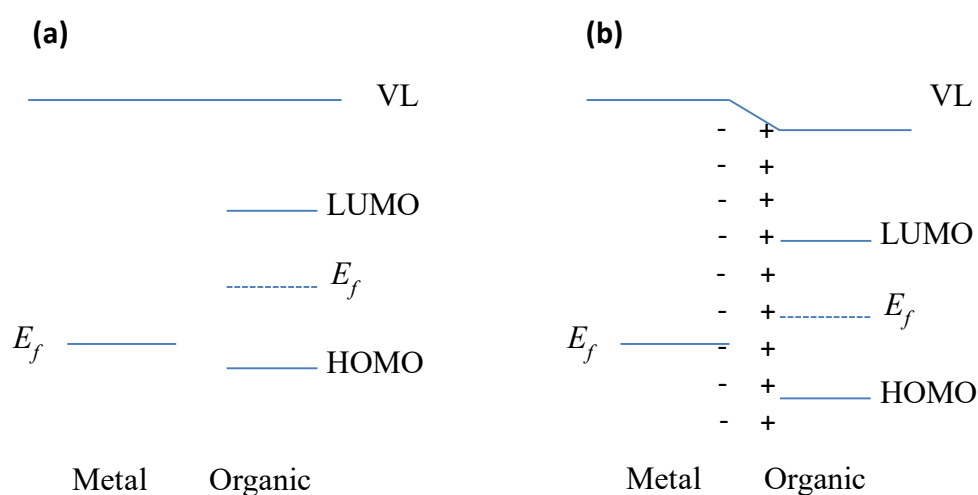


**Figure 1.5:** Schematic Energy level diagram of the interface between a metal and an organic semiconductor (a) before and (b) after interface formation.

VL shifts due to dipole layer formation are most pronounced at metal | organic interfaces because there is a large dipole at the metal surface due to spilling of conduction band electron density into the vacuum.

When the organic semiconductor layer becomes thick enough a ‘*bending*’ of the bands and VL can start to occur due to charge transfer into or out of the bulk of the

semiconductor, just as at the interface between a metal and a conventional semiconductor, as shown in Figure 1.6. This arises due to the tendency of electrons to move to the lowest available energy state until the  $E_f$  of both of the materials comes into alignment as a result of a shift in the vacuum level establishing equilibrium. Since the  $E_f$  in semiconductors is in the band-gap, dopant states are required as a source of electron density if charge is to be donated from the semiconductor into the metal (i.e. if  $\Phi_{\text{organic}} < \Phi_{\text{metal}}$ ) (Figure 1.6(a)), or there must be defect states to accept the charge from the metal if  $\Phi_{\text{metal}} < \Phi_{\text{organic}}$  (Figure 1.6(b)).

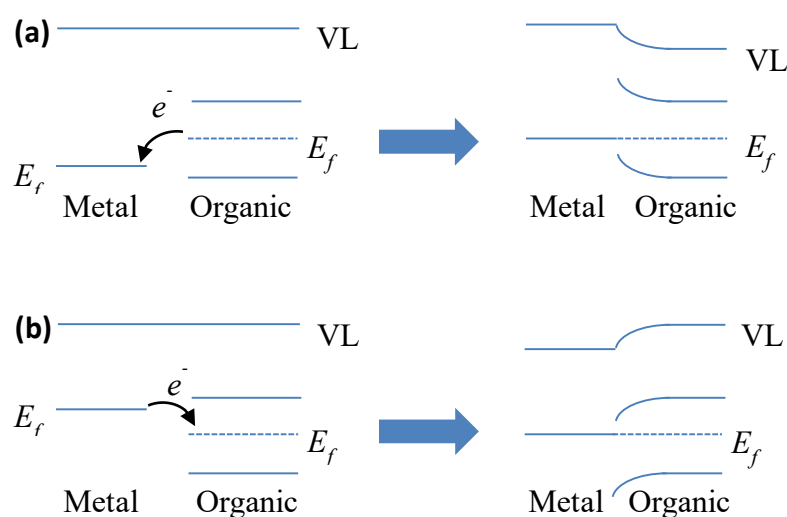


**Figure 1.6:** Schematic frontier orbital diagram showing charge transfer between a metal and an organic semiconductor when (a)  $\Phi_{\text{organic}} < \Phi_{\text{metal}}$  and (b)  $\Phi_{\text{metal}} < \Phi_{\text{organic}}$

Since organic semiconductors used in OPVs are not usually intentionally doped, and the concentration of defects and unintentional dopant states is too low in high purity organic semiconductors to effectively transport enough charge to reach thermal equilibrium, alignment of  $E_f$  across the interface only occurs for very thick films of organic semiconductors, and will often not be achieved for the thickness used in an

OPV device.<sup>34</sup> The redistribution of charges that occurs when a metal-organic semiconductor interface is formed results in a potential gradient in the depletion region, described by the Poisson equation (Equation 1.3):

$$\frac{d^2V(x)}{dx^2} = -\frac{\rho(x)}{\epsilon_r\epsilon_0} \quad \text{Equation 1.3}$$

where  $V$  = the potential,  $x$  = the depletion region width,  $\rho(x)$  = the space charge distribution,  $\epsilon_0$  = the permittivity of free space and  $\epsilon_r$  = the relative permittivity.<sup>35</sup>

### 1.5 Principles of OPV Operation

The simplest structure for a single junction OPV is two organic semiconductors, which together serve as the photoactive layer, sandwiched between two electrodes. The frontier molecular orbital energies of the two semiconductors are chosen to be offset such that one serves as an electron acceptor with respect to the other when photo-excited, as in Figure 1.7(a). One of the electrodes must be transparent to allow light to enter the device and the other must be highly reflective to recycle light not absorbed by the semiconductors on the first pass through the photoactive layer back into the device. In order to convert the incoming light into an electrical current in the external circuit four processes must occur, as shown schematically in Figure 1.7(b). These are: (1) Light absorption resulting in the formation of an exciton.; (2) Exciton diffusion to a heterojunction between donor and acceptor molecules.; (3) Exciton dissociation to form a charge transfer exciton.; (4) charge carrier transport and extraction to the external circuit.

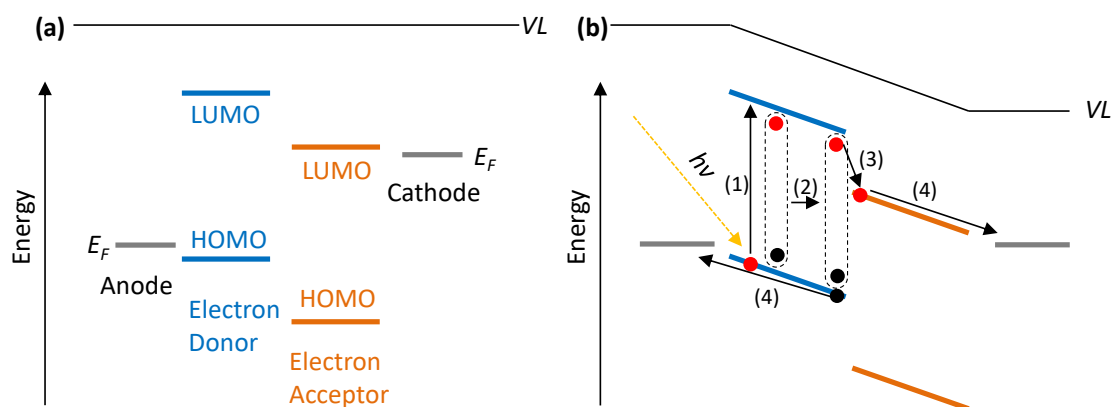


**Figure 1.7:** Schematic energy level diagram for an OPV depicting a (a) zero-field (flat band) diagram and (b) a device at the short circuit condition (see main text for discussion of the four basic processes).

When the incident photons have an energy equal to or larger than the band-gap in either of the organic semiconductors comprising the heterojunction, an electron will be promoted from the HOMO to the LUMO creating a Frenkel exciton. These diffuse randomly between molecules until they either relax back to the ground state or are dissociated to form a free electron and hole. Relaxation to the ground state usually takes place within  $\leq 1$  ns for singlet excitons, which are the majority of Frenkel excitons in OPV devices. The efficiency of light absorption ( $\eta_{abs}$ ) depends on the transparency of the electrode, the path length through the photoactive layer, and the absorption coefficient ( $\alpha$ ) of the organic semiconductors. For a path length of 100 nm, the active layer in an OPV must have an absorption coefficient of at least  $10^5$   $\text{cm}^{-1}$  to absorb 100% of the incident light.

Following formation the exciton will diffuse randomly, unaffected by the electric field, until it reaches an interface between the different organic semiconductors

that make up the photoactive layer. The distance that an exciton can diffuse before recombining ( $L_D$ ) is a function of the exciton lifetime ( $\tau$ ) and the diffusion coefficient ( $D$ ), which is a measure of the speed of diffusion due to Brownian motion as shown in Equation 1.4. Typical values of  $D$  are  $1 \times 10^{-4}$  -  $1 \times 10^{-3}$   $\text{cm}^2 \text{s}^{-1}$  whilst  $\tau$  can be between 0.1-0.5 ns for the organic semiconductors used herein.<sup>36,37</sup>

$$L_D = \sqrt{D\tau} \quad \text{Equation 1.4}$$

The exciton diffusion length limits the dimensions of each of the two organic semiconductors comprising the heterojunction to between 5-50 nm depending on the material. In a bilayer structure, where the semiconductors are simply stacked on top of one another as discrete layers, this severely limits the amount of light absorbed by the OPV. However, by creating a mixed interpenetrating network of donor and acceptor semiconductors in a BHJ, it is possible to ensure that the majority of excitons are generated within an  $L_D$  of a heterojunction interface so that the efficiency of diffusion ( $\eta_{diff}$ ) is high. The BHJ architecture allows thicker photoactive layers to be used; 60-300 nm, so that a larger proportion of the incident light can be absorbed. However, there is still an upper limit to the BHJ thickness set by the electrical resistance to the extraction of free charge carriers to the external circuit. Excitons formed within an  $L_D$  of an electrode often relax to the ground state due to quenching by the electrode, as a result of the close proximity of the high density of metal states.

In order to dissociate the exciton into the individual free charge carriers the binding energy between the electron and hole must be overcome. This is achieved at the interface between different semiconductors if the offset between the frontier orbitals is greater than the exciton binding energy. The dissociation of the exciton at this heterojunction is a two-step process: (i) The exciton is dissociated across the junction

with the electron transferred to the LUMO of the electron acceptor and the hole in the HOMO of the electron donor, but is still coulombically bound with an energy of  $\sim 0.1$  eV<sup>32</sup> as a charge transfer exciton.; (ii) This geminate pair then dissociates into free charge carriers, or undergoes geminate recombination to the ground state. The efficiency of this charge transfer process ( $\eta_{ct}$ ) is related to the size of the frontier orbital offset and the electric field in the active layer due to both the built in applied potential.

Finally, the separated hole and electron undergo transport through the HOMO of the electron donor and into the anode, and the LUMO of the electron acceptor and into the cathode respectively. The efficiency of charge collection ( $\eta_{cc}$ ) depends on the mobility of the charges as defined in Equation 1.5.

$$\mu = -\frac{q\tau}{m}E \quad \text{Equation 1.5}$$

where  $\mu$  is the mobility of the charge carrier,  $q$  is the charge on the particle,  $\tau$  is the scattering time (i.e. the time the charge carrier is accelerated by the field before scattering),  $m$  is the charge carrier mass, and  $E$  is the electric field strength. A large difference in the mobility of the electrons and the holes can lead to an accumulation of one carrier type in the device due to the different rates of extraction of electrons and holes. If this occurs there will be a space charge of the lower mobility charge carrier type leading to lowering of the electric field in the device and a reduced *PCE*.

The total incident photon to current efficiency (IPCE), also known as the external quantum efficiency (EQE), is given by the product of the efficiency of each of these steps as shown in Equation 1.6.

$$EQE = \eta_{abs} \cdot \eta_{diff} \cdot \eta_{ct} \cdot \eta_{cc} \quad \text{Equation 1.6}$$

## 1.6 *JV* Device Characteristics

A typical current density-voltage (*JV*) curve for a PV device under illumination and in the dark is shown in Figure 1.8. The PV device acts as a diode in the dark (dashed line) and current generator under illumination (solid line). When analysing the *JV* curves of a PV device there are 4 key terms that are used to characterise its performance: (i) The short circuit current density ( $J_{sc}$ ); (ii) The open circuit voltage ( $V_{oc}$ ); (iii) The fill factor (*FF*); and (iv) the power conversion efficiency (*PCE*).  $J_{sc}$  is the current density at the short-circuit condition, which corresponds to when the load resistance is  $0 \Omega$  (Figure 1.8(a)). The  $V_{oc}$  is the maximum voltage between the two electrodes and is achieved when the load resistance is high enough to be considered infinite, such that no current flows.

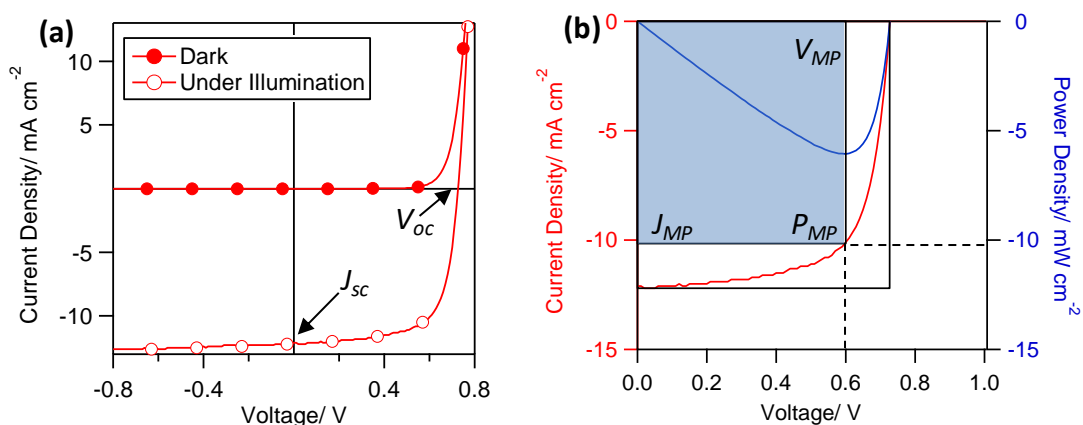


**Figure 1.8:** (a) Representative *JV* characteristics for a PV device in the dark (filled dots) and under illumination (empty dots) with  $J_{sc}$  and  $V_{oc}$  marked; (b) *JV* characteristic showing how the maximum power point ( $P_{MP}$ ) is determined.

To a first approximation the potential difference between the HOMO of the electron donor and the LUMO of the electron acceptor gives the maximum achievable  $V_{oc}$  in an

OPV device. The point at which the product of current and voltage gives the maximum power is called the maximum-power-point ( $P_{MP}$ ) at which the current density and voltage are denoted as  $J_{MP}$  and  $V_{MP}$  respectively (Figure 1.8(b)). The  $FF$  measures the ratio between this maximum point and the product of  $V_{oc}$  and  $J_{sc}$  as given in Equation 1.7. As such, the  $FF$  can be considered a measure of the *squareness* of the  $JV$  characteristic and has a maximum theoretical value of  $\sim 0.8$ .

$$FF = \frac{J_{MP}V_{MP}}{J_{sc}V_{oc}} \quad \text{Equation 1.7}$$

The product of  $J_{sc}$ ,  $V_{oc}$  and  $FF$  therefore gives  $P_{MP}$  which, along with the total power available from the incident light ( $P_{inc}$ ), can be used to calculate the  $PCE$ :

$$PCE = \frac{P_{MP}}{P_{inc}} = \frac{J_{sc}V_{oc}FF}{P_{inc}} \quad \text{Equation 1.8}$$

In an ideal case a PV device can be thought of as a photocurrent source connected in parallel with a rectifying diode. However, in reality the series resistance ( $R_{series}$ ) and shunt resistance ( $R_{shunt}$ ) also have to be included in the equivalent circuit diagram as illustrated in Figure 1.9.  $R_{series}$  results from electrical losses due to resistance to charge carrier transport through the device, and takes into account the charge carrier mobility in the various layers and the resistance to charge transport across the various interfaces.  $R_{series}$  can be estimated from a  $JV$  curve by taking the inverse of the gradient of tangent to the curve at the open-circuit condition.

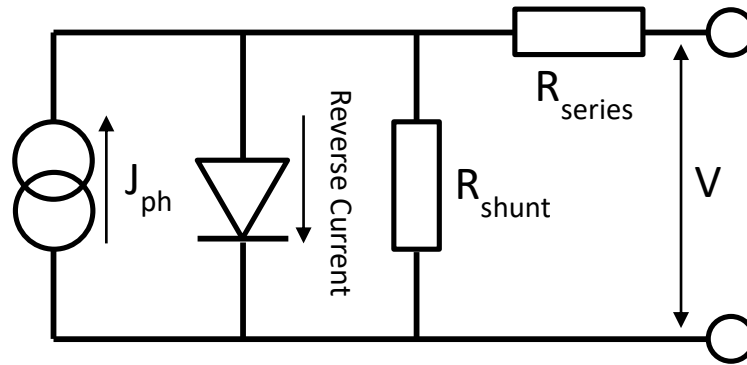


**Figure 1.9:** Equivalent circuit diagram of a PV device, with arrows depicting the direction of current flow.

$R_{\text{shunt}}$  is the resistance to photo-generated charge carriers moving directly between the electrodes which can occur due to pin-holes and non-uniformities in the active layer.  $R_{\text{shunt}}$  can be approximated from the gradient of a tangent to the JV curve at the short-circuit condition. In an ideal PV device,  $R_{\text{series}}$  would be  $0 \Omega$  and  $R_{\text{shunt}}$  would be infinitely large. However, in a real device this is not the case which leads to an erosion of the  $FF$  as shown in Figure 1.10.

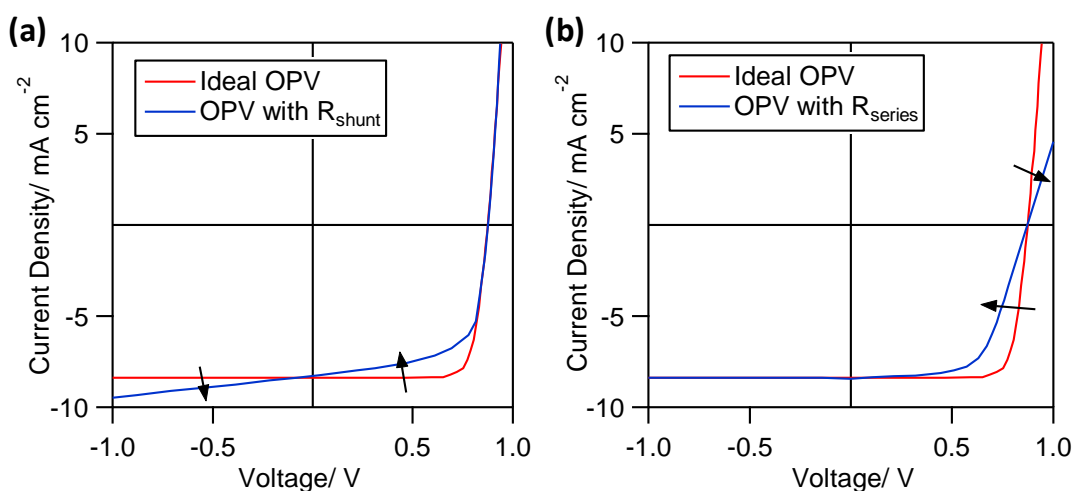


**Figure 1.10:** JV curves illustrating the effect of (a) an increased series resistance and (b) an increased shunt resistance, on the  $FF$ .

---

## 1.7 OPV Processing Techniques

Key considerations for organic semiconductors used in OPVs is a strong absorption of light in the solar spectrum and have a high enough charge carrier mobility to efficiently transport the photo-generated charge carriers to the external circuit.

To deposit these materials either high vacuum techniques (e.g. thermal evaporation) or solution processing techniques (e.g. spin coating, spray coating, or doctor blading) are used, although it is generally accepted that solution processing methods are needed to minimise the cost of manufacturing OPVs, thereby maximising their cost advantage over other PV technologies. This is due to the lower energy input, lower temperature processing, and faster processing speeds possible with solution processing.<sup>17,38</sup> There are, however, limitations to the solution processing such as the need for solvent orthogonality between adjacent layers, a constraint that limits the complexity of the structures that can be fabricated and the materials used.<sup>39</sup> The most common technique for depositing small molecule organic semiconductors, metals, and metal oxides is thermal sublimation in a high vacuum ( $<1 \times 10^{-5}$  mbar), which has a number of advantages over solution processing: (i) Firstly it is easier to produce high quality, pristine films due to the very controlled processing environment.; (ii) Secondly, vacuum processing techniques give a much higher degree of control over film thickness over larger areas (to within  $\pm 0.1$  nm) than solution processing.; (iii) Finally, since vacuum deposition is a solvent free process, multiple sequential layers can be deposited without significantly affecting the underlying films. The flexibility and simplicity in this technique make it very useful and as such it is used extensively in the electronics<sup>39</sup> and packaging industries for small molecule and metal deposition. However, the large energy input required to generate and maintain the vacuum adds to the cost of

---

fabricating OPVs using this technique, which in turn leads to an increased cost-per-watt of electricity generated.

### 1.8 OPV Materials

Electron accepting materials need to be able to accept and transport electrons from the electron donor material. The former requires a  $\geq 0.15$  eV offset between the LUMO energy of the acceptor and the donor. Additionally, there must be a large difference in energy between the acceptor LUMO and the donor HOMO to ensure a large  $V_{oc}$ . Ideally the band-gap of the acceptor is also low enough to efficiently absorb light in the useful part of the solar spectrum for PV applications. Energy levels aside, the acceptor should also have a high electron mobility, a large exciton diffusion length, and sufficient solubility in the case of materials used for solution processed BHJ applications. An ideal BHJ donor-acceptor domain size of 10-20 nm is typically needed to achieve efficient exciton dissociation, which requires spontaneous phase separation as the solvent evaporates.<sup>40,41</sup> The focus of this section is on the use of fullerene electron acceptors (Figure 1.11) because they are the most widely used acceptor in the OPV research and the only type used in the research presented in this thesis.

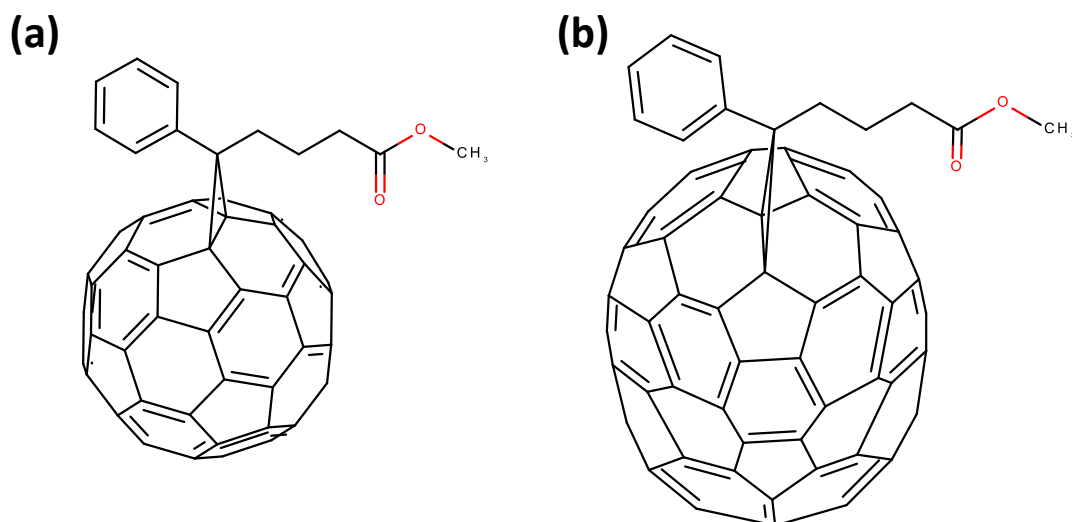


**Figure 1.11:** Molecular structures of electron accepting molecules used in this thesis; (a) PC<sub>61</sub>BM and (b) PC<sub>71</sub>BM.

The use of fullerene compounds as electron acceptors in conjunction with semiconducting polymers was initiated in 1992 with buckminsterfullerene exhibiting rapid, long lived photo-induced charge transfer from poly[2-methoxy,5-(2'-ethylhexyloxy)-p-phenylene vinylene]<sup>20</sup> and poly(3-hexylthiophene)<sup>19</sup>. This was followed by demonstration of a BHJ OPV in 1995 in which the fullerene derivative [6,6]-phenyl C<sub>61</sub> butyric acid methyl ester (PC<sub>61</sub>BM) served as the electron acceptor.<sup>42</sup> PC<sub>61</sub>BM consists of a 60 carbon atom sphere functionalised with phenyl butyric acid methyl ester (Figure 1.11(a)) to improve solubility in common solvents. To a good approximation all of the carbon atoms in the fullerene are sp<sup>2</sup> hybridised and blended thin films of this molecule have a relatively high electron mobility, for an organic semiconductor, of 10<sup>-2</sup>-10<sup>-3</sup> cm<sup>2</sup> V<sup>-1</sup> s<sup>-1</sup>.<sup>43</sup> The latter is due to its close and ordered packing in the solid state, which helps to maximize the overlap between LUMO levels on adjacent molecules. It has been shown that increasing the length of the side chain, increases steric hindrance between

molecules reducing the electron mobility.<sup>44</sup> Unfortunately, whilst the absorption coefficient of PC<sub>61</sub>BM is  $\sim 10^5 \text{ cm}^{-1}$  at 350 nm it falls to  $\sim 10^4 \text{ cm}^{-1}$  at 600 nm.<sup>45</sup> Due to the relatively low cost of synthesis, and very fast electron transfer PC<sub>61</sub>BM has become the ubiquitous acceptor molecule used in OPVs.

After the success of PC<sub>61</sub>BM a number of variants on this structure have been synthesised with the aim of improving the performance of OPVs. One such is [6,6]-phenyl-C<sub>71</sub>-butyric acid methyl ester (PC<sub>71</sub>BM) which has a 70 carbon atom fullerene structure (Figure 1.11(b)). Due to its reduced symmetry, as compared to PC<sub>61</sub>BM, there are fewer disallowed transitions which leads to a stronger absorption in the visible spectrum and so larger photocurrent in OPVs.<sup>46,47</sup> However this improvement in the optical properties is at the expense of a reduced electron mobility,  $\sim 6.8 \times 10^{-4} \text{ cm}^2 \text{ V}^{-1} \text{ s}^{-1}$ ,<sup>48</sup> in the PC<sub>71</sub>BM material due to less efficient packing.

Electron donors should have a high absorption coefficient and large exciton diffusion length, combined with a high hole-mobility. For polymeric semiconductors (Figure 1.12) the molecular weight can have a large effect on OPV performance, since differences in BHJ segregation morphology, charge carrier mobility, polymer solubility, and film crystallinity can all stem from variations in molecular weight.<sup>49-51</sup> Poly(3-hexylthiophene) (P3HT) has long been the workhorse donor material in OPV research, achieving a maximum *PCE* in OPV devices of 4-5%.<sup>52,53</sup> P3HT is based on thiophene units with a solubilising hydrocarbon carbon chain (Figure 1.12(a)) and can be produced in a three-step reaction mechanism. Its widespread use is in large part due to its miscibility with PC<sub>61</sub>BM, stability in air, and simple synthesis. However its relatively large band-gap of  $\sim 2.0 \text{ eV}$  means that it only absorbs photons with wavelength in the range 450-600 nm, leaving a large section of the useful part of the solar spectrum (450-1100 nm) unused, which severely limits the *PCE*.

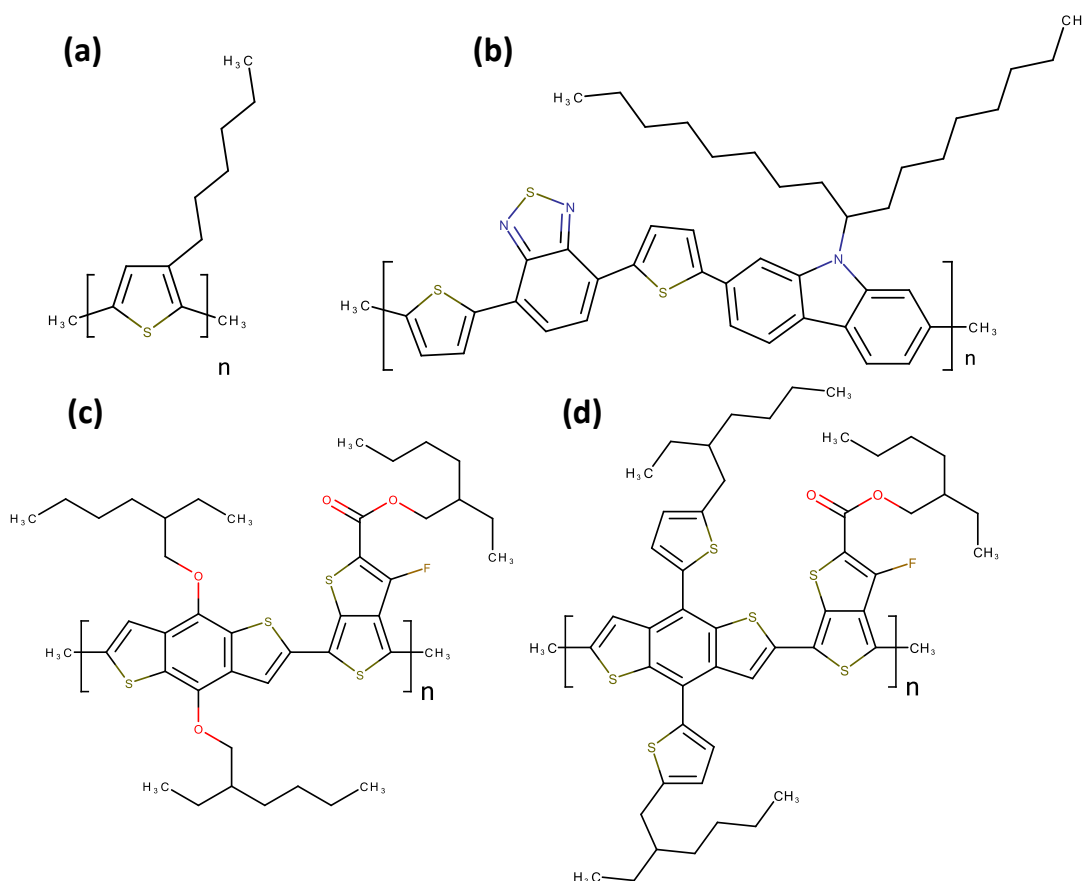


**Figure 1.12:** Molecular structures of electron donating polymers used in this thesis: **(a)** P3HT, **(b)** PCDTBT, **(c)** PTB7, and **(d)** PTDTTT-EFT

Additionally, having a LUMO level of roughly 3.1 eV below the VL leads to an offset with the LUMO of PC<sub>61</sub>BM/PC<sub>71</sub>BM of ~1 eV, which is much larger than is necessary for efficient exciton splitting. The relatively small  $I_p$  also limits the maximum achievable  $V_{oc}$  to around 0.62V<sup>52,54</sup> which further constrains the maximum achievable *PCE*.

The polymeric electron donor Poly[N-90-heptadecanyl-2,7-carbazole-alt-5,5-(40,70-di-2-thienyl-20,10,30-benzothiadiazole)] (PCDTBT) was first synthesised and implemented in OPVs in 2007 and so is a much less well studied system than P3HT.<sup>55</sup>

As shown in Figure 1.12(b) it consists of a carbazole group, with solubilising alkyl chains attached to the central nitrogen, linked to a benzothiadiazole structure via a thiophene linkage. PCDTBT has a donor-acceptor (D-A) type structure with alternating electron donor (thiophenes) and acceptor (benzothiadiazole) groups making up the conjugated backbone.<sup>56</sup> Due to hybridization of the orbitals of these groups a lower band-gap than in P3HT, of  $\sim 1.9$  eV,<sup>57</sup> is achieved. Electron density transfer between these units stabilises the resonant structures leading to less alternation of bond lengths between the double and single bonds which makes the levels more degenerate and so functions to reduce  $E_g$ .<sup>58</sup> PCDTBT has a LUMO level of 3.5 eV and a relatively deep HOMO level at 5.3 eV below the VL, which leads to large  $V_{oc}$  of  $> 0.9$  V in OPV devices using this material as the electron donor, which in turn leads to  $PCE$  as high as 7.5%.<sup>59</sup> In addition to the improved  $PCE$ , and of arguably greater importance, is the substantial increase in operating lifetime and thermal stability<sup>60</sup> of PCDTBT BHJs, which has been shown to be as high as 7 years of use.<sup>50</sup> This excellent stability is attributed to the reduced susceptibility of this polymer towards oxidation, due to the very deep HOMO level. However, a relatively high degree of energetic disorder in this material means that there is a high density of trap states intrinsic to these films as well as low crystallinity in PCDTBT:PCBM BHJs. Consequently the hole mobility is relatively low;  $6 \times 10^{-5}$  cm<sup>2</sup> V<sup>-1</sup> s<sup>-1</sup>,<sup>61</sup> which necessitates the use of thinner films than needed to absorb all of the incident light, of  $\sim 70$  nm.<sup>60</sup>

In order to achieve broad band absorption as well a large  $V_{oc}$ , small band-gap deep HOMO level electron donors are required. One of these is polythieno[3,4-b]-thiophene-co-benzodithiophene (PTB7) which consists of an electron rich benzodithiophene group linked to an electron deficient thienothiophene group, again with solubilising alkyl chains (Figure 1.12(c)). The PTB7:PC<sub>71</sub>BM system can achieve

efficiencies greater than 9%, in large part due to high  $J_{sc}$  values of 15-17 mA cm<sup>-2</sup> whilst retaining a good  $FF$ .<sup>62</sup> The large  $J_{sc}$  is primarily due to very efficient free carrier generation and charge transport, which stems from the low binding energy between charge transfer excitons<sup>62</sup> and the high hole mobility ( $2 \times 10^{-4}$  cm<sup>2</sup> V<sup>-1</sup> s<sup>-1</sup>)<sup>63</sup> when part of a BHJ. The HOMO and LUMO energy levels are at  $\sim 5.2$  eV and  $\sim 3.3$  eV below the VL respectively, leading to a band-gap of  $\sim 1.8$  eV.<sup>64</sup> Consequently, strong absorption is achieved up to  $\lambda \sim 650$  nm after which it tails off rapidly. In order to improve the efficiency of PTB7:PC<sub>71</sub>BM BHJs a small amount ( $\sim 3\%$  vol.) of the high boiling point solvent diiodooctane (DIO) is often added to the solution prior to deposition in order to optimize the morphology of BHJ.<sup>65,66</sup> This additive serves to increase the solubility of PC<sub>71</sub>BM aggregates, promotes smaller domain sizes (from  $>100$  nm to 20 nm) and leads to better PC<sub>71</sub>BM intercalation in PTB7 phase. Unfortunately, PTB7 is relatively unstable: In a study conducted by Soon *et al.*<sup>67</sup> it was shown that PTB7 undergoes rapid photo-oxidation to produce singlet oxygens when illuminated leading to large losses in absorption.

In an effort to improve upon the success of PTB7 the similar polymer Poly[4,8-bis(5-(2-ethylhexyl)thiophen-2-yl)benzo[1,2-b;4,5-b']dithiophene-2,6-diyl-alt-(4-(2-ethylhexyl)-3-fluorothieno[3,4-b]thiophene-)-2-carboxylate-2-6-diyl)] (PBDTTT-EFT) was developed. This involved replacing the alkoxy groups on BDT with thienyl groups as shown in Figure 1.12(d).<sup>68</sup> This modification was found to lead to a smaller band-gap, as compared to PTB7, and a slight reduction in the HOMO (HOMO = 5.24 eV, LUMO = 3.66 eV,  $E_g = 1.55$  eV) which gives an absorption spectrum that peaks at roughly 700 nm and has been shown to absorb out to as far as 800 nm.<sup>68-70</sup> This polymer is used in this thesis as an example of next generation donor type polymer

materials which is designed to have a small band-gap, deep HOMO energy level and good long term stability.

The frontier orbital diagram showing the HOMO and LUMO levels of the organic semiconductors used as the photoactive layers in this thesis, as just discussed, are shown in Figure 1.13

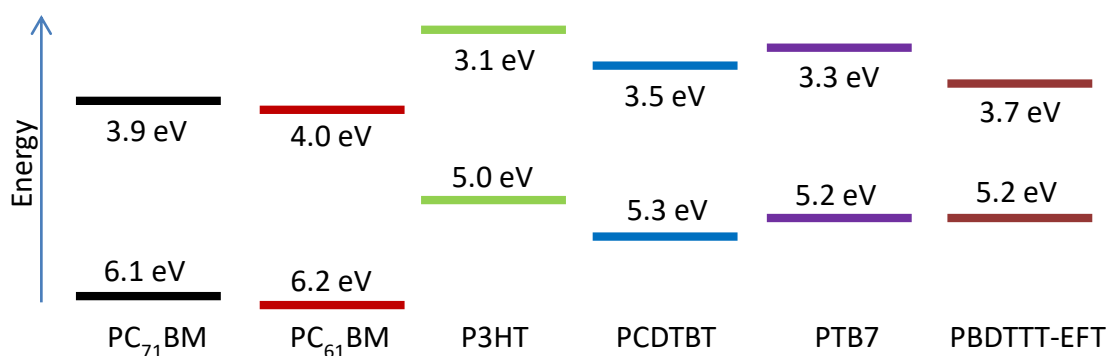


**Figure 1.13:** Frontier orbital diagram showing the HOMO and LUMO levels for the range of organic semiconductors used in the photoactive layer in this thesis.<sup>57,64,68,71–73</sup>

### 1.9 Interfacial Layers for Charge Extraction in OPVs

The performance of OPVs can be greatly improved by the addition of charge transport layers (CTL) at the electrode interfaces, due to a variety of optical and electronic effects. Firstly, the layer can act to align the Fermi level of the electrode close to the relevant frontier molecular orbital in the adjacent organic semiconductor, which minimises losses in the potential energy of the extraction charge carriers. For instance, when extracting electrons if the  $\Phi$  of the electrode (anode) is greater than the difference in energy between the VL and the LUMO of the electron acceptor, then the Fermi level will not be aligned to the LUMO unless there is a high density of *n*-type dopants in the organic semiconductor. This results in a sub-optimal  $V_{oc}$  (labelled  $V_{oc}'$  in Figure 1.14),

given by the difference in the  $\Phi$  of the electrodes, rather than the maximum achievable  $V_{oc}$  ( $V_{oc}^{\max}$ ) which is given by the difference in energy between the LUMO of the acceptor and the HOMO of the electron donor (Figure 1.14(a)). The same is true if the hole-extracting electrode (cathode) has a  $\Phi$  that is too small. Whilst this problem can be resolved by using an electrode with an appropriate  $\Phi$ , this is not always possible due to the limited pallet of metal electrodes to choose from. An interfacial layer with a suitable  $\Phi$  can be used, which allows charge transfer between the electrode and the semiconductor LUMO or HOMO, for electron and hole extraction respectively, resulting in pinning of  $E_f$  and a larger achievable  $V_{oc}$  (labelled  $V_{oc}''$  in Figure 1.14) as shown in Figure 1.14(b). In this way even a high  $\Phi$  electrode such as ITO can act as an electron-extracting electrode, despite its high  $\Phi$ , by depositing a thin film of  $ZnO_x$ .<sup>74</sup>

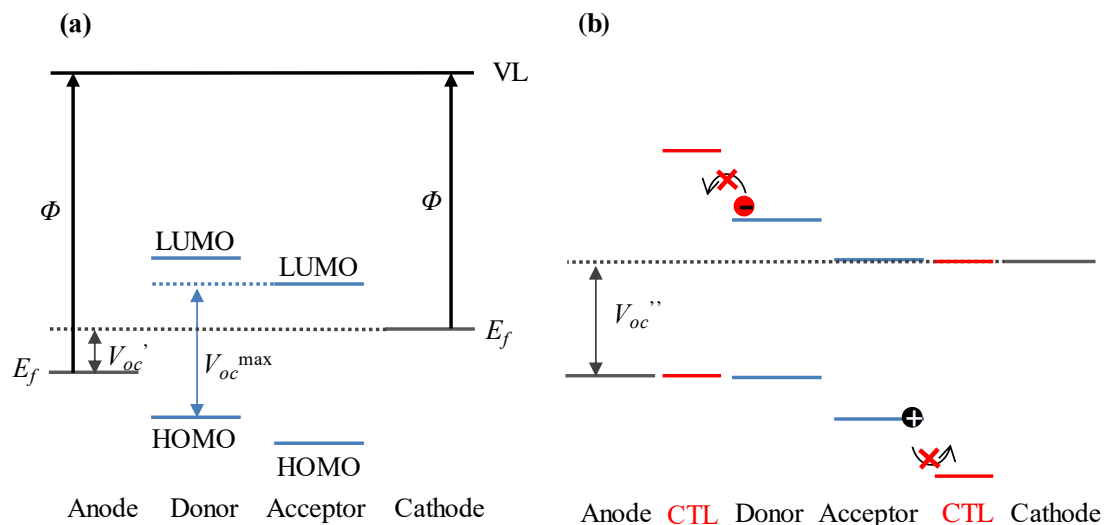


**Figure 1.14:** (a) Schematic energy level diagram showing the maximum voltage ( $V_{oc}^{\max}$ ) achievable in an OPV and how the electrode work function affects the actual voltage ( $V_{oc}'$ ). (b) MO diagram showing the effect of fermi level pinning by interfacial layers on the voltage ( $V_{oc}''$ ) and the charge selectivity of the electrode.

---

As well as Fermi level pinning, CTLs can also act to improve the charge carrier selectivity at the electrode | BHJ interface by having a large barrier to the extraction of the unwanted charge carrier type as illustrated in Figure 1.14(b). For this reason, CTLs are invariably wide band-gap materials which also ensures that they are transparent to light. The improved rectification resulting from using a CTL has been shown to lead to large improvements to the  $FF$  in OPVs.<sup>74–76</sup> The use of these wide band-gap CTLs can also reduce exciton quenching at the electrode contact leading to longer exciton lifetime and improved  $J_{sc}$ .<sup>77</sup>

Wide band-gap CTLs deposited onto the reflective substrate electrode can also function to increase the  $J_{sc}$  by acting as an optical spacer layer enabling the light intensity in the photoactive layer to be maximised, as illustrated in Figure 1.15.<sup>78</sup> Optical spacers can have a large effect on the performance of OPVs that utilise a sub-optimal thickness photoactive layer. Incident light that is not absorbed by the photoactive layer is reflected off the opaque electrode back into the absorbing semiconductor. A microcavity will occur if the reflectivity at the window electrode interface is significant (which it often is when using a thin metal film electrode) as an increased optical field will occur across the gap between the electrodes, trapping the light and forming a standing wave.<sup>79</sup> The redistribution of the optical field can be controlled by varying the thickness and optical constants of the CTL so that a greater absorption of light is achieved (Figure 1.15).<sup>78</sup> The potential of this approach for light management in the device has been demonstrated using  $ZnO_x$ , with theoretical improvements in  $J_{sc}$  of up to 20% for common active layer thicknesses.<sup>80</sup>

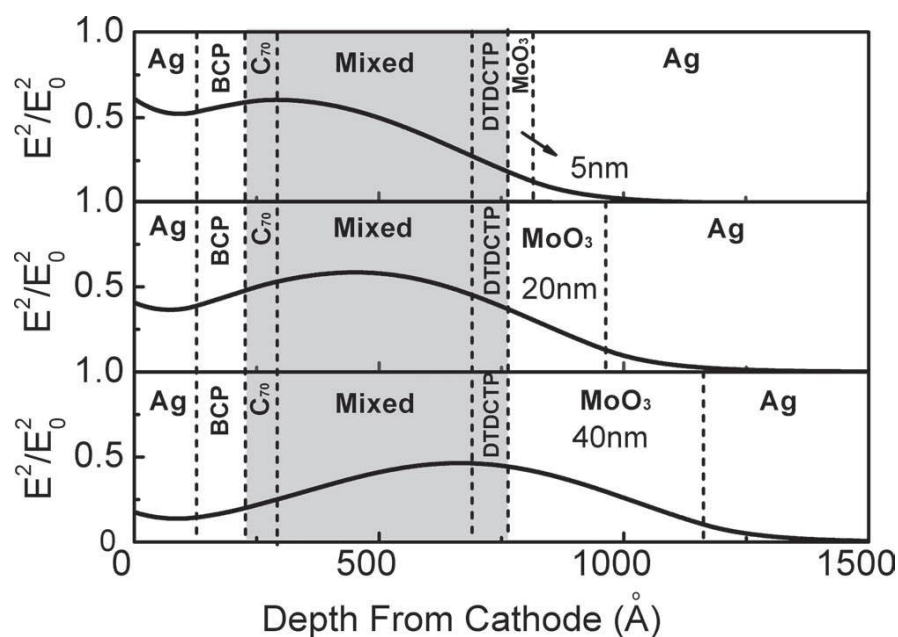


**Figure 1.15:** Calculated optical-field distributions at the wavelengths of 590 nm in a top illuminated OPV. The grey area indicates the solar-absorbing active layers. Reproduced from Lin *et al.*, S.-W. Chiu, L.-Y. Lin, Z.-Y. Hung, Y.-H. Chen, F. Lin and K.-T. Wong, *Adv. Mater.*, 2012, **24**, 2269–2272.

However, in practice the improvement is much lower than theory predicts and the layer thickness has to be very carefully controlled to achieve any significant improvement,<sup>81</sup> adding complexity which inevitably increases fabrication cost. Additionally, as this approach is highly dependent on the path length of the light entering the device the efficacy of the optical spacer depends on the angle of incident light, which constantly changes for a PV in real world conditions.

The CTL can also act as a physical buffer layer protecting the organic semiconductors during deposition of the metal electrode<sup>82</sup> and to improve the device stability by helping to block the ingress of water and oxygen into the device.<sup>83</sup> Many metals, for instance Au, readily diffuse through organic semiconductor layers leading to

filamentary shorts which erodes  $R_{\text{shunt}}$ . The prevalence of such a short can be greatly reduced using a CTL.

### 1.10 Transition Metal Oxides as Interfacial layers

Transition metal oxides (TMOs) were first introduced as CTLs in the late 1990's as hole-injection layers in organic light emitting diodes<sup>84</sup> using the metals V, Mo and Ru to make their respective oxides. In the mid-2000's  $\text{MoO}_3$  and  $\text{V}_2\text{O}_5$  were then shown to act as efficient hole-extracting CTLs to replace PEDOT:PSS in OPVs.<sup>85</sup> Since then the use of TMOs as interfacial layers for hole-extraction has seen widespread use in OPVs. Interest in TMOs primarily stems from their exceptionally high  $\Phi$ , moderate charge carrier mobilities and large band-gap, the latter of which results in a low absorption coefficient for wavelengths of  $>400$  nm.  $\text{MoO}_3$  is exclusively used throughout this thesis so is the focus of this section, although the electronic and optical properties of  $\text{V}_2\text{O}_5$  and  $\text{WO}_3$  have a great deal in common with that of  $\text{MoO}_3$ , and these materials are used for the same purpose in OPVs.  $\text{MoO}_3$  is the most commonly used TMO in OPVs due to its lower evaporation temperature than  $\text{V}_2\text{O}_5$  or  $\text{WO}_3$ , meaning it is easier to process through vacuum evaporation and potentially less damaging to the organic photoactive layer.

$\text{MoO}_3$  is typically *n*-type doped due to oxygen array vacancies forming in the lattice, so the correct descriptor is  $\text{MoO}_{3-x}$ , where *x* is in the range 0 to 0.99. However, in keeping with the literature convention, this material is referred to as  $\text{MoO}_3$  throughout this work. The *n*-type doping imparts a small but significant electrical conductivity of the order of  $10^{-7}$  S  $\text{cm}^{-1}$  at room temperature<sup>86</sup> whereas without the doping the large band-gap of 3.0 eV makes the material very insulating and so restricts

the total thickness used.<sup>87</sup> The band edges in MoO<sub>3</sub> with respect to the VL, as measured using UPS, are shown in Figure 1.16.<sup>86</sup> The VB edge results primarily from occupied O 2p orbitals whilst the CB is dominated by the Mo 4d orbitals.<sup>88</sup>

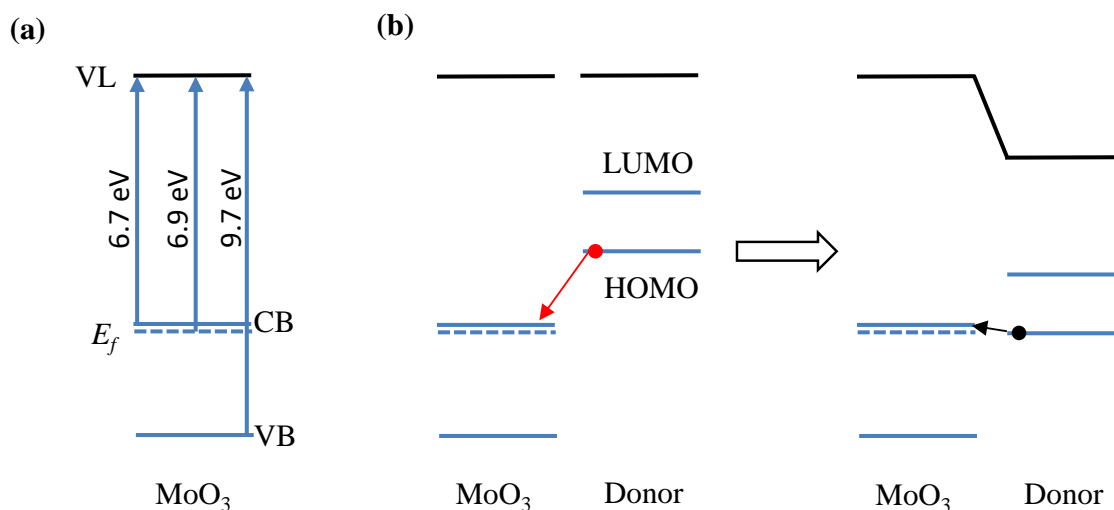


**Figure 1.16:** Energy level diagram depicting (a) the energies of the valence and conduction band edge, and the Fermi level in MoO<sub>3</sub> with respect to the VL, taken from reference 54, and (b) a schematic diagram showing alignment of the HOMO of an electron donor material with the CB of MoO<sub>3</sub> due to charge transfer.

It is into the CB band that electron density from the electrons that would otherwise be binding to oxygen reside when oxygen vacancies occur.

MoO<sub>3</sub> performs exceptionally well as a CTLs for hole-extraction in OPVs, although since the  $I_p$  of most donor type organic semiconductors is in the range 4.8-5.7 eV it is clear that transport of holes is not via the MoO<sub>3</sub> VB which is 9.7 eV below the VL. When organic semiconductors are deposited onto MoO<sub>3</sub>, thermodynamic equilibrium is spontaneously achieved due to transfer of electrons from the organic semiconductor to MoO<sub>3</sub>. This charge is accommodated in the conduction band and

---

oxygen vacancy defect states in the MoO<sub>3</sub> band-gap, which leads to close alignment of the HOMO of organic semiconductor with the CB of the MoO<sub>3</sub> as depicted in Figure 1.16(b). Holes produced due to photo-excitation in the organic semiconductor are extracted to the external circuit via the MoO<sub>3</sub> interlayer through two possible mechanisms: (i) Holes are transported through a high density of filled defect states just below the CB edge, composed primarily of oxygen vacancies. This will occur only if the defect density is large enough that these states overlap to form a continuum. (ii) Alternatively, electrons are transported from the electrode into the HOMO of the organic semiconductor via the MoO<sub>3</sub> CB, which is equivalent to hole extraction. This is made possible because of the close alignment of the HOMO of the donor and CB of MoO<sub>3</sub>. As the density of dopant levels in MoO<sub>3</sub> is strongly affected by the adjacent metal<sup>89</sup> the validity of either mechanism will change with different OPV structures.

### **1.11 Top-Illuminated OPV Device Architectures**

Conventionally thin film PVs allow light into the device through a thick transparent substrate (usually glass) coated with a transparent substrate electrode, which also serves as a supporting substrate. Whilst this architecture provides a mechanically strong and stable substrate on which to fabricate a PV device, there are number of situations where it would be beneficial to use an architecture in which light enters through the top non-supporting electrode as shown in Figure 1.17.

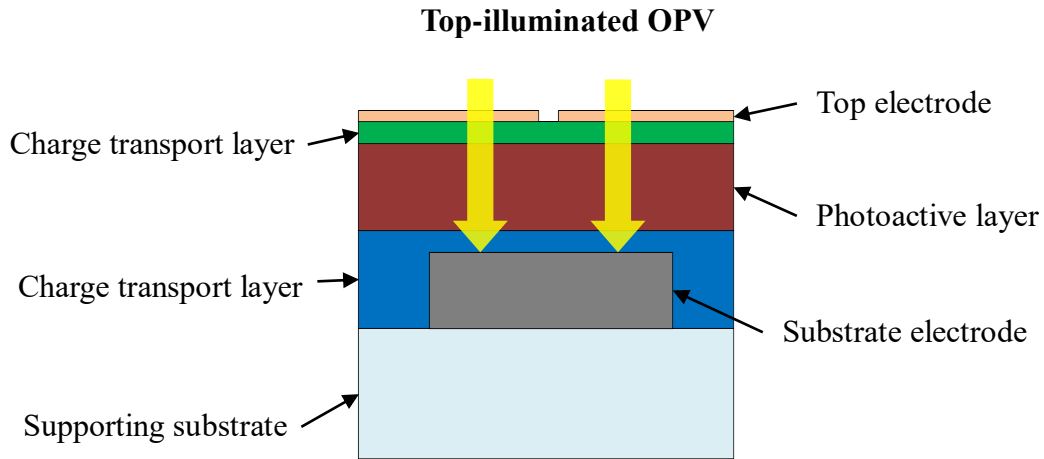


**Figure 1.17:** Schematic diagram of the structure of a top-illuminated OPV.

The current industry standard for transparent substrate electrodes is a glass substrate coated with a 100-300 nm thick film of the *n*-type degenerate semiconductor, tin-doped indium oxide (ITO). This electrode is highly transparent and conductive, although it requires relatively thick films to achieve the necessary  $R_{\text{sheet}}$  of  $< 10 \Omega \text{ sq}^{-1}$ , needed for large area OPV applications, which limits the transparency to between 70-80% across the visible spectrum.<sup>90,91</sup> Unfortunately, ITO is also prohibitively expensive for OPV applications, since OPVs will need to be low cost if they are to be economically viable. ITO is also not amenable to rapid solution processing using roll-to-roll deposition or for mechanically flexible device applications because it is intrinsically brittle. Cheaper transparent metal oxides have been researched as replacements to ITO, such as Al doped  $\text{ZnO}_x$  and fluorine doped  $\text{SnO}_2$ , however these are brittle electrode materials and have a high surface roughness which renders them poorly matched to OPVs where the photoactive layer thickness is typically less than 100 nm.<sup>92,93</sup> Top-illuminated OPVs are not reliant on ITO as a substrate electrode but require a highly reflective mirror electrode at the substrate instead. ITO cannot be used

---

as the top electrode either since in order to achieve a high transparency it must be sputtered followed by annealing at 300°C, both of which would damage the underlying organic semiconductors. Top-illuminated device architectures remove the use of ITO and so allows for the production of mechanically flexible and cheaper OPVs. Top-illuminated OPVs offer much greater versatility in the choice of supporting substrate and so a greater degree of freedom in design for different uses. For example, they can be deposited on materials of technological importance, such as aluminium for automotive applications and steel for building integration where considerations such as flexibility, weight, price, and/or stability of the substrate are an issue.

In order to achieve high performance top-illuminated OPVs a low cost, highly reflective substrate electrode with good long term stability towards oxidation in air is required. Consequently, optically thick films of Ag and Al are most often used because these have high reflectivity over the relevant wavelength range for PV applications; 400-1100 nm. Additionally, they have the added benefits of being mechanically flexible when in thin film form, as well as being easy to deposit reproducibly using high speed roll-to-roll vacuum evaporation.<sup>94</sup> Another important consideration for the substrate electrode in top-illuminated OPVs is the stability, to oxidation in air and other chemical processes used when fabricating the device. The substrate electrode must also be smooth enough not to cause parasitic shunting in the device. Whilst Al is cheaper than Ag it does have the disadvantage of forming a native oxide that is thick enough to adversely affect the efficiency of charge collection at the interface leading to an increased  $R_{\text{series}}$  in PVs. An Al:Au alloy was shown by Chen *et al.* to function well as an electron-extracting electrode in OPVs as well as being highly resistant to oxidation.<sup>95</sup> A Ag | AgO<sub>x</sub> electrode has been shown to perform much better as the hole-extraction electrode than the Ag alone due to an increased  $\Phi$ , which aligns the electrode  $E_f$  more

---

closely with the HOMO of the electron donor.<sup>96–98</sup> In a similar vein an electrode structure of Cr (5 nm) | Al (5 nm) | Cr (5 nm) has been shown to form smooth and stable substrate electrodes.<sup>99,100</sup> In that case, the stability is attributed to the partial oxidation of the Cr during the OPV fabrication leading to a conductive CrO capping layer. A number of groups have also shown that it is possible to fabricate OPVs directly onto stainless steel, so that it functions as both the supporting substrate and an electrode.<sup>101,102</sup>

Another approach to improving the performance of top-illuminated OPVs is through nano-structuring of the back contact to increase the electrode surface area and/or to improve light trapping in the device.<sup>103–105</sup> With large structures, scattering of the incident light occurs, which leads to a longer path length of the light through the photoactive layer and so more efficient harvesting of the incident light. Nano-structuring with dimensions much less than the wavelength of the incident light has also been shown to increase *PCE* due to surface plasmon enhanced absorption in OPVs. Surface plasmons are collective oscillations of conduction band electrons that localise and concentrate incident light at the metal | semiconductor interfaces for frequencies at and below the surface plasmon resonant frequency of the metal.<sup>106</sup> For this application Ag is the metal of choice due being highly conductive and having low losses due to inter-band transitions below ~3.9 eV, with a strong plasmonic absorption in the visible spectrum.<sup>107,108</sup>

As previously alluded to, when considering alternatives to ITO as a transparent electrode a  $R_{\text{sheet}}$  of  $< 10 \Omega \text{ sq}^{-1}$  and a far field transparency of  $> 80 \%$  are both essential for practical applications. Too high a  $R_{\text{sheet}}$  results in ohmic losses which, whilst not always noticeable for small area lab scale devices, become very significant in devices with a practical photoactive area.<sup>90,109</sup> For all window electrode types there is a trade-off

---

between transparency and  $R_{\text{sheet}}$  and it is a false economy to improve one of these parameters at the expense of the other. As with the substrate electrode the window electrode must also be stable towards oxidation, flexible, and cheap. Currently the electrode materials most intensively investigated for the transparent electrodes in top-illuminated OPVs are graphene/graphene oxide,<sup>110–112</sup> carbon nanotubes,<sup>113</sup> conductive polymers,<sup>114,115</sup> metal nanowires<sup>116</sup> and thin metal films.<sup>78,117</sup> These are often used in conjunction with a grid of optically opaque current collecting bars which have a thickness in the order of micrometres overlaid onto a transparent electrode with sub-optimal  $R_{\text{sheet}}$ .<sup>118</sup> In this way more resistive but higher transparency electrodes can be used and still be able to efficiently extract charge due to the close proximity to the current collecting bars.<sup>100,119</sup> However, this composite approach has a number of issues including adding complexity/cost to the device, partially shadowing the photoactive layer, and leading to an increased likelihood of shunting between the two electrodes when used as the substrate electrode due to the large thickness of the bus bars as compared to the photoactive layer. Thin metal films, deposited by vacuum evaporation, provide a simple and controllable way to achieve transparent conducting electrodes, with thicker films leading to a lower sheet resistance at the expense of reduced transparency. Vacuum evaporation is well-established in the packaging industry as a low cost, large area processing method for the deposition of thin metal films that is compatible with roll-to-roll deposition onto flexible substrates, and offers the necessary high degree of control over metal film thickness.<sup>120</sup> Ag is the metal of choice for this application because it has the highest conductivity<sup>121</sup> and the lowest absorbance<sup>122</sup> of the earth abundant metals over the visible spectrum, combined with relatively high stability towards oxidation in air.

---

In order to reduce the losses in transparency upon increasing the film thickness, champion top-illuminated OPV devices use a triple layer window electrode structure of dielectric | metal | dielectric (DMD) with the dielectrics being materials with a high refractive index such as metal oxides or polymers.<sup>105,117,123,124</sup> This structure acts to increase the transparency of the electrode by suppressing losses due to surface plasmon excitation and reducing reflection. Surface plasmons occur when the real part of the dielectric constant of the metal is negative and has a greater magnitude than that of the dielectric layer at the interface. Therefore, the far-field transparency of the metal can be increased by depositing materials with a large dielectric constant. For Ag the transparency has been shown to increase when deposited on materials such as WO<sub>3</sub> or MoO<sub>3</sub>.<sup>92,125</sup> The optical transmittance of the metal is also increased due to a decrease in the reflectivity of the film when capped with dielectric materials. This effect is shown to increase with materials with higher refractive indexes due to the refractive index of the DMD structure being closer to that of air than the bare metal structure.<sup>78,92,125</sup> Additionally, the underlying dielectric layer must also serve as a CTL, since it is inside the device, which limits the range of materials that can be used for this purpose. Sandwiching metal electrodes between dielectric layers allows metal thickness above the metal percolation threshold to be used (11-15 nm) such that the necessary conductivity can be achieved whilst retaining a high degree of transparency as shown in Figure 1.18.

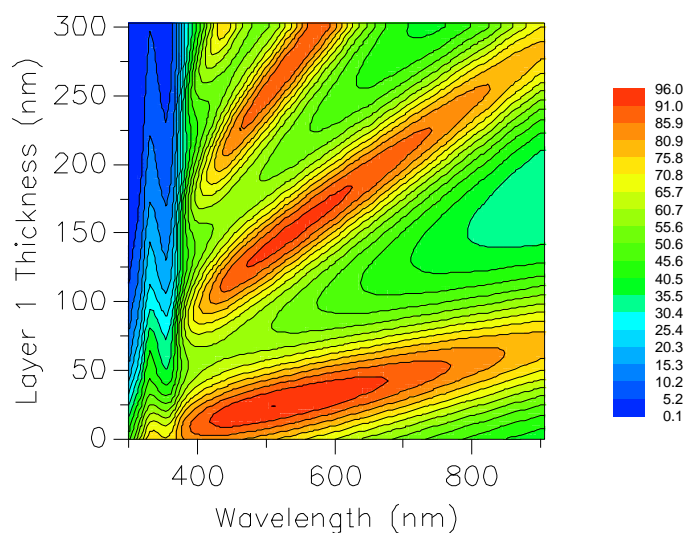


**Figure 1.18:** Modelled variation in transparency (MacLeod Thin Film Centre) of a glass | MoO<sub>3</sub> (10 nm) | Ag (11 nm) | MoO<sub>3</sub> film with varied MoO<sub>3</sub> thickness

The DMD electrode structure can be used to trap light in the OPV *via* a microcavity effect, although as already stated there are drawbacks to this approach. These are that it requires a very high degree of control over the thickness of each layer in the device over a large area, is wavelength dependent, and requires optimisation for different angles of incident of light. It is therefore important to explore other ways to produce more transparent metal films, the simplest of which is to make the Ag layer thinner. However, Ag has a high surface energy and so thin films of this metal typically have a high percolation thickness of > 10 nm, below which they form discontinuous island like structures which are poorly conductive and couple strongly with visible light due to excitation of localised surface plasmons.<sup>126</sup> This is particularly the case when evaporating Ag onto the transition metal oxide and/or organic semiconductors invariably used for extraction of charge carriers in OPVs, since Ag binds very weakly to these classes of materials and the surface energy mismatch is a powerful driver for nanoparticle formation.<sup>123,127</sup> To counteract this, a number of strategies have been

---

proposed: A thin (1 nm) metal seed layer of either Al or Au has been shown, by the groups of Leo<sup>123,128</sup> and Yang<sup>124</sup>, to lead to much better film forming properties of evaporated Ag. An alternate approach proposed by Schubert *et al.*<sup>129</sup> is to make a Ca:Ag composite electrode which was shown to have a high transparency whilst maintaining a relatively low sheet resistance of 27.3 ohm sq<sup>-1</sup>, although this is too high for use in practical OPV devices. Zuo *et al.* designed a gradient Ag electrode with increasing electrode thickness (15-32 nm) as it approached the current extraction grid.<sup>117</sup> This approach takes advantage of the intensity gradient of thermal dissipation losses, which is less intense far from the extraction grid and so a less conductive, but more transparent, film can be used.

In summary top-illuminated OPV device architectures are at a relatively early stage of development but show promise for a number of OPV applications. There are challenges still to be addressed with this architecture particularly with regards to both the transparent and reflective electrodes, which are the topic of this thesis. In Chapter 3 of this thesis the development of a novel reflective substrate electrode based on an Al | Cu bilayer with an ultra-thin Al layer is discussed. This same electrode is used in Chapter 4 due to its remarkably low work function and stability to probe the interface between the electrode and organic semiconductors and thus propose a new design-rule for BHJ OPVs. In Chapter 5 the focus moves to the transparent top-electrode in which a novel solution processed organo-molybdenum oxide bronze is developed and characterised. This is shown to effectively act as a seed layer to promote the growth of highly transparent, low sheet resistance, stable silver window electrodes for top-illuminated OPVs as well as fulfilling the role of a charge blocking layer. In the final results chapter, Chapter 6, preliminary results are shown relating to the nano-structuring

of the back electrode as a method to increase the path length of light in the OPV and thus enhance absorption.

---

## Chapter 2.

# Experimental Techniques

This chapter gives an overview of the experimental techniques and methods used to acquire the results presented in Chapters 3-6 of this thesis. Details of particular relevance to specific experiments are also provided at the beginning of each results chapter.

### 2.1 Thin Film Fabrication Techniques

#### 2.1.1 Substrate Preparation

Glass substrates were prepared by cutting 1.2 mm thick glass microscope slides (VWR Super Premium) to sizes of either  $12 \times 12$  mm,  $18 \times 18$  mm, or  $26 \times 26$  mm depending on the application.  $12 \times 12$  mm glass substrates with an 8 mm wide ITO strip were purchased from Thin Film Devices Inc. with an ITO stated thickness of  $145 \text{ nm} \pm 10 \text{ nm}$  and a sheet resistance of  $15 \Omega \text{ sq}^{-1} \pm 3 \Omega \text{ sq}^{-1}$ . Immediately prior to use the slides were cleaned by:

- Rinsing to remove debris from the cutting procedure (glass substrates only),
- Ultra-sonic agitation for 10 minutes in a dilute aqueous solution of DECON surfactant (Neutracon),
- Rinsing with high purity ( $>10 \text{ M}\Omega \text{ cm}$ ) deionised water,
- Ultra-sonic agitation for 10 minutes in high purity deionised water,
- Rinsing with iso-propanol (IPA),
- Ultra-sonic agitation for 10 minutes in IPA,

- 
- Drying in a stream of nitrogen.
  - Suspension in hot acetone vapour for 10 seconds then drying in a stream of nitrogen.

Ultra-sonic agitation was performed with a Fisherbrand FB11002 ultrasonic bath.

The substrates were then exposed to ozone generated from ambient air using an ultra-violet light (UV/O<sub>3</sub> treatment) to remove solvent residue and physisorbed hydrocarbon contaminants from the atmosphere at the glass surface. This treatment also raises the surface energy of the glass and so increases the hydrophilicity, and is an essential treatment immediately prior to surface chemical derivatisation with a molecular monolayer (see below). UV/O<sub>3</sub> treatment was conducted for 15 minutes followed by 5 minutes in the chamber with the UV lamp off, during which the ozone level gradually decayed. The chamber was then removed of all ozone vapour with a rotary pump. A Novascan PSD-UVT UV/O<sub>3</sub> rig with a UV lamp (185 nm and 254 nm, 20mW cm<sup>-2</sup>) was used to generate ozone.

### **2.1.2 Molecular Monolayer Deposition**

Molecular monolayers can be used to promote the adhesion of some metals onto the surface of glass.<sup>130</sup> This increased binding strength reduces the diffusion of the metal atoms when they arrive at the glass surface from the vapour phase, so they are more likely to form a continuous metal film at very low thicknesses than would otherwise be the case. To deposit these monolayers glass slides are UV/O<sub>3</sub> treated to functionalise the surface with a high density of hydroxyl moieties. These are then immediately transferred to a desiccator containing a small volume (< 0.5 ml) of the molecule used to form the monolayer in a vial and the pressure is reduced to 20-50 mbar. The molecular

adhesive molecules used were 3-mercaptopropyltrimethoxysilane (MPTMS, Sigma Aldrich) and 3-aminopropyltrimethoxysilane (APTMS, Sigma Aldrich), 4 drops of each, or separately with 8 drops dispensed from a standard glass pipette. These molecules both have methoxysilane groups which are able to bind to the treated glass hydroxyl moieties via siloxane linkages to form a dense monolayer (Figure 2.1). The second functional group; either thiol or amine, is chosen to promote the adhesion with the metals Cu, Ag, or Au, binding them strongly to the glass surface.<sup>131,132</sup> It has been shown previously by Stec *et al.*<sup>130</sup> that the amine group in APTMS also acts to catalyse the formation of the siloxane linkages to the glass surface. Due to this a much shorter time is required to deposit a dense monolayer of APTMS or mixed APTMS and MPTMS (1 hour), as compared to MPTMS only (>70 hours). This procedure can also be applied to ITO coated glass and various other films which have native surface hydroxyl groups, such as aluminium oxide or molybdenum oxide. As also shown in Figure 2.1 crosslinking can also occur between adjacent molecules.

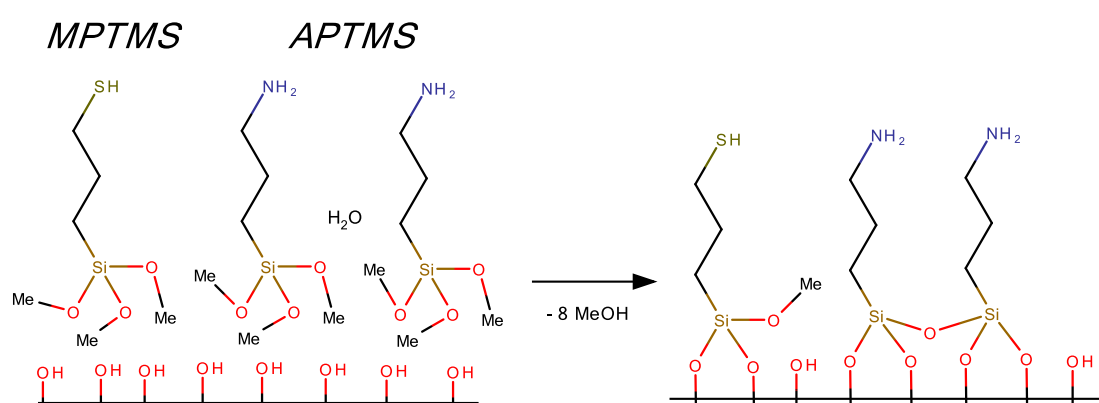


**Figure 2.1:** A schematic showing the molecular structure and proposed binding mechanism of MPTMS and APTMS to a surface with native hydroxyl groups.

### 2.1.3 Vacuum Evaporation Deposition

Vacuum evaporation of thin films of metals, metal oxides and small organic molecules was performed using a CreaPhys Organic molecular evaporator housed in an MBRAUN MB 20G LMF N<sub>2</sub> filled glove box. Small molecule organic semiconductors and metals were evaporated from resistively heated boron nitride crucibles and tungsten filament boats respectively. Metal oxides were evaporated from a boron nitride crucible housed in a tungsten boat. High vacuum was achieved using a two stage pump process, a first stage in which a rotary pump achieves a pressure of ~0.1 mbar followed by a turbo-molecular pump stage which reduces the pressure to  $<1 \times 10^{-5}$  mbar, which is suitable for evaporation. The sample substrates were mounted ~30 cm above the sources on a rotating holder and were shielded from the sources by a shutter that is opened only when the required deposition rate is achieved for the material. Rotation ensured homogeneous material deposition over a number of separate substrates. Two calibrated quartz crystal microbalances (QCMs) mounted on either side of the rotating substrate holder were used to monitor the rate and thickness of source material deposition onto the substrates. Typical deposition rates, source temperatures, and film thicknesses for each material are given in each results chapter.

The thickness of the films deposited in the evaporator is monitored using a QCM which allows for real time accurate monitoring of the film thickness.<sup>133</sup> An oscillating electric field is applied to the quartz crystal via Au electrodes which induces an oscillating acoustic wave perpendicular to the crystal surface. When incoming material condenses on the crystal the magnitude of dampening of the frequency of oscillation depends on the thickness, density and impedance of the material condensing on the crystal surface, and so from the change in frequency the thickness of the material can be calculated providing its density and shear modulus is known. This is described by the

---

Sauerbrey equation (Equation 2.1) which relates the observed change in oscillation frequency of the QCM to the change in mass of the crystal.<sup>134</sup>

$$\frac{\Delta f}{f} = -C_q f \Delta M_f \quad \text{Equation 2.1}$$

Where  $f$  is the original frequency of oscillation,  $\Delta f$  is the change in frequency of the crystal caused by the change in mass,  $\Delta M_f$ , due to the evaporation of the foreign material, and  $C_q$  is the crystal constant of the clean material, i.e. quartz. As  $\Delta M_f$  is equal to the density multiplied by the thickness of the foreign material if the density is known then the thickness can be calculated through changes in frequency. The accuracy of this measurement is increased by including a Z-match term which takes into account differences between the shear modulus and density of the incoming material and the quartz.<sup>135</sup>

Even though the QCM is positioned as close to the substrate as possible there is often some discrepancy between the thickness given by the QCM and that measured directly post-deposition using atomic force microscopy (AFM). This difference is seen when there is geometric misalignment or when the incoming material is highly viscoelastic, as is often the case for organic semiconductors, as the Sauerbrey equation assumes a completely rigid material.<sup>134</sup> This is corrected by determining a tooling factor for each source and material whereby the output from the QCM is the product of the QCM reading and the tooling factor. In order to determine the tooling factor for each source a thick film (typically, 50-100 nm) is deposited onto a very flat substrate and the thickness measured directly by scoring a step edge in the film, taking care not to scratch the underlying substrate (Figure 2.2).

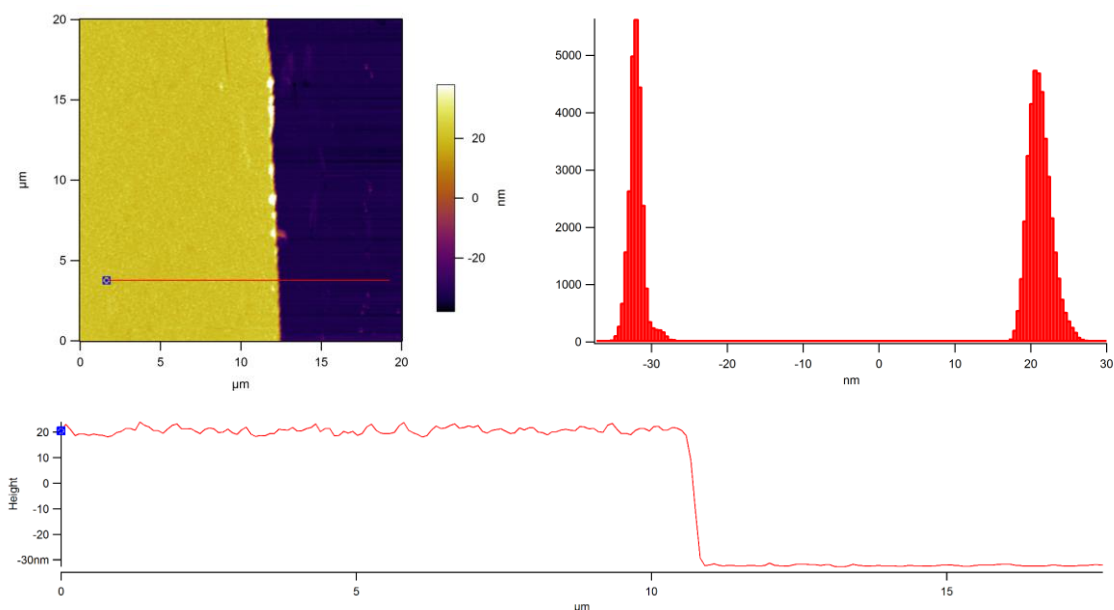


**Figure 2.2:** (a) An AFM image of a step in an evaporated film with (b) a histogram showing the height distribution and (c) a representative line scan taken from the image in the top left.

Multiple step edges are scored on each sample and the mean step height determined for each image from the peak-to-peak difference in a histogram of the pixel heights that make up the image, as shown in Figure 2.2. The tooling factor can then be calculated as:

$$F_m = F_i \frac{T_m}{T_i} \quad \text{Equation 2.2}$$

where  $F_m$  is the new tooling factor required,  $F_i$  is the tooling factor used in the evaporation (initially set to 100 for an unknown material),  $T_m$  is the film thickness measured by AFM, and  $T_i$  is the thickness indicated by the QCM.

### 2.1.4 Spin Coating

In order to deposit thin films of organic semiconductors from solution, concentrated solutions were deposited using the spin coating method, which is a reproducible within

---

$\pm 5\%$  for films with thicknesses  $< 0.5 \mu\text{m}$  over small areas. The substrate is placed on a stage and held in place with a vacuum chuck, before rapidly rotating the stage which drives the excess solution off the surface via centripetal force, leaving a uniform thin film.<sup>136</sup> Films were deposited either by drop casting, in which the surface of the substrate is covered by the solution and then spun, or by spin casting where the solution is dropped onto a spinning substrate. Spin casting typically results in smoother films, though requires a good wetting of the substrate, and is the preferred method for use with volatile solvents such as chloroform. The spin speed, spin time, and solution concentration are used to control the film thickness. Spin coating was performed using a Krüss spin-coater integrated in the glove box, unless otherwise stated. Spin coating in air was performed using a Chemat Technology Spin-Coater KW-4A system.

## **2.2 OPV Device fabrication**

OPV devices were fabricated in both top-illuminated and conventional bottom-illuminated architectures as shown in Figure 2.3. These two classes of device structure can further be separated into inverted and non-inverted structures where electrons (inverted) or holes (non-inverted) are extracted from the supporting substrate electrode. Device fabrication and testing was carried out in the same nitrogen filled glovebox unless otherwise stated.

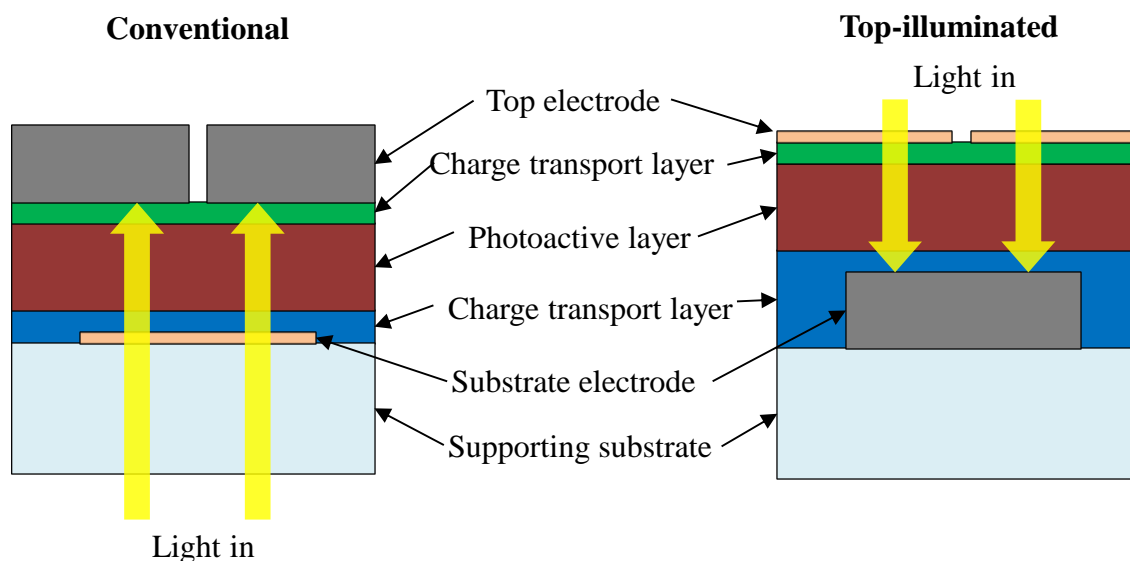


**Figure 2.3:** Schematics of a conventional and top-illuminated OPV device architecture indicating the layers used and the direction of light through the device.

### 2.2.1 Metal electrode deposition

Reflective substrate electrodes were fabricated on pre-cleaned glass slides by thermally evaporating a 60 nm thick film of either Ag (at  $0.1 \text{ nm s}^{-1}$ ), Al (at  $0.1\text{-}1 \text{ nm s}^{-1}$ ), or a triple layer of Al ( $60 \text{ nm}$  at  $0.1\text{-}1 \text{ nm s}^{-1}$ ) | Cu ( $5\text{-}20 \text{ nm}$  at  $0.1 \text{ nm s}^{-1}$ ) | Al ( $0.8\text{-}1.2 \text{ nm}$  at  $0.02\text{-}0.04 \text{ nm s}^{-1}$ ) as described in Chapter 3. Metal electrode deposition was through a shadow mask to form electrodes of size  $8 \times 12 \text{ mm}$  to achieve the desired device layout Figure 2.4(a). Opaque top electrodes of Al or Ag were deposited in the same manner at thicknesses  $>60 \text{ nm}$  through a six pixel ( $4 \times 3 \text{ mm}$ ) per substrate mask arrangement as shown in Figure 2.4(b).

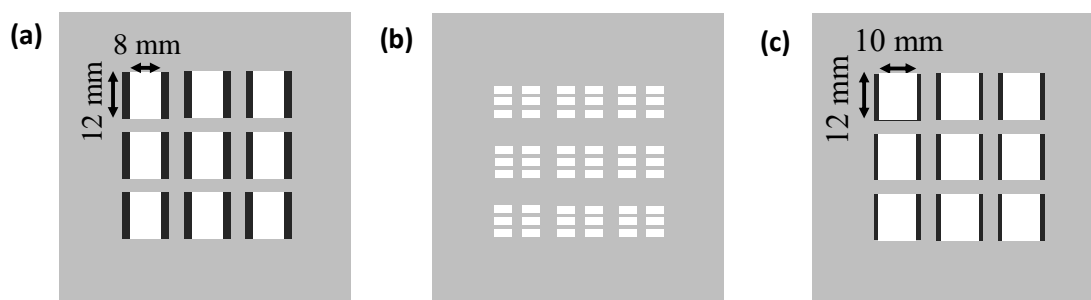


**Figure 2.4:** Shadow mask dimensions used with the thermal evaporator for (a) substrate electrodes, (b) top electrodes, and (c) charge extraction layers.

Transparent top electrodes of Ag or Cu were thermally evaporated onto the underlying substrate at a rate of  $0.2 \text{ nm s}^{-1}$ , unless otherwise stated, through the shadow mask shown in Figure 2.4(b). In order to achieve well-defined electrode areas with sharp edges the substrates were not rotated during evaporation.

The purity and suppliers of any evaporation materials used in this thesis are given in Table 2.1

Material	Supplier	Purity
Cu	Kurt J. Lesker	99.99%
Al	Kurt J. Lesker	99.99%
Au	Kurt J. Lesker	99.99%
Ag	Alfa Aesar	99.999%
MoO <sub>3</sub>	Sigma Aldrich	99.99%
BCP	Alfa Aesar	98%

**Table 2.1:** Supplier and purity of evaporated materials used in this thesis.

### 2.2.2 Charge extraction layer deposition

Zinc oxide ( $\text{ZnO}_x$ ): The zinc oxide hole-blocking layer used in Chapters 3 and 4 was prepared by dissolving zinc acetate dihydrate (Sigma Aldrich,  $\geq 99\%$ ) and ethanolamine (Alfa Aeser, 99+%) 1:1 (at concentrations of 0.08, 0.16 or 0.5 M) in 2-methoxyethanol and stirring in air for 12 hours prior to use. The 0.5 M solution was drop cast onto substrates at 4000 rpm for 60 seconds followed by annealing at  $150^\circ\text{C}$  for 10 minutes in air, which resulted in a film with a worm-like surface structure (Figure 2.5(a)). The 0.08 and 0.16 M solutions were drop cast at 5000 rpm for 60 seconds followed by annealing at  $100^\circ\text{C}$  for 10 minutes in air which gave flat films as shown in Figure 2.5(b) for the 0.16 M solution.

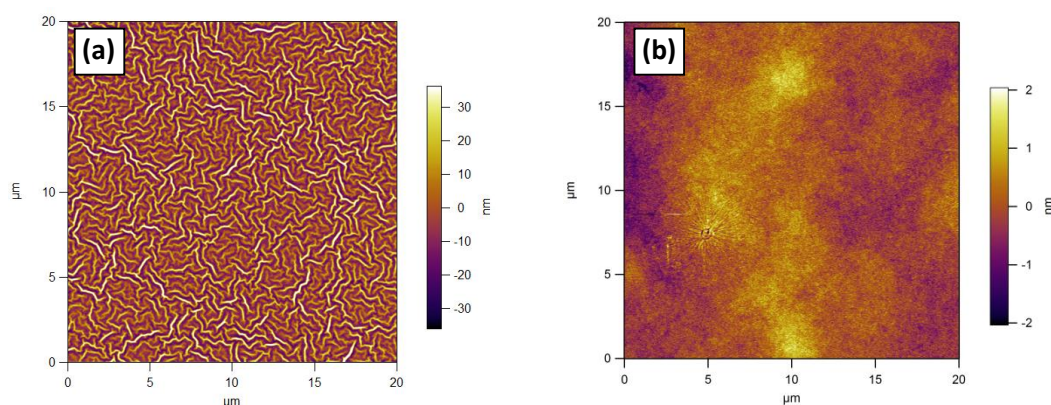


**Figure 2.5:** Morphology of  $\text{ZnO}_x$  films spun at (a) 4000 rpm for 60 seconds from a 0.5 M solution and (b) at 5000 rpm for 60 seconds from a 0.16 M solution.

$\text{MoO}_3$ : The  $\text{MoO}_3$  electron-blocking layer used in Chapters 3, 4, 5 and 6 was deposited by thermal evaporation at a thickness of 5-10 nm at  $0.03 \text{ nm s}^{-1}$  through the shadow mask shown in Figure 2.4(c). Alternatively a solution processed molybdenum oxide bronze film was deposited as described in Chapter 5. In Chapter 6 evaporated  $\text{MoO}_3$  is used as a capping layer at a thickness of 34 nm deposited at  $0.03 \text{ nm s}^{-1}$ .

---

$H_yMoO_{3-x}$ :  $H_yMoO_{3-x}$  was synthesised by dispersing molybdenum powder (Alfa Aeser, 99.95%, -100 mesh, 0.1 g) in ethanol (10 ml) by ultra-sonication agitation for 10 minutes. The solution was heated to 40°C followed by addition of  $H_2O_2$  (Sigma Aldrich, 30% in  $H_2O$ , 0.35 ml) under vigorous stirring. This solution turned yellow after 10 hours then blue after 48 hours. After 72 hours reaction (unless otherwise stated) the solution was removed from the heat and allowed to cool, filtered through a 0.2  $\mu m$  PTFE filter and dried using a rotary evaporator. The solutions were then made up to 20  $mg\ ml^{-1}$  in ethanol and ultra-sonically agitated to fully dissolve the powder. Before use all solutions were centrifuged at 10,000 rpm for 10 mins. To prepare the 5-10 nm thick films used in OPVs, 5  $mg\ ml^{-1}$  solutions were drop cast at 3000 rpm for 60 seconds in the glovebox followed by annealing at 80°C for 10 mins, also in the glovebox. Varied concentrations and spin speeds were used to fabricate different film thicknesses as required.

Bathocuproine: The small molecule Bathocuproine (BCP) was used as an electron extraction layer in Chapter 6 and was deposited by thermal evaporation at a thickness of 8 nm at 0.05  $nm\ s^{-1}$  at 150°C.

### 2.2.3 Photoactive layer deposition

All organic semiconductors in this section were purchased from Ossila and used without further purification. Solvents used are anhydrous and purchased from Sigma Aldrich unless otherwise stated. BHJ solutions were all prepared and deposited under nitrogen in the glovebox as follows: PTB7:PC<sub>71</sub>BM (1:1.5) was dissolved at a concentration of 25  $mg\ ml^{-1}$  in dichlorobenzene (DCB):diiodotane (DIO) (Alfa Aeser, 98%) (97:3 vol.%) followed by stirring at 60°C for 1 hour then heating at 40°C for 17 hours, then allowing

to cool before use. The solution was drop cast onto substrates by spinning at 1000 rpm for 60 seconds, before increasing the spin speed to 6000 rpm for 4 seconds.; P3HT:PC<sub>61</sub>BM (1:1) was dissolved at a concentration of 40 mg ml<sup>-1</sup> in DCB followed by stirring at 45°C for 1 week, then filtered through a 0.2 µm PTFE filter prior to use. The solution was drop cast onto substrates spinning at 600 rpm for 120 seconds before increasing the spin speed to 1000 rpm for 4 seconds. The still wet film was left to dry under nitrogen for 45 minutes followed by annealing at 120°C for 20 minutes. PCDTBT:PC<sub>71</sub>BM (1:3) was dissolved at a concentration of 4 mg ml<sup>-1</sup> in chloroform by stirring at 65°C for 1 hour. The solution was then spin cast onto substrates spinning at 6000 rpm for 60 seconds followed by annealing at 80°C for 30 minutes. PBDTTT-EFT:PC<sub>71</sub>BM (1:1.5) was dissolved at a concentration of 25 mg ml<sup>-1</sup> in chlorobenze (CB):(DIO) (97:3 vol.%) by stirring at 70°C for 16 hours then heating at 70°C for 1 hour prior to use. The solution was then drop cast onto substrates spinning at 1000 rpm for 120 seconds then left under vacuum ( $< 1 \times 10^{-1}$  bar) for 3 hours for the film to dry.

#### 2.2.4 OPV Device Layout

Devices were arranged on each 12 × 12 mm glass substrate according to the design shown in Figure 2.6. The six devices per substrate share a common substrate electrode to which electrical connection was made by removing the semiconductor layer(s) at the point labelled with an X in Figure 2.6. Conductive silver paint (RS Materials) was used to form consistently good contact between the electrodes and the probes connecting to the external circuit.

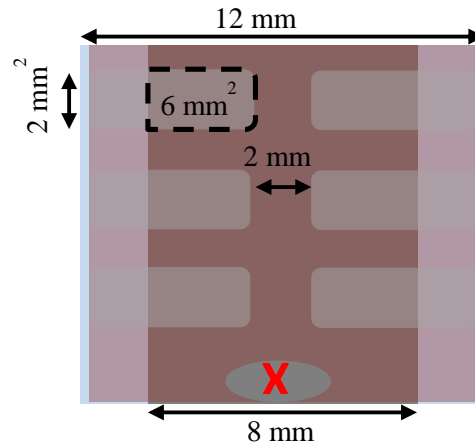


**Figure 2.6:** Layout of OPV devices fabricated on 12 × 12 mm glass slides.

## 2.3 OPV testing

### 2.3.1 OPV Current Density vs Voltage Analysis

Current density-voltage ( $JV$ ) characteristics were measured using a Keithley 2400 source-meter in the dark and under AM1.5G solar illumination at  $100 \text{ mW cm}^{-2}$  (1 sun). A custom Labview interface was used to change the voltage and measure the current and calculate the  $J_{sc}$ ,  $V_{oc}$ ,  $FF$  and  $PCE$ . The light source used throughout was an ABET technologies Sun 2000 Solar Simulator using a Xenon short arc lamp with AM 1.5 filters with the output intergrated into the glovebox so that testing could be carried out under a nitrogen atmosphere. The light source was calibrated using a silicon diode (PV measurements Inc.) with KG5 colour filter which yields a short circuit current of  $47 \text{ mA cm}^{-2}$  under AM 1.5. So that the the active quarter of the  $JV$  characteristic of inverted and non-onverted device architectures are easily comparable, the applied voltage is reversed between inverted and non-inverted devices.

### 2.3.2 OPV External Quantum Efficiency Analysis

External quantum efficiency (EQE) spectra, also called Incident-Photon-to-Converted-Electron (IPCE) spectra, show how many electrons are extracted into the external circuit from each photon incident on the device as a function of photon wavelength<sup>137</sup>:

$$EQE(\lambda) = \frac{J_{sc}(\lambda)}{qN(\lambda)} \quad \text{Equation 2.3}$$

where  $q$  is the elementary charge and  $N(\lambda)$  is the flux density at a specific wavelength. Ideally the EQE is equal to one across all wavelengths harvested, but in practice losses due to recombination, limited absorption by the photoactive layer, and reflection and absorption of light by the transparent electrode reduce this value. From the EQE spectrum  $J_{sc}$  can be calculated by integrating under the curve:

$$J_{sc} = \int_{\lambda_1}^{\lambda_2} b(\lambda).EQE(\lambda).d\lambda \quad \text{Equation 2.4}$$

where  $b$  is the solar photon flux of the light source. The EQE spectrum provides invaluable evidence for localised optical effects such as those due to optical microcavities or surface plasmon resonances, as discussed in Chapters 4 and 6 respectively. A typical EQE spectrum for an OPV device using PTB7:PC<sub>71</sub>BM as the photoactive layer is shown in Figure 2.7.

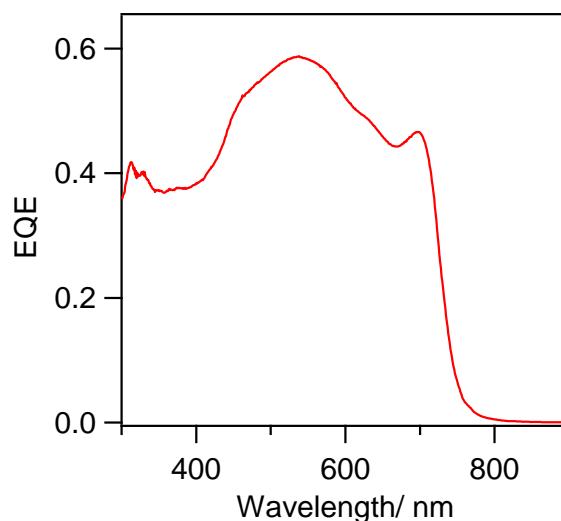


**Figure 2.7:** A typical EQE spectra of an OPV device with an active layer of PTB7:PC<sub>71</sub>BM.

EQE and reflectance measurements were carried out using a custom Labview interface, a Sciencetech SF150 xenon arc lamp and a monochromator (Photon Technology International), focussing and splitting lenses, a current-voltage amplifier (Femto DHPA-100) and a lock-in amplifier (Stanford Research Systems SR 830). The incoming monochromatic light was chopped at 190 Hz to enable the lock in amplifier to remove any signal generated from background light and to mitigate charge build up. The monochromatic light intensity was calibrated using a pair of Si photodiodes (Newport 818-UV) as the light is not split equally at every wavelength and so the ratio between the reference and the sample has to be taken into consideration.

---

## 2.4 Characterisation Techniques

### 2.4.1 X-ray photoelectron spectroscopy and Auger electron spectroscopy

X-ray photoelectron spectroscopy (XPS) is a technique commonly used for the surface characterisation of thin films.<sup>138</sup> It provides the binding energy of core shell electrons which can be used to give the elemental composition of the film being probed as well information about the chemical bonding environment. To do this an X-ray photon is directed onto the sample in ultra-high vacuum. Photoelectrons are ejected from the material in accordance with Einstein's photoelectric effect leaving behind empty energy states as shown schematically in Figure 2.8(a) and (b).

The number of photoelectrons that are ejected is recorded to give the XPS spectrum of counts versus electron binding energy. The binding energy of core electrons is very sensitive to the chemical environment that the atom is in, because the valance electrons which are already involved with bonding screen the coulombic attraction between the ejected electron and the nucleus. The bonding environment can lead to an increase or decrease in the binding energy of the core electrons depending on whether the valence electron density is decreased or increased due to chemical bonding. The small shifts in the binding energy of the core electrons that result from differences in the electron density distribution around the nucleus due to the chemical bonding environment are called chemical shifts. The sensitivity of XPS is such that it can detect as little as 1% of a monolayer of species on a surface.<sup>139</sup> It is a surface sensitive technique with 95% of the signal typically originating from a depth of  $\leq 10$  nm below the sample surface for most materials. This surface sensitivity is not due to the penetration depth of the X-ray, which is typically of the order of microns, but rather the inelastic mean free path of the photo-excited electrons, which must be able to reach the

material surface in order to escape into the vacuum interface before dissipating their energy via collisions with the material lattice.

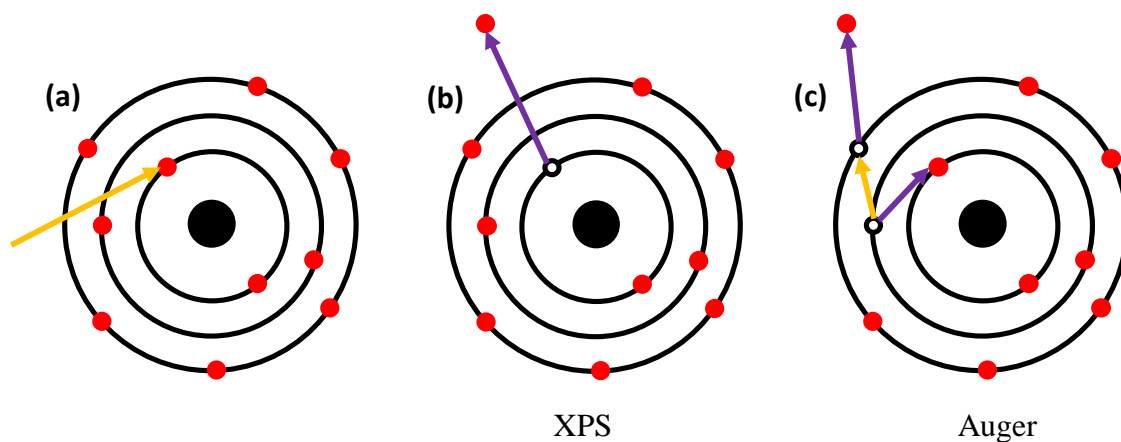


**Figure 2.8:** A schematic diagram showing the action of the photoelectric effect exploited in XPS and AES: **(a)** An X-ray energy photon excites a core shell electron **(b)** causing it to be ejected leaving behind a vacancy. **(c)** Higher energy electrons can relax into this vacancy which results in energy being transferred to another bound electron giving it enough energy to be ejected as an Auger electron.

The binding energy of the electron (B.E.) is determined from the known energy of the photon used to excite the electron ( $h\nu$ ), the kinetic energy of the emitted photon (K.E) measured at the detector and the work function of the detector ( $\Phi_D$ ) as given by Equation 2.5 and illustrated pictorially in Figure 2.9. Since there is  $E_f$  alignment between the sample and detector, the electron binding energy is relative to the  $E_f$  of the sample.

$$B.E. = h\nu - K.E. - \Phi_D \quad \text{Equation 2.5}$$

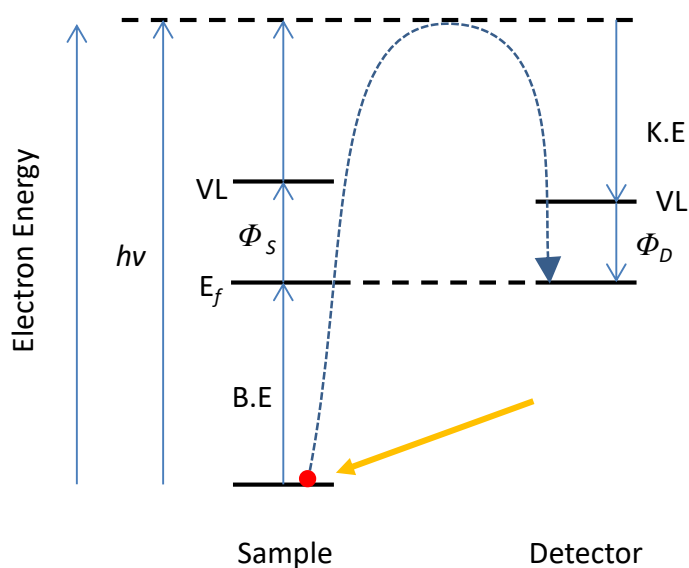


**Figure 2.9:** A schematic energy level diagram illustrating how the binding energy is extracted from the kinetic energy of the photoelectrons at the detector.

Auger electron spectroscopy (AES) is similar to XPS and is often used in conjunction with XPS as it has superior spatial resolution, although at the expense of sensitivity, and provides insight into the detailed electronic structure. The mechanism for the release of Auger electrons, as shown in Figure 2.8(c), proceeds *via* the relaxation of an electron into a vacancy left by an ejected core electron. The energy released from this transition then excites an outer shell electron which is ejected from the sample. As with XPS, AES is also a surface sensitive technique as the Auger electrons are still prone to inelastic scattering.

The XPS measurements presented in thesis were collected using a Kratos Axis Ultra DLD spectrometer or an Omicron sphere spectrometer. The samples were illuminated using X-rays from a monochromated Al  $K\alpha$  source ( $h\nu = 1486.6$  eV) and detected at a take-off angle of 90 degrees. The resolution, binding energy referencing

and transmission function of the analyser were determined using a clean polycrystalline Ag foil. Analysis of the data was undertaken with the CasaXPS package, incorporating Voigt (mixed Gaussian-Lorentzian) line shapes and a Shirley background.

### 2.4.2 Ultraviolet photoelectron spectroscopy

Ultraviolet photoelectron spectroscopy (UPS) is based, as with XPS, on the photoelectric effect, although uses much lower energy photons to excite the electrons; 21.2 eV, and therefore only probes the valence electrons and the top ~1 nm of the sample surface. UPS is used to probe the frontier orbitals and is used to measure the work function and the energy of the valence band edge of the material with respect to  $E_f$  (Figure 2.10). To determine the  $\Phi$  and  $I_p$  from a UPS spectrum equation 2.6 and equation 2.7 can be used such that:

$$\Phi_S = h\nu - B.E_{max} \quad \text{Equation 2.6}$$

and

$$I_p = \Phi_S + B.E_{min} \quad \text{Equation 2.7}$$

Binding energies of the materials can again be measured due to the  $E_f$  alignment of the detector and the sample (Figure 2.10). The values of  $B.E_{max}$  and  $B.E_{min}$  are extracted from the secondary electron cut-off and valence band edge, respectively, as shown in Figure 2.11.<sup>140</sup>

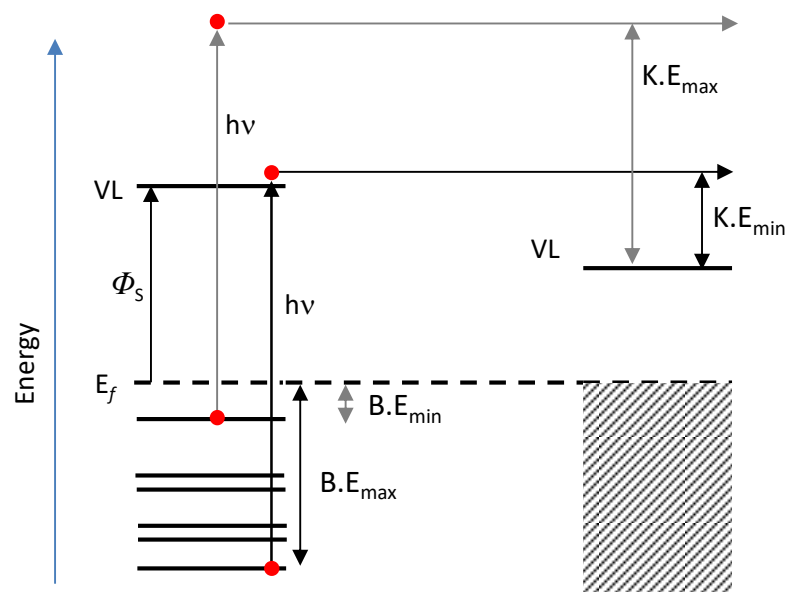


**Figure 2.10:** A schematic energy level diagram illustrating how the work function of the sample ( $\Phi_s$ ) is extracted from the kinetic energy of the photoelectrons at the

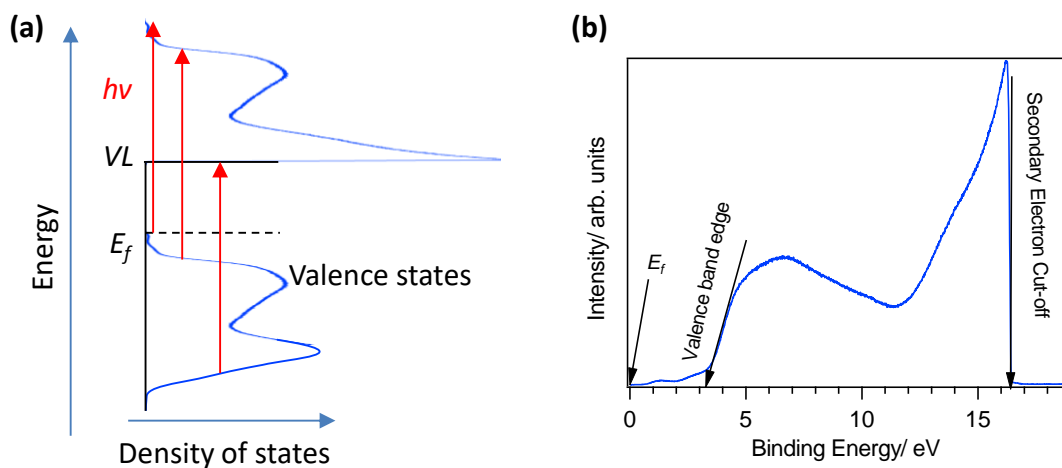


**Figure 2.11:** (a) A schematic diagram displaying the relationship between the density of states of electrons when bound and when ejected by  $h\nu$ . (b) A representative UPS spectra showing the valence band edge, Fermi edge, and secondary electron cut-off.

The large peak at the secondary electron cut-off does not provide any information about the density of occupied electron states. The large flux of electrons ejected in this part of the spectrum are due to secondary excitation of electrons from smaller potential energy bands due to inelastic scattering by other electrons. In heterogeneous/amorphous samples, i.e. molecular solids, there are variations in the local work function due to differences in local crystallinity and dopant density. Importantly, the value of  $\Phi_s$  measured with UPS gives the lowest possible work function, by comparing the Fermi-edge and secondary-electron cut-off, and gives the  $\Phi$  and VB edge energy to within an accuracy of  $\pm 0.1$  eV. This uncertainty must be taken into account when interpreting UPS data.<sup>141</sup>

### 2.4.3 Kelvin Probe

Kelvin probe is a non-invasive technique for the measurement of the average work function under the probe, which in this case has an area of  $5 \text{ mm}^2$ . To do this the contact potential difference is recorded between the sample and an oscillating probe, which are positioned parallel to one another to form the two plates of a parallel plate capacitor.<sup>142</sup> When electrically disconnected the probe and sample can be depicted as in Figure 2.12(a). However, when electrically connected equilibrium is established, due to  $E_f$  alignment, as shown in Figure 2.12(b), which results in an opposite charge forming on the probe and sample surface. The capacitance of this arrangement is given by Equation 2.8:

$$C = \frac{Q}{V_{CPD}} = \frac{\epsilon\epsilon_0 A}{d} \quad \text{Equation 2.8}$$

$$V_{CPD} = \frac{Qd}{\epsilon_0 \epsilon A} \quad \text{Equation 2.9}$$

where  $C$  is capacitance,  $Q$  is the charge on the plates,  $V_{CPD}$  is the contact potential difference,  $\varepsilon$  is the relative permittivity of the material between the electrodes ( $\varepsilon_{\text{air}} \sim 1$ ),  $\varepsilon_0$  is the electric permittivity of free space,  $d$  is the distance between plates and  $A$  is the area of overlap between the two plates. Equation 2.8 can then be rearranged to give Equation 2.9 which shows the dependence of  $V_{CPD}$  on the distance between the sample and probe.

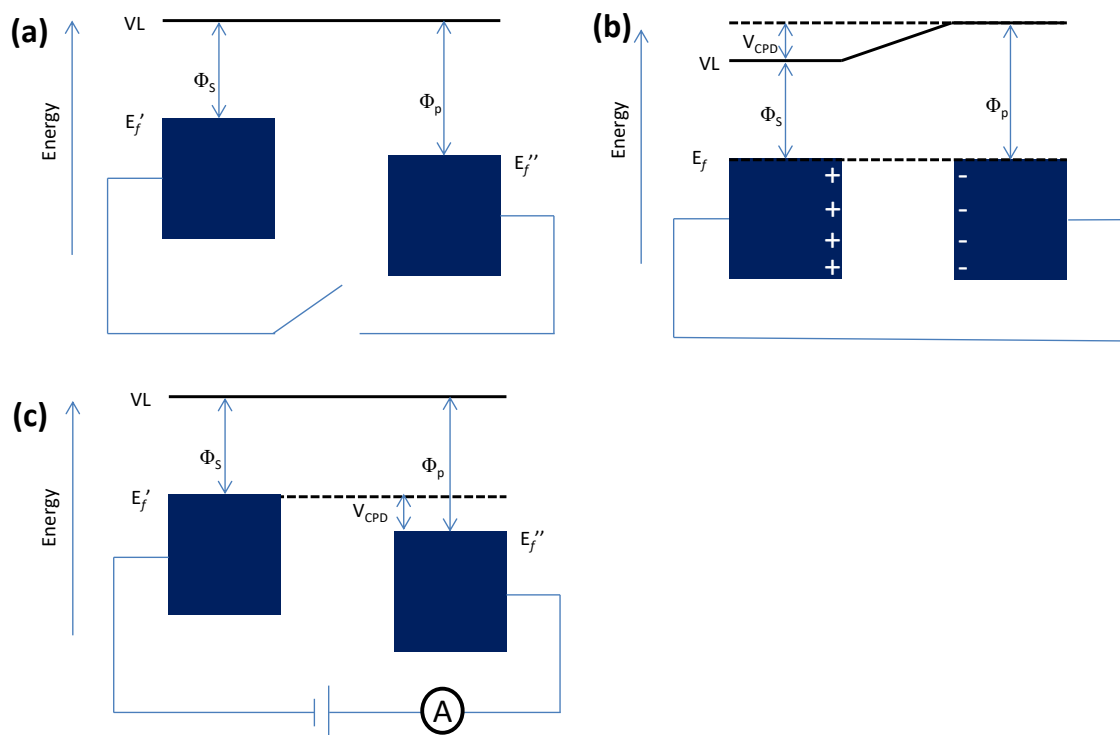


**Figure 2.12:** Energy level diagrams of two metals in close proximity to each other **(a)** when electrically disconnected, **(b)** electrically connected and **(c)** when a bias is applied equal to counteract the  $V_{CPD}$ .

$V_{CPD}$  cannot be measured directly and so the probe must be oscillated vertically with respect to the sample to produce an oscillating current in the wire connecting the sample to the probe due to the change in capacitance. By applying a counter bias  $V_{CPD}$  can be

---

nulled so that there is no change in the capacitance with oscillation, and so no current flows between the sample and probe as in Figure 2.12(c). The null bias is equal in magnitude but opposite in polarity to the  $V_{CPD}$ . Once the contact potential difference between the probe and the sample is known the work function of the sample can be determined either by knowing the probe work function or using a reference sample with known work function.

For the measurements report in this thesis a piece of freshly cleaved highly ordered pyrolytic graphite (HOPG) with a mosaic spread of  $3.5^\circ \pm 1.5^\circ$  was used as the reference. HOPG has a work function of 4.475 eV and so the  $V_{CPD}$  between the probe and HOPG can be used in conjunction with the contact potential difference between the probe and the sample to determine the work function of the sample.<sup>143</sup>

Kelvin probe measurements were made in the same glovebox as used for spin coating and evaporating films using a Kelvin Probe S and the Kelvin Control 07 electronic control unit (Besocke Delta Phi GmbH). The position of the 5 mm<sup>2</sup> Au probe is manipulated in the  $x$ ,  $y$ ,  $z$  using micrometers external to the isolating Faraday cage in which the probe is located. The Au probe is oscillated by a piezoelectric transducer and is held ~1 mm above the sample where it oscillates with an amplitude of 0.5 mm at 200 Hz. The applied null potential is varied using the gain control until the current signal monitored on an oscilloscope is nulled. This technique is extremely sensitive to changes in the work function and can detect differences in work function  $< 5$  meV.

### 2.4.4 Atomic Force Microscopy

AFM is a powerful surface imaging technique with nanoscale resolution at room temperature and pressure. A vertical resolution of up to 0.1 nm can be achieved although the lateral resolution is much lower due to the diameter of the tip. Unlike other microscope techniques with nanoscale resolution, such as scanning electron microscopy (SEM), there is no need for the sample to be conductive and samples can even be imaged submerged in a liquid.

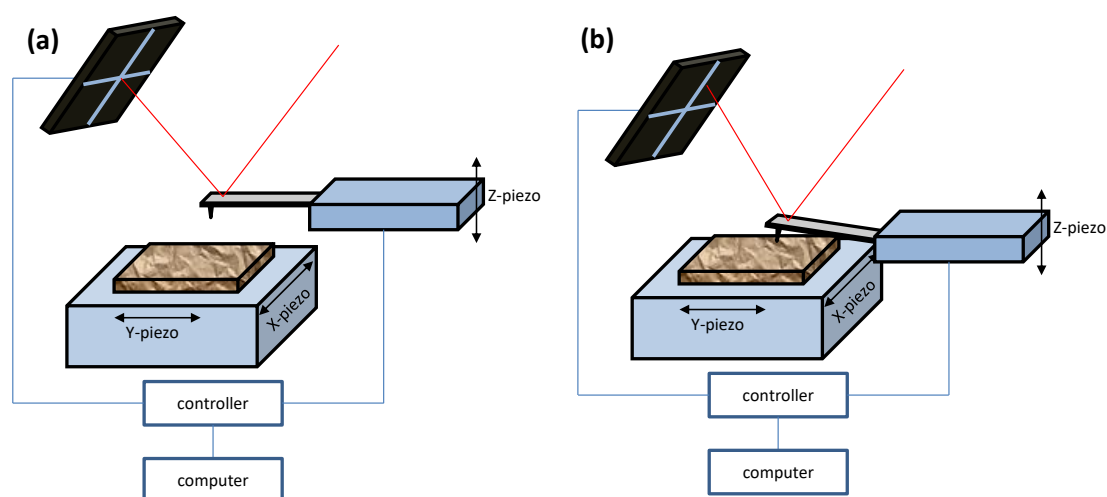


**Figure 2.13:** Illustration showing the operation of an AFM in contact mode where (a) the tip is not in contact with the surface and (b) where the cantilever has been pushed upwards due to the surface.

AFM images of the surface of a sample were obtained by measuring the interatomic forces between the surface and a very fine tip (diameter  $\sim 10$  nm) mounted on the end of a cantilever. The force exerted on the tip as it approaches the surface is measured by the deflection of a laser reflecting off the cantilever onto a photodiode.

The two most commonly used AFM imaging techniques are contact mode and tapping mode. In contact mode the tip is brought down towards the surface until intermolecular forces between the tip and the surface cause the cantilever to deflect leading to a perturbation of the laser position on the photodiode. The tip is held at a constant height by maintaining a set value of this perturbation (Figure 2.13). A z-piezoelectric transducer controls the tip height above the sample, then uses a feedback loop to maintain this force on the cantilever and so maintain the same distance between the sample and the surface, provided the surface composition remains homogeneous. The tip is rastered over the surface in order to form an image. In contact mode there is a high chance of damaging the surface or tip by either too rough a surface or simply through the constant contact between tip and surface. For this reason, all topography measurements reported in this thesis were recorded using tapping mode AFM. In tapping mode, the tip is oscillated at a frequency ~5% off of its resonant frequency. As the cantilever is brought near to the surface this oscillation is typically dampened until it reaches a set frequency at which it is then held whilst rastering over the surface. Tapping mode is sensitive to changes in intermolecular forces without touching the surface and so is much less likely to damage the tip or surface, than contact mode.

To compare sample surface roughnesses the root-mean-squared roughness ( $R_{RMS}$ ) is most often used, which is defined as the root-mean-square of any deviations from the mean height of the sample:

$$R_{RMS} = \sqrt{\frac{1}{N} \sum_i^N (Z_i - Z_{avg})^2} \quad \text{Equation 2.10}$$

Unless otherwise stated, all surface roughness data given in this thesis relates to root-mean-square roughness. Tapping mode AFM imaging was performed in air using an Asylum Research MFP3D or a Veeco multimode.

---

### 2.4.5 Scanning Electron Microscopy

Another imaging technique that is routinely used to image conductive surfaces is scanning electron microscopy (SEM). In SEM an electron beam is focused onto the surface from an electron gun via electromagnetic lenses to form a spot size in the nanometre range. This spot is then rastered over the surface to collect the image. Since the wavelength of accelerated electrons, given by the De Broglie equation, is much smaller than visible light, SEM offers much higher spatial resolution than can be achieved with a light microscope. Modern SEMs can offer sub-1nm spatial resolution, although the smallest feature size that can be resolved with the instrument used for the research reported herein is  $\sim 3$  nm. When the electron beam impinges on the sample the electrons penetrate the surface and cause the ejection of secondary electrons due to inelastic scattering. These ejected electrons come from the top few nanometres of the sample and the intensity of these secondary electrons is used to form the image with a higher electron count leading to a brighter pixel spot. For soft samples and high electron kinetic energies it is even possible to image to within a few nanometres below the surface. However, because the incoming beam causes the ejection of electrons the sample can easily become charged, leading to erosion of the image quality. Therefore, SEM can only be used for samples that are suitably conductive or that have been sputtered with a highly conductive carbon layer to aid the removal of charge. The image quality can also be deteriorated by the decomposition of organic contaminants on the surface of the sample by the high energy electron beam, forming a thin amorphous carbon layer. These contaminants typically originate from the atmosphere when loading the sample into the SEM vacuum system, or from solvent residue in the case of samples prepared from solution, although can also originate from the vacuum chamber itself.<sup>144</sup> Due to this film of organic contamination the underlying fine detail of the surface is

obscured leading to a lower quality image. This is particularly apparent when collecting images of OPVs. Unfortunately, when scanning electrodes on top of OPVs it is impossible to avoid organic contamination, which makes collecting images difficult due to rapid darkening of the image for scan sizes of less than 10  $\mu\text{m}$  due to the high intensity of the electron beam. It was found that a large degree of organic contamination was occurring due to the silver conductive paint used to electrically contact the sample to the base. This could be greatly reduced by allowing the silver paint to dry under vacuum for at least 15 minutes prior to scanning. SEM images were collected with a Zeiss SUPRA 55-VP

#### 2.4.6 Sheet Resistance

In order to quantify the lateral resistance of a thin film the sheet resistance;  $R_{\text{sheet}}$ , is used as this measures a dimensionless resistance so is useful for universal comparisons.  $R_{\text{sheet}}$  is measured using the Van der Pauw (VdP) method which is applicable to thin films due to being based on a two-dimensional current distribution.<sup>145</sup>  $R_{\text{sheet}}$  is calculated as shown in Equation 2.11:

$$R_{\text{sheet}} = \frac{\rho}{d} = \frac{\pi R}{\ln 2} \quad \text{Equation 2.11}$$

where  $\rho$  is the resistivity of the material,  $d$  is the film thickness and  $R$  is the resistance measured by the VdP method. In order for the measurement to be accurate the sample should be of uniform thickness and resistivity and the dimensions of the contacts used should be small in comparison to the film dimensions. The sample is set up as shown in Figure 2.14.

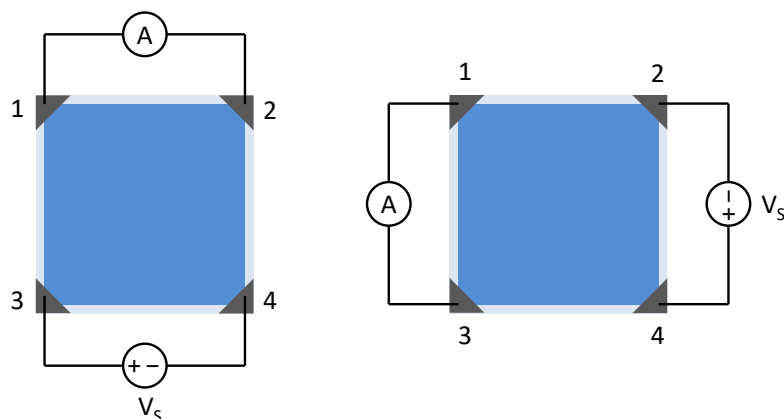


**Figure 2.14:** Schematic diagrams showing the experimental set up to measure an average  $R_{\text{sheet}}$  on one sample.

A Keithley 2400 source-meter is used to apply a voltage of 5 mV to contacts 3 and 4 whilst a current is measured from contacts 1 and 2. Due to the symmetry of the sample the difference between the two configurations shown in Figure 2.14 should be non-existent however in order to verify the reliability of the data measurements were taken for both sample orientations for all samples.

#### 2.4.7 Absorption/ Reflection spectroscopy

In order to fully characterise metal films for application in OPVs it is often necessary to determine their absorbance and reflectance as a function of wavelength. The absorption of thin films can give information about many useful properties including the degree of crystallinity or, in the case of semiconductors/insulators, the HOMO-LUMO gap. Since OPVs deal exclusively with harvesting the solar spectrum, which is most intense for  $\lambda = 300\text{-}900$  nm this is the wavelength range of interest. The absorbance of a film is given by the Beer-Lambert Law:

---

$$Abs = -\log_{10} \left( \frac{I}{I_0} \right) = \epsilon cl = \alpha l \quad \text{Equation 2.12}$$

where *Abs* is the absorbance, *I* is the light intensity exiting the sample, *I*<sub>0</sub> is the incident light intensity,  $\epsilon$  is the molar extinction coefficient, *c* is the molar concentration,  $\alpha$  is the absorption coefficient and *l* is the path length through the sample. Measurements were performed using a Perkin-Elmer Lambda 25 UV-VIS spectrometer using the software UVWINLAB.

Reflectivity is closely related to absorbance in that it is the inverse of transmittance (*I*/*I*<sub>0</sub>). It is important to have knowledge of the reflectivity of the opaque electrodes used in OPVs to know how much light is being parasitically absorbed. The experimental set-up is very similar to the way absorbance is measured: light is passed through a monochromator across the wavelength range of interest incident on the sample and the reflected light is collected by a diode that is referenced to the same light source pre-reflection. Spectroscopic reflectivity measurements were carried out in the same set-up as the EQE measurements with a chopper speed of 500 Hz

#### **2.4.8 Contact Angle Measurements**

The wettability of a drop of liquid on a surface can give useful information about the surface energy and surface roughness. In this case wettability is quantified in terms of the angle between the droplet and the substrate surface as shown in Figure 2.15. Contact angles on substrates coated with PTB7:PC<sub>71</sub>BM and PCDTBT:PC<sub>71</sub>BM were measured for molybdenum oxide bronze solutions (20 mg ml<sup>-1</sup>) as discussed in Chapter 5. Freshly deposited films were exposed to the air for the shortest time possible, ~1 minute, prior to contact angle measurement to avoid contamination of the surface by atmospheric

contaminants, such as water or hydrocarbons. Contact angle measurements were recorded using a Krüss DSA100 Drop Shape Analysis System with droplets between 3-5  $\mu\text{l}$  and recorded at a tilt of  $2^\circ$  in static mode. The Conic section (tangent 1) computational method is used to find the contact angle.

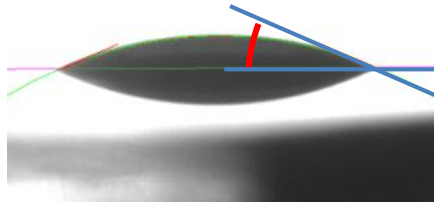


**Figure 2.15:** Example of a static contact angle measurement.

#### 2.4.9 Optical Simulations

Optical simulations for transparency, reflectivity and electric field intensity were carried out using The Essential Macleod Software from Thin Film Center Inc. Refractive index and extinction coefficient data as a function of wavelength were entered into the software for each material. This data was obtained from the literature and an in-built Macleod database. This simulation package assumes the films are homogenous slabs with smooth interfaces.

---

## Chapter 3.

# A Silver-Free, Reflective Substrate Electrode for Electron Extraction in Top-Illuminated Organic Photovoltaics

The majority of the work presented in this chapter has been published in:

*A Silver-Free, Reflective Substrate Electrode for Electron Extraction in Top-Illuminated Organic Photovoltaics*, Martin S. Tyler, Oliver S. Hutter, Marc Walker, and Ross A. Hatton, *ChemPhysChem*. **2015**, DOI: 10.1002/cphc.201402880

### 3.1 Summary

The choice of metals suitable as the reflective substrate electrode for top-illuminated OPVs is extremely limited. In this chapter the development of a novel substrate electrode for this class of OPV architecture based on an Al (>60 nm) | Cu (8 nm) | AlO<sub>x</sub> (~1 nm) triple layer is described. This new electrode offers a reflectivity comparable to that of Al over the wavelength range  $\lambda = 400\text{-}900$  nm and a work function suitable for efficient electron-extraction in OPVs along with high stability towards oxidation. In addition to reporting the advantage of this electrode over Al in model top-illuminated OPVs, the results of a photoelectron spectroscopy study show that the oxidised ~1 nm AlO<sub>x</sub> layer, formed by evaporation then oxidation of Al on a thermally evaporated Al | Cu reflective substrate electrode, is sufficient to block oxidation of the underlying Cu. This is remarkable given that the self-limiting oxide thickness of bulk Al metal is greater than 2 nm.

### 3.2 Introduction

In conventional OPV architectures electrons are extracted to the external circuit by the reflective metal electrode which is deposited onto a photoactive organic semiconductor layer supported on a transparent electrode, most commonly ITO coated glass.<sup>146</sup> For efficient electron-extraction the reflective metal electrode is preferably a low  $\Phi$  metal such as Ca or Mg, although parasitic optical absorption by these metals is known to reduce the photocurrent in OPVs, so the highly reflective metals Al and Ag are most often used.<sup>72,81</sup> The  $\Phi$  of both Al; 4.2-4.4 eV,<sup>147</sup> and Ag; 4.3-4.7 eV;<sup>148</sup> is too high for efficient electron-extraction from the LUMO of most electron acceptor molecules used in OPVs (e.g. PC<sub>71</sub>BM = 3.9 eV<sup>71</sup>, C<sub>60</sub>= 4.2 eV<sup>149</sup> and perylene = 3.8 eV<sup>150</sup>) (Figure 3.1) and so these metals must be used in conjunction with a charge extraction layer to ensure good alignment between the LUMO of the electron acceptor and the  $E_f$  of the metal electrode.<sup>151</sup>

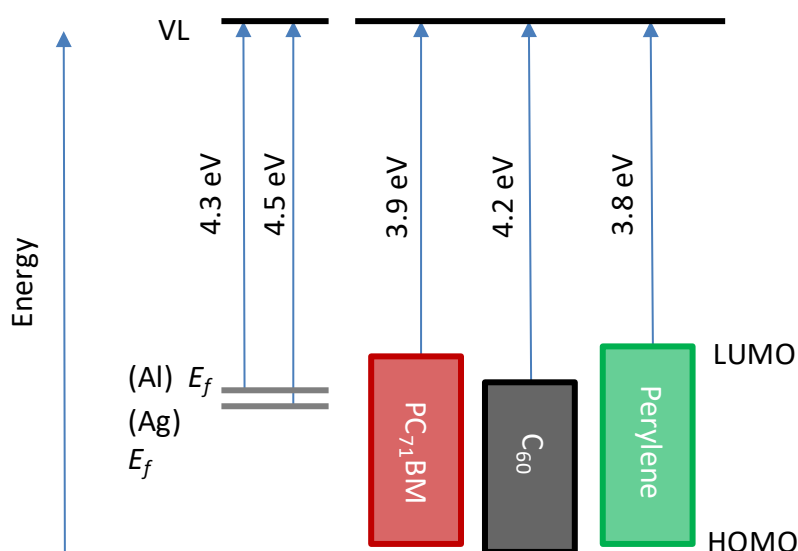


**Figure 3.1:** Schematic energy diagram showing the LUMO energy of three widely used electron acceptor molecules and the energy of the  $E_f$  (with respect to the vacuum level) for both Al and Ag.

The two most widely used electron-extracting layers are the wide band-gap partially reduced oxides  $\text{ZnO}_x$ <sup>152,153</sup> and  $\text{TiO}_x$ <sup>154,155</sup> which serve to block the unwanted extraction of holes by the electrode - a process that competes with the photovoltaic effect in BHJ OPVs because both donor and acceptor phases can contact both electrodes. These interface layers are ordinarily processed by deposition of an organometallic precursor from solution onto the supporting electrode followed by heating in air to form the oxide, a process that is incompatible with metal substrate electrodes that are susceptible to oxidation, such as Al.

Record laboratory efficiencies for top-illuminated OPVs are now approaching those of conventional architecture OPVs.<sup>104,129</sup> However, these devices invariably use an optically thick ( $\geq 50$  nm) Ag or Al reflective substrate electrode. Unfortunately, Al is extremely susceptible to oxidation and the oxide formed at its surface is self-passivating at a thickness of 2-4 nm.<sup>156</sup> This thickness is too great to be transparent to the flow of electrons, as has been demonstrated for other insulating materials used in OPVs and organic light emitting diodes, such as LiF.<sup>157,158</sup> Oxidation of the Al electrode is also known to be a major degradation pathway in conventional architecture OPVs<sup>159,160</sup> and so, in general, Al is poorly suited as the substrate electrode in top-illuminated OPVs. Whilst Ag is much more stable towards oxidation than Al, its use erodes the cost advantage of OPVs over other types of thin film PVs due to its high cost.<sup>161</sup> The pallet of potential alternatives to Ag for top-illuminated OPVs in which the reflective substrate electrode also serves as the electron-extracting electrode is extremely limited, since most low  $\Phi$  metals either exhibit unacceptable optical absorption losses<sup>72</sup> or are too easily oxidised. Petoukhoff *et al.*<sup>72</sup> have shown that Cu, which is 1% of the cost of Ag,<sup>161</sup> is a potential alternative to Ag in OPVs. However, Cu is susceptible to oxidation in air and for  $\lambda < 600$  nm optical losses due to inter-band transitions are large.<sup>72,107</sup> The

$\Phi$  of Cu (4.5-4.6 eV)<sup>162</sup> is also too high to be suitable as an electron-extracting electrode. It is therefore evident that for top-illuminated OPVs to achieve their full potential there is a need for a new reflective substrate electrode with high stability towards oxidation based on low cost earth abundant materials.

In this chapter a new substrate electrode for top-illuminated OPVs is described based on an Al | Cu | AlO<sub>x</sub> triple layer structure which offers a reflectivity comparable to that of Al over the spectral range  $\lambda = 400\text{-}900$  nm and low  $\Phi$  comparable to that of Mg<sup>163</sup>, combined with high stability towards oxidation. The latter is achieved using a strategy recently proposed by the Hutter *et al.* for the passivation of optically thin Cu films on glass; namely passivation of Cu with a 0.8 nm AlO<sub>x</sub> capping layer.<sup>164</sup> In addition to demonstrating the advantage over Al as the reflective substrate electrode in model top-illuminated OPVs, the results of a photoelectron spectroscopy study of the surface of this composite electrode provide new insight into the nature of the ultra-thin surface passivation layer.

### 3.3 Experimental

The layered electrode was fabricated by sequentially evaporating Al, Cu (1.0 Ås<sup>-1</sup>) and Al (0.2-0.3 Ås<sup>-1</sup>) without breaking vacuum of  $\leq 1 \times 10^{-5}$  mbar. Notably, it was found that a previously unused tungsten boat resulted in much smoother films, although the reason for this is as yet unclear. Alternatively, Al (60 nm, 1.0 Ås<sup>-1</sup>) only was deposited as the electrode. Oxidation treatment was carried out in a sealed antechamber using dry air (50 ppm H<sub>2</sub>O). To form the ZnO<sub>x</sub> electron-extracting layer zinc acetate dihydrate (0.5M) and ethanolamine (0.5M) in 2-methoxyethanol was drop cast at 4000 rpm followed by annealing at 150°C for 10 minutes in air to form ZnO<sub>x</sub> films.

OPVs were fabricated by spin coating PCDTBT:PC<sub>71</sub>BM, as stated in Chapter 2, onto the electrode substrate followed by thermal evaporation of MoO<sub>3</sub> (5 nm, 0.3 Ås<sup>-1</sup>) and Ag (11 nm, 1 Ås<sup>-1</sup>) unless otherwise stated.

### 3.4 Results and Discussion

The  $\lambda$  range of most importance for thin film PV is 400-900 nm and so the opaque reflective electrode must efficiently reflect light across this range. The reflectance of a 100 nm Al film at near normal incidence, shown in Figure 3.2, is above 80% over this range of  $\lambda$ , with a minimum at  $\lambda \sim 800$  nm and an average reflectance of 88%.

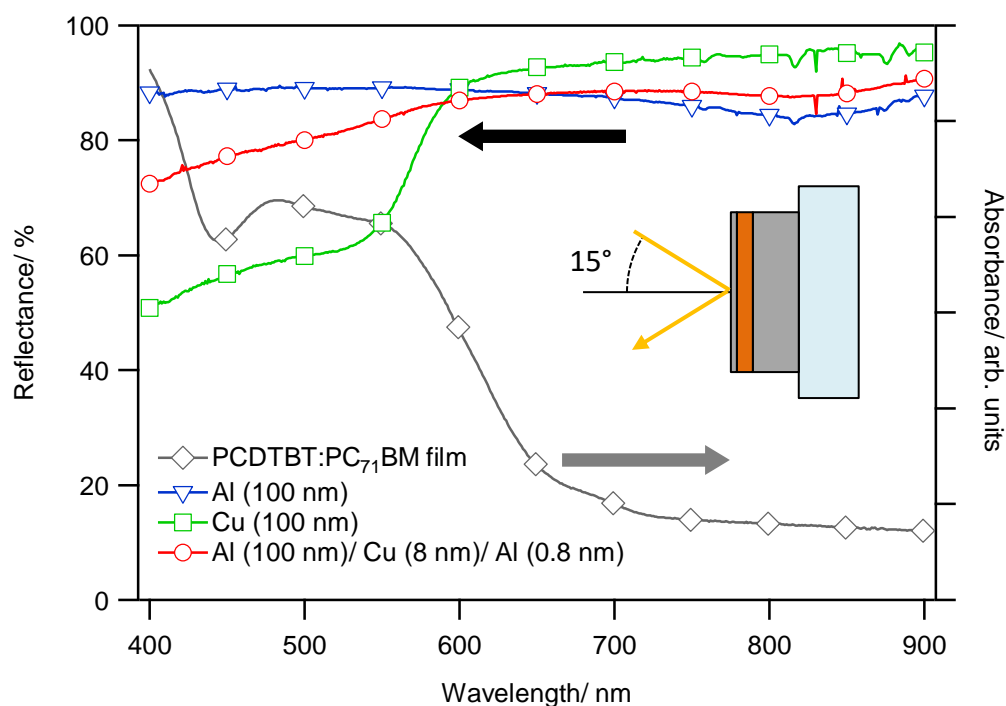


**Figure 3.2:** Reflectance spectra of Al (100 nm), Cu (100 nm) and Al (100 nm) | Cu (8 nm) | Al (0.8 nm) substrates. The angle of the incident and reflected light was 15° to the normal. Also shown is the absorbance) of the BHJ used in this study: namely PCDTBT:PC<sub>71</sub>BM.

---

This high reflectance combined with the relatively low cost of Al has resulted in its widespread use as the reflective electrode in conventional architecture OPVs. It is evident from Figure 3.2 that the reflectance of an optically thick Cu film is over 90% for  $\lambda > 600$  nm, although this high value is offset by strong absorption for  $\lambda < 600$  nm such that the mean reflectance between 400-900 nm is only ~78%. Whilst there has been a great deal of progress in the development of narrow band-gap polymers and small molecule organic semiconductors for BHJ OPVs<sup>165-169</sup>, the organic semiconductors used in today's BHJ OPVs primarily absorb light of  $\lambda < 700$  nm and so the reflectance of Cu is too low to be a viable alternative to Al. To achieve high reflectivity across the entire  $\lambda$  range of interest, combined with high resistance to oxidation in air, the possibility of using a multilayer electrode with the structure: Al (60 nm) | Cu ( $x$  nm) | Al (0.8 nm) was investigated. This electrode structure offers the advantage that it can be readily integrated with sheet Al or deposited onto another supporting substrates used in the building and automotive industries such as steel or plastic. In the first instance a number of thicknesses of Cu in the range 5 – 20 nm were investigated, the reflective properties of these are shown in Figure 3.3 along with plane-wave optical simulations of these thicknesses based on the transfer matrix method (The Essential Macleod, Thin Film Centre Inc.)

An Al substrate thickness of 100 nm was used to ensure complete opacity (<0.01% transmission) of the film, in conjunction with an Al capping layer thickness of 0.8 nm in the first instance. It was found that a Cu thickness of 8 nm resulted in the highest mean reflectivity (~86%) although the reflectance is lower than predicted by simulation. This difference is evident across all samples although is most pronounced for Cu thickness  $\leq 7$  nm (Figure 3.3) for which there are three possible explanations: Firstly, because an integrating sphere was not used to capture all the reflected light there

is inevitably some loss due to diffuse reflectance, as is evident from the difference between the measured and modelled reflectance for aluminium films also shown in Figure 3.3.

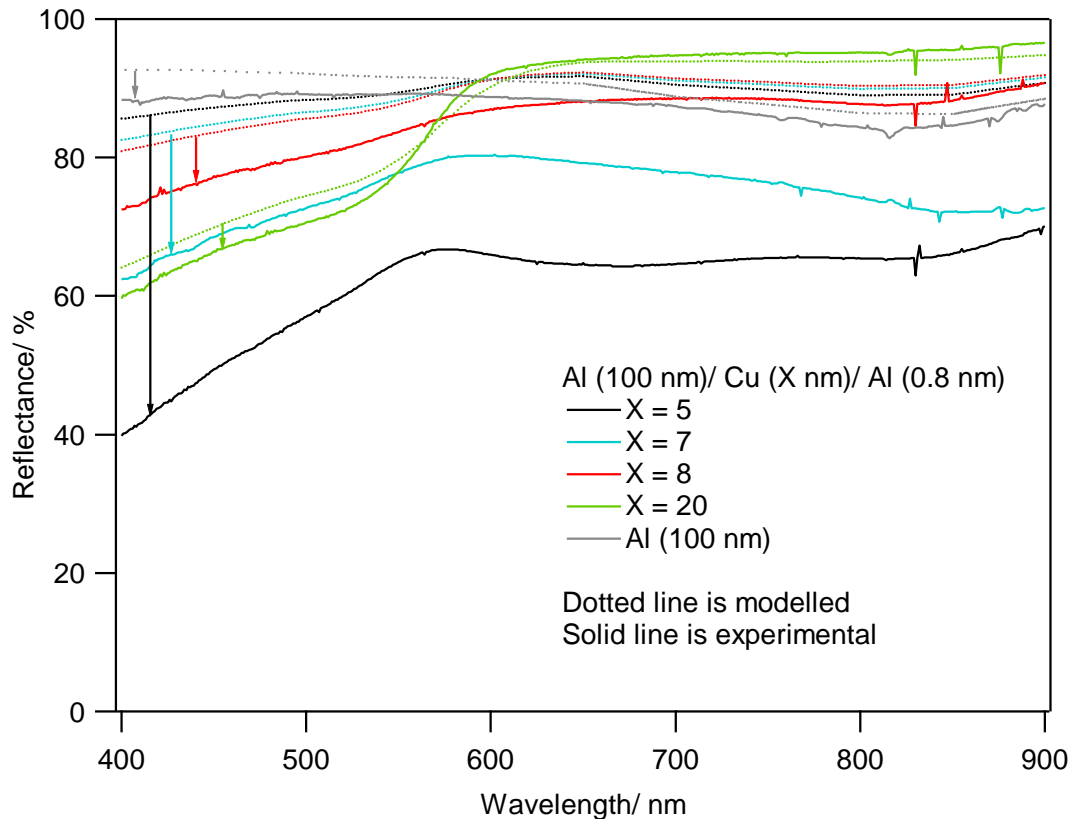


**Figure 3.3:** Measured (solid line) and simulated (dotted line) reflectance spectra of Al | Cu ( $x$  nm) | Al (0.8 nm) films with varying thickness ( $X$ ) of the Cu layer as well as of an Al (100 nm) film. Experimental data collected at an angle of incidence of  $15^\circ$ . Arrows are included to show the discrepancy between the experimental and modelled spectra.

Additionally, there is likely to be partial inter-mixing at the Al | Cu interface since Cu is known to readily alloy with a variety of metals, including Al.<sup>170-172</sup> A mixed interfacial layer would have unique electronic and optical properties, not accounted for by the optical model and this effect would be expected to be most pronounced for the thinner

---

Cu films where the percentage of bulk Cu would be smallest. Additionally, for Cu thicknesses <8 nm the much larger discrepancy between simulated and experimental reflectance could indicate a rougher Cu film, perhaps even to the extent of particle formation as opposed to a continuous film. This is likely to occur for Cu due to its high surface tension ( $1.30 \text{ N m}^{-1}$ ) as compared to Al ( $0.87 \text{ N m}^{-1}$ ) such that evaporated Cu will favourably form particles rather than conformally wetting the underlying Al substrate.<sup>173</sup> A rougher or more particulate film would scatter light more strongly which would explain the higher reflectance of the thinner Cu films.

Due to its comparable average reflectance to Al films (86% vs. 88%) the Al | Cu (8 nm) | Al (0.8 nm) electrode, hereafter referred to as Al | Cu | Al, was tested further for use as a reflective electrode in model top-illuminated OPVs. Notably, the reflectance of this electrode remained unchanged after storage in a nitrogen filled glove box for 144 days (Figure 3.4(a)) and after heat treatment at  $50^\circ\text{C}$ , which is the working temperature of an OPV (Figure 3.4(b)). Additionally, there is only a slight reduction in reflectivity after heating in air at  $100^\circ\text{C}$  for 10 min (Figure 3.4(c)), although there is a larger decrease when the heating temperature is raised to  $150^\circ\text{C}$ . Notably however, the decrease in reflectance is still much smaller than for a pure Cu film after identical treatment (Figure 3.4(d)), consistent with increased stability after capping with an Al (0.8 nm) film.

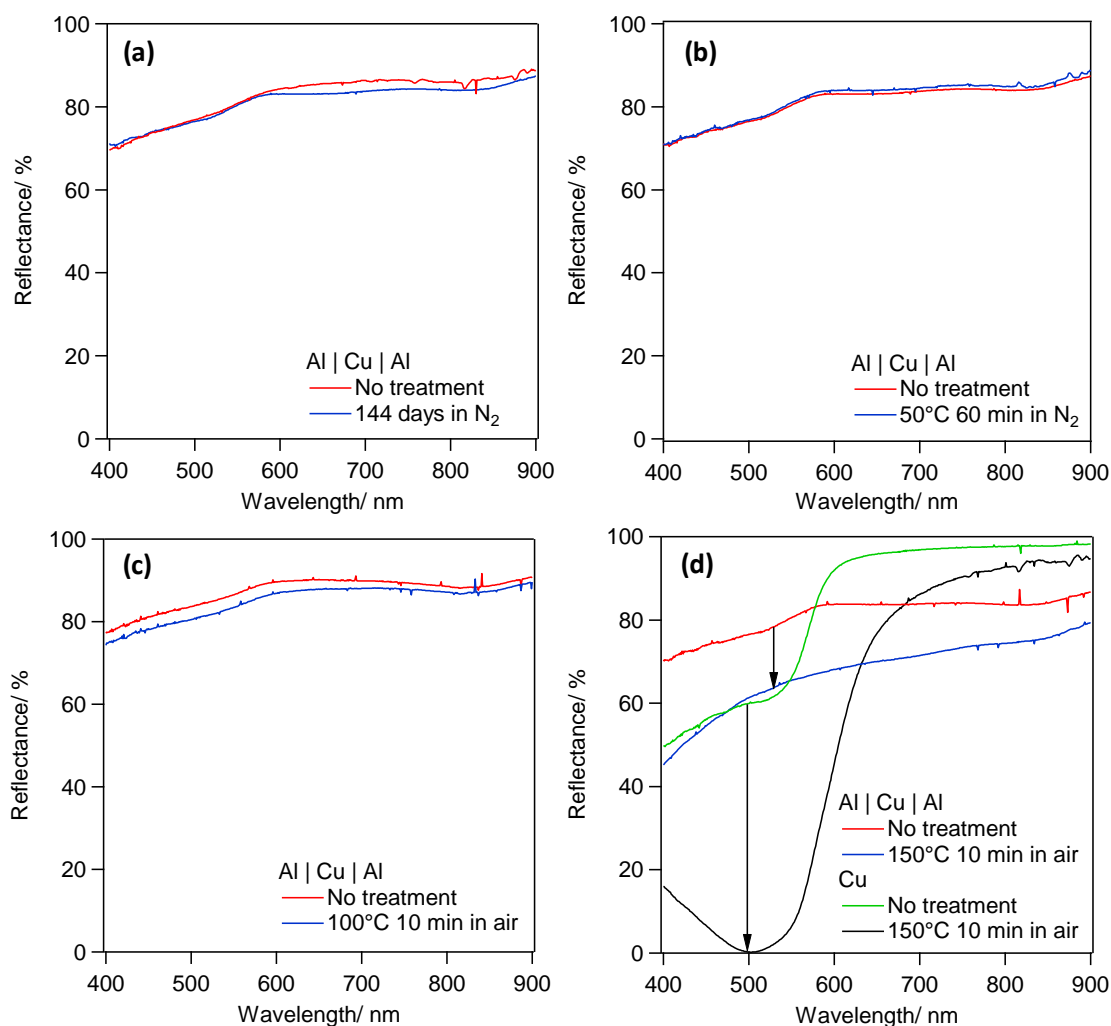


**Figure 3.4:** Reflectance spectra of an Al (100 nm) | Cu (8 nm) | Al (0.8 nm) electrode recorded before and after; (a) 144 days stored in nitrogen (b) 50°C treatment for 60 minutes in nitrogen; (c) 100°C treatment for 10 minutes in air and; (d) 150°C treatment for 10 minutes in air with a Cu (100 nm) film as a comparison.

To test the utility of the Al | Cu | Al electrode in top-illuminated OPVs it was incorporated into the OPV structure Al | Cu | Al | PCDTBT:PC<sub>71</sub>BM | MoO<sub>3</sub> (5 nm) | Ag (11 nm). In order to simplify the structure no interfacial electron-extraction layer was used. Representative *JV* curves for OPVs with Al only and composite substrate

electrodes are shown in Figure 3.5(a) and (b) respectively. The full data set is given in (Table 3.1)

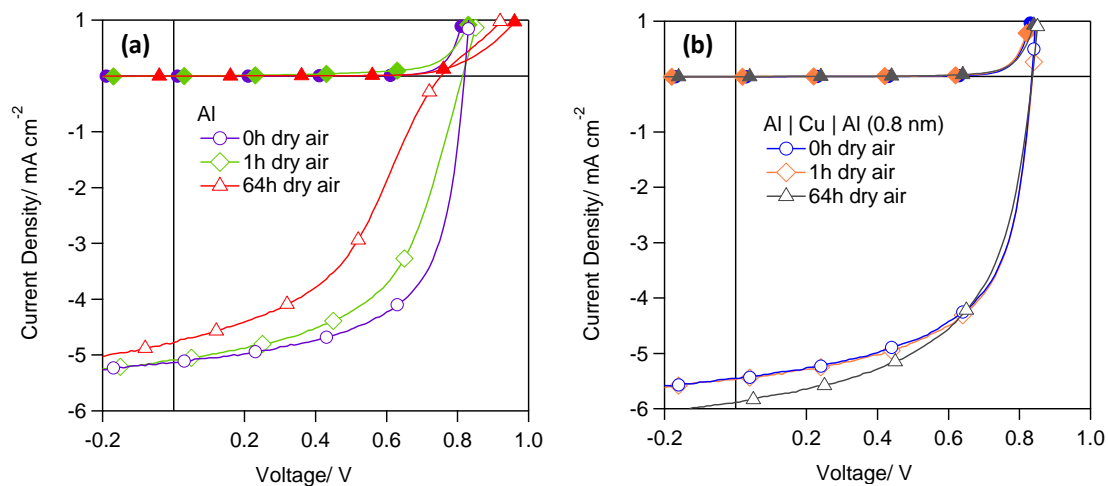


**Figure 3.5:** *JV* characteristics of OPVs with the structure: substrate electrode | PCDTBT:PC<sub>71</sub>BM | MoO<sub>3</sub>(5 nm) | Ag (11 nm) where the substrate electrode is: **(a)** Al (60 nm); and **(b)** Al (60 nm) | Cu (8 nm) | Al (0.8 nm), with varied time in hours the substrate electrode was exposed to air prior to device fabrication. Filled and empty markers indicate dark and light characteristics respectively.

It is evident from Figure 3.5 (and Table 3.1) that for OPV devices using the triple layer Al | Cu | Al electrode both the  $J_{sc}$  and stability are increased as compared to devices using Al only as the reflective electrode. The higher  $J_{sc}$  for the Al | Cu | Al electrode is unexpected because the absolute reflectivity of this electrode is lower than that of Al, as shown in Figure 3.2.

Substrate electrode	Air exposure time/ hours	$J_{sc}/ \text{mA cm}^{-2}$	$V_{oc}/ \text{V}$	$FF$	$PCE/ \%$
Al (60 nm)	0	$5.01 \pm 0.08$	$0.82 \pm 0.01$	$0.62 \pm 0.01$	$2.53 \pm 0.05$
	1	$4.83 \pm 0.13$	$0.82 \pm 0.01$	$0.55 \pm 0.01$	$2.18 \pm 0.05$
	64	$4.68 \pm 0.10$	$0.81 \pm 0.03$	$0.43 \pm 0.02$	$1.63 \pm 0.09$
Al   Cu   Al (0.8 nm)	0	$5.41 \pm 0.22$	$0.84 \pm 0.01$	$0.60 \pm 0.01$	$2.73 \pm 0.13$
	1	$5.49 \pm 0.17$	$0.84 \pm 0.01$	$0.60 \pm 0.01$	$2.73 \pm 0.05$
	64	$6.23 \pm 0.28$	$0.84 \pm 0.02$	$0.55 \pm 0.01$	$2.87 \pm 0.23$

**Table 3.1:** Key OPV performance characteristics for OPVs of structure: opaque substrate electrode | PCDTBT:PC<sub>71</sub>BM | MoO<sub>3</sub>(5 nm) | Ag (11 nm), where the electrode is either Al (60 nm) only, or Al (60 nm) | Cu (8 nm) | Al (0.8 nm) and has been exposed to air for 0, 1 or 64 hours prior to device fabrication.

This unexpected improvement can be explained either by: (i) the formation of an AlO<sub>x</sub> film at the Al | Cu | Al surface, that is thin enough to not hinder the flow of photo-generated electrons, that serves to hinder quenching of excitons by the electrode; (ii) a greater efficiency of charge extraction across the interface between the electrode and semiconductor, due to the smaller  $\Phi$  of the hybrid electrode ( $\sim 3.2$  eV) as compared to that of Al (4.2 eV)<sup>147,174</sup>; (iii) a variation in wetting of the BHJ on the electrode due to a change in the surface energy leading to a more favourable morphology. Whilst Al is widely used as the reflective electrode in conventional OPV architectures the oxide layer that forms at its surface upon oxidation due to the inevitable ingress of air into the device impedes electron extraction, resulting in electron accumulation at the contact and an S-shaped  $JV$  characteristic which leads to a reduction in  $FF$ ,  $V_{oc}$ , and  $J_{sc}$ <sup>175,176</sup>.

---

The onset of this *S*-shape is evident in the *JV* characteristics of OPVs using an Al substrate electrode after 1 hour and 64 hours air oxidation of the electrode prior to device fabrication (Figure 3.5(a)). After 64 hours air exposure the *FF* is reduced from  $\sim 0.62$  to  $\sim 0.43$ . However, for OPVs using the Al | Cu | Al substrate electrode there is no change in *FF* when the electrode is exposed to air for 1 hour, and after 64 hours air exposure the reduction in *FF* is  $\leq 10\%$ .

To further test the stability of the Al (60 nm) | Cu (8 nm) | Al (0.8 nm) electrode a ZnO<sub>x</sub> electron transport layer was deposited onto the composite electrode and an Al reference substrate prior to deposition of the organic photoactive layer. Representative *JV* characteristics are shown in Figure 3.6(a) with device data given in Table 3.2. The ZnO<sub>x</sub> electron-transport layer was found to have a wavelike surface structure as shown in Figure 3.6(b). The performance of OPVs fabricated on an Al only substrate electrode is very poor, consistent with the formation of a thick AlO<sub>x</sub> layer at the substrate electrode surface. This result is expected, since ZnO<sub>x</sub> film deposition involves conversion of zinc hydrate in ethanolamine into ZnO<sub>x</sub> by heating in air at 150°C for 10 minutes, which is a highly oxidising processing, and so this step is incompatible with easily oxidised metals such as Al.

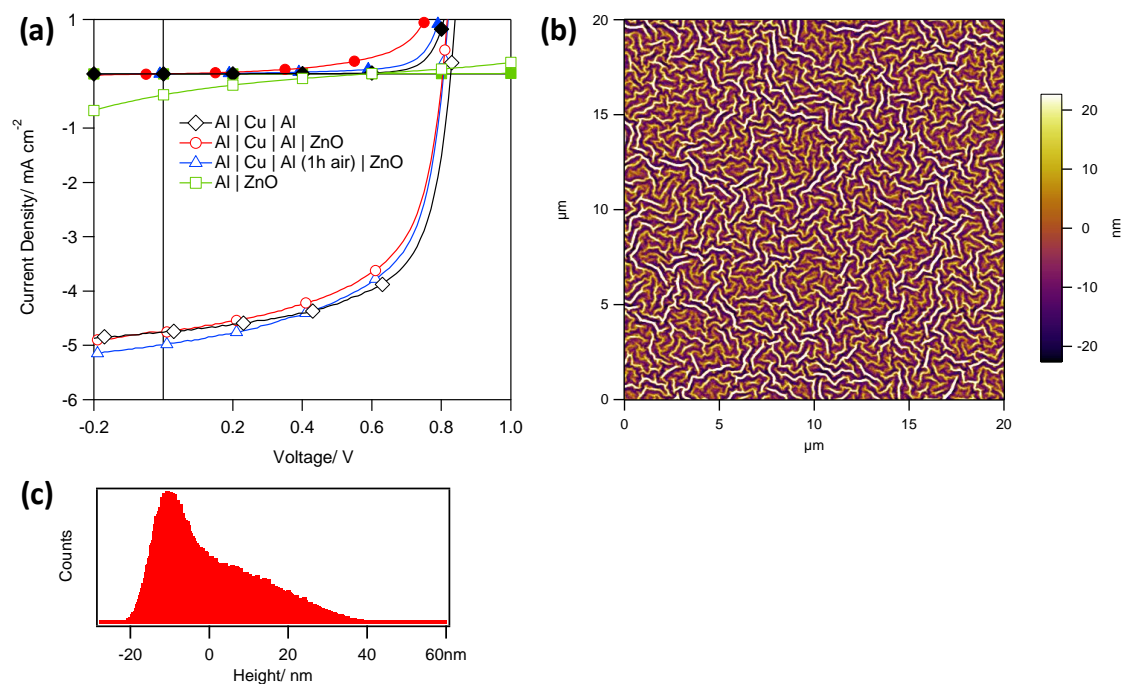


**Figure 3.6:** (a) *JV* characteristics of Al | Cu (7 nm) | Al | ZnO<sub>x</sub> | PCDTBT: PC<sub>71</sub>BM | MoO<sub>3</sub> (5 nm) | Ag (7 nm) OPVs with and without a ZnO<sub>x</sub> interlayer and with and without a pre-air oxidation of the composite Al | Cu | Al film. Representative data for OPVs fabricated on an Al only electrode with a ZnO<sub>x</sub> layer is also included. Filled and empty markers indicate dark and light characteristics respectively. (b) Morphology of a ZnO<sub>x</sub> film spun onto glass recorded with AFM and (c) the corresponding height histogram of the ZnO<sub>x</sub> film.

	$J_{sc}/ \text{mA cm}^{-2}$	$V_{oc}/ \text{V}$	$FF$	$PCE/ \%$
Al   Cu   Al	4.78 $\pm$ 0.14	0.81 $\pm$ 0.01	0.60 $\pm$ 0.06	2.34 $\pm$ 0.27
Al   Cu   Al   ZnO <sub>x</sub>	4.81 $\pm$ 0.24	0.77 $\pm$ 0.07	0.57 $\pm$ 0.02	2.19 $\pm$ 0.11
O <sub>x</sub> -Al   Cu   Al   ZnO <sub>x</sub>	4.75 $\pm$ 0.30	0.80 $\pm$ 0.02	0.57 $\pm$ 0.05	2.17 $\pm$ 0.26
Al   ZnO <sub>x</sub>	0.20 $\pm$ 0.14	0.27 $\pm$ 0.18	0.23 $\pm$ 0.02	0.02 $\pm$ 0.02

**Table 3.2:** Key OPV performance characteristics for device architecture: Al | Cu (7 nm) | Al | ZnO<sub>x</sub> | PCDTBT:PC<sub>71</sub>BM | MoO<sub>3</sub> (5 nm) | Ag (7 nm). The abbreviation O<sub>x</sub> means that the composite electrode was oxidised in air for 1 hour prior to ZnO<sub>x</sub> deposition.

Conversely, the performance of OPVs fabricated on the composite electrode using a ZnO<sub>x</sub> electron extracting layer is only marginally deteriorated as compared to that without; a  $\leq 10\%$  reduction in  $FF$  being the only significant difference in performance characteristics. This loss in  $FF$  is consistent with that seen for OPVs using a composite electrode exposed to air for 64 hours and is further compelling evidence that the 0.8 nm layer is extremely effective at passivating the underlying Cu | Al electrode from oxidation. Interestingly no significant improvement is seen with the ZnO<sub>x</sub> films, although this may result from the reduced reflectance after heating of 150°C in air (Figure 3.4(d)). This phenomenon is investigated in Chapter 4 of this thesis for ZnO<sub>x</sub> films processed at 100°C, a temperature at which reflectance is not significantly altered (Figure 3.4(c)).

In an effort to prevent the small reduction in  $FF$  of OPVs fabricated on the composite electrode after an extended period of air oxidation or ZnO<sub>x</sub> layer deposition, the Al capping layer thickness was increased from 0.8 nm to 1.2 nm in 0.2 nm steps. It was

---

hoped that these thicker films would provide better coverage of the Cu whilst still being thin enough to not adversely affect the resistance in the device. Representative  $JV$  plots are given in Figure 3.7 and the full data set is given in Table 3.3. From this it is evident that increasing the Al capping layer thickness actually results in a *larger* degradation in  $FF$  (inset Figure 3.7(b)) due to an increased series resistance and a significant reduction in  $V_{oc}$  after air oxidation of the electrode. Both of these changes can be rationalised in terms of the formation of an oxide layer that readily forms at the surface of the composite electrode that is too thick to be completely transparent to the flow of electrons across the interface. The resulting accumulation of electron density at the contact would give rise to the observed reduction in  $V_{oc}$ . Since Al undergoes a  $\sim 30\%$  increase in volume upon conversion to  $Al_2O_3$ <sup>177</sup> it is plausible that oxidation of the Al capping layer alone would be sufficient to form a layer too thick to be transparent to the flow of electrons.

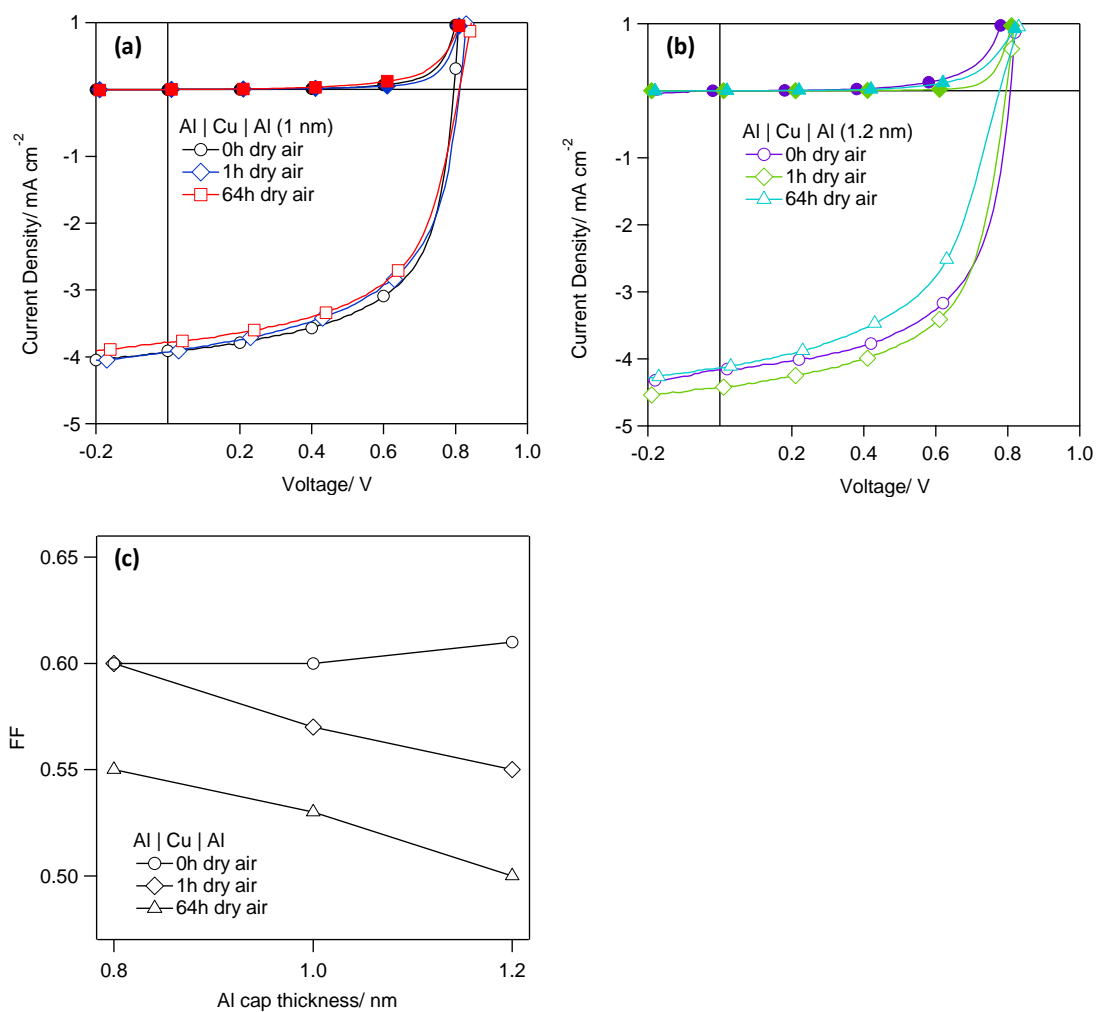


**Figure 3.7:** Representative  $JV$  characteristics of OPVs with the structure: Al (60 nm) | Cu (8 nm) | Al | PCDTBT:PC<sub>71</sub>BM | MoO<sub>3</sub>(5 nm) | Ag (11 nm) at substrate electrode oxidation times of 0, 1 and 64 hours prior to device fabrication for capping thicknesses of (a) 1 nm and (b) 1.2 nm. Filled and empty markers indicate dark and light characteristics respectively. The variation of  $FF$  for OPVs is shown in (c) with the composite substrate electrode and an Al capping layer of thickness 0.8–1.2 nm, with increasing air exposure time of the substrate electrode prior to device fabrication.

Substrate electrode	Air exposure time/ hours	$J_{sc}/ \text{mA cm}^{-2}$	$V_{oc}/ \text{V}$	$FF$	$PCE/ \%$
Al   Cu   Al (1.0 nm)	0	4.11 ±0.17	0.79 ±0.01	0.60 ±0.01	1.95 ±0.13
	1	4.00 ±NA	0.79 ±NA	0.57 ±NA	1.81 ±NA
	64	4.06 ±0.40	0.78 ±0.03	0.53 ±0.04	1.69 ±0.29
Al   Cu   Al (1.2 nm)	0	4.11 ±0.10	0.77 ±0.01	0.61 ±0.01	1.91 ±0.05
	1	4.03 ±0.14	0.77 ±0.01	0.55 ±0.07	1.69 ±0.29
	64	4.51 ±0.38	0.76 ±0.01	0.50 ±0.02	1.72 ±0.17

**Table 3.3:** Key OPV performance characteristics for device architecture: Al (60 nm) | Cu (8 nm) | Al | PCDTBT:PC<sub>71</sub>BM | MoO<sub>3</sub>(5 nm) | Ag (11 nm), where the Al cap is either 1.2 or 1.0 nm, with respect to the number of hours exposed to air.

Since a drop in  $FF$  is seen for even the optimised thickness capping layer (Figure 3.5(b)) it is evident that the optimal Al capping layer thickness of 0.8 nm is not completely passivating the underlying Al | Cu electrode. This is likely due to insufficient surface coverage resulting from the relatively high surface roughness; ~3 nm of the Al | Cu substrates as measured using AFM (Figure 3.8(b)). As the Al capping layer cannot be increased in thickness due to degradation in OPV  $PCE$ , it was attempted to fabricate a smoother electrode to achieve a better electrode passivation. It was found that the surface roughness can be tuned by simply varying the deposition rate of the opaque Al film in the range 1-10 Å s<sup>-1</sup>. A slow rate of deposition resulted in Al films with a large surface roughness (Figure 3.8(a)), whilst an increased rate resulted in much smoother electrode formation (Figure 3.8(b) and (c)).

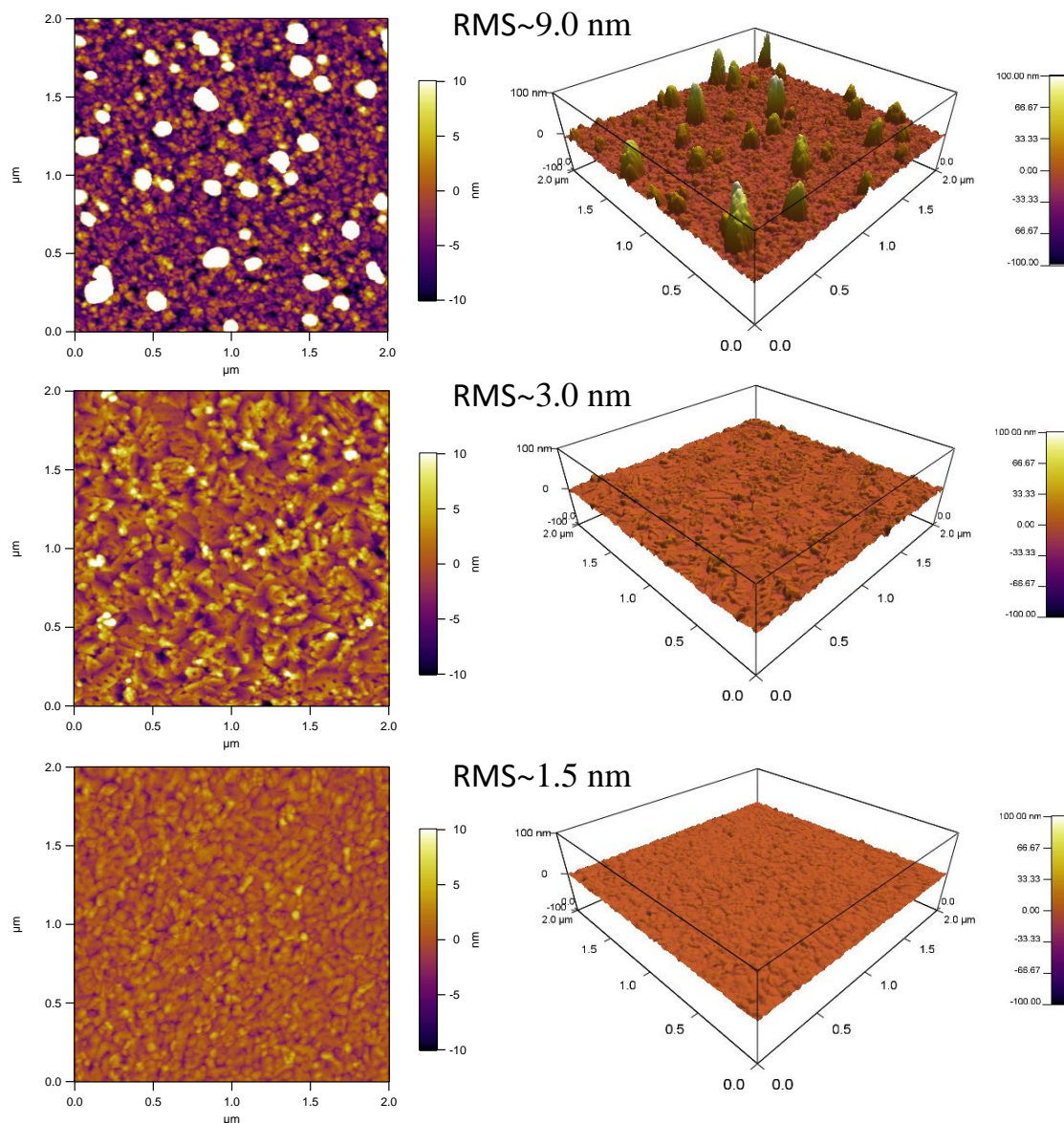


**Figure 3.8:** AFM image showing a 2D (left) and 3D (right) representations of an Al (60 nm) | Cu (8 nm) | Al (0.8 nm) substrate with the bottom Al layer deposited at (a) 0.2-1  $\text{\AA s}^{-1}$ , (b) 2-5  $\text{\AA s}^{-1}$  and (c) 10  $\text{\AA s}^{-1}$  with RMS surface roughness shown.

It was expected that these smoother films would lead to improved surface passivation due to a more complete coverage of the Cu film by the Al capping layer. Since the  $\Phi$  of metals is strongly dependent on the surface chemical state the Kelvin probe technique was used to monitor the time dependence of the surface oxidation

process for Al | Cu substrates with high ( $\sim 9$  nm) and low ( $\sim 1.5$  nm) surface roughness, (Figure 3.8(a) and (c) respectively) when an 0.8 nm Al capping layer is used (Figure 3.9).

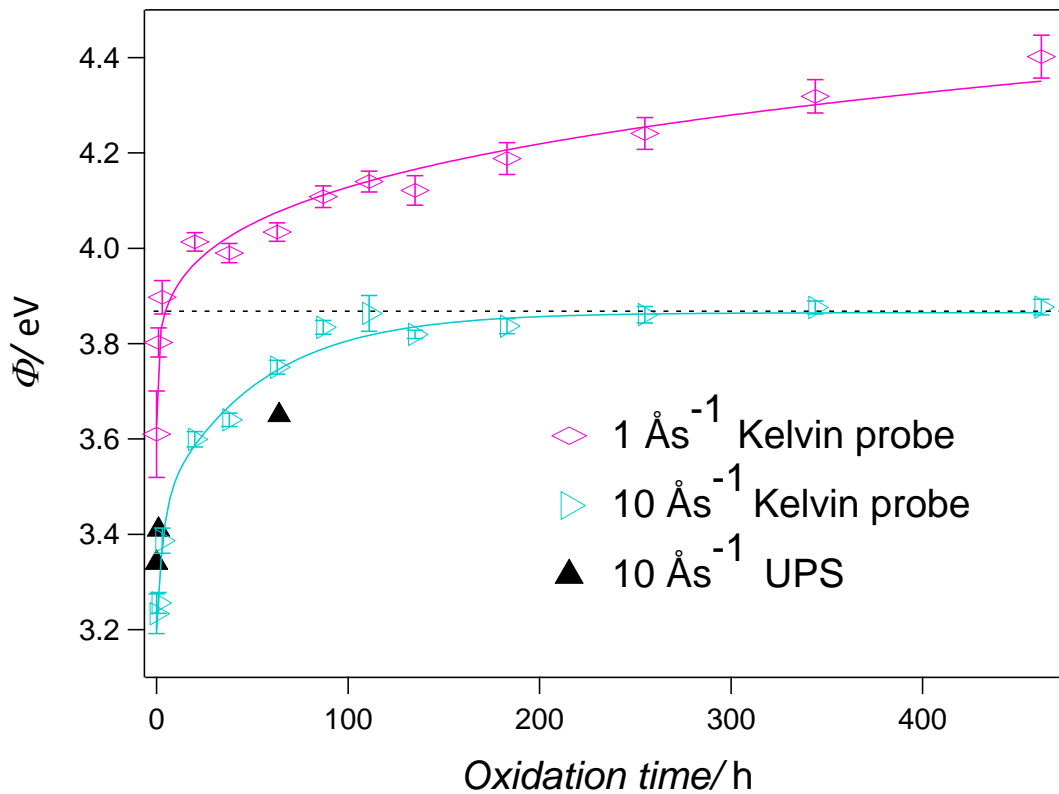


**Figure 3.9:** The evolution of  $\Phi$ , measured using the Kelvin probe technique and ultraviolet photoelectron spectroscopy (UPS) with air oxidation time for: Al (60 nm) | Cu (8 nm) | Al (0.8 nm) films with a fast ( $1 \text{ nm s}^{-1}$ ) and slow ( $0.1 \text{ nm s}^{-1}$ ) Al base layer evaporation rate, which results in a surface roughness of  $\sim 1.5$  nm (triangles) and  $\sim 9$  nm (diamonds) respectively.

It is evident from Figure 3.9 that the  $\Phi$  of the highest roughness substrate electrode, before oxidation, was significantly higher than that of the smoother electrode ( $\sim 3.6$  eV vs.  $\sim 3.2$  eV) which is consistent with there being some areas of exposed Cu

---

( $\Phi = 4.5\text{-}4.6\text{ eV}$ )<sup>162</sup> in the former, since Cu has the higher  $\Phi$  of the two metals. This conclusion is supported by the continuous increase in  $\Phi$  with increasing oxidation time towards that typical of Cu oxide ( $\Phi \sim 4.76\text{ eV}$ )<sup>178</sup>, since it is known that the oxidation of Cu occurs via the diffusion of  $\text{Cu}^+$  to the surface of the film along  $\text{Cu}^+$  grain boundaries<sup>179,180</sup> and so it is plausible that those parts of the Al | Cu substrate that are not capped with an ultra-thin Al layer are the source of Cu which diffuses over the surface and oxidises. Conversely, the  $\Phi$  of the composite electrode with a very low surface roughness saturated at  $\sim 3.9\text{ eV}$  after  $\sim 200$  hours, consistent with passivation of the electrode surface as previously reported by Hutter *et al.* for ultra-smooth Cu films on glass.<sup>164</sup> Collectively these results show that it should be possible to completely passivate this composite reflective electrode towards oxidation in air provided the roughness of the supporting substrate is sufficiently low. Importantly the increase in  $\Phi$  from  $\sim 3.2\text{ eV}$  to  $\sim 3.9\text{ eV}$  that occurs as a result of oxidation would not be expected to bring about any change in the degree of alignment between the electrode  $E_f$  and the LUMO of the electron acceptor since the LUMO of  $\text{PC}_{71}\text{BM}$  is  $\sim 3.9\text{ eV}$  below the vacuum level.<sup>181</sup> Consequently, provided the oxide thickness remains sufficiently low not to impede the flow of electrons across the interface this change in  $\Phi$  should not adversely impact OPV device performance.

To test the conclusion of complete passivation by the smoother film OPVs are fabricated on substrate electrodes comprising a very smooth Al substrate (roughness  $\sim 1.5\text{ nm}$ ),  $8\text{ nm}$  Cu layer and  $0.8\text{ nm}$  Al passivation layer. The full data set is shown in Table 3.4 with *JV* curves shown in Figure 3.10.

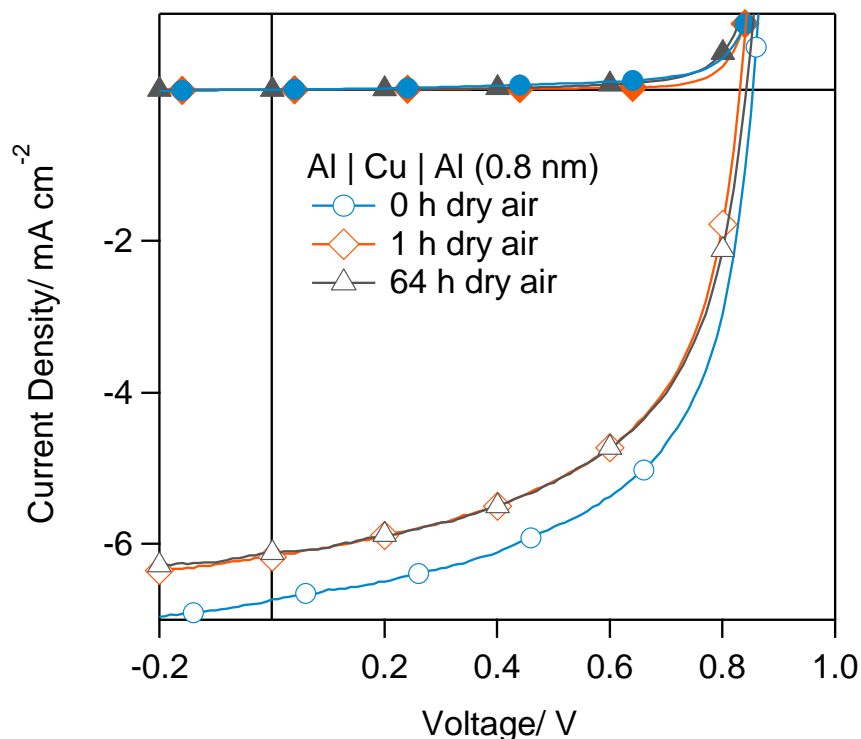


**Figure 3.10:** Representative  $JV$  characteristics of OPVs in the light (empty) and dark (filled) with the structure Al | Cu | Al | PCDTBT: PC<sub>71</sub>BM | MoO<sub>3</sub> (5 nm) | Ag (7 nm) under various dry air exposure times with an Al | Cu | Al bottom electrode roughness of 1.49 nm.

Dry air exposure/ hours	$J_{sc}/ \text{mA cm}^{-2}$	$V_{oc}/ \text{V}$	$FF$	$PCE/ \%$
0	$6.69 \pm 0.29$	$0.85 \pm 0.01$	$0.56 \pm 0.03$	$3.22 \pm 0.20$
1	$6.18 \pm 0.45$	$0.84 \pm 0.01$	$0.56 \pm 0.03$	$2.95 \pm 0.11$
64	$6.18 \pm 0.19$	$0.85 \pm 0.01$	$0.57 \pm 0.02$	$2.97 \pm 0.10$

**Table 3.4:** Key OPV performance characteristics for OPV architecture: Al (50 nm) | Cu (8 nm) | Al (0.8 nm) | PCDTBT: PC<sub>71</sub>BM | MoO<sub>3</sub> (5 nm) | Ag (7 nm) under various dry air exposure times with an Al | Cu | Al bottom electrode RMS roughness of 1.49 nm.

---

It can be seen that  $V_{oc}$  and  $FF$  are unchanged even after 64 hours air exposure of the substrate electrode which indicates an unchanged resistivity of the electrode. Whilst there is a loss in  $J_{sc}$  upon air exposure it is likely this is due to a change in the BHJ morphology, on account of a different surface energy of the electrode, and not due to any intrinsic detrimental effects from the electrode as evidenced by the aforementioned stable  $FF$  and  $V_{oc}$ .

It is assumed that, due to the high reactivity of Al, all of the ultra-thin Al capping layer at the composite electrode surface is ultimately oxidised when exposed to air for an extended period. However, the extent to which the underlying Cu is also oxidised is not known. To address this important fundamental question High resolution XPS (HRXPS) was used to probe the chemical composition of the uppermost surface of the Al | Cu | Al substrate electrode after 0, 1, and 64 hours exposure to air. All substrates were exposed to the laboratory environment for  $\sim 2$  minutes whilst loading into the spectrometer, so even for *zero* hours oxidation some oxide is present. It is evident from Figure 3.11 that the Cu  $2p_{3/2}$  core level peaks are symmetric with a narrow full-width-at-half-maximum of  $\sim 1$  eV at binding energies of 932.8 eV and 932.7 eV for films exposed to dry air for 0 and 64 hours respectively, which indicates that all Cu is in the  $Cu^0$  oxidation state even after 64 hours air oxidation. There is no evidence for CuO for which the Cu  $2p_{3/2}$  binding energy is expected to be 933.6-933.8 eV.<sup>182-184</sup> The absence of a satellite peak at  $\sim 943.6$  eV corroborates this conclusion.<sup>182,183</sup> However, the presence of  $Cu_2O$  cannot be ruled out, since the Cu  $2p_{3/2}$  peaks for  $Cu^0$  and  $Cu^{1+}$  species are known to be within 0.1 eV of one another and so are difficult to resolve.<sup>183-185</sup>

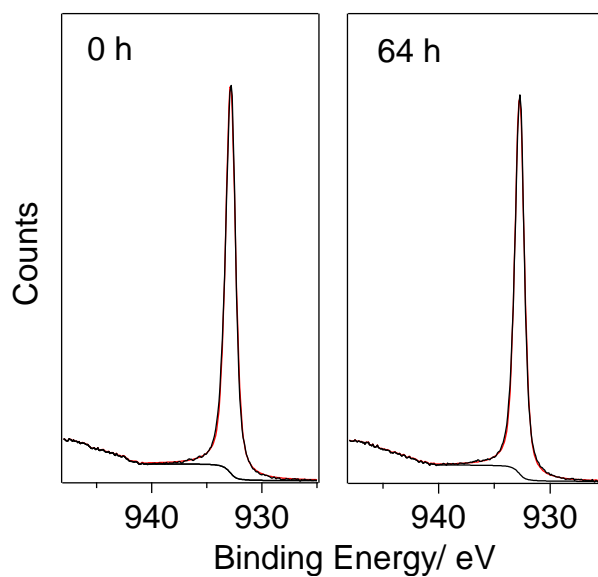


**Figure 3.11:** Cu  $2p^{3/2}$  core level HRXPS spectra with peak fitting (red lines) for Al (60 nm) | Cu (8 nm) | Al (0.8 nm) substrates, after 0 and 64 hours air oxidation.

The Cu LMM Auger spectra is therefore probed to look for the presence of any  $\text{Cu}_2\text{O}$ . It is evident from Figure 3.12 that there is no significant change in the Cu LMM Auger spectral peaks for samples exposed to air for 0 hours and 64 hours, and both spectra are essentially identical to that previously reported for freshly sputtered polycrystalline Cu films by Platzman *et al.*<sup>183</sup> and Greiner *et al.*<sup>89</sup>, which is compelling evidence that no  $\text{Cu}_2\text{O}$  is formed.

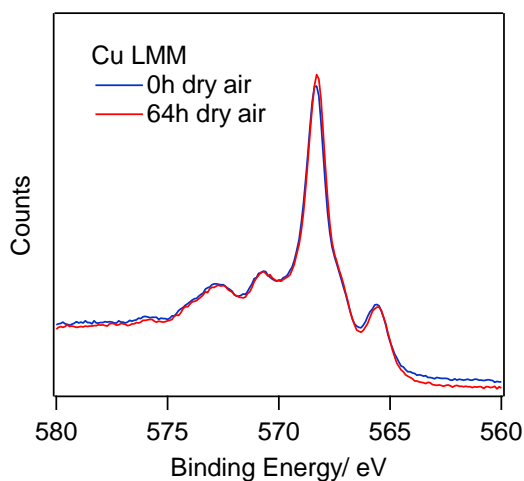


**Figure 3.12:** Cu LMM Auger spectra for Al (60 nm) | Cu (8 nm) | Al (0.8 nm) substrates, after 0 and 64 hours air oxidation.

Further evidence for the absence of Cu oxides is provided by an analysis of the core level peaks associated with the O1s electrons (Figure 3.13). For all samples the broad asymmetric O1s peak can be fitted with two peaks at ~532 eV and ~533 eV.

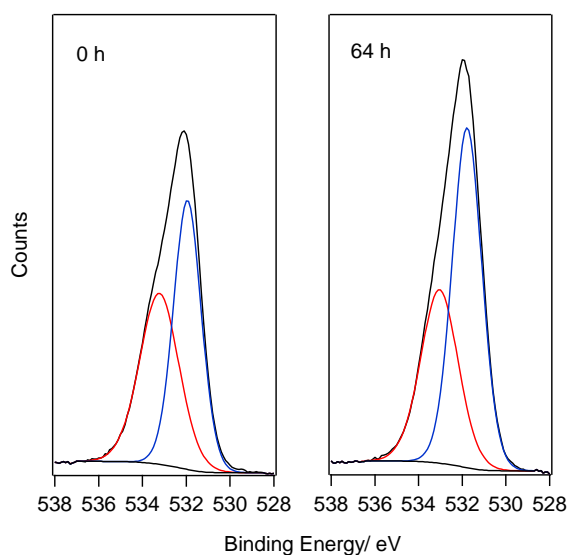


**Figure 3.13:** O 1s core level HRXPS spectra with peak fitting for Al (60 nm) | Cu (8 nm) | Al (0.8 nm) substrates, after 0 and 64 hours air oxidation.

---

Peaks in the XPS spectra that are indicative of Cu oxides occur at  $\leq 530.5$  eV<sup>183,184,186-189</sup> and so the absence of a shoulder at low binding energy, even after 64 hours air exposure, is consistent with the absence of Cu oxides. The peak at  $\sim 533$  eV is attributed to H<sub>2</sub>O adsorbed whilst loading the samples into the vacuum system<sup>183</sup> and the peak at  $\sim 532$  eV is assigned to AlO<sub>x</sub>.<sup>189,190</sup> Consistent with the gradual oxidation of the ultra-thin Al capping layer, the intensity of the latter increases with increasing air oxidation time as compared to the peak associated with adsorbed H<sub>2</sub>O, as is evident from the change in ratio of these two peaks: 1:1.11, 1:1.40 and 1:1.55 for 0, 1 and 64 hours respectively.

Direct evidence for the presence of AlO<sub>x</sub> and for Al<sup>0</sup> is also provided by the peaks associated with Al 2s electrons (Figure 3.14) at binding energies of 120.4 eV and 118.1 eV respectively.<sup>191</sup> Whilst the former partially overlaps with the peak centred at 122.8 eV, which can be assigned to Cu 3s,<sup>188,192</sup> the separation is sufficient to be confident of the assignment.

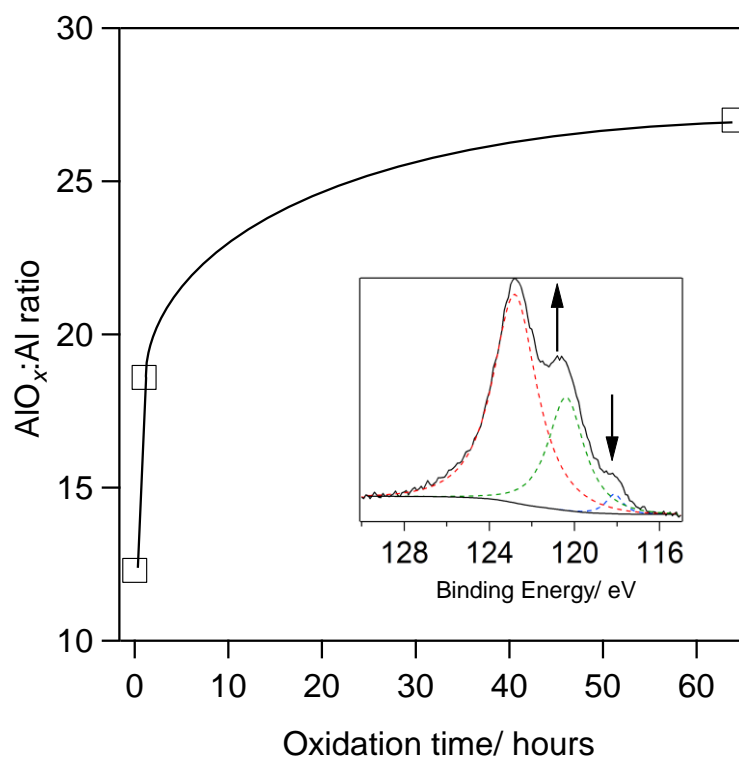


**Figure 3.14:** Graph of the ratio of HRXPS peaks assigned to  $\text{AlO}_x$  (~120 eV) and Al (~118 eV) at the surface of an Al (60 nm) | Cu (8 nm) | Al (0.8 nm) substrate as a function of air oxidation time. The line is intended to guide the eye and is not a rigorous fit. The inset shows the Al 2s binding energy region after 0 hours oxidation. All samples were briefly exposed to the laboratory environment whilst loading into the spectrometer vacuum system.

Notably the ratio between these peaks increases with oxidation time from 12.3 to 18.6 and finally to 27.0 indicative of the gradual conversion of Al to  $\text{AlO}_x$ . Whilst the preferential oxidation of Al over Cu at the composite electrode surface can be understood in terms of the much greater heat of oxide formation of  $\text{AlO}_x$  ( $-1675.69 \text{ kJ mol}^{-1}$ )<sup>193</sup> as compared to  $\text{Cu}_2\text{O}$  ( $-170.71 \text{ kJ mol}^{-1}$ )<sup>193</sup> and  $\text{CuO}$  ( $-156.06 \text{ kJ mol}^{-1}$ )<sup>193</sup>, it is

---

remarkable that such a thin Al capping is so effective at passivating the film even after 64 hours.

### **3.5 Conclusion**

In summary, in this chapter a new substrate electrode for top-illuminated OPVs based on the triple layer structure: Al (> 60 nm)| Cu (8 nm) | AlO<sub>x</sub> (0.8 nm) has been developed, which has a reflectance comparable to that of Al, with the advantages of high stability towards oxidation and low raw materials cost. It has also been shown that a 0.8 nm Al capping layer deposited by thermal evaporation is sufficient to block oxidation of the reflective Al | Cu substrate, which is a remarkable finding given that the self-limiting oxide thickness on Al metal is greater than 2 nm.

---

## Chapter 4.

# Elucidating an Electrode Design Rule for High Performance Top-Illuminated Organic Photovoltaics

The majority of the work presented in this chapter has been published in:

*An Electrode Design Rule for High Performance Top-Illuminated Organic Photovoltaics* Martin S. Tyler, Immad M. Nadeem, Ross A. Hatton, *Mater. Horiz.* **2016**, DOI:10.1039/C6MH00124F

### 4.1 Summary

This chapter proposes an electrode design rule for high performance top-illuminated bulk-heterojunction organic photovoltaics, which enables the device architecture to be simplified by removing the need for the electron selective layer at the interface with the low work function reflective electrode. This new guideline for electrode design is underpinned by device studies in conjunction with a study of the energetics at the interface between five widely used solution processed organic semiconductors of both electron donor and acceptor type, and a stable low work function reflective substrate electrode. The magnitude and distribution of space charge resulting from ground-state electron transfer from the electrode into each organic semiconductor upon contact formation is derived from direct measurements of the interfacial energetics using the Kelvin probe technique, which enables the variation in potential across the entire film thickness used in the devices to be probed.

## 4.2 Introduction

It is widely accepted that OPVs based on a solution processed BHJs of electron donor and electron acceptor type organic semiconductors offer the lowest cost path to the fabrication of OPVs.<sup>194</sup> For this type of OPV it is considered essential to include wide band-gap charge extraction layers at both electrode interfaces to ensure optimised interfacial energetics and guarantee charge carrier selectivity, since both donor and acceptor type organic semiconductors can contact both electrodes.<sup>195,196</sup> The thickness of these charge extraction layers is typically in the range 3-50 nm<sup>74,101,197-200</sup>, sufficient to block the extraction of one carrier type whilst at the same time not significantly contributing to device series resistance or parasitic absorption of incident light. For hole-blocking layers (HBLs) the wideband-gap oxides ZnO<sub>x</sub> and TiO<sub>x</sub> are the materials of choice because they can be deposited from solvents that are orthogonal to those used for organic semiconductors and have the deep lying valance band edge needed to block unwanted hole-extraction by the electrode, a process that erodes device  $FF$  and  $J_{sc}$ .<sup>74,76</sup> These materials are  $n$ -type with a conduction band edge at comparable energy to the LUMO in the electron-acceptor component of the BHJ, and so serve to align the electrode  $E_f$  to the LUMO of the organic electron-acceptor which maximises the electric field strength across the BHJ. The use of these metal oxides removes the need for a low work function reactive metal electrode such as Ca because they can be used in conjunction with relatively high work function, and thus relatively stable metals such as Ag.<sup>81,199</sup> It has been proposed that these wide band-gap interfacial layers also offer the benefit of: (i) reduced quenching of excitons formed in the BHJ near to the reflective electrode, leading to improved  $J_{sc}$ ,<sup>77</sup>; and (ii) increased  $J_{sc}$  by acting as an optical spacer layer, which enables tuning of the optical field distribution to maximise absorption of light.<sup>13</sup>

As described in Chapter 1, OPVs with a top-illuminated architecture are increasingly attracting attention because they remove the need for costly conducting oxide coated glass and increase the range of potential applications by giving more flexibility in terms of the materials used as the supporting substrate.<sup>82,101,105,114</sup> In this class of OPV the preferred location of the HBL is at the contact with the reflective substrate electrode, which has proved to be the most stable device architecture.<sup>152</sup> The potential benefit of an optical spacer at the interface with the reflective electrode in top-illuminated OPVs has been explored by Lin *et. al*<sup>78</sup> in the context of OPV devices based on very thin films of evaporated small molecule organic semiconductors. The thickness of the optical spacer layer needs to be very carefully controlled and this approach is only useful for a narrow range of incident angles, so is not a panacea for light management in top-illuminated OPVs.<sup>81</sup>

In this chapter the results of a study of the energetics at the interface between five widely used solution processed organic semiconductors and a low work function ( $\sim 3.25$  eV) electrode, in conjunction with OPV device studies for three different BHJ systems, are presented. The results of this study are used to under-pin a new electrode design rule for top-illuminated OPVs in which the reflective electrode is also the electron extracting electrode. All published reports at the time of writing relate to the study of energy level alignment at the interface between substrate electrodes and solution processed organic semiconductors have been limited to relatively high work function ( $\geq 3.8$  eV) electrode materials<sup>181,201,202</sup>, or electrodes capped with an HBL such as  $\text{ZnO}_x$ <sup>142,203</sup>, possibly due to the difficulty of working with low work function metals outside of a vacuum system. In Chapter 3 a means of rendering Al films sufficiently stable towards oxidation for practical application as a substrate electrode in top-illuminated OPVs is shown, using a very thin capping layer of Cu | Al.<sup>204</sup> This triple

layer metal electrode is well-matched to the requirements of top-illuminated OPVs because it offers the advantages of high reflectivity, low metal cost, and the rare combination of high stability towards oxidation and very low work function of  $3.25 \text{ eV} \pm 0.08 \text{ eV}$ .<sup>204</sup> In this chapter this electrode is used because it enabled an investigation of the energetics at the interface between a low work function electrode and solution processed organic semiconductor junction, without the complexity associated with interfacial chemical reaction and uncontrolled oxidation.

### 4.3 Experimental

To fabricate the reflective electrodes onto cleaned  $12 \times 12 \text{ mm}^2$  glass slides was thermally evaporated Al (60-100 nm,  $1 \text{ nm s}^{-1}$ ), Cu (8 nm,  $0.1 \text{ nm s}^{-1}$ ), Al (0.8 nm,  $0.01\text{-}0.03 \text{ nm s}^{-1}$ ) without breaking the vacuum between depositions followed by oxidation in dry air for 1 hour, as previously reported,<sup>20</sup> to ensure oxidation of the thin capping layer.

Organic semiconductor films of increasing thickness were deposited from solutions fabricated using the spin coating technique with concentrations and spin speeds as follows; PC<sub>71</sub>BM in CHCl<sub>3</sub> (24, 12, 6, 3, 1, 0.2 mg ml<sup>-1</sup>) spin cast at 6000 rpm for 60s followed by annealing at 80°C for 30 mins; PC<sub>61</sub>BM in CHCl<sub>3</sub> (24, 12, 6, 0.5 mg ml<sup>-1</sup>) spin cast at 6000 rpm for 60s followed by annealing at 80°C for 30 mins; PTB7 in 1,2-dichlorobenzene (DCB) (10, 5, 2.5, 1 mg ml<sup>-1</sup>) drop cast at 1000 rpm for 60 s dried under vacuum for 1 h; P3HT in DCB (20, 10, 5, 1 mg ml<sup>-1</sup>) drop cast then spun at 1000 rpm for 120 s followed by 30 mins under N<sub>2</sub> then annealed at 120°C for 30 mins, PCDTBT in CHCl<sub>3</sub> (4, 2, 1 mg ml<sup>-1</sup>) drop cast then spun at 1000 rpm for 60s or spin cast at 6000 or 3000 rpm all then annealed at 80°C for 30 mins. Film thickness was

---

measured by scoring the film to form a step and measuring the step height using AFM and referencing to a clean electrode as shown in the experimental.

In order to deposit a  $\text{ZnO}_x$  layer from solution the proven low temperature method described by Jagadamma *et al*<sup>74</sup> was used:  $\text{ZnO}_x$  HBL zinc acetate dihydrate (0.08M or 0.16M) and ethanolamine (0.08M or 0.11M) were added to 2-methoxyethanol and stirred in air for 12 hours prior to use (for 5 nm and 11 nm films respectively). A film was then formed by drop casting the solution followed by spinning at 4000 rpm for 60 seconds and annealing at 100°C for 10 minutes in air. This method has been shown to result in compact  $\text{ZnO}_x$  films compatible with processing on flexible plastic or oxidisable substrates, and offers the advantage of reduced cost as compared to high temperature processing.<sup>74,197,205</sup>

#### 4.4 Results & discussion

To probe the interfacial energetics upon contact formation the Kelvin probe technique<sup>203,206</sup> was used to measure the change in energy of the vacuum level relative to  $E_f$ , denoted as  $\varepsilon_F^{vac}$ , upon deposition of organic semiconductor layers from solution onto Al | Cu | Al electrodes. Importantly, measurements were made under nitrogen immediately after organic semiconductor deposition without exposure to the laboratory atmosphere. Unlike UPS, which is most widely used to make measurements of interfacial energetics, the maximum film thickness that can be probed using the Kelvin probe technique is not limited by sample charging as it does not cause charged particles to be emitted.<sup>203,207-210</sup> As a result the change in potential across film thicknesses comparable to that used in OPV devices can be probed. Measurements were made for two archetypal electron acceptors; PC<sub>71</sub>BM and PC<sub>61</sub>BM (Figure 4.1(a) and (c)), and

three widely used electron donors; PCDTBT, PTB7, and P3HT (Figure 4.2(a), (c) and (e)). Uniform thin films of these materials were deposited by spin coating whilst the thickness was tuned via the solution concentration ( $0.1 \text{ mg ml}^{-1}$ - $24 \text{ mg ml}^{-1}$ ) and spin speed.

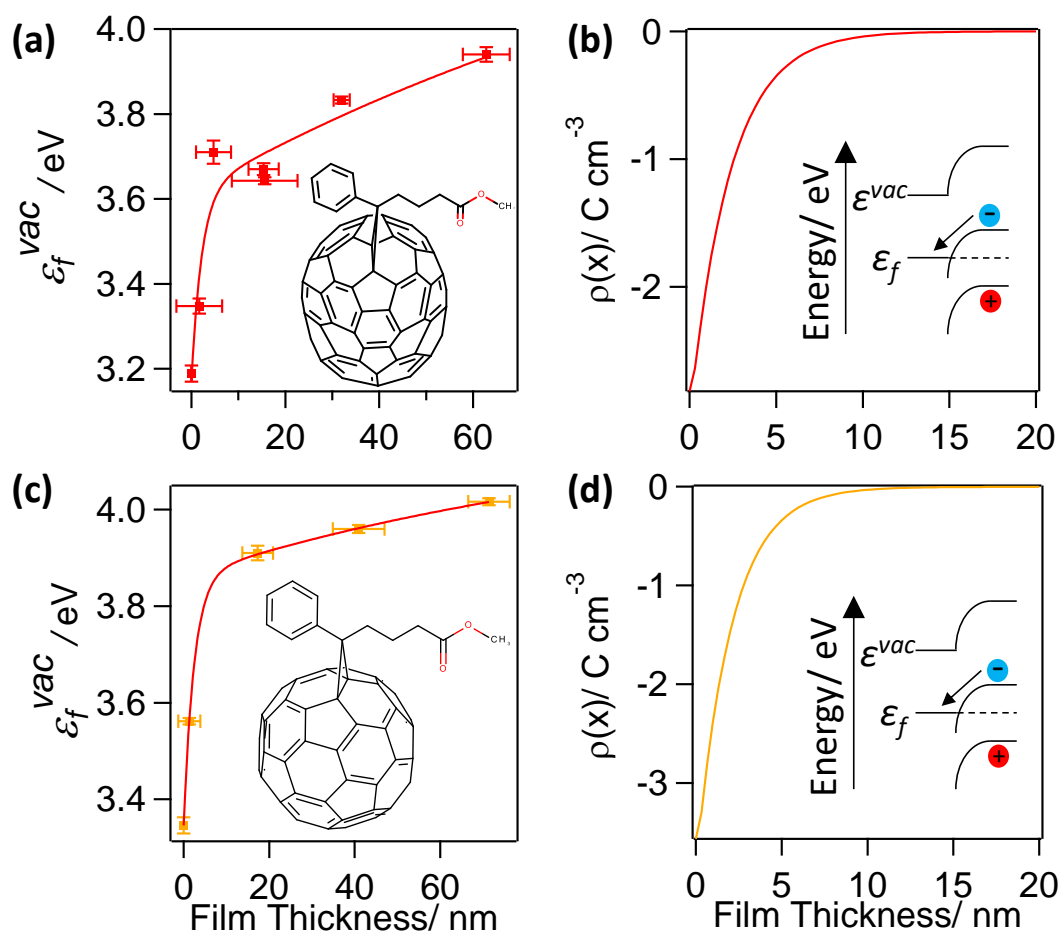


**Figure 4.1:** (a) & (c) show the variation in  $\varepsilon_F^{vac}$  for PC<sub>71</sub>BM and PC<sub>61</sub>BM films supported on an Al | Cu | Al electrode. The  $\varepsilon_F^{vac}$  data is fitted with a double exponential function. The insets show the corresponding structures of the molecules.; (b) & (d) show the space charge density distribution,  $\rho(x)$ , calculated using Equation 4.1, that would give rise to the measured variation in potential.

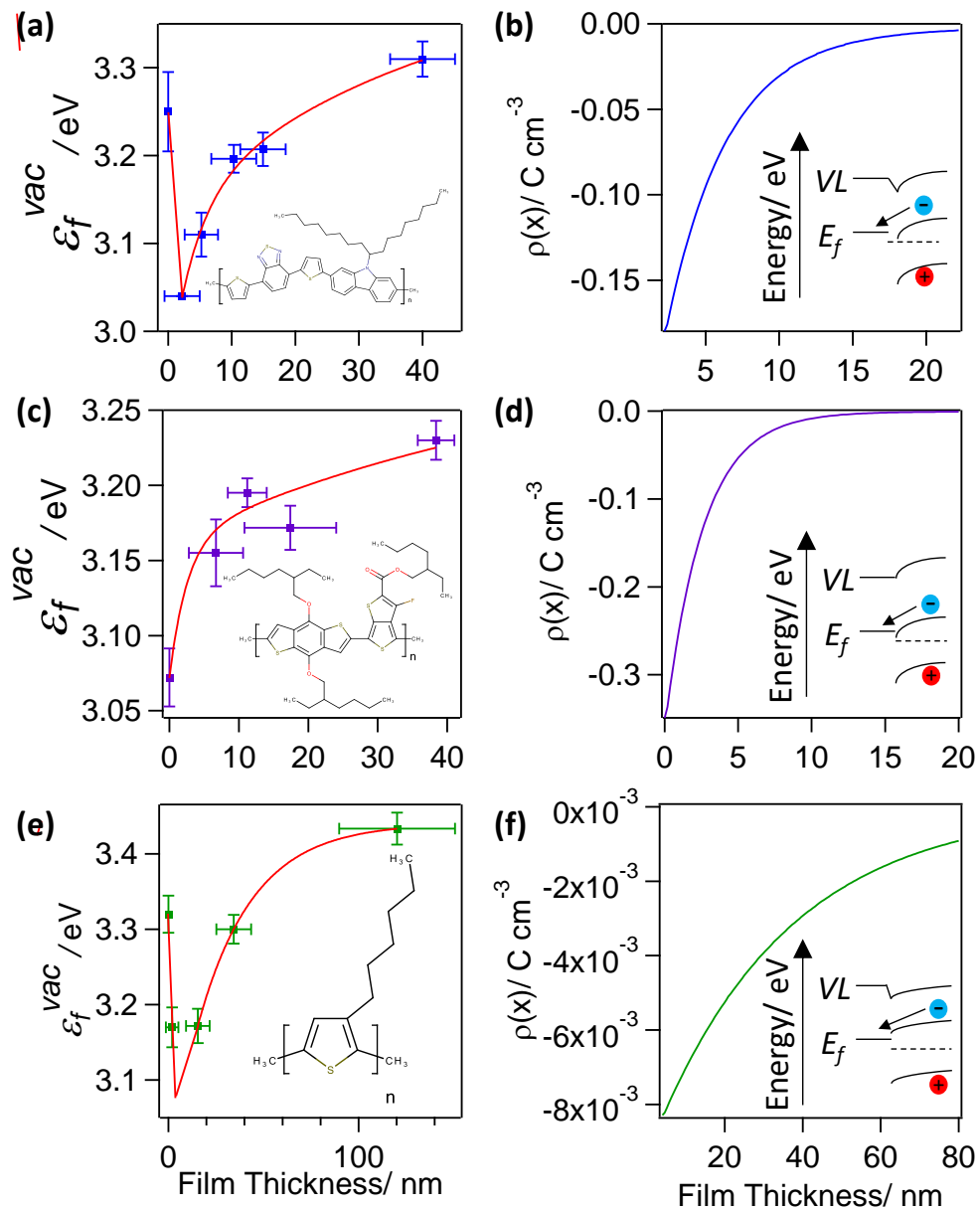


**Figure 4.2:** Variation in  $\epsilon_F^{vac}$  (a), (c) & (e) and charge distribution (b), (d) & (f) for donor organic semiconductor thin films supported on an Al | Cu | Al electrode as a function of semiconductor film thickness for: PCDTBT (a) & (b); PTB7 (c) & (d); and P3HT (e) & (f). The insets show the corresponding structures of the molecules and schematic energy level diagrams. The  $\epsilon_F^{vac}$  data is fitted with a double exponential function. For the cases of PCDTBT and P3HT, for which the push back effect is observed, the total space charge was calculated for thicknesses after the initial abrupt decrease in the vacuum level.

It is evident from Figure 4.1(a) and (c) that for both PC<sub>71</sub>BM and PC<sub>61</sub>BM films there is an ~ 0.7 eV increase in  $\varepsilon_F^{vac}$  across the thickness of the fullerene layers, most of which occurs within the first 10 nm of the interface. In both cases the change is consistent with spontaneous transfer of electron density from the electrode into the adjacent fullerene layer, giving rise to a static space charge region near to the interface and band bending, as depicted in Figure 4.1(b) and (d). For each of the measurements of interfacial energetics the space charge distribution,  $\rho(x)$ , that would give rise to the measured variation in potential is calculated using Poisson's equation:

$$\frac{d^2V(x)}{dx^2} = -\frac{\rho(x)}{\varepsilon_r\varepsilon_0} \quad \text{Equation 4.1}$$

where  $\varepsilon_0$  is the permittivity of free space and  $\varepsilon_r$  is the relative permittivity of each organic semiconductor, assumed to be 4 and 3 for the fullerenes electron acceptors and polymer electron donors respectively.<sup>35,181,209,211</sup>  $\rho(x)$  is therefore calculated by twice differentiating the double exponential fit of the variation of  $\varepsilon_F^{vac}$  across the film thickness and multiplying by  $(\varepsilon_r\varepsilon_0)$ . Thermodynamic equilibrium across the interface between un-doped organic semiconductors and electrodes cannot be assumed for the semiconductor thicknesses used in OPVs because the density of unintentional impurities in the organic semiconductor capable of donating or accepting charge may be too low.<sup>203,208,210</sup> However in the current case the LUMO energies of PC<sub>71</sub>BM and PC<sub>61</sub>BM are ~3.77 eV and ~3.78 eV below the vacuum level respectively<sup>212</sup> much lower than the energy of the electrode  $E_f$  (at ~3.25 eV below the vacuum level), so there is a high density of states available to accommodate the transferred charge.

In the context of a BHJ OPV *both* the donor and acceptor phases can have an interface with *both* electrodes, and so it is interesting to consider the energetics at the

contact between the donor type organic semiconductor and the low work function electrode, a class of interface that has been sparsely investigated to date and only in the context of vacuum deposited small molecules.<sup>207,213,214</sup> It is evident from Figure 4.2(a), (c) and (e) that the extent of electron transfer from the Al | Cu | Al electrode into the three donor type semiconductors investigated is much less than that at the interface with the fullerenes, which is consistent with the shallower LUMO states in donor type organic semiconductors.<sup>196</sup> For both PTB7 (3.3-3.5 eV)<sup>215,216</sup> and PCDTBT (3.4-3.6 eV)<sup>57,73</sup> the LUMO is below the  $E_f$  of the electrode, so there is a high density of empty states into which electron density can be accepted. Consequently, most of the potential energy change occurs very close to the electrode in both of these cases, just as for the fullerenes. Conversely, the rate of change in potential energy in P3HT is much more gradual and occurs over a much greater film thickness, due to the shallow LUMO of P3HT; only ~3.0 eV below the vacuum level.<sup>64,217</sup> The LUMO of P3HT is in fact above the  $E_f$  of the electrode and so the electron density transferred (which is motivated by the difference in chemical potential) must be accommodated in defect states in the P3HT band-gap. Since the density of unintentional electron accepting defects states in the band-gap of P3HT is expected to be relatively low in high purity polymers such as those used in this study<sup>218</sup>, band bending is much more gradual than in the case for PTB7 and PCDTBT. Crucially, high performance donor-type polymers are invariably characterised by a narrower band-gap than P3HT (< 1.8 eV vs  $\geq 2.0$  eV) and a larger ionisation potential ( $\geq 5.2$  eV vs  $\leq 5.0$  eV)<sup>57,64,68,73,215,216,219</sup>, the latter of which ensures the HOMO energy is sufficiently deep lying to achieve a large  $V_{oc}$ .<sup>220</sup> The HOMO and LUMO energies, with respect to VL, of those used herein and state-of-the-art polymer electron donors used in OPVs are shown in Figure 4.3. Consequently, the LUMO in high performance donor type polymers is, by design, much lower lying than in P3HT.

Therefore, the pictures of the interfacial energetics at the interface with PTB7 and PCDTBT shown in Figure 4.2(b) and (d) are most representative of the energetics that would be achieved at the interface between the low work function electron-extracting electrode and a high performance narrow band-gap donor-type polymer in the absence of a HBL.

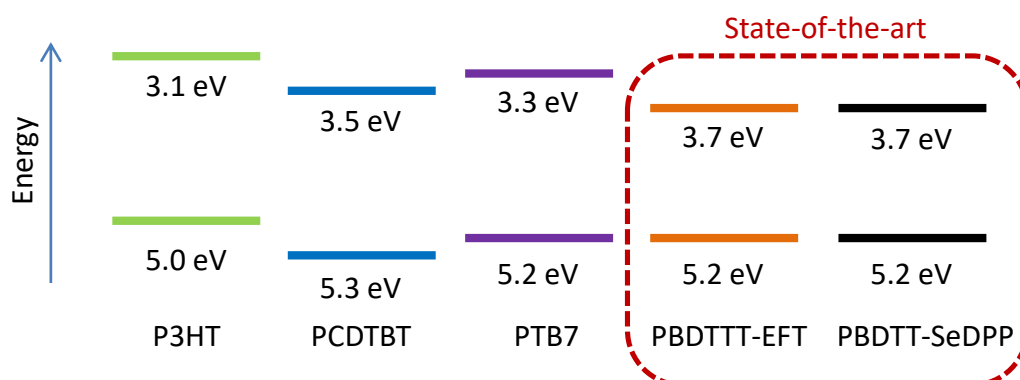


**Figure 4.3:** Frontier orbital diagram showing the HOMO and LUMO levels for a series of electron donor polymers used in OPVs.

As is evident from Figure 4.1 and Figure 4.2, all of the organic semiconductor films accept electron density from the low work function electrode. Interestingly, for the cases of PCDTBT and P3HT (Figure 4.2(a) and (e)) there are two distinct parts to the change in  $\varepsilon_F^{vac}$ ; an initial sharp decrease in  $\varepsilon_F^{vac}$  followed by the aforementioned more gradual increase. The latter occurs over a film thickness equivalent to the first few molecular layers of the organic semiconductor. This effect, which has been widely documented to occur at the interface between vacuum deposited small organic molecule films,<sup>221–223</sup> although sparsely reported at the interface between electrodes and solution processed organic semiconductors,<sup>224</sup> is attributed to the *pushback effect*. The pushback effect occurs due to a repulsion of the electron cloud at the surface of the metal back

into the bulk by the adsorbed molecules, leading to an effectively positively charged vacuum side of the film as compared to the bare surface. This shift in  $\varepsilon_F^{vac}$  is therefore due to a reduction in the size of the dipole layer at the surface of the electrode rather than charge transfer from the organic semiconductor layer into the electrode.<sup>210</sup>

Using Poisson's Equation (Equation 4.1) the average space charge density in each of the organic semiconductors within 5 nm of the interface is calculated to be: PC<sub>71</sub>BM;  $-1.2 \text{ C cm}^{-3}$ , PC<sub>61</sub>BM;  $-1.5 \text{ C cm}^{-3}$ , PCDTBT;  $-0.11 \text{ C cm}^{-3}$ , PTB7;  $-0.16 \text{ C cm}^{-3}$ , and P3HT;  $-7.3 \times 10^{-3} \text{ C cm}^{-3}$ , which are all greater than the space charge density associated with the photo-current in high performance OPVs. For example, the hole density at the short-circuit condition under one sun illumination in an OPV based on PTB7:PC<sub>71</sub>BM is estimated to be  $4\text{-}5 \times 10^{-4} \text{ C cm}^{-3}$  assuming a photocurrent of 12-15 mA cm<sup>-2</sup> and the charge carrier mobilities reported by Ebenhoch *et al.*<sup>63</sup> This is three orders of magnitude lower than that formed at the interface due to spontaneous ground state electron transfer, and so it is reasonable to conclude that this space charge distribution in the PTB7 phase persists under illumination, and the energy level diagram depicted in Figure 4.2(d) is a true picture of the energetics close to the interface in a working device. For the case of P3HT:PC<sub>61</sub>BM OPVs the space charge density due to current flow can be as high as  $1.7 \times 10^{-3} \text{ C cm}^{-3}$  in optimised devices<sup>52</sup> (assuming the charge carrier mobilities from Huang *et al.*<sup>225</sup>) which is much closer to the space charge density formed at the interface due to spontaneous ground state electron transfer, although is still several times smaller. Collectively these measurements show that for BHJ OPVs using high performance donor type materials in conjunction with a low work function reflective electrode there should be no need for a HBL because the formation of a Schottky type junction in *both* donor and acceptor phases should enable efficient

electron-extraction whilst presenting a barrier to unwanted hole-extraction as depicted in Figure 4.4.

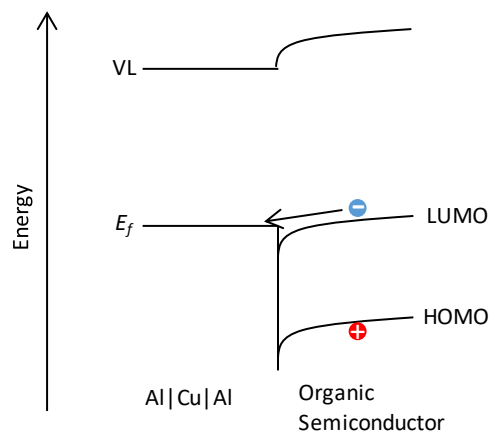


**Figure 4.4:** Schematic energy level diagram of the frontier orbitals of an organic semiconductor and an Al | Cu | Al electrode as found from kelvin probe experiments showing the proposed selective extraction of electrons due to Schottky barrier formation at the interface.

To test the proposed design rule three different top-illuminated OPVs using the Al | Cu | Al electrode as the electron extracting back reflective electrode with and without a thin  $\text{ZnO}_x$  HBL were fabricated and tested. Importantly, it is evident from Figure 4.5 that the reflectivity of the Al | Cu | Al electrode is not significantly altered under the reaction conditions used to deposit this  $\text{ZnO}_x$  layer; 100°C heating in air.

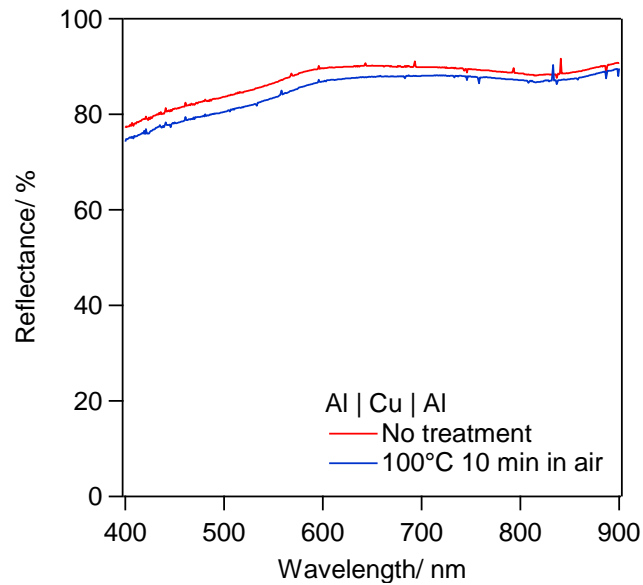


**Figure 4.5:** Reflectance of an Al | Cu | Al electrode before and after annealing at 100°C in air for 10 minutes, an identical treatment is used in the formation of ZnO<sub>x</sub>.

The first OPV tested used PCDTBT:PC<sub>71</sub>BM as the BHJ in the structure Al | Cu | Al | ZnO<sub>x</sub> (11 nm) | BHJ | MoO<sub>3</sub> (5 nm) | Ag (11 nm) and it is evident from Figure 4.6 the addition of the ZnO<sub>x</sub> HBL leads to a significant improvement in the device performance due to an improved  $J_{sc}$  (Table 4.1). However, this improvement cannot be attributed only to hole-blocking at the electron extracting electrode because it is evident from the EQE measurements in Figure 4.6(b), that the improvement in  $J_{sc}$  largely results from a large improvement in light harvesting efficiency for  $\lambda \sim 500\text{-}700$  nm. The simulation of the optical field intensity and distribution in the device (Figure 4.6(c) and (d)), shows that this difference is due to a more intense optical field centred around  $\lambda \sim 650$  nm when the ZnO<sub>x</sub> is used, and so the origin of the increase in  $J_{sc}$  is an optical microcavity effect rather than electrical hole-blocking effect. If the increase in  $J_{sc}$  was due to a hole blocking effect, then the EQE would be expected to increase equally across all wavelengths.

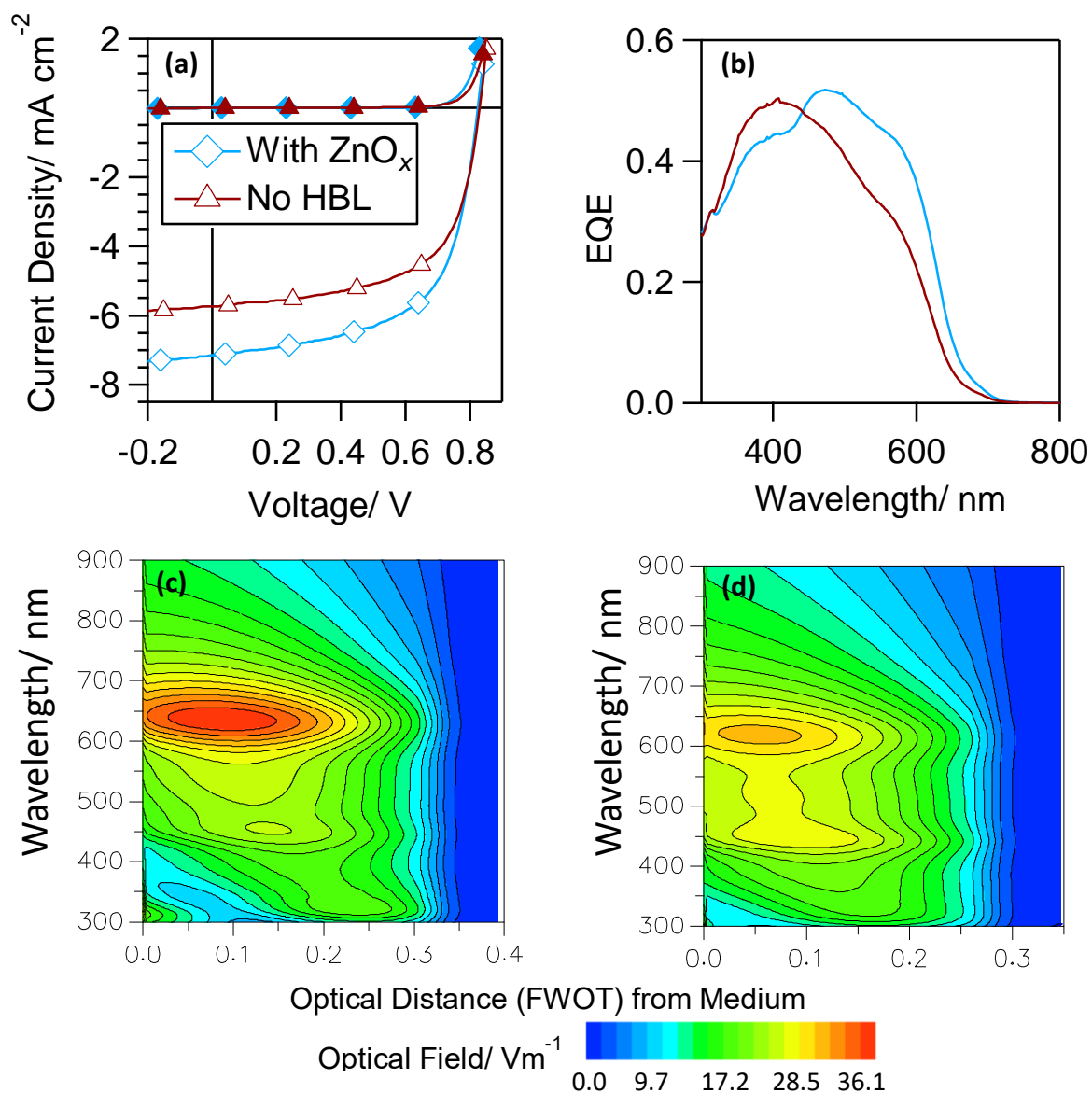


**Figure 4.6:** Performance characteristics of OPV devices with the structure: Al (70 nm) | Cu (8 nm) | Al (0.8 nm) |  $\text{ZnO}_x$  (11 nm) | PCDTBT:  $\text{PC}_{71}\text{BM}$  |  $\text{MoO}_3$  (5 nm) | Ag (11 nm) with and without a  $\text{ZnO}_x$  HBL: (a)  $JV$  characteristics in the dark (filled markers) and under 1 sun illumination (empty markers); (b) Corresponding EQE spectra.; Models of the optical field distribution in the device with (c) and without (d) a  $\text{ZnO}_x$  HBL performed using *The Essential Macleod, Thin Film Centre Inc.* software simulation package.

	$J_{sc}/\text{mA cm}^{-2}$	$V_{oc}/\text{V}$	$FF$	$PCE/\%$
ZnO <sub>x</sub> (11 nm)	7.17 ±0.25	0.84 ±0.01	0.58 ±0.04	3.49 ±0.29
No HBL	5.70 ±0.53	0.84 ±0.01	0.62 ±0.01	2.94 ±0.27

**Table 4.1:** Key OPV performance characteristics under 1 sun simulated solar illumination for OPV architecture: Al (70 nm) | Cu (8 nm) | Al (0.8 nm) | ZnO<sub>x</sub> (11 nm) | PCDTBT: PC<sub>71</sub>BM | MoO<sub>3</sub> (5 nm) | Ag (11 nm) with and without ZnO<sub>x</sub>.

The optical effect seen with PCDTBT:PC<sub>71</sub>BM is very pronounced due to the thin BHJ used; ~60 nm, and relatively thick ZnO<sub>x</sub> film; 11 nm, which results in a significant increase in the total film thickness of the device; ~18%, and so gives rise to a large change in the light intensity.

In order to disentangle optical effects from electronic effects, which can be challenging for high performance OPVs based on very thin photoactive layers, the ZnO<sub>x</sub> film thickness was reduced to 5 nm ±1.7 nm coupled with thicker BHJ systems. To this end OPVs with the structure Al | Cu | Al | ZnO<sub>x</sub> (5 nm) | PTB7: PC<sub>71</sub>BM (~90 nm) | MoO<sub>3</sub> (5 nm) | Ag (11 nm) were fabricated. As shown in Figure 4.7(a) and Table 4.2, PTB7 OPVs have virtually identical J<sub>sc</sub>, V<sub>oc</sub> and FF. The EQE spectra of the OPVs with and without the ZnO<sub>x</sub> (Figure 4.7(b)) still however exhibits a mismatch in shape, which, based on the results of optical simulations (Figure 4.7(c) & (d)), can again be attributed to slight differences in the optical field distribution in the device, because there is good correlation between the simulated differences in optical field intensity and the variation in EQE spectra. At shorter wavelengths (~350 nm) there is, however, no difference in the EQE with or without an HBL, which corroborates the conclusion that

the  $\text{ZnO}_x$  film is not needed as a HBL and is simply serving to modify the light intensity distribution in the OPV.

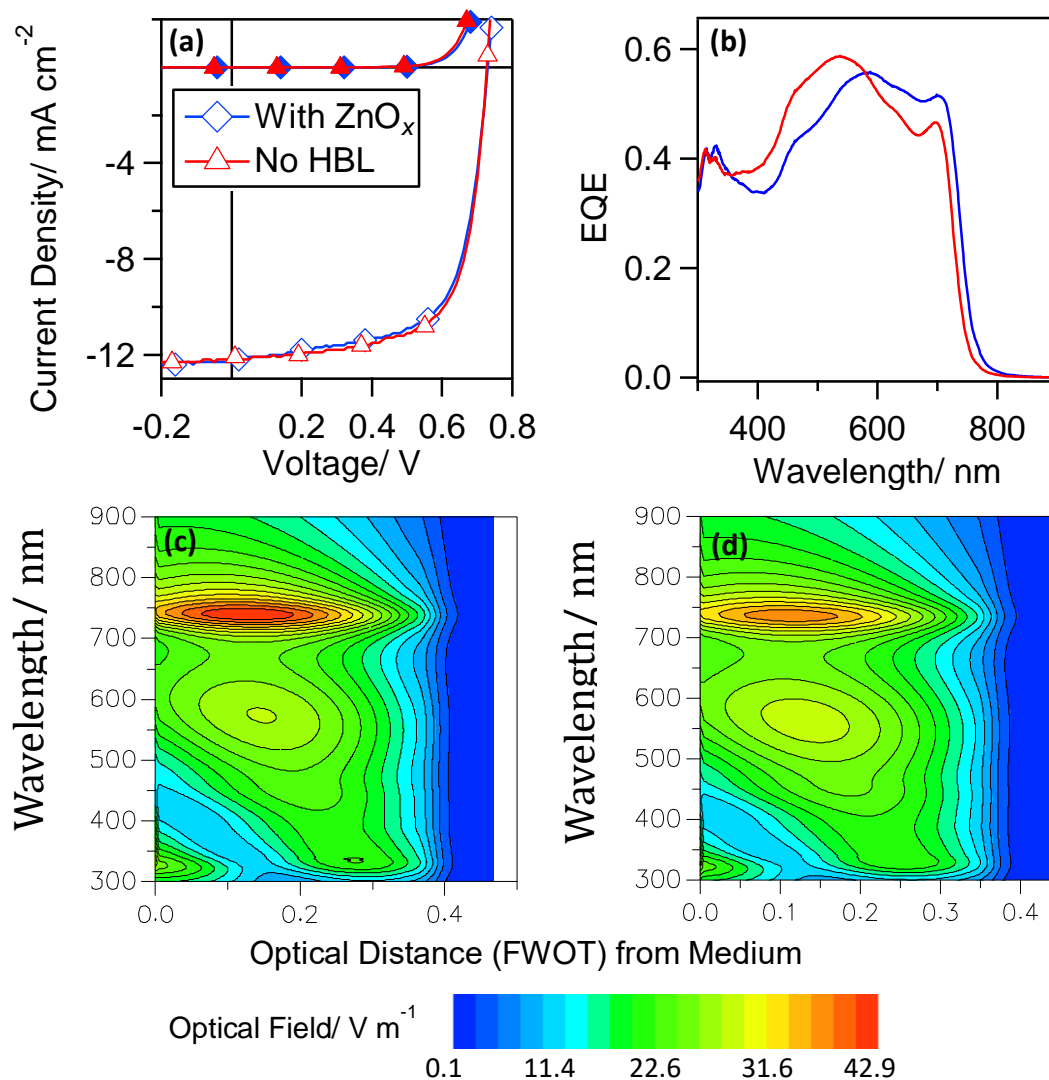


**Figure 4.7:** Performance characteristics of OPV devices with the structure: Al (70 nm) | Cu (8 nm) | Al (0.8 nm) |  $\text{ZnO}_x$  (5 nm) | PTB7:  $\text{PC}_{71}\text{BM}$  |  $\text{MoO}_3$  (5 nm) | Ag (11 nm) with and without a  $\text{ZnO}_x$  HBL: (a) *JV* characteristics in the dark (filled markers) and under 1 sun illumination (empty markers).; (b) Corresponding EQE spectra.; Models of the optical field distribution in the device with (c) and without (d) a  $\text{ZnO}_x$  HBL performed using *The Essential Macleod, Thin Film Centre Inc.* software simulation package.

	$J_{sc}/\text{mA cm}^{-2}$	$V_{oc}/\text{V}$	$FF$	$PCE/\%$
ZnO <sub>x</sub> (5 nm)	11.50 ±0.39	0.72 ±0.01	0.65 ±0.02	5.41 ±0.25
No HBL	11.41 ±0.31	0.72 ±0.01	0.66 ±0.03	5.37 ±0.44

**Table 4.2:** Key OPV performance characteristics under 1 sun simulated solar illumination for OPV architecture: Al (70 nm) | Cu (8 nm) | Al (0.8 nm) | ZnO<sub>x</sub> (5 nm) | PTB7:PC<sub>71</sub>BM | MoO<sub>3</sub> (5 nm) | Ag (11 nm) with and without ZnO<sub>x</sub>.

In order to test the generality of the latter conclusion and to further reduce complexity associated with optical effects, OPVs were fabricated using the archetypal bulk heterojunction P3HT:PC<sub>61</sub>BM with and without a 5 nm ZnO<sub>x</sub> film at the interface with the low work function reflective electrode. The large photoactive layer thickness, of ~220 nm, whilst not optimal for achieving high power conversion efficiency in these device architectures, serves to further minimise optical effects resulting from the inclusion of a 5 nm ZnO<sub>x</sub> HBL, since the ZnO<sub>x</sub> thickness is < 2% that of the photoactive layer thickness in this case. It is evident from Figure 4.8(a) and Table 4.3 that, as for the PTB7:PC<sub>71</sub>BM OPVs, removal of the ZnO<sub>x</sub> layer has no adverse impact on OPV performance. There is also no significant difference in the photo-response across the visible wavelength region (Figure 4.8(b)), consistent with the results of the optical simulations which show that there is no significant change in the light intensity distribution (Figure 4.8(c) and (d)).

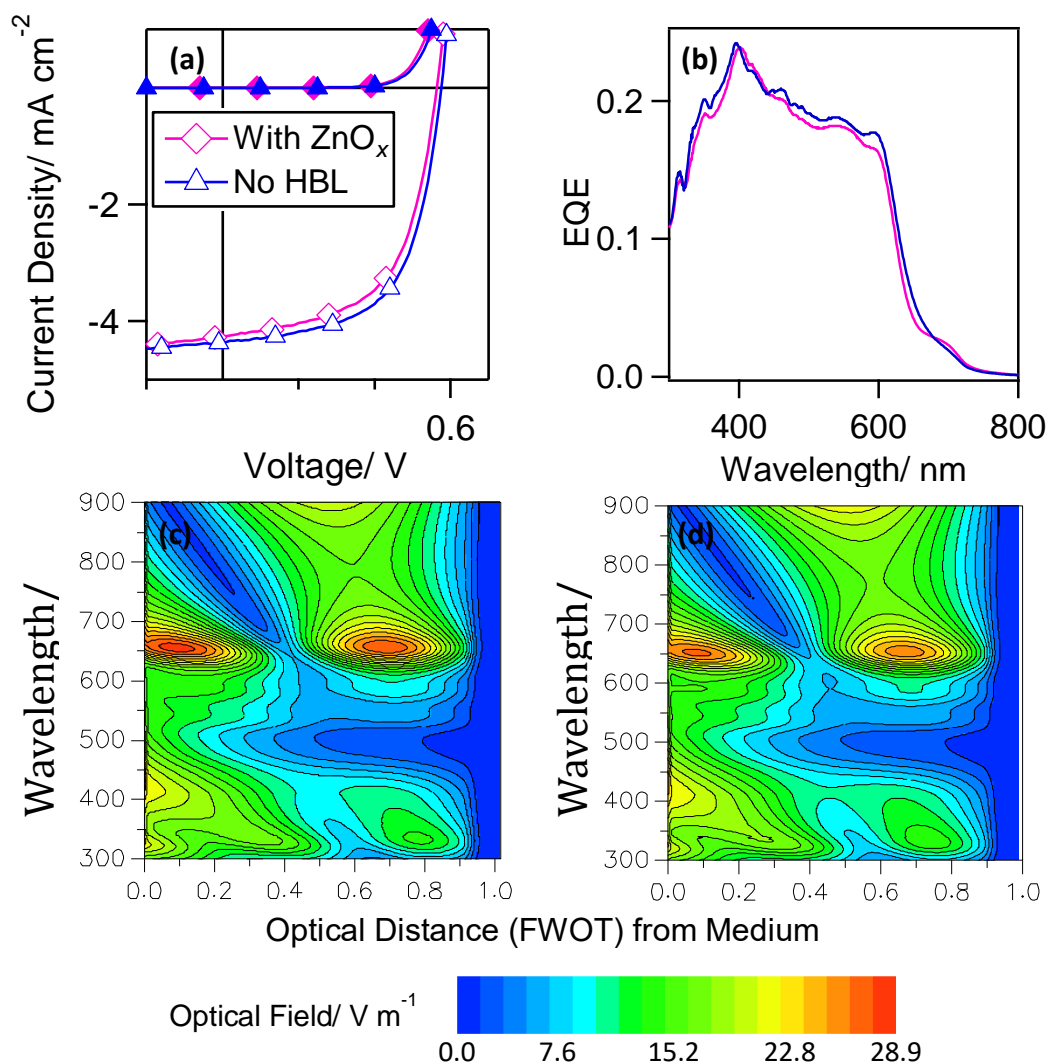


**Figure 4.8:** Performance characteristics of OPV devices with the structure: Al (70 nm) | Cu (8 nm) | Al (0.8 nm) | ZnO<sub>x</sub> (5 nm) | P3HT: PC<sub>61</sub>BM | MoO<sub>3</sub> (5 nm) | Ag (11 nm) with and without a ZnO<sub>x</sub> HBL: (a) *JV* characteristics in the dark (filled markers) and under 1 sun illumination (empty markers).; (b) Corresponding EQE spectra.; Models of the optical field distribution in the device with (c) and without (d) a ZnO<sub>x</sub> HBL. *The Essential Macleod, Thin Film Centre Inc.* software simulation package.

	$J_{sc}/\text{mA cm}^{-2}$	$V_{oc}/\text{V}$	$FF$	$PCE/\%$
ZnO <sub>x</sub> (5 nm)	4.08 ±0.17	0.56 ±0.01	0.59 ±0.01	1.35 ±0.06
No HBL	4.05 ±0.17	0.57 ±0.002	0.61 ±0.01	1.42 ±0.05

**Table 4.3:** Key OPV performance characteristics under 1 sun simulated solar illumination for OPV architecture: Al (70 nm) | Cu (8 nm) | Al (0.8 nm) | ZnO<sub>x</sub> (5 nm) | P3HT: PC<sub>61</sub>BM | MoO<sub>3</sub> (5 nm) | Ag (11 nm) with and without ZnO<sub>x</sub>.

## 4.5 Conclusions

In summary, the results presented in this chapter show that in the context of top-illuminated BHJ-OPVs for which the reflective substrate electrode extracts electrons, an electron selective interfacial layer is not required provided the work function of the electron-extracting electrode is less than the energy of LUMO of the donor material. Importantly, the latter requirement is easily met for high performance narrow band-gap electron donor polymers because these materials are characterised by a narrow band-gap and relatively large ionisation potential, which results in a low lying LUMO energy. Through a study of the energetics at the interface between five widely used solution processed organic semiconductors (both donor and acceptor type) and the stable low work function reflective substrate electrode described in Chapter 3, it has been shown that this electron selective/hole-blocking mechanism results from spontaneous ground state electron transfer from the electrode to both components of the BHJ, giving rise to a Schottky-type junction which facilitates electron extraction and blocks hole extraction. Removing this layer simplifies the fabrication of this important class of OPVs and so will help to maximise the cost advantage over other types of PV technology.

---

## Chapter 5.

# High Performance Silver Window Electrodes for Top-Illuminated Organic Photovoltaics Using an Organo-Molybdenum Oxide Bronze Interlayer

The majority of the work presented in this chapter has been published in:

*High-Performance Silver Window Electrodes for Top-Illuminated Organic Photovoltaics Using an Organo-Molybdenum Oxide Bronze Interlayers* Martin S. Tyler, Marc Walker, Ross A. Hatton, *ACS Appl. Mater. Interfaces*, **2016**, DOI:10.1021/acsami.6b02647

### 5.1 Summary

The research presented in this chapter relates to the development of an organo-molybdenum oxide bronze hole-extraction material that enables the fabrication of high performance Ag window electrodes for top-illuminated solution processed OPVs without complicating the process of device fabrication. It is shown that this composite material combines the function of wide band-gap interlayer for the efficient extraction of holes from organic semiconductors, with the role of seed layer for the formation of robust sub-10 nm thick silver film electrodes, and can be processed from ethanol which ensures orthogonality with a large range of solution processed organic semiconductors used in OPVs. The organic component is the low cost small molecule 3-mercaptopropionic acid (MPA) which is shown to: (i) bind to the oxide matrix and Ag electrode, promoting Ag film formation and robustness at low Ag thickness.; (ii) reduce

---

the contact resistance at the Ag | bronze interface and.; (iii) improve the film forming properties when deposited directly onto organic semiconductor films. Ag film electrodes with a thickness of 8 nm deposited by simple vacuum evaporation onto this hybrid interlayer have a sheet resistance as low as  $9.7 \Omega \text{ sq}^{-1}$  and mean transparency  $\sim 80\%$  over the wavelength range  $\lambda=400\text{-}900 \text{ nm}$ , without the aid of an anti-reflecting layer, which makes them well-matched to the needs of organic photovoltaics.

## 5.2 Introduction

It is widely recognised that the full-cost advantage of solution processed OPVs over conventional crystalline silicon PV will only be achieved if an alternative window electrode to the conducting oxide coated glass used in the current generations of OPV is forthcoming. In top-illuminated OPVs the window electrode is often an optically thin silver electrode<sup>78,105,117,226,227</sup>, which has been shown to achieve comparable device performance to conventional device architectures using a conducting oxide window electrode in wholly vacuum deposited small molecule OPVs.<sup>123</sup> Ag is the metal of choice for this application because it has the highest conductivity<sup>121</sup> and the lowest absorbance over the visible spectrum<sup>122</sup> of the earth abundant metals, combined with relatively high stability towards oxidation in air. However, Ag also has a high surface energy and so thin films of this metal have a high percolation thickness of  $> 10 \text{ nm}$ , below which they form a discontinuous island like structure which is poorly conductive and strongly absorbs visible light due to excitation of localised surface plasmons.<sup>126</sup> This limitation is particularly pronounced when evaporating Ag onto polymer and small molecule semiconductors because Ag tends to bind weakly to these classes of materials

---

and the high surface energy of Ag is a powerful driver for the formation of Ag nanoparticles.<sup>123,127</sup>

In practice, for PV applications the sheet resistance of the window electrode cannot realistically exceed  $10 \Omega \text{ sq}^{-1}$  without incurring an unacceptable loss in device fill-factor or requiring a relatively dense array of opaque current carrying bus-bars.<sup>90,109,228</sup> Additionally, the electrode transparency across the wavelength range  $\lambda=400\text{-}900 \text{ nm}$  must be  $\geq 80\%$  to be competitive with a  $10 \Omega \text{ sq}^{-1}$  conducting oxide coated glass (e.g. F:SnO<sub>2</sub> and Sn:In<sub>2</sub>O<sub>3</sub>).<sup>90</sup> In recent years Schubert *et al.*<sup>5</sup> and Yang *et al.*<sup>13</sup> have shown that it is possible to achieve a sheet resistance of  $\sim 19 \Omega \text{ sq}^{-1}$  and  $\sim 16 \Omega \text{ sq}^{-1}$  respectively for sub-10 nm Ag window electrodes in top-illuminated OPV, with peak transparencies of  $\sim 80\%$  although with much lower transparency in other useful parts of the spectrum. In both cases the Ag electrodes were fabricated by depositing a 1 nm Au seed layer immediately prior to Ag deposition. The disadvantages of that approach are: (i) the cost incurred by adding an extra step to the fabrication process.; (ii) the use of Au which is almost certainly too costly to be used in PV applications, even at such a low thickness<sup>161</sup>. It is also unclear as to the extent the stability of the Ag window electrode is affected when using a 1 nm Au seed layer. Co-depositing Ag with Ca in conjunction with a 1 nm Al seed layer has also been shown to be a promising approach to enable the fabrication of Ag-based window electrodes for top-illuminated OPV, offering a transparency greater than 90% over a large portion of the visible spectrum. However, the sheet resistance of these three metal electrodes;  $27.3 \Omega \text{ sq}^{-1}$ , is too high to be implemented in PVs, and the susceptibility of Ca to oxidation is a major drawback.<sup>129</sup> What is needed is a means of enabling the formation of highly conductive, sub-10 nm Ag films on the top surface of OPV that does not complicate the process of device fabrication and is applicable to solution processed device architectures, since it is

widely regarded that solution processing offers the lowest cost path to PV device fabrication.<sup>229,230</sup>

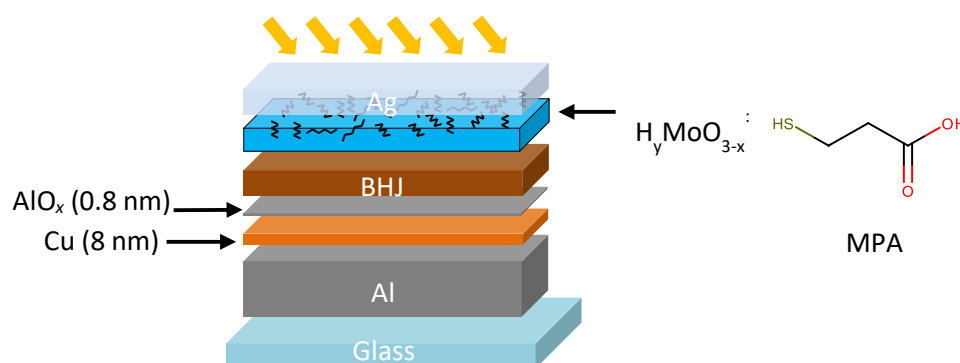


**Figure 5.1:** A schematic diagram of the top-illuminated OPV architecture used in this chapter with the MPA doped  $H_yMoO_{3-x}$  layer highlighted. The reflective substrate electrode is the same described in Chapter 3.

In this chapter the development of an organo-molybdenum oxide bronze is described;  $MPA:H_yMoO_{3-x}$ , that combines the function of wide band-gap interlayer for the efficient extraction of holes from organic semiconductors, with the role of seed layer for the formation of robust sub-10 nm Ag films in top-illuminated solution processed PV devices (Figure 5.1). Transition metal charge extraction layers, including transition metal bronzes,<sup>231,232</sup> are an essential component of high performance OPVs<sup>233,234</sup> and so, unlike the use of an ultra-thin Au interlayer, the hybrid reported herein does not complicate the process of device fabrication. The organic component of this new composite is the small molecule MPA which is shown to have three functions: (i) It binds to the  $H_yMoO_{3-x}$  matrix and Ag electrode, promoting Ag film formation and robustness at low Ag thickness.; (ii) reduces the contact resistance of the Ag |  $H_yMoO_{3-x}$  interface.; (iii) and it improves the film forming properties on the surface of organic

semiconductor films. Additionally, the composite is processed from ethanol which is environmentally sustainable and ensures orthogonality with a large range of solution processed organic semiconductors.

### 5.3 Experimental

*Molybdenum Bronze synthesis:*  $H_yMoO_{3-x}$  was synthesised by dispersing molybdenum powder (0.1 g) in ethanol (10 ml) by ultra-sonic agitation for 10 minutes. This solution was heated to 40°C followed by addition of  $H_2O_2$  (30%, 0.35 ml) under vigorous stirring. This solution turned yellow after 10 hours then blue after 48 hours. After 72 hours reaction the solution was removed from the heat (unless otherwise stated), filtered through a 0.2  $\mu m$  PTFE filter and dried using a rotary evaporator. The solutions were then made up to 20 mg ml<sup>-1</sup> in ethanol and ultra-sonically agitated to fully dissolve the powder. Solutions were left for  $\geq 1$  week before use. Before use all solutions were centrifuged at 10,000 rpm for 10 mins.

*Film deposition:* For XPS/UPS and Kelvin probe measurements a 5 mg ml<sup>-1</sup> solution of  $H_yMoO_{3-x}$ , doped with either 0, 10 or 30 mM MPA, was spin coated onto Au (50 nm) electrodes at 800 rpm for 60 s followed by annealing at 80°C for 10 mins under  $N_2$ . This was repeated 6 times to achieve thick films. To measure conductivity unipolar diodes were fabricated on Au (50 nm) electrodes by spin casting  $H_yMoO_{3-x}$  (20 mg ml<sup>-1</sup>) solution with 0, 40 or 120 mM MPA, which correlate to 0:1, 0.29:1 and 0.86:1 MPA:Mo ratios respectively, at 1000 rpm for 60 s followed by annealing at 80°C for 10 mins under  $N_2$ . Onto these was then evaporated Ag (50 nm, 1  $\text{\AA s}^{-1}$ ) or Au (20 nm, 1  $\text{\AA s}^{-1}$ ).

For transparency and  $R_{\text{sheet}}$  measurements a BHJ of PTB7:PC<sub>71</sub>BM (4 mg: 6 mg in 0.4 ml dichlorobenzene:diiodooctane, 97:3 vol%, stirred at 60°C for 16 hours prior to use) was deposited on cleaned 18 × 18 mm<sup>2</sup> glass slides by spin coating at 1000 rpm for 60 seconds followed by 6000 rpm for 4 seconds then dried under N<sub>2</sub> for 30 minutes. H<sub>y</sub>MoO<sub>3-x</sub> solution (5 mg ml<sup>-1</sup>) was then spin coated at 3000 rpm for 60 seconds followed by annealing at 80°C for 10 minutes under N<sub>2</sub> to achieve 10 nm films. Ag (8 nm, 2 Ås<sup>-1</sup>) was then deposited. This was repeated with a BHJ of PCDTBT:PC<sub>71</sub>BM (2 mg: 6 mg in 0.5 ml chloroform stirred at 70°C for 1 hour) which was spin cast dynamically onto a slide spinning at 6000 rpm for 60 seconds followed by annealing at 70°C for 30 minutes.

*OPV fabrication:* Substrate illuminated electrodes were fabricated by vapour depositing APTMS (1 hour, 30 mbar) onto ITO followed by deposition of the BHJ as above. Either MoO<sub>3</sub> (5 nm or 10 nm, 0.3 Ås<sup>-1</sup>) was then thermally evaporated or H<sub>y</sub>MoO<sub>3-x</sub> was deposited as above followed by thermal evaporation of Ag (70nm, 1 Ås<sup>-1</sup>). Top-illuminated OPVs were fabricated by thermally evaporating Al (60 nm, 5.0 Ås<sup>-1</sup>) | Cu (8 nm, 1.0 Ås<sup>-1</sup>) | Al (0.8 nm, 0.2 Ås<sup>-1</sup>) onto glass without breaking the vacuum between Al and Cu layer deposition. The rest of the device was then deposited as above. PBDTTT-EFT:PC<sub>71</sub>BM (1:1.5) deposition is as described in Chapter 2.

## 5.4 Results & Discussion

### 5.4.1 H<sub>y</sub>MoO<sub>3-x</sub> synthesis

MoO<sub>3-x</sub> is one of the most widely used hole-extraction materials in organic electronics and is typically deposited by vacuum evaporation, although solution processing methods which include a post-deposition annealing step have also begun to

emerge.<sup>71,230,234</sup> Depositing very thin (i.e. 5-10 nm) films of metal oxides from solution directly onto organic semiconductors is particularly challenging due to the need for solvent orthogonality between layers and the constraint on post-deposition annealing temperature imposed by the underlying organic semiconductor. One transition metal oxide that has been successfully applied from solution directly onto the surface of organic semiconductors by the group of Choy is molybdenum oxide bronze;  $H_yMoO_{3-x}$ .<sup>231,235,236</sup> In this wide band-gap semiconductor oxygen vacancies and hydrogen serve as deep and shallow *n*-type dopants respectively.<sup>237</sup>

It has been reported by Kurusu<sup>238</sup> that when molybdenum powder is oxidised with an excess of  $H_2O_2$  (30%) it forms a yellow solution  $MoO_2(OH)(OOH)$ . Conversely if the molybdenum powder is in excess then a dark blue solution forms due to the insertion of hydrogen into the lattice, forming  $MoO_2(OH)_2$ .<sup>238</sup> A similar effect to this is seen by Ayyappan *et al.*<sup>239</sup> whereby refluxing  $MoO_3$  in ethylene glycol also gave dark blue molybdenum bronze solutions. Herein, the molybdenum bronze  $H_yMoO_{3-x}$  is synthesised using an adaptation of the approach reported by Xie *et al.*<sup>231</sup> wherein the rapid reaction with  $H_2O_2$  is controlled by performing the reaction in ethanol which slows the reaction, acts as a reducing agent, and provides a source of protons for inserting into the bronze. The method has been modified to include additional heating steps and an increased reaction time because shorter reaction times (~20 hours) at room temperature gave a yellow solution consistent with the formation of an only partially reduced bronze. It was found that in order to achieve the target product of sub-stoichiometric  $H_yMoO_{3-x}$ , which is blue in colour, a longer time of ~168 hours was required when performing the reaction at room temperature. Importantly, when used in OPVs the solution processed  $H_yMoO_{3-x}$  films showed a comparable performance to

films with an evaporated hole transport layer (HTL) of MoO<sub>3</sub> (5 nm) (Figure 5.2) with average PCEs of 2.9% ( $\pm 0.13$ ) and 3.1% ( $\pm 0.19$ ) respectively (Table 5.1).

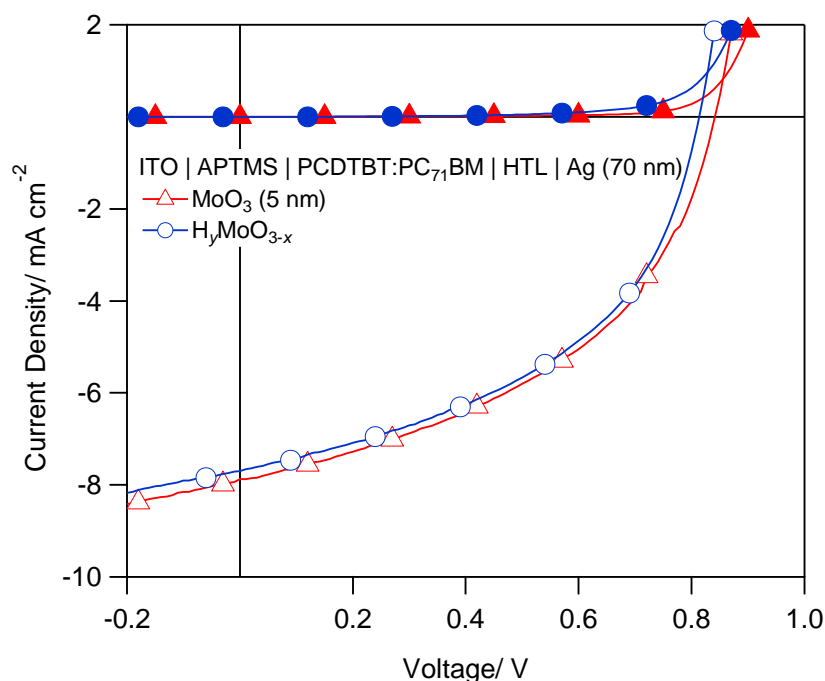


**Figure 5.2:** Representative  $JV$  characteristics under illumination (empty markers) and in the dark (filled markers) of devices with structure; ITO | APTMS | PCDTBT:PC<sub>71</sub>BM | HTL | Ag (70 nm) using either evaporated MoO<sub>3</sub> or solution processed H<sub>y</sub>MoO<sub>3-x</sub> as a hole-transport layer. In this device APTMS is acting to decrease the work function of the ITO glass and so facilitate electron extraction.

HTL	$J_{sc}/\text{mA cm}^{-2}$	$V_{oc}/\text{V}$	$FF$	$PCE/\%$
MoO <sub>3</sub>	$8.06 \pm 0.41$	$0.85 \pm 0.01$	$0.46 \pm <0.01$	$3.14 \pm 0.19$
H <sub>y</sub> MoO <sub>3-x</sub>	$7.78 \pm 0.20$	$0.79 \pm 0.02$	$0.47 \pm 0.02$	$2.87 \pm 0.13$

**Table 5.1:** Key device parameters from devices of structure ITO | APTMS | PCDTBT:PC<sub>71</sub>BM | HTL | Ag (70 nm) with either evaporated MoO<sub>3</sub> or solution processed H<sub>y</sub>MoO<sub>3-x</sub> as a hole-transport layer.

In order to reduce the reaction time required to produce  $H_yMoO_{3-x}$  with the target stoichiometry the temperature was increased from room temperature to  $40^\circ\text{C}$  which resulted in the colour change to yellow after  $\sim 6$  hours and blue after  $\sim 60$  hours, a large time saving over the previous 168 hour reaction time. Aliquots were taken from the reaction solution after 63, 87, 114 and 135 hours all of which produced fine dark blue crystals when dried. As shown in Figure 5.3 and Table 5.2, when used as the hole-extraction layer in top-illuminated OPVs all of these performed comparably to an evaporated  $MoO_3$  film, except for the device using the aliquot taken after 135 hours which exhibited reduced  $J_{sc}$  and  $V_{oc}$ .

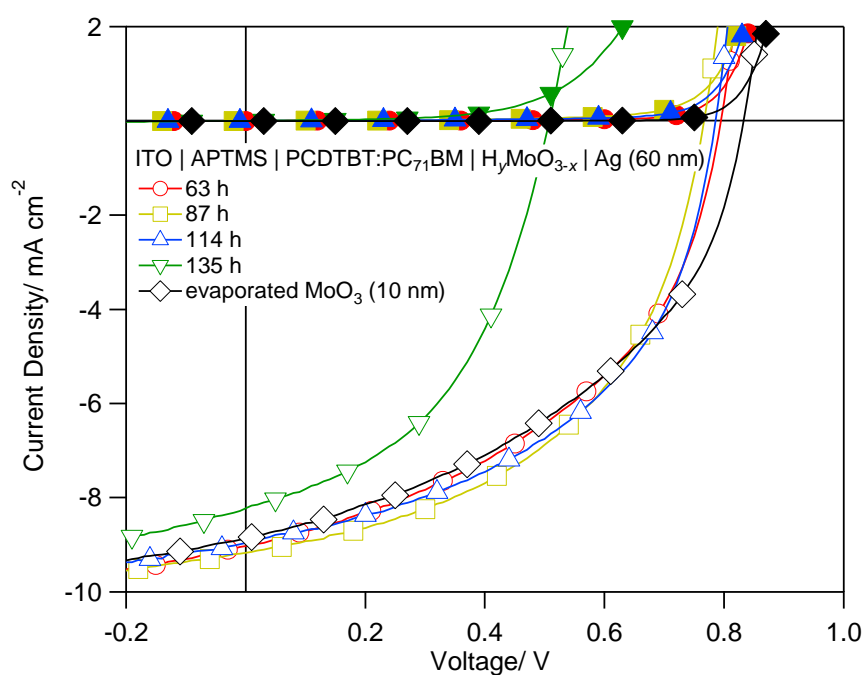


**Figure 5.3:** Representative  $JV$  characteristics under illumination (empty markers) and in the dark (filled markers) of devices with structure; ITO | APTMS | PCDTBT:PC<sub>71</sub>BM | HTL | Ag (70 nm) with either evaporated  $MoO_3$  or solution processed  $H_yMoO_{3-x}$  after reacting at 63, 87, 114 or 135h as the HTL.

HTL	$J_{sc}/\text{mA cm}^{-2}$	$V_{oc}/\text{V}$	$FF$	$PCE/\%$
MoO <sub>3</sub> (10 nm)	8.80 ±0.27	0.84 ±0.01	0.47 ±0.03	3.45 ±0.31
63 h H <sub>y</sub> MoO <sub>3-x</sub>	8.96 ±0.19	0.80 ±0.02	0.47 ±0.03	3.32 ±0.26
87 h H <sub>y</sub> MoO <sub>3-x</sub>	9.27 ±0.42	0.79 ±0.02	0.50 ±0.02	3.62 ±0.15
114 h H <sub>y</sub> MoO <sub>3-x</sub>	9.10 ±0.30	0.80 ±0.01	0.48 ±0.03	3.48 ±0.32
135 h H <sub>y</sub> MoO <sub>3-x</sub>	8.13 ±0.36	0.44 ±0.05	0.46 ±0.03	1.69 ±0.28

**Table 5.2:** Key device parameters from devices of structure ITO | APTMS | PCDTBT:PC<sub>71</sub>BM | HTL | Ag (70 nm) with either evaporated MoO<sub>3</sub> or solution processed H<sub>y</sub>MoO<sub>3-x</sub> as a hole transport layer after reacting at 63, 87, 114 or 135h.

This is likely due to a combination of a decrease in the shunt resistance, as is evident from the difference in the gradient of the line at short circuit, and an excessive reduction in the oxidation state of the Mo. The latter is shown in subsequent sections to result in a reduced work function which would inhibit the functionality of the film as a HTL due to poor alignment between the HOMO of PCDTBT and the CB edge of H<sub>y</sub>MoO<sub>3-x</sub>. Consequently, a reaction time of 72 hours at 40°C was considered optimal.

A further variable that was found to have a large effect on the synthesis of H<sub>y</sub>MoO<sub>3-x</sub> was the age of the H<sub>2</sub>O<sub>2</sub> (30% in H<sub>2</sub>O) used in the synthesis. Since the H<sub>2</sub>O<sub>2</sub> initially rapidly oxidises the molybdenum metal powder the rate at which this happens is a key determinant of the stoichiometry of the final product: H<sub>y</sub>MoO<sub>3-x</sub>. To this end 3 solutions of H<sub>2</sub>O<sub>2</sub> were sourced for the synthesis; a recently acquired H<sub>2</sub>O<sub>2</sub> solution, a solution aged for over a year, and a recently acquired H<sub>2</sub>O<sub>2</sub> solution diluted in H<sub>2</sub>O (1:1). Whilst the diluted and aged solution of peroxide produced H<sub>y</sub>MoO<sub>3-x</sub> solution that acted well as a HTL, the films from the reaction using the newest H<sub>2</sub>O<sub>2</sub> solution

performed very poorly, with similar device characteristics as seen when the solution was over reduced by excessive reaction time (Figure 5.4 and Table 5.3). This suggests that the stoichiometry of reactants used have a large effect on the composition of the  $H_yMoO_{3-x}$  produced, which in turn can have a significant effect on the quality of the film for use as an HTL in OPVs.  $H_2O_2$  degrades spontaneously to water and oxygen and so it can be reasoned that the more recent  $H_2O_2$  solution is more concentrated than the other samples and so the rate of Mo oxidation was a lot higher.

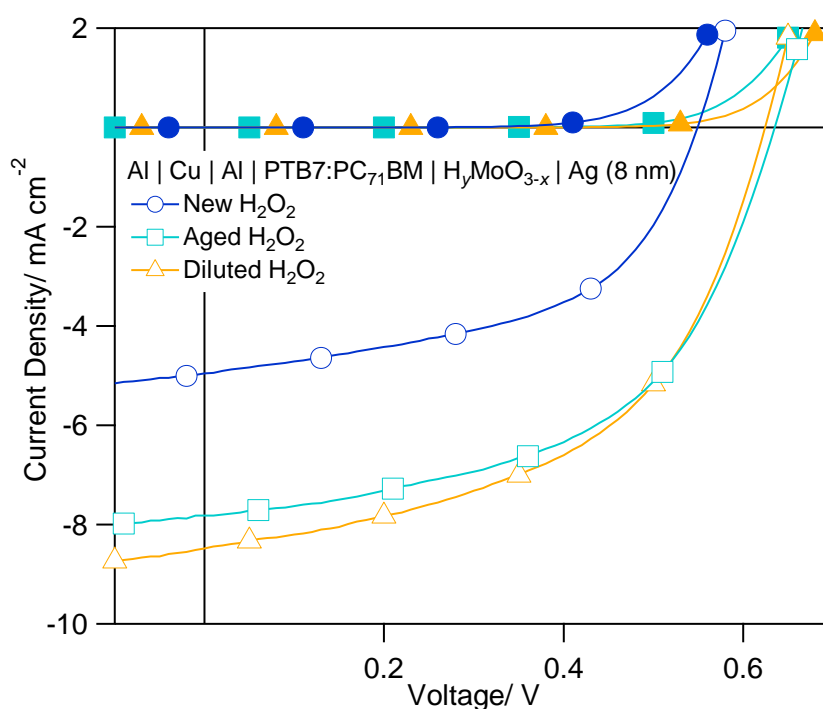


**Figure 5.4:** Representative *JV* characteristics under illumination (empty markers) and in the dark (filled markers) of devices with structure; Al (60 nm) | Cu (8 nm) | Al (0.8 nm) | PTB7:PC<sub>71</sub>BM | MoO<sub>3</sub> | Ag (8 nm) with  $H_yMoO_{3-x}$  films using fresh, aged or diluted  $H_2O_2$  in the synthesis.

<b>H<sub>2</sub>O<sub>2</sub> condition</b>	<b><math>J_{sc}/\text{mA cm}^{-2}</math></b>	<b><math>V_{oc}/\text{V}</math></b>	<b><math>FF</math></b>	<b><math>PCE/\%</math></b>
Fresh	5.08 ±0.24	0.55 ±0.04	0.52 ±0.01	1.48 ±0.16
Aged	7.90 ±0.21	0.64 ±0.02	0.52 ±0.01	2.63 ±0.10
Diluted	8.60 ±0.37	0.63 ±0.02	0.51 ±0.01	2.76 ±0.18

**Table 5.3:** Key device parameters from devices of structure Al (60 nm) | Cu (8 nm) | Al (0.8 nm) | PTB7:PC<sub>71</sub>BM | MoO<sub>3</sub> | Ag (8 nm) with H<sub>y</sub>MoO<sub>3-x</sub> films using fresh, aged or diluted H<sub>2</sub>O<sub>2</sub> in the synthesis

Using these optimised conditions for synthesising H<sub>y</sub>MoO<sub>3-x</sub>, film thickness was optimised for use in OPVs by preparing solutions with H<sub>y</sub>MoO<sub>3-x</sub> loadings in the range 2-20 mg ml<sup>-1</sup> in ethanol and spin coating onto BHJ films at 3000 rpm. From the key device parameters given in Table 5.4 and the *JV* characteristics shown in Figure 5.5, it is evident that the best device performance was achieved for films deposited from a 4 mg ml<sup>-1</sup> solution, due mainly to increased  $J_{sc}$  and  $FF$  when compared to that achieved using thicker films, and an increased  $V_{oc}$  and  $J_{sc}$  as compared to that achieved using thinner films. H<sub>y</sub>MoO<sub>3-x</sub> films prepared from a 4 mg ml<sup>-1</sup> alcoholic solution were found to have a thickness in the range of 9-12 nm, as determined from a scored step edge the height of which was measured using AFM.

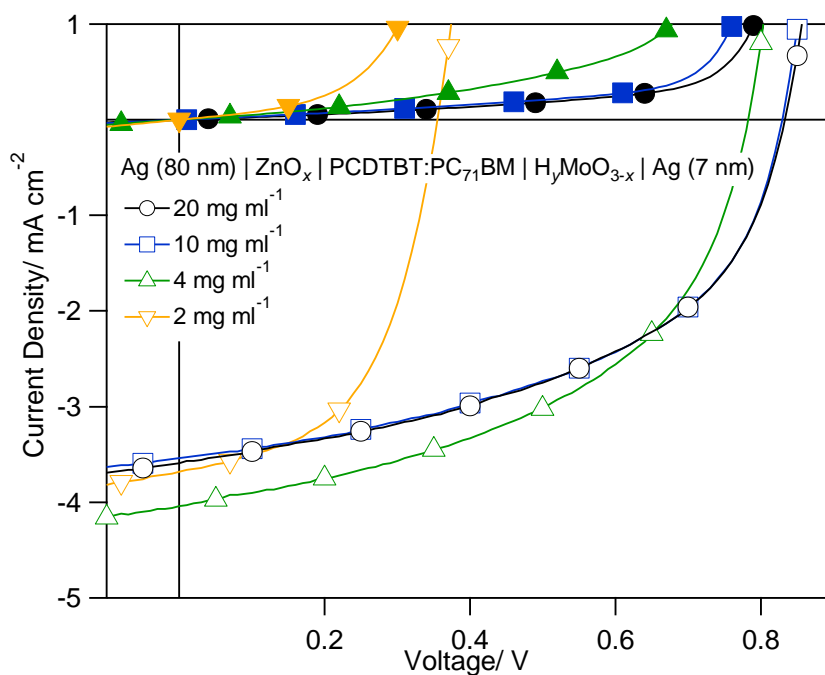


**Figure 5.5:** Representative  $JV$  characteristics under illumination (empty markers) and in the dark (filled markers) of devices with structure Ag (80 nm) | PCDTBT:PC<sub>71</sub>BM | H<sub>y</sub>MoO<sub>3-x</sub> | Ag (7 nm) with H<sub>y</sub>MoO<sub>3-x</sub> concentration of 2-20 mg ml<sup>-1</sup>.

H <sub>y</sub> MoO <sub>3-x</sub> conc.	$J_{sc}/ \text{mA cm}^{-2}$	$V_{oc}/ \text{V}$	$FF$	$PCE/ \%$
20 mg ml <sup>-1</sup>	3.67 ±0.15	0.78 ±0.04	0.41 ±0.05	1.08 ±0.38
10 mg ml <sup>-1</sup>	3.88 ±0.11	0.77 ±0.04	0.43 ±0.05	1.29 ±0.18
4 mg ml <sup>-1</sup>	4.17 ±0.28	0.74 ±0.03	0.46 ±0.02	1.43 ±0.14
2 mg ml <sup>-1</sup>	3.86 ±0.08	0.35 ±0.02	0.49 ±0.03	0.66 ±0.08

**Table 5.4:** Key device parameters from devices Ag (80 nm) | PCDTBT:PC<sub>71</sub>BM | H<sub>y</sub>MoO<sub>3-x</sub> | Ag (7 nm) with H<sub>y</sub>MoO<sub>3-x</sub> concentration of 2-20 mg ml<sup>-1</sup>

### 5.4.2 $H_yMoO_{3-x}$ characterisation

Following optimisation of the  $H_yMoO_{3-x}$  preparative method the effect of doping with MPA was investigated. MPA was added to alcoholic solutions of  $H_yMoO_{3-x}$  and all films were briefly annealed at 80°C under nitrogen to remove residual solvent. Due to the very mild annealing temperature thin films of this material are essentially amorphous as shown by the absence of well-defined peaks in the X-ray diffraction pattern (Figure 5.6).

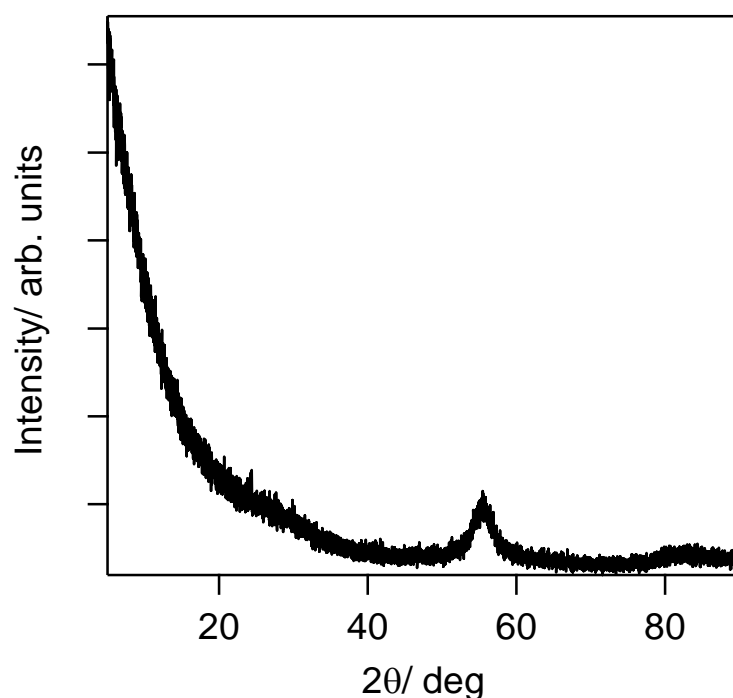


**Figure 5.6:** Grazing incidence X-ray diffraction pattern of a spin cast  $H_yMoO_{3-x}$  film on silicon after annealing at 80°C for 10 minutes under  $N_2$ . The peak at  $\sim 55^\circ$  results from the underlying Si substrate.

XPS was used to determine how incorporation of MPA into the  $H_yMoO_{3-x}$  matrix alters its electronic structure. All spectroscopic characterisation was performed for samples with loadings of 0.29 or 0.86 MPA molecules per Mo atom, which was found to be the optimal loading for OPV applications - as detailed in subsequent

sections of this chapter.  $H_yMoO_{3-x}$  films were supported on a gold substrate. It is evident from the high resolution XPS (HRXPS) spectrum of the Mo 3d region of  $H_yMoO_{3-x}$  without MPA; Figure 5.7(a), that Mo is present in both the 6+ and 5+ oxidation states. The ratio of the Mo3d<sub>5/2</sub> peaks at ~232.6 eV and ~231.4 eV, which are assigned to Mo<sup>+6</sup> and Mo<sup>+5</sup> respectively, is 1:0.6 which yields an average Mo oxidation state of 5.62.

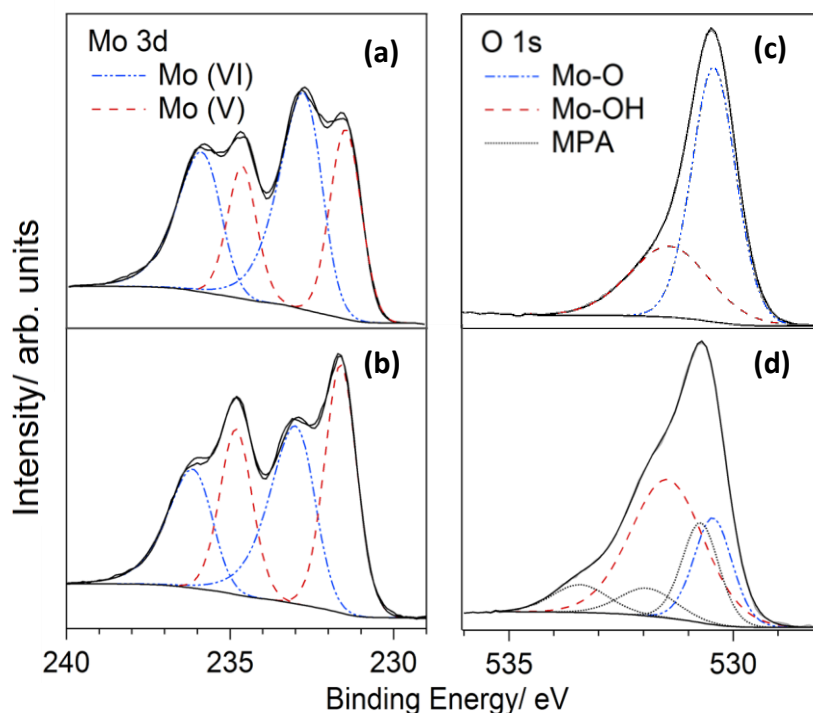


**Figure 5.7:** HRXPS binding energy spectra of: (a) the Mo 3d regions in  $H_yMoO_{3-x}$  and (b) MPA doped  $H_yMoO_{3-x}$ ; (c) the O 1s regions for  $H_yMoO_{3-x}$  (d) and MPA doped  $H_yMoO_{3-x}$ . The MPA:Mo ratio in MPA doped samples is 0.86:1. The MPA peak assignments are: C=O (531.9 eV) C-OH (533.4 eV) and COO<sup>-</sup> (530.7 eV).

The O1s region of the spectrum, shown in Figure 5.7(c), can be fitted with two components at ~530.4 eV and ~531.4 eV which are assigned to Mo-OH (or Mo-OQH) and Mo-O-Mo (or Mo=O/Mo-OQH) chemical environments respectively.<sup>71,240,241</sup> If it is

assumed that hydrogenation is the only source of reduction, then the average Mo oxidation state calculated from the O1s peak intensities is 5.67 although it should be noted this is an over estimate due to advantageous absorption of H<sub>2</sub>O and O<sub>2</sub>. The difference between this value and the actual value; 5.62 (determined from the Mo<sup>+6</sup>:Mo<sup>+5</sup> peak intensities) can be assigned to the presence of oxygen vacancy defects and so the average stoichiometry is calculated to be H<sub>0.24</sub>MoO<sub>2.95</sub>. It is evidence from Figure 5.7(b) that addition of MPA results in a further reduction in the average Mo oxidation state because the Mo<sup>+6</sup>:Mo<sup>+5</sup> ratio is reduced to 5.51 for an MPA:Mo loading of 0.86:1. The O1s region for H<sub>y</sub>MoO<sub>3-x</sub> with MPA (Figure 7(d)) includes three additional peaks corresponding to two oxygen environments in carboxylic acid; C=O (531.9 eV) and C-OH (533.4 eV)<sup>242</sup>, and one in deprotonated carboxylic acid; COO<sup>-</sup> (530.7 eV)<sup>243</sup>. By constraining the Mo-O and Mo-OH peak positions and FWHM to those in Figure 5.7(c) and assuming an MPA: H<sub>y</sub>MoO<sub>3</sub> ratio of 0.86:1 (confirmed from the XPS peak intensities), the deconvolution of the O1s peak is as given in Figure 5.7(d). It is evident from Figure 5.7(d) that the peak attributed to Mo-OH at 531.5 eV has increased in intensity with respect to the Mo-O peak at 530.5 eV, which is further evidence for the reduction of H<sub>y</sub>MoO<sub>3-x</sub> by MPA. It is also evident that there is a significant amount of deprotonated MPA in the H<sub>y</sub>MoO<sub>3-x</sub> film and so the additional Mo reduction upon doping with MPA can be attributed to donation of hydrogen by the carboxylic acid group resulting in the formation of Mo-OH/Mo-OOH. The HRXPS spectrum of the S2p region (Figure 5.8(a)) is consistent with this conclusion, since the sulphur is primarily present as unreacted thiol.<sup>244</sup>

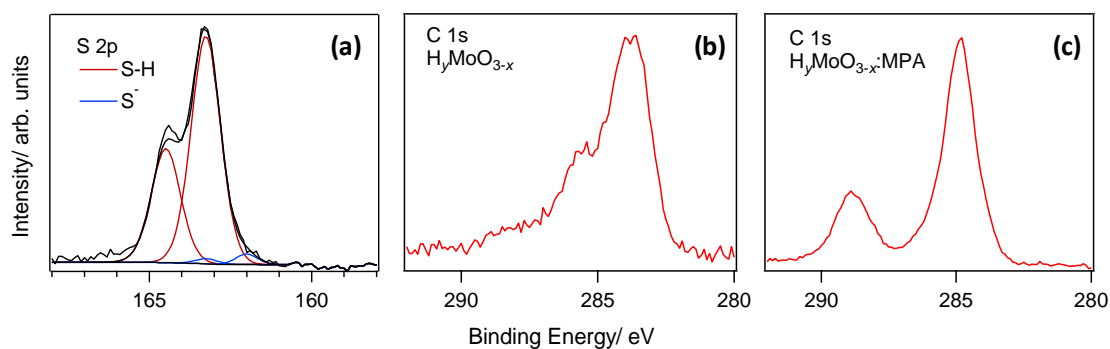


**Figure 5.8:** HRXPS spectra of the (a) S2p region of a spin cast  $H_yMoO_{3-x}$ : MPA film (1:0.86), (b) C1s region of  $H_yMoO_{3-x}$  and (c)  $H_yMoO_{3-x}$ : MPA

Due to advantageous carbon adsorption onto the films from any non-vacuum environment, it is hard to distinguish between the C 1s peaks in the bronze from MPA (and likely ethanol) and contaminants from the atmosphere. However, if the films with 0.86:1 and 0:1 MPA:  $H_yMoO_{3-x}$  ratio are directly compared (Figure 5.8(b) and (c)) evidence for the MPA components is very clear at 288.7 eV, which can be assigned to the carbon in a protonated carboxylic acid.<sup>244</sup> A slight shoulder is evident in this peak at lower binding energies which could be evidence of deprotonation to  $COO^-$ . The contaminants make assigning the peaks responsible for the alkyl carbons difficult; however, there are clearly a large number of components centred on the peak at 284.7 eV.

The UPS spectra shown in Figure 5.9 corroborates the conclusion that MPA serves as a source of hydrogen, and therefore as a shallow  $n$ -type dopant, since the energy difference between the  $E_f$  and the VB edge increases from  $\sim 3.21$  eV with no MPA, to  $\sim 3.35$  eV and  $\sim 3.61$  eV with increasing MPA loading (Figure 5.9(a)). It is important to note that the work function is a function of both the chemical and the surface potential so the movement of  $E_f$  nearer to the CB edge does not necessarily

mean the work function will be reduced as the effect on the surface potential is not known, though it is likely quite significant due to our high level of doping. The two small peaks in the band-gap, labelled  $d_1$  and  $d_2$ , can be assigned to occupied defect states due to hydrogen insertion and oxygen vacancies, since both are known to be present in reduced molybdenum oxides.<sup>89,237</sup> The increased intensity of  $d_2$  upon addition of MPA can be rationalised in terms of increased occupancy of the available defect states due to  $n$ -type doping.

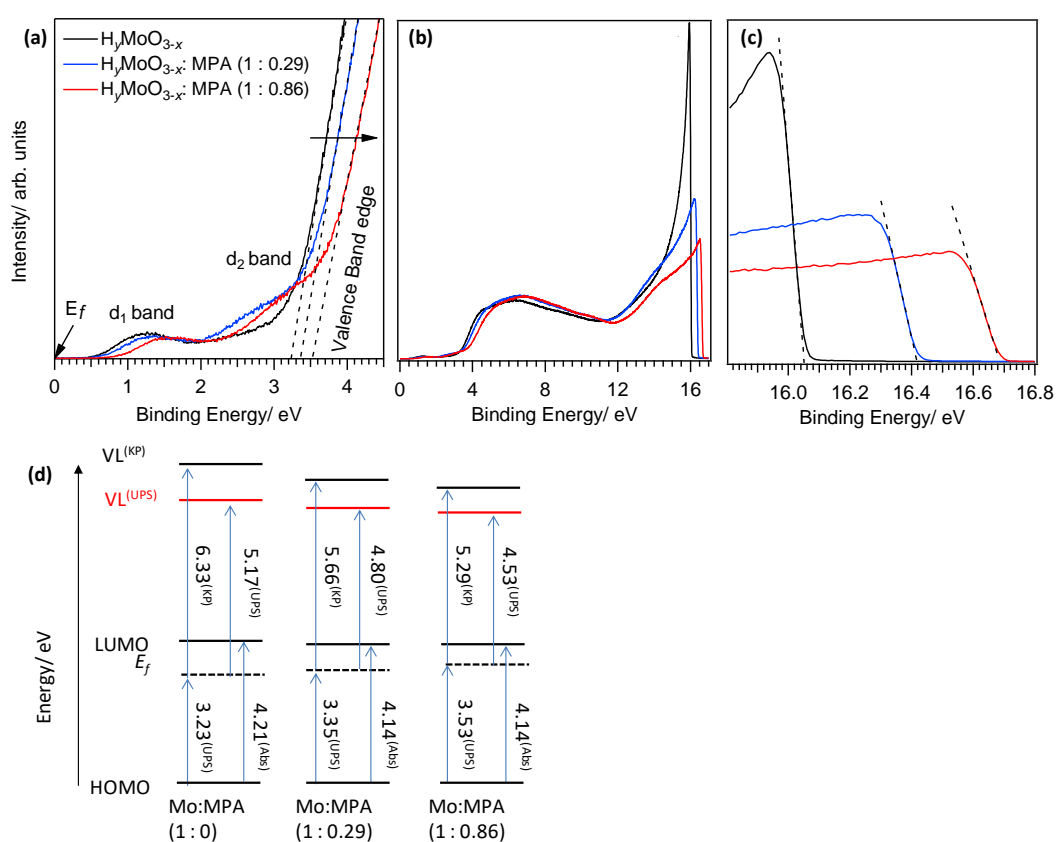


**Figure 5.9:** UPS spectra of  $H_yMoO_{3-x}:MPA$  films with increasing MPA loading showing (a) the valence band edge region, (b) the survey scan and (c) the secondary-electron cut-off. (d) Energy levels of  $H_yMoO_{3-x}$  films with loadings of 1:0, 1:0.29 and 1:0.86 Mo:MPA extracted from UPS, Kelvin probe and Tauc plots from the absorption spectra as labelled.

The optical band-gap of  $\text{H}_y\text{MoO}_{3-x}$  was estimated to be  $\sim 4.21$  eV from the absorption spectrum by plotting  $(ah\nu)^2$  versus  $h\nu$  in a Tauc plot (Figure 5.10(a)). Upon addition of MPA the band-gap was found to undergo a slight reduction to a value of  $\sim 4.14$  eV. The absorption coefficient of  $\text{H}_y\text{MoO}_{3-x}$  films is increased from  $\sim 0.2$   $\text{m}^{-1}$  to  $\sim 0.3$   $\text{m}^{-1}$  in the wavelength range  $\lambda = 400$ - $600$  nm and reduced by a commensurate amount for  $\lambda = 600$ - $900$  nm and so the mean value across the range  $\lambda = 400$ - $900$  nm is not significantly changed (Figure 5.10(b)).

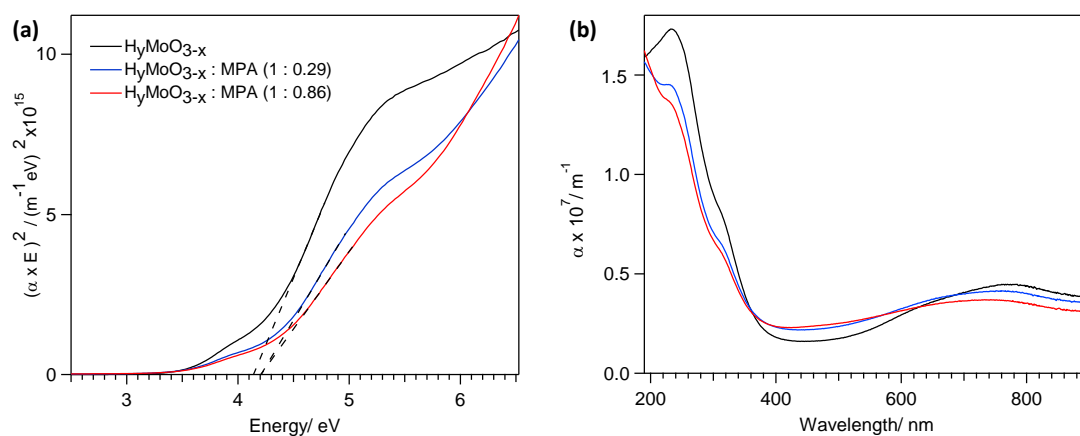


**Figure 5.10:** (a) Tauc plot of  $(\text{absorptivity} \times \text{energy})^2$  versus energy from which optical band-gap is determined with an MPA:Mo loading of 0:1, 0.29:1, and 0.86:1.; (b) Corresponding absorption coefficient of  $\text{H}_y\text{MoO}_{3-x}:\text{MPA}$  films.

Addition of MPA to  $\text{H}_y\text{MoO}_{3-x}$  also resulted in a reduction in its work function, as measured from the UPS secondary-electron cut-off (Figure 5.9(c)) and the Kelvin probe technique. Figure 5.9(d) shows a schematic energy level diagram summarizing this data, along with the energy difference between the valance band edge and  $E_f$  from the UPS valance band edge (Figure 5.9(a)) and the band-gap from Tauc plots (Figure 5.10(a)). Notably, whilst UPS and Kelvin probe show the same trend in work function

---

the work function measured using UPS is consistently lower than that measured using the Kelvin probe. This difference can in part be explained by the fact that UPS is known to measure the lowest work function, and the Kelvin probe the average work function under the probe.<sup>141,245</sup> However, for UPS measurements the samples were briefly exposed to the laboratory environment when loading into the UPS vacuum chamber, and modification of the surface potential contribution to work function by surface contamination is likely. Conversely the Kelvin probe measurements were made using an instrument located in the same nitrogen filled glove box used for film deposition, and so measurements made using the Kelvin probe technique are considered to be more reliable in this instance, a conclusion corroborated by the device studies described in a subsequent part of this paper. The work function measured using the Kelvin probe is reduced from 6.33 eV ( $\pm 0.14$  eV) for the  $\text{H}_y\text{MoO}_{3-x}$  without MPA, to 5.66 eV ( $\pm 0.06$  eV) and 5.29 eV ( $\pm 0.15$  eV) after doping with MPA:Mo loadings of 0.29:1 and 0.86:1 respectively. Since the largest change in work function;  $\Delta \sim 1.04$  eV, is much greater than the change in the position of  $E_f$  in the band-gap (figure 5.9(d)), the MPA must be acting to lower the surface potential contribution to the work function in addition to changing the chemical potential, which is consistent with the very high MPA doping level used. For transition metal oxide hole-extraction layers efficient hole-extraction from an organic semiconductor is only achieved when the oxide work function is higher or comparable to  $I_p$  of the adjacent organic semiconductor.<sup>246</sup> A similar decrease in work function of  $\text{H}_y\text{MoO}_{3-x}$  is reported by Li *et al.*<sup>235,236</sup> by increased doping with Cs, which eventually leads to  $\text{H}_y\text{MoO}_{3-x}$  efficiently acting as an electron-transport layer. However in this case, even for the highest MPA doping level tested the work function of  $\text{H}_y\text{MoO}_{3-x}:\text{MPA}$  should still be sufficiently large to ensure optimised interfacial energy

level alignment for most donor-type organic semiconductors.<sup>220</sup> This conclusion is supported by the OPV device studies reported in a subsequent section of this paper.

Current-voltage analysis of unipolar diodes with the structures; Au | H<sub>y</sub>MoO<sub>3-x</sub> | Ag and Au | H<sub>y</sub>MoO<sub>3-x</sub> | Au were used to determine the effect of MPA doping on the electrical conductivity and contact resistance with the electrode. The conductivity was extracted from the *IV* plots shown in Figure 5.11 using Equation 5.1:

$$\frac{1}{\sigma} = \rho = \frac{R \times A}{l} \quad \text{Equation 5.1}$$

where  $\sigma$  =conductivity,  $\rho$  =resistivity,  $R$  =resistance,  $A$  =area of measurement and  $l$  = the thickness of the film.

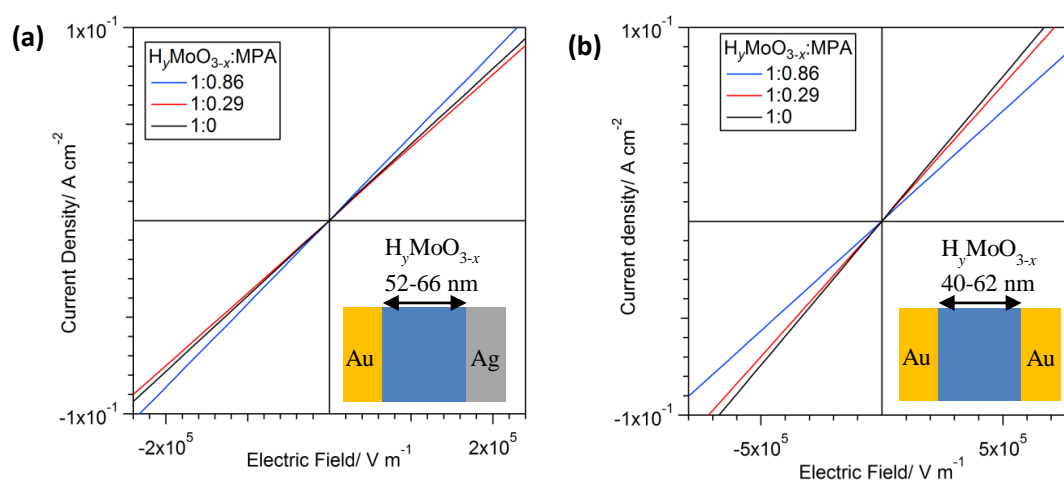


**Figure 5.11:** Current density vs. Electric field for unipolar diodes of structure (a) Au | H<sub>y</sub>MoO<sub>3-x</sub> | Ag with and without MPA doping at thicknesses of 52 nm, 64 nm and 66 nm for Mo:MPA ratios of 1:0, 1:0.29 and 1:0.86 respectively and (b) Au | H<sub>y</sub>MoO<sub>3-x</sub> | Au with and without MPA doping at thicknesses of 48 nm, 62 nm and 40 nm for Mo:MPA ratios of 1:0, 1:0.29 and 1:0.86 respectively.

---

For the Au |  $H_yMoO_{3-x}$  | Ag diode conductivities of  $3.94 \times 10^{-3} \text{ S m}^{-1}$  ( $\pm 0.53 \times 10^{-3}$ ) to  $3.80 \times 10^{-3} \text{ S m}^{-1}$  ( $\pm 0.53 \times 10^{-3}$ ) and  $4.33 \times 10^{-3} \text{ S m}^{-1}$  ( $\pm 0.68 \times 10^{-3}$ ) were measured for films with a Mo:MPA loading of 1:0, 1:0.29 and 1:0.86 respectively. There is a slight increase in the mean conductivity upon MPA doping although the change is statistically insignificant, since all of the values are within one standard deviation of each other. Conversely, for the Au |  $H_yMoO_{3-x}$  | Au diodes conductivities of  $1.50 \times 10^{-3} \text{ S m}^{-1}$  ( $\pm 0.27 \times 10^{-3}$ ) to  $1.41 \times 10^{-3} \text{ S m}^{-1}$  ( $\pm 0.35 \times 10^{-3}$ ) and  $1.14 \times 10^{-3} \text{ S m}^{-1}$  ( $\pm 0.13 \times 10^{-3}$ ) were measured for films with a Mo:MPA loading of 1:0, 1:0.29 and 1:0.86 respectively. In this case there is a slight decrease in the mean conductivity upon doping, but again the change is very small and within the uncertainty of the measurement.

There are three effects due to MPA doping that can affect the measured conductivity: (i) a decrease in charge carrier mobility.; (ii) an increase in free charge carrier density.; (iii) and a decreased contact resistance upon doping. The change in the measured conductivity of the  $H_yMoO_{3-x}$  film with a varied electrode contact must be due to a change in the contact resistance between the films, with Ag forming a more conductive contact compared to Au leading to a 3-fold increase in conductivity. It is likely this effect is outweighed by the loss in mobility in the case of the Au contacts. Regardless of the causes the changes in the conductivity of the  $H_yMoO_{3-x}$  films upon doping are found to be very small and are not significant enough to affect the performance of these films in OPVs where the series resistance of the semiconductors is over 100 times larger than the contact resistance at the electrode interface, as shown in a subsequent section of this chapter.

To test the film forming properties when deposited directly onto organic semiconductors two widely used BHJs were used as model substrates; PTB7:PC<sub>71</sub>BM

and PCDTBT:PC<sub>71</sub>BM. The morphology of a ~10 nm H<sub>y</sub>MoO<sub>3-x</sub> film spin cast directly onto a PTB7:PC<sub>71</sub>BM BHJ film, measured using AFM, is shown in Figure 5.12, from which it is evident that addition of MPA (1:0.86 Mo:MPA) dramatically reduces the RMS roughness of the bronze over layer from 4.3 nm (±0.5) to 2.0 nm (±0.3).

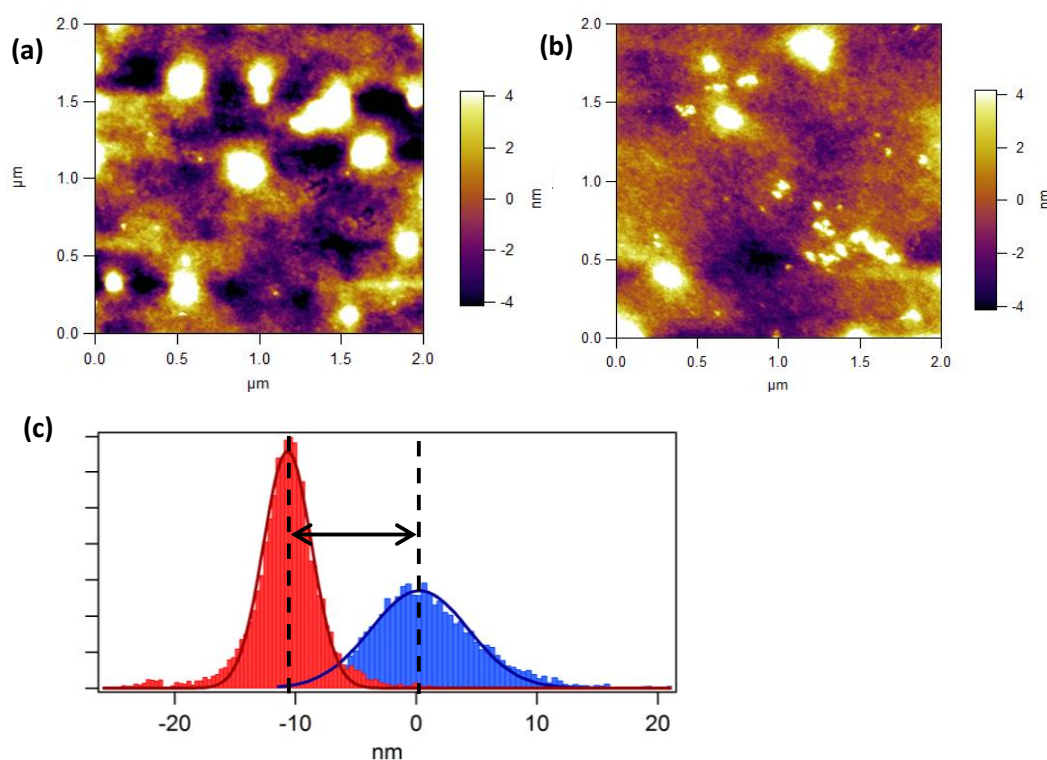


**Figure 5.12:** Morphology measured using AFM of H<sub>y</sub>MoO<sub>3-x</sub> without (a) and with (b) MPA, spun cast on glass | PTB7:PC<sub>71</sub>BM; (c) step height of a scratch in a H<sub>y</sub>MoO<sub>3-x</sub> film (5 mg ml<sup>-1</sup>, 3000rpm 60s).

Conversely, as is evident from Figure 5.13, H<sub>y</sub>MoO<sub>3-x</sub> films spun directly onto glass with and without MPA doping exhibit no significant difference in surface roughness (3.35 nm with MPA vs 3.25 nm without). Therefore, the difference in film roughness when deposited directly onto BHJ films can be attributed to improved wetting due to the

presence of MPA, rather than suppression of aggregate formation in the  $H_yMoO_{3-x}$  solution when MPA is added.

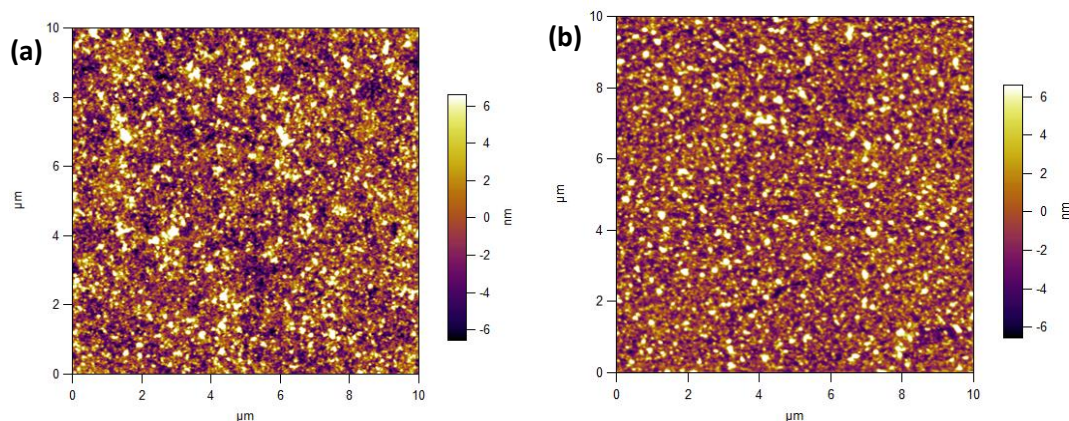


**Figure 5.13:** Morphology of spin cast  $H_yMoO_{3-x}$  films onto glass (measured using AFM) with a MPA:Mo ratio of 0.86:1 **(a)** and without MPA **(b)**.

This marked improvement in film forming properties is evidence that the  $H_yMoO_{3-x}$  solution wets the organic semiconductor surface more readily when MPA is added, further evidence for which is provided by measurement of the static contact angle of droplets of  $H_yMoO_{3-x}$  solution on PTB7:PC<sub>71</sub>BM BHJ films;  $< 2^\circ$  with 1:0.86 MPA doping *vs*  $19.53^\circ (\pm 3.6)$  without (Figure 5.14).  $H_yMoO_{3-x}$  films spin cast onto PCDTBT:PC<sub>71</sub>BM showed no significant difference in surface roughness, although the static contact angle measurements provided evidence of improved wetting;  $13.1^\circ (\pm 2.5)$  with 1:0.29 MPA doping and  $18.6^\circ (\pm 1.8)$  without (Figure 5.14).

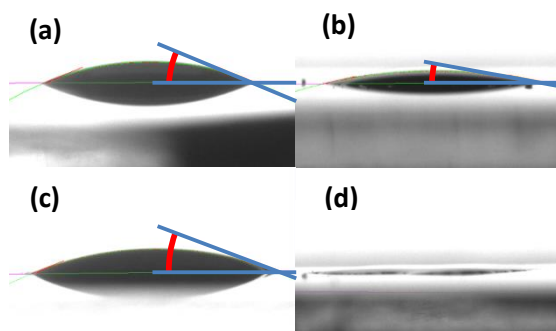


**Figure 5.14:** Static contact angle measurements of: (a)  $H_yMoO_{3-x}$  on PCDTBT:PC<sub>71</sub>BM.; (b)  $H_yMoO_{3-x}$ :MPA on PCDTBT:PC<sub>71</sub>BM.; (c)  $H_yMoO_{3-x}$  on PTB7:PC<sub>71</sub>BM.; (d)  $H_yMoO_{3-x}$ :MPA drop showing the case of a contact angle too low to measure with the program. The droplet volume was 3-5  $\mu$ l.

### 5.4.3 Ag Window Electrode Characterisation

To fabricate Ag window electrodes with properties comparable to that in top-illuminated device structures Ag films of thickness 8 nm were thermally evaporated onto  $H_yMoO_{3-x}$  coated BHJ films supported on glass. Again the widely used BHJs PTB7:PC<sub>71</sub>BM and PCDTBT:PC<sub>71</sub>BM were used as model substrates. A Ag thickness of 8 nm was chosen because it was found to be the minimum needed to achieve the target  $R_{sheet}$  of  $\sim 10 \Omega \text{ sq}^{-1}$  when deposited on a glass |  $H_yMoO_{3-x}$  substrate whereas a thinner Ag film (6 nm) gave  $R_{sheet}$  values of  $\sim 20 \Omega \text{ sq}^{-1}$ .

The results from a representative batch of electrodes on PTB7:PC<sub>71</sub>BM films are shown in Figure 5.15(a), which show the mean  $R_{sheet}$  is decreased from  $14.8 \Omega \text{ sq}^{-1}$  ( $\pm 2.2$ ) to  $11.1 \Omega \text{ sq}^{-1}$  ( $\pm 0.6$ ) when MPA is added to  $H_yMoO_{3-x}$  with a MPA:Mo ratio of 0.86:1. The decrease in  $R_{sheet}$  correlates with a significant decrease in Ag film roughness, which is  $\sim 20\%$  lower upon addition of MPA (Figure 5.16(a)) compared to

the un-doped film (Figure 5.16(c)), primarily due to a smoother underlying  $\text{H}_y\text{MoO}_{3-x}$  layer (Figure 5.12). This reduction in electrode roughness would decrease ohmic losses due to scattering of electrons, offering a plausible explanation for the improvement in  $R_{\text{sheet}}$  upon addition of MPA.

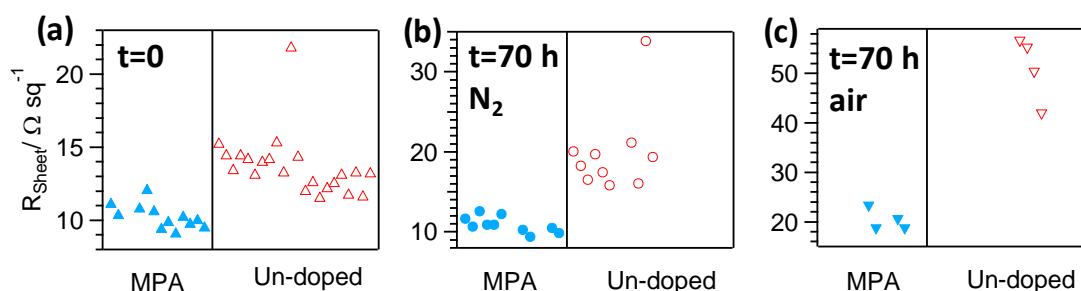


**Figure 5.15:**  $R_{\text{sheet}}$  of 8 nm Ag films supported on glass | PTB7:PC<sub>71</sub>BM |  $\text{H}_y\text{MoO}_{3-x}$ , with 1:0.86 Mo:MPA doped  $\text{H}_y\text{MoO}_{3-x}$  and without MPA; (a) immediately after fabrication; (b) after 70 hours in  $\text{N}_2$ ; (c) after 70 hours in air. Electrode size was  $18 \times 18$  mm.

In addition to the ~25% reduction in sheet resistance the addition of MPA to the bronze also greatly improves the electrode stability: After 70 hours storage in nitrogen ( $< 1$  ppm  $\text{O}_2$  and  $\text{H}_2\text{O}$ ) the  $R_{\text{sheet}}$  of films supported on MPA doped  $\text{H}_y\text{MoO}_{3-x}$  was not significantly different at  $11.5 \Omega \text{ sq}^{-1}$  ( $\pm 0.7$ ) (Figure 5.15(b)). In contrast the  $R_{\text{sheet}}$  of Ag electrodes supported on  $\text{H}_y\text{MoO}_{3-x}$  without MPA was either in the range  $18.3 \Omega \text{ sq}^{-1}$  ( $\pm 1.8$ ) or was too high to measure ( $R_{\text{sheet}} \geq 200000 \Omega \text{ sq}^{-1}$ ). The AFM images in Figure 5.16 show that the surface roughness of Ag films supported on  $\text{H}_y\text{MoO}_{3-x}$  without MPA, greatly increases upon storage in nitrogen, due to the formation of large aggregates, which is not the case when MPA is incorporated into the  $\text{H}_y\text{MoO}_{3-x}$  underlayer. For Ag films supported on a layer of un-doped  $\text{H}_y\text{MoO}_{3-x}$  which gave an  $R_{\text{sheet}}$  too high to

measure, the Ag film was found to have formed large isolated island, as shown in Figure 5.17. This data supports the conclusion that the MPA serves as a molecular adhesive, helping to bind Ag atoms onto the  $H_yMoO_{3-x}$ , and so counteract the thermodynamic instability in thin Ag films that stems from its high surface energy.

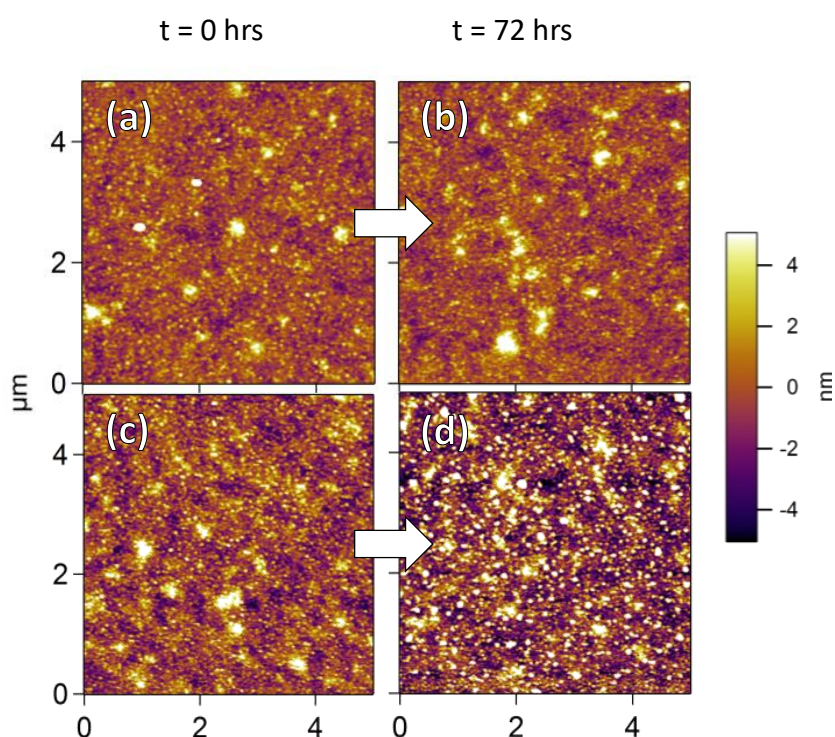


**Figure 5.16:** Morphology of 8 nm Ag film supported on glass | PTB7:PC<sub>71</sub>BM |  $H_yMoO_{3-x}$  with MPA doping at a MPA:Mo ratio of 0.86:1 ((a) & (b)) and without ((c) & (d)) immediately after fabrication ((a) & (c)) and after 72 hours storage in  $N_2$  (< 1 ppm  $O_2$  and  $H_2O$ ) ((b) & (d)).

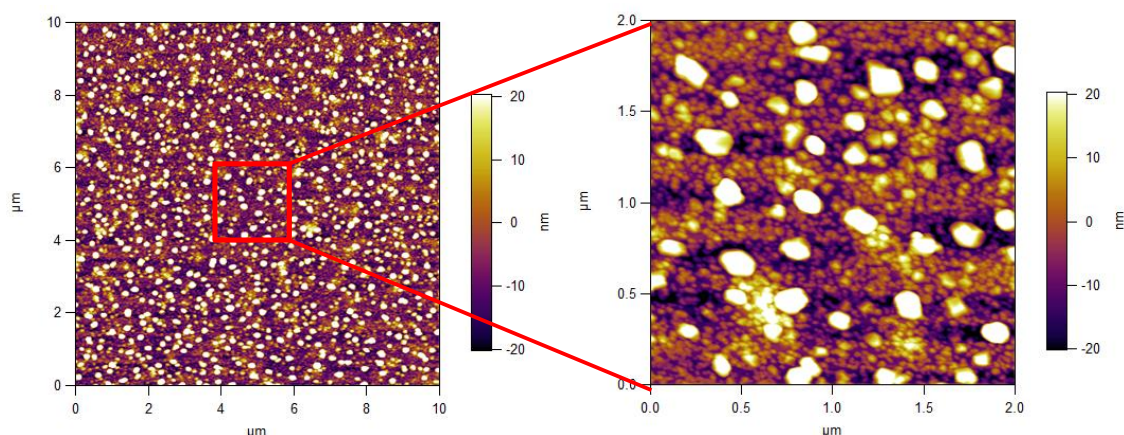


**Figure 5.17:** Morphology of an 8 nm Ag deposited onto un-doped  $H_yMoO_{3-x}$  after 65h under  $N_2$ .

The stability of these films was further tested as a function of storage time in ambient air; 20°C and relative humidity 30-40% (Figure 5.15(c)). After 70 hours in air the sheet resistance of Ag films supported on MPA doped  $H_yMoO_{3-x}$  had increased from  $10.2 \Omega \text{ sq}^{-1}$  ( $\pm 0.8$ ) to  $20.4 \Omega \text{ sq}^{-1}$  ( $\pm 1.9$ ). Without MPA the change was much more pronounced, since the  $R_{\text{sheet}}$  increased from  $13.7 \Omega \text{ sq}^{-1}$  ( $\pm 2.1$ ) to  $51.1 \Omega \text{ sq}^{-1}$  ( $\pm 5.8$ ). In both cases the  $R_{\text{sheet}}$  did not correlate with an increase in surface roughness, presumably due to the formation of a constraining silver oxide capping layer.

To test the generality of these results the same experiment was performed using PCDTBT:PC<sub>71</sub>BM as the underlying organic semiconductor (Figure 5.18(a)). Again, the  $R_{\text{sheet}}$  of the electrode was reduced upon addition of MPA to the  $H_yMoO_{3-x}$  under-layer from  $10.9 \Omega \text{ sq}^{-1}$  ( $\pm 0.4$ ) without MPA to  $9.7 \Omega \text{ sq}^{-1}$  ( $\pm 0.5$ ) with an MPA:Mo loading of 0.29:1.

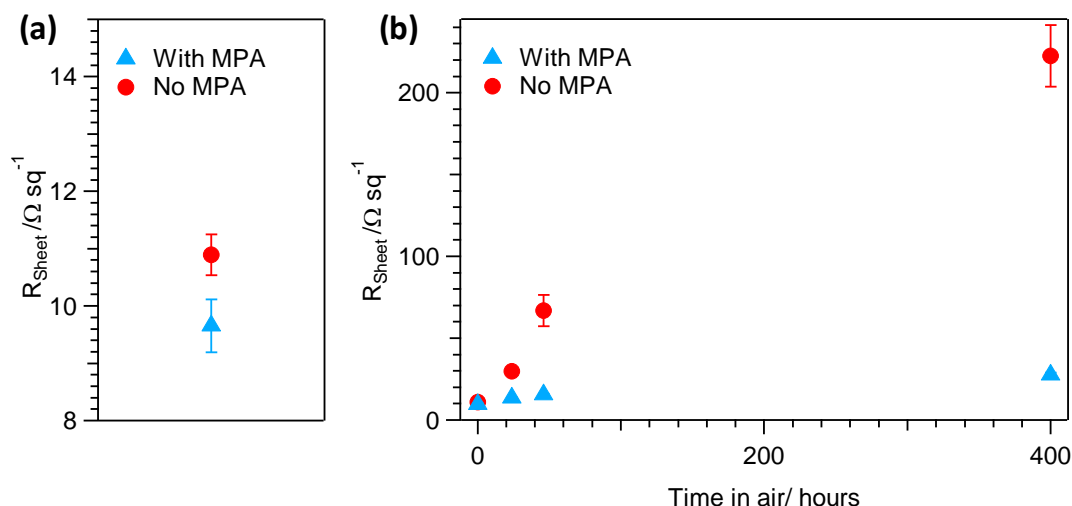


**Figure 5.18:**  $R_{\text{sheet}}$  of 8 nm Ag films supported on glass | PCDTBT:PC<sub>71</sub>BM | H<sub>y</sub>MoO<sub>3-x</sub> with and without 0.29:1 MPA:Mo doping immediately after fabrication (a) and as a function of time stored in air (b). The electrode size was 18 × 18 mm.

There is no significant increase in the  $R_{\text{sheet}}$  for electrodes supported on MPA doped H<sub>y</sub>MoO<sub>3-x</sub> when stored under N<sub>2</sub> after 384 hours. However, with this BHJ the same is also true for the electrode without MPA in the H<sub>y</sub>MoO<sub>3-x</sub> under-layer. This result is attributed to the lower surface roughness of the underlying BHJ film; roughness ~1.6 nm for PCDTBT:PC<sub>71</sub>BM BHJ compared to ~2.8 nm for PTB7:PC<sub>71</sub>BM (Figure 5.19(a) and (b)), in conjunction with a smoother bronze layer. This led to a smoother Ag film for PCDTBT:PC<sub>71</sub>BM (Figure 5.19(c)) with less features as compared to PTB7:PC<sub>71</sub>BM (Figure 5.19(d)) with higher inherent stability due to a reduced surface area.

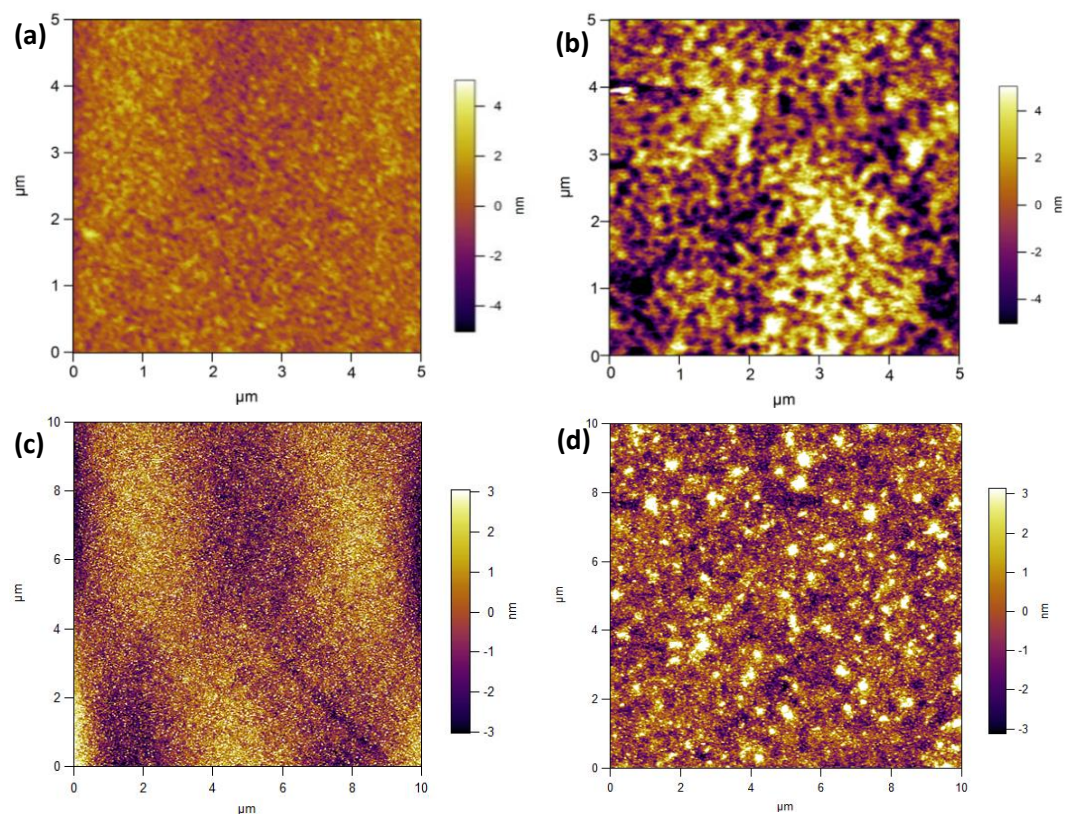


**Figure 5.19:** Morphology of (a) PCDTBT:PC<sub>71</sub>BM; (b) PTB7:PC<sub>71</sub>BM; (c) PCDTBT:PC<sub>71</sub>BM | H<sub>y</sub>MoO<sub>3-x</sub> | Ag; (d) PTB7:PC<sub>71</sub>BM | H<sub>y</sub>MoO<sub>3-x</sub> | Ag measured using AFM.

Conversely, the difference in rate of degradation of these electrodes in ambient air is very pronounced as shown in Figure 5.18(b). After 400 hours the  $R_{\text{sheet}}$  of electrodes without MPA had degraded from  $10.9 \Omega \text{ sq}^{-1} (\pm 0.4)$  to  $222.6 \Omega \text{ sq}^{-1} (\pm 18.8)$  whereas those with MPA had degraded to a much smaller extent from  $9.7 \Omega \text{ sq}^{-1} (\pm 0.5)$  to  $27.6 \Omega \text{ sq}^{-1} (\pm 1.5)$ . It is likely that the degradation of these films in ambient air is due to oxidation of surface Ag and uptake of H<sub>2</sub>O by the hydrophilic H<sub>y</sub>MoO<sub>3-x</sub> film, causing swelling and resulting in an increased roughness in films without MPA from 1.5 nm to 1.8 nm. However, the films with MPA doping exhibited no significant change in surface roughness after exposure to air: 1.0 nm (before) to 1.1 nm (after).

The lower  $R_{\text{sheet}}$  and improved stability of the Ag electrodes supported on both model BHJs upon incorporation of MPA into the  $\text{H}_y\text{MoO}_{3-x}$  layer is consistent with improved interfacial adhesion. XPS studies were conducted to probe the nature of this interaction by acquiring spectra before and after depositing an ultra-thin Ag film with a thickness equivalent to 1.1 nm. To avoid complexity resulting from uncontrolled oxidation or contamination by air exposure the experiment was conducted under high vacuum with a Ag evaporation source co-located in the XPS chamber. It is evident from the HRXPS spectra in Figure 5.20 that the sulphur on the MPA molecules exists primarily in one chemical environment when incorporated into  $\text{H}_y\text{MoO}_{3-x}$ , which can be attributed to the free thiol<sup>244</sup>, with a very small proportion; 1:29, existing as thiolate,  $\text{S}^-$ , possibly due to coordination with a Mo atom. Upon evaporation of a thin Ag layer the signal intensity is reduced because the photoelectrons must now come from beneath the Ag over-layer. The  $\sim 1.4$  eV reduction in the binding energy of the S 2p electrons upon Ag deposition is compelling evidence for thiolate-Ag bond formation.<sup>244</sup>

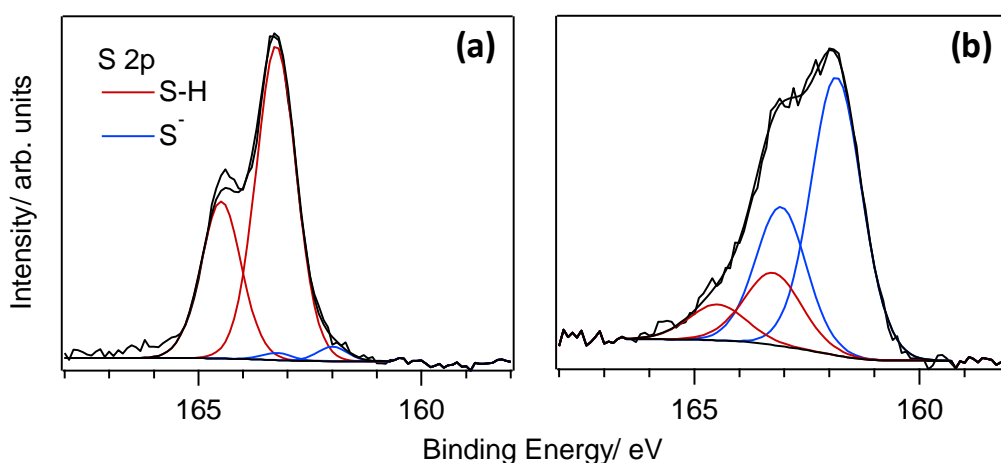


**Figure 5.20:** HRXPS spectra of  $\text{H}_y\text{MoO}_{3-x}$ : MPA S 2p region (a) before and (b) after deposition of 1.1 nm Ag.

---

The improvement in stability of the film under  $N_2$  is therefore likely due to this binding interaction between the thiol functionality on MPA and the evaporated metal, which serves to help immobilise the incident Ag atoms when they arrive on the  $H_yMoO_{3-x}$  film surface.

Additionally, upon deposition of the Ag film the oxidation state of the Mo was probed using HRXPS. From this a reduction of the Mo species at the interface is evident from the appearance of a doublet at lower binding energies, 230 eV and 233 eV for  $3d_{5/2}$  and  $3d_{3/2}$  respectively, than before Ag deposition (Figure 5.21(a) and (b)) which is assigned to  $Mo^{+4}$  environment.<sup>89</sup> This led to a shift in the oxidation state compositions from 53%  $Mo^{+6}$ : 47%  $Mo^{5+}$  to 3%  $Mo^{+6}$ : 54%  $Mo^{+5}$ : 43%  $Mo^{+4}$ . This effect is mirrored in the doped species as shown in Figure 5.21(c) and (d) where the compositions shift from 53%  $Mo^{+6}$ : 47%  $Mo^{5+}$  to 5%  $Mo^{+6}$ : 46%  $Mo^{+5}$ : 49%  $Mo^{+4}$ .

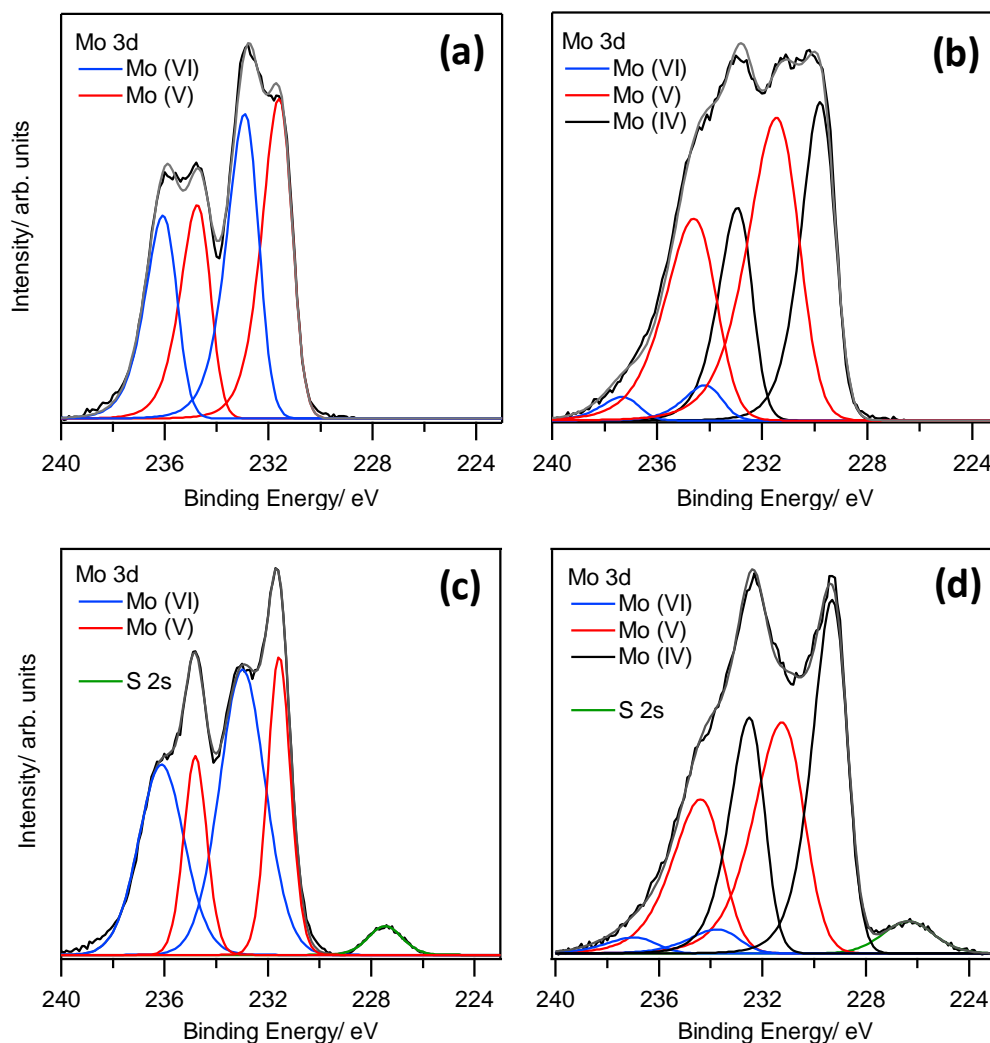


**Figure 5.21:** HRXPS spectra of  $H_yMoO_{3-x}$  films Mo 3d region (a) before and (b) after deposition of 1.1 nm Ag and of  $H_yMoO_{3-x}$ : MPA films (c) before and (d) after deposition of 1.1 nm Ag. The grey line is the sum of the components

Despite this reduction in the Mo species there is no indication of significant  $AgO_x$  formation for either species, as evidenced by the Auger MNN spectra (Figure 5.22) which is identical for both doped and undoped films. As discussed by Ferraria *et al.*<sup>247</sup> these spectra can be assigned to  $Ag^0$  due to the characteristically high KE of the peaks. It is therefore likely that the reduction is due to electron transfer from the Ag, due

to its smaller  $\Phi$  than  $H_yMoO_{3-x}$ , causing a charging of the Ag film *rather than* an oxidation. As described by Greiner *et al.*<sup>89</sup>, for a Au electrode with evaporated  $MoO_3$ , the Ag doesn't oxidise due to the much larger gibbs free energy of oxidation of  $MoO_2 \rightarrow MoO_3$  ( $\Delta G_{O_2} = -275.6 \text{ kJ mol}^{-1}$ ) as compared to  $Ag \rightarrow AgO_x$  ( $\Delta G_{O_2} < -10 \text{ kJ mol}^{-1}$ ). This partial reduction of Mo at the interface in OPVs could have a number of effects on the performance. Whilst an increased conductivity will occur due to filling of the  $H_yMoO_{3-x}$  CB, the reduction of Mo will also lead to a lowered work function at the interface and so a barrier to hole-extraction. It is uncertain how the interplay between these two effects alters the efficiency of the  $H_yMoO_{3-x}$  film.

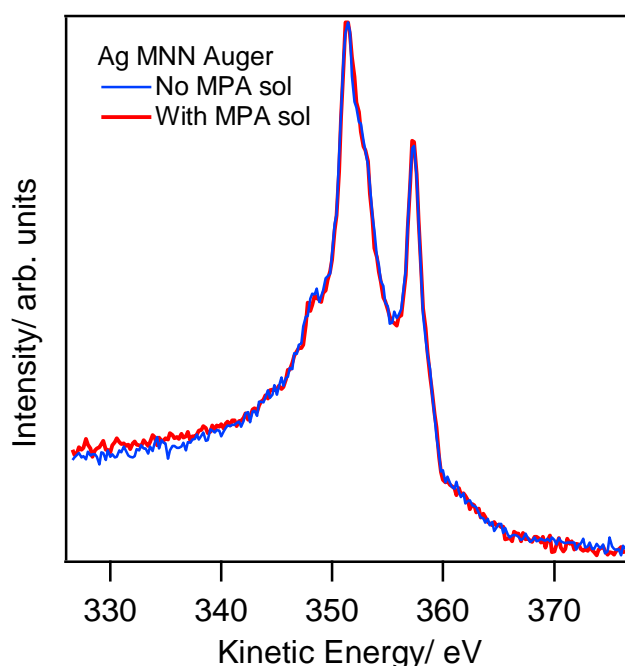


**Figure 5.22:** AES spectra of MPA doped and un-doped  $H_yMoO_{3-x}$  films Ag MNN region after 1.1 nm Ag deposition.

Figure 5.23 shows the far-field transparency of 8 nm Ag electrodes on both PTB7:PC<sub>71</sub>BM and PCDTBT:PC<sub>71</sub>BM films over the wavelength range  $\lambda = 400-900$

nm, with the absorption and reflection of the underlying BHJ |  $H_yMoO_{3-x}$  subtracted. On PTB7:PC<sub>71</sub>BM, which has the higher surface roughness of the two BHJs, the mean transparency of the Ag electrode is very slightly improved upon incorporation of MPA into the  $H_yMoO_{3-x}$  layer, from 79.9% ( $\pm 0.4$ ) to 80.5% ( $\pm 0.9$ ). Conversely the transparency when deposited onto a PCDTBT:PC<sub>71</sub>BM BHJ is very slightly decreased from 85.8% ( $\pm 0.5$ ) to 85.6% ( $\pm 0.6$ ) when MPA is added.

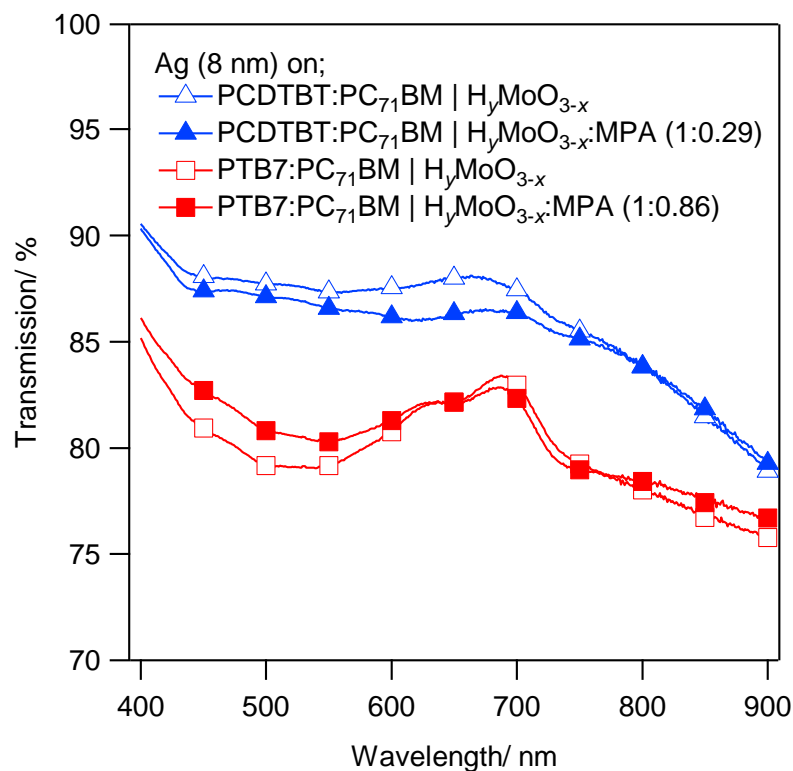


**Figure 5.23:** Far-field transparency of 8 nm Ag films deposited on glass | BHJ |  $H_yMoO_{3-x}$  with and without MPA doping of Mo:MPA ratios of 1:0.29 and 1:0.86 on PCDTBT:PC<sub>71</sub>BM and PTB7:PC<sub>71</sub>BM BHJs respectively. The absorption and reflection of the underlying BHJ| $H_yMoO_{3-x}$  has been subtracted.

The difference in transparency between electrodes deposited on these different BHJ films can be understood in terms of the large difference in the surface roughness of

these BHJ films; 1.6 nm for PCDTBT:PC<sub>71</sub>BM and 2.8 nm for PTB7:PC<sub>71</sub>BM as shown in Figure 5.19. Since even for conformal Ag films the increase in the roughness of the underlying substrate will result in increased absorption due to excitation of surface plasmons and an increased light scattering. For Ag films deposited onto the *same* BHJ the differences in surface roughness are too small to significantly change the transparency because the absolute roughness is two orders of magnitude smaller than the wavelength of the incident light. However, these differences are large enough to significantly affect the  $R_{\text{sheet}}$  since they are of the same order as the metal thickness. Overall the mean transparency of the electrodes supported on MPA doped H<sub>y</sub>MoO<sub>3-x</sub> is superior to that reported using a Au seed layer and compares well to that of 8.5  $\Omega \text{ sq}^{-1}$  indium tin oxide coated glass across the wavelength range.<sup>90</sup> Additionally the  $R_{\text{sheet}}$  of < 10  $\Omega \text{ sq}^{-1}$  and increased stability of the electrode makes these electrodes viable for use as the window electrode in high performance top-illuminated OPVs.

#### 5.4.4 Device Studies

The performance of these electrodes was evaluated in model top-illuminated OPV devices, with the structure: Al | Cu | Al | BHJ | H<sub>y</sub>MoO<sub>3-x</sub> | Ag (8 nm), where the BHJ is either PTB7:PC<sub>71</sub>BM, PCDTBT:PC<sub>71</sub>BM or PBDTTT-EFT:PC<sub>71</sub>BM. The Al | Cu | Al electrode described in Chapter 3 of this thesis was used as the back reflective electrode due to its stable low work function and high reflectivity.<sup>204</sup> For devices based on a PTB7:PC<sub>71</sub>BM BHJ there is a marked improvement in the  $J_{sc}$  upon addition of MPA into the bronze hole-extraction layer, from 8.27 mA cm<sup>-2</sup> ( $\pm 0.71$ ) to 10.92 mA cm<sup>-2</sup> ( $\pm 0.28$ ), which led to a commensurate increase in  $PCE$ ; Figure 5.24(a) and Table 5.5.

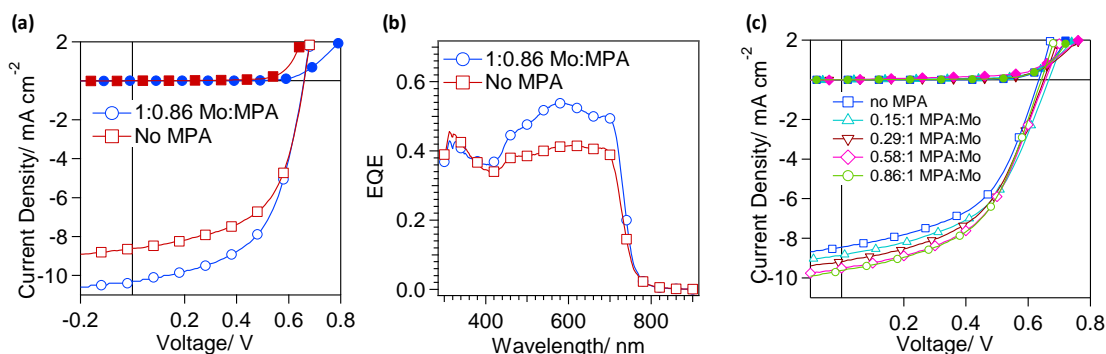


**Figure 5.24:** Characterisation of Al | Cu | Al | PTB7:PC<sub>71</sub>BM | H<sub>y</sub>MoO<sub>3-x</sub> | Ag (8 nm) OPVs of (a) *JV* of optimised MPA concentration; (b) EQE of optimised MPA concentration (c) *JV* over varied MPA concentration. *JV* curves are shown under illumination (empty markers) and in the dark (filled markers)

	$J_{sc}/\text{mA cm}^{-2}$	$V_{oc}/\text{V}$	$FF$	$PCE/\%$	$R_{series}/\Omega \text{cm}^2$
No MPA	$8.27 \pm 0.71$	$0.64 \pm 0.02$	$0.51 \pm 0.04$	$2.69 \pm 0.40$	$13.46 \pm 1.32$
With MPA	$10.92 \pm 0.28$	$0.65 \pm 0.03$	$0.51 \pm 0.07$	$3.65 \pm 0.62$	$13.24 \pm 1.82$

**Table 5.5:** Key device parameters of Al | Cu | Al | PTB7:PC<sub>71</sub>BM | H<sub>y</sub>MoO<sub>3-x</sub> | Ag (8 nm) OPVs with and without an MPA doping of 0.86:1 MPA:Mo. Series resistance estimated from the gradient of the *JV* curve under open circuit.

This effect was found to increase with higher loadings of MPA (from 0.15 to 0.86 molecules per Mo) yielding an optimised ratio of 0.86:1 at which point the improvement saturated (Figure 5.24(c)). This improvement cannot be attributed to the increased conductivity of the H<sub>y</sub>MoO<sub>3-x</sub> with MPA doping since the contribution to the device series resistance from a ~10 nm H<sub>y</sub>MoO<sub>3-x</sub> layer is calculated to be  $0.030 \Omega \text{cm}^2$

---

and  $0.024 \Omega \text{ cm}^2$  for un-doped and doped  $\text{H}_y\text{MoO}_{3-x}$  layers respectively, which is small compared to the total series resistance in the OPV (Table 5.5). This does however explain why there is no significant improvement in device  $FF$  upon MPA doping.<sup>248</sup> It is evident from the EQE data shown in Figure 5.24(b) that the improvement in PCE is due to an increased photo-conversion in the longer wavelength region of the spectrum. Scanning electron microscopy and AFM imaging (Figure 5.25) of the Ag electrode surface reveals a large difference in surface roughness for Ag films supported on  $\text{H}_y\text{MoO}_{3-x}$  films with and without MPA: 2.8 nm (with MPA) vs. 10.1 nm (without). This difference must in large part result from a difference in wetting of the BHJ on the AlCuAl electrode, as compared to glass and is further compelling evidence that adding MPA to  $\text{H}_y\text{MoO}_{3-x}$  greatly improves the film forming properties. This large increase in roughness of the Ag electrode is due to both the increased roughness of the underlying  $\text{H}_y\text{MoO}_{3-x}$  film and the formation of 50-100 nm diameter Ag particles resulting from reduced adhesion between the Ag and the  $\text{H}_y\text{MoO}_{3-x}$ . The difference in  $J_{sc}$  is therefore tentatively ascribed to losses due to plasmon-excitation followed by thermalisation in the rougher Ag electrode when the  $\text{H}_y\text{MoO}_{3-x}$  charge extraction layer is used without MPA.

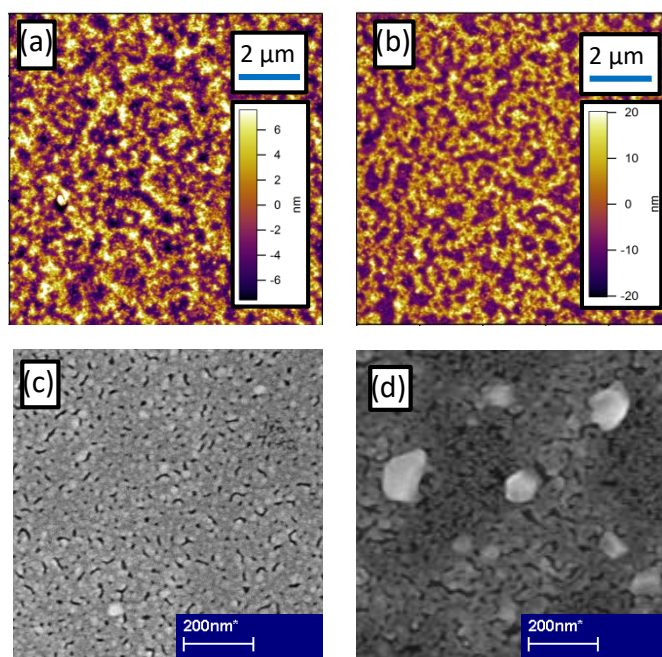


**Figure 5.25:** Morphology of layers in a PTB7:PC<sub>71</sub>BM OPV; H<sub>y</sub>MoO<sub>3-x</sub> layers measured with AFM for (a) MPA doped and (b) un-doped films.; Morphology of Ag electrode measured with SEM for (c) MPA doped and (d) un-doped films.

In order to get some handle on the optical properties of the top electrodes in the device environment, reflectance measurements were made of the whole device stack at an angle of incidence of 15°, as well as of the BHJ and H<sub>y</sub>MoO<sub>3-x</sub> layers also in a device configuration (Figure 5.26(a)). Since the Al | Cu | Al substrate electrode transmits <1% of the incoming light, any loss in the reflectance out of the OPV can be attributed to absorption by the various layers. For the case with just the BHJ deposited on the electrode the result is very similar to that predicted by optical simulation (Figure 5.26(b)). Any absorption by the films at wavelengths  $\geq 800$  nm is due to the back electrode as the absorption of PTB7 does not extend this far into the infra-red. Upon deposition of a  $\sim 10$  nm H<sub>y</sub>MoO<sub>3-x</sub> film a very large increase in absorption occurs for wavelengths  $\geq 600$  nm. The results of this measurement are contrary to the modelled

data, which suggests that any capping layer will lead to an increased reflection. This is disparity is attributed to diffuse scattering of light which cannot be taken account for in the model system as it assumes a completely flat film.

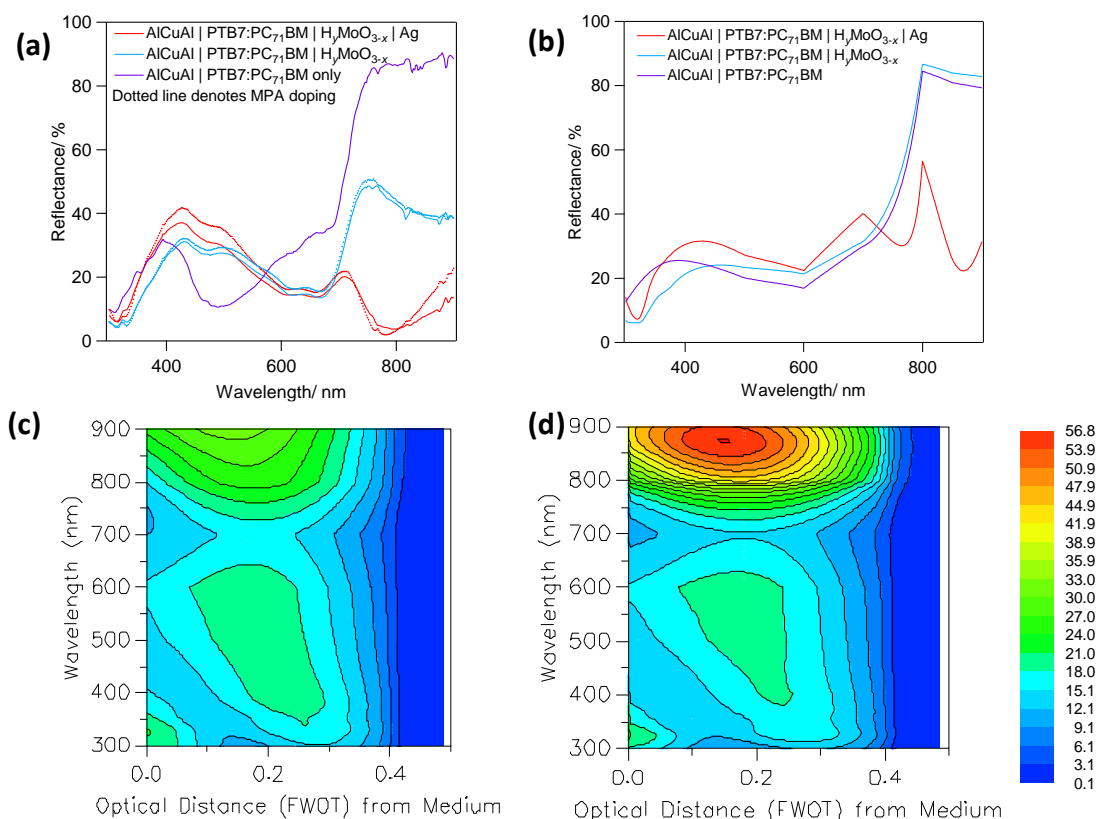


**Figure 5.26:** Reflectance of Al | Cu | Al | PTB7:PC<sub>71</sub>BM | H<sub>y</sub>MoO<sub>3-x</sub> | Ag films at various stages through the device fabrication process for experimental (a) and modelled (b) data. Total optical field of glass | Al | Cu | Al<sub>2</sub>O<sub>3</sub> | PTB7:PC<sub>71</sub>BM | MoO<sub>3</sub> | Ag without (c) and with (d) Ag top electrode.

It is evident that the evaporation of the Ag films causes a large decrease in reflection of the device stack in the longer wavelength region however, this is not the case for wavelengths <700 nm where the reflection is only 0-5 % higher than the underlying film. This is clear evidence for the micro-cavity effect occurring upon deposition of Ag,

which is confirmed by modelling the total field in the device and finding that the field is greatly enhanced between 750-900 nm (Figure 5.26(c) and (d)). Upon addition of MPA to  $H_yMoO_{3-x}$  an increased reflectance is seen after Ag evaporation. This occurs at  $\geq 400$  nm which aligns well with the improvement seen in the EQE spectra (Figure 5.24(b)). It is likely therefore that the rougher, nano-particulate Ag film in the non MPA doped device stack is causing an attenuation of light entering the device stack due to increased diffuse scattering and plasmonic absorption.

Similarly, for OPV devices based on a PCDTBT:PC<sub>71</sub>BM BHJ there is also an improvement in  $J_{sc}$  (Figure 5.27(a) and Table 5.6) upon incorporation of MPA into the  $H_yMoO_{3-x}$  layer, which is optimised for a lower MPA loading; 0.29:1 of MPA to Mo (Figure 5.27(c)).

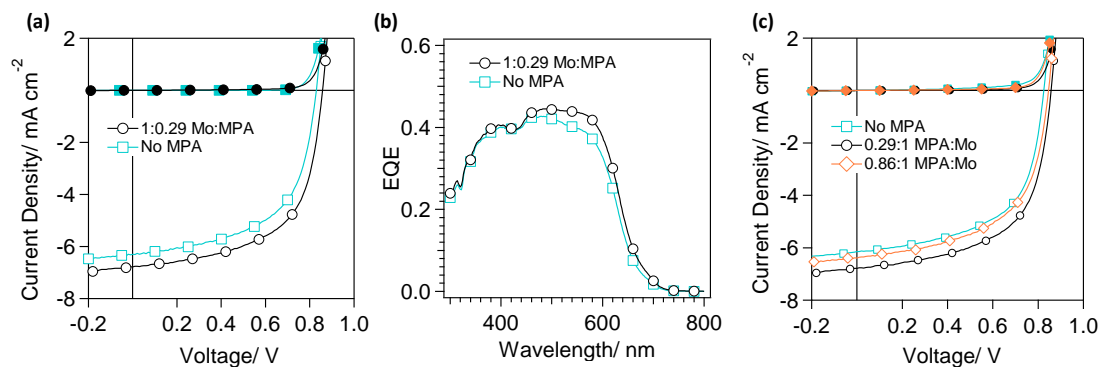


**Figure 5.27:** Characterisation of Al | Cu | Al | PCDTBT:PC<sub>71</sub>BM |  $H_yMoO_{3-x}$  | Ag (8 nm) OPVs of (a)  $JV$  of optimised MPA concentration; (b) EQE of optimised MPA concentration (c)  $JV$  over varied MPA concentration.  $JV$  curves are shown under illumination (empty markers) and in the dark (filled markers)

	$J_{sc}/\text{mA cm}^{-2}$	$V_{oc}/\text{V}$	$FF$	$PCE/\%$	$R_{series}/\Omega \text{cm}^2$
No MPA	$6.06 \pm 0.28$	$0.81 \pm 0.03$	$0.58 \pm 0.15$	$2.88 \pm 0.15$	$13.19 \pm 0.74$
With MPA	$6.56 \pm 0.40$	$0.86 \pm 0.01$	$0.59 \pm 0.02$	$3.33 \pm 0.17$	$11.72 \pm 0.83$

**Table 5.6:** Key device parameters of Al | Cu | Al | PCDTBT:PC<sub>71</sub>BM | H<sub>y</sub>MoO<sub>3-x</sub> | Ag (8 nm) OPVs with and without an MPA doping of 0.29:1 MPA:Mo. Series resistance estimated from the gradient of the *JV* curve under open circuit condition.

Interestingly the higher loading of 0.86:1 MPA:Mo results in less of an improvement in device performance. It is evident from the EQE in Figure 5.27(b) that the improvement in  $J_{sc}$  is again due to increased photo-conversion in the longer wavelength region of the spectrum. Whilst a smoother H<sub>y</sub>MoO<sub>3-x</sub> film is found after doping with MPA: 1.3 nm vs 1.8 nm (Figure 5.28), the change is not as large as seen for the PTB7:PC<sub>71</sub>BM films.

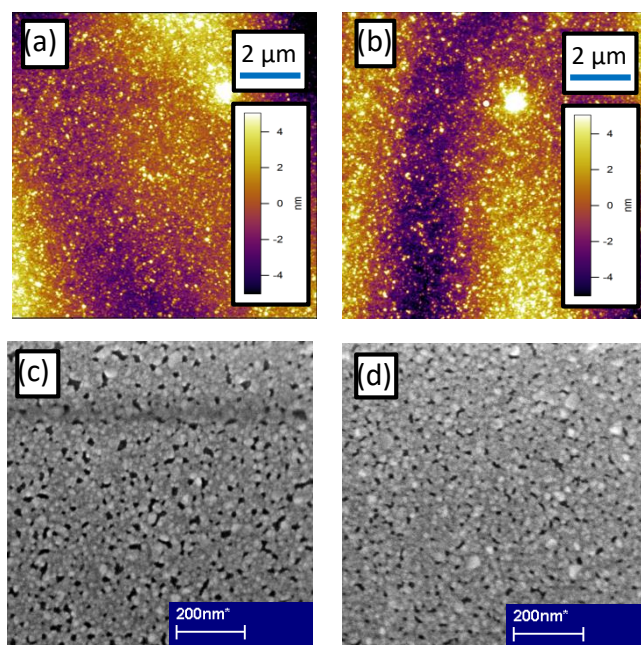


**Figure 5.28:** Morphology of layers in a PCDTBT:PC<sub>71</sub>BM OPV; H<sub>y</sub>MoO<sub>3-x</sub> layers measured with AFM for (a) MPA doped and (b) un-doped films.; Morphology of Ag electrode measured with SEM for (c) MPA doped and (d) un-doped films.

The increase in  $J_{sc}$ , is therefore smaller although it most likely occurs for the same reason as evidenced by the increase in EQE only at  $\lambda > 450$  nm. Additionally, an increase in  $V_{oc}$  is apparent upon doping with MPA which is usually associated with improved energy level alignment at the electrode interfaces. This may be caused here by the lowered  $E_f$  upon doping of the  $H_yMoO_{3-x}$  leading to improved alignment with PCDTBT. Alternatively, an increased  $V_{oc}$  is often associated with decreased charge carrier recombination.

Due to the higher stability of PCDTBT as compared to PTB7,<sup>50,67</sup> the stability of the electrode under constant 1 sun illumination in a nitrogen atmosphere was evaluated in top-illuminated OPV devices based on a PCDTBT:PC<sub>71</sub>BM BHJ light harvesting layer. It is evident from Figure 5.29 that there is a significant reduction in the rate of device degradation when the  $H_yMoO_{3-x}$  is doped with MPA. The degradation is primarily due to a loss in  $V_{oc}$ , although losses in  $J_{sc}$  and  $FF$  are also apparent.

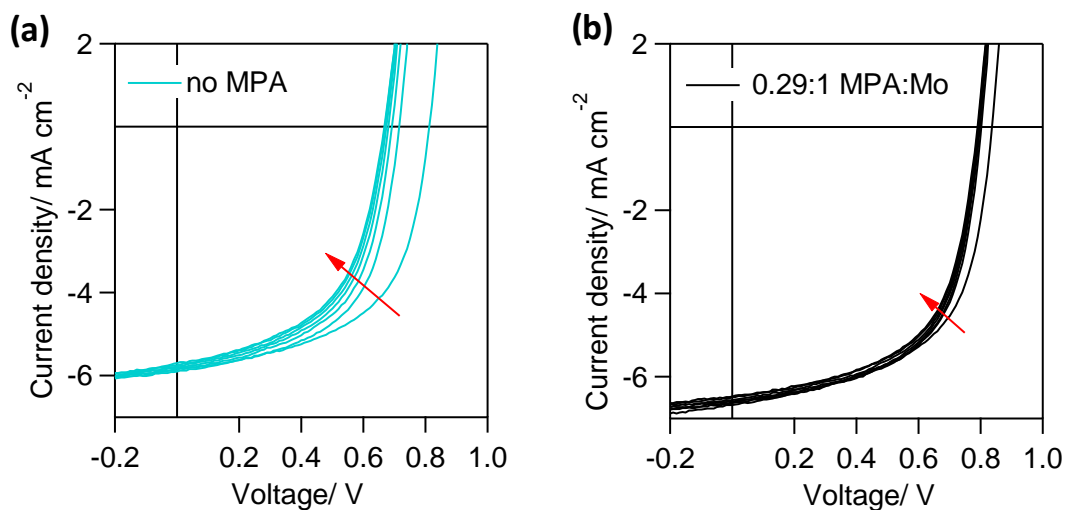


**Figure 5.29:** Stability of Al | Cu | Al | PCDTBT:PC<sub>71</sub>BM |  $H_yMoO_{3-x}$  | Ag (8 nm) OPVs under illumination for 60 mins without (a) and with (b) doping of  $H_yMoO_{3-x}$  with MPA. The red arrow indicates the direction of change in the current-voltage characteristic with increasing time.

---

The exact reason for the improvement in device stability with MPA doping is not yet known, although likely reasons include; (i) an increased electrode stability due to improved adhesion between the Ag electrode and  $H_yMoO_{3-x}$  charge extraction layer.; (ii) improved  $H_yMoO_{3-x}$  layer stability towards the movement of ions in the bronze in the very high electric field in the device.; and (iii) improved wetting of the  $H_yMoO_{3-x}$  layer on the BHJ stopping delamination at the BHJ | bronze interface.

Top-illuminated OPV devices based on the high efficiency BHJ PBDTTT-EFT:PC<sub>71</sub>BM were then fabricated. The surface roughness of the  $H_yMoO_{3-x}$  film again shows significant changes upon incorporation of MPA: 1.2 nm (0.58:1 MPA:Mo) vs 1.7 nm (un-doped) (Figure 5.30(a) & (b)). A difference in surface roughness of the Ag electrode is also evident (Figures 5.30(c) & (d)) that mirrors that of the underling  $H_yMoO_{3-x}$  layer.

As shown in Figure 5.31(a) and Table 5.7, inclusion of MPA into the  $H_yMoO_{3-x}$  results in an improvement in device performance due to a significantly enhanced  $J_{sc}$ . Whilst, as is evident from the EQE spectrum shown in Figure 5.31(b), there is still suppression of plasmonic absorption losses in the MPA doped device stack Ag electrode, there also appears to be a secondary effect leading to increased photo-conversion in the shorter wavelength region which is attributed to scattering of the incoming light.

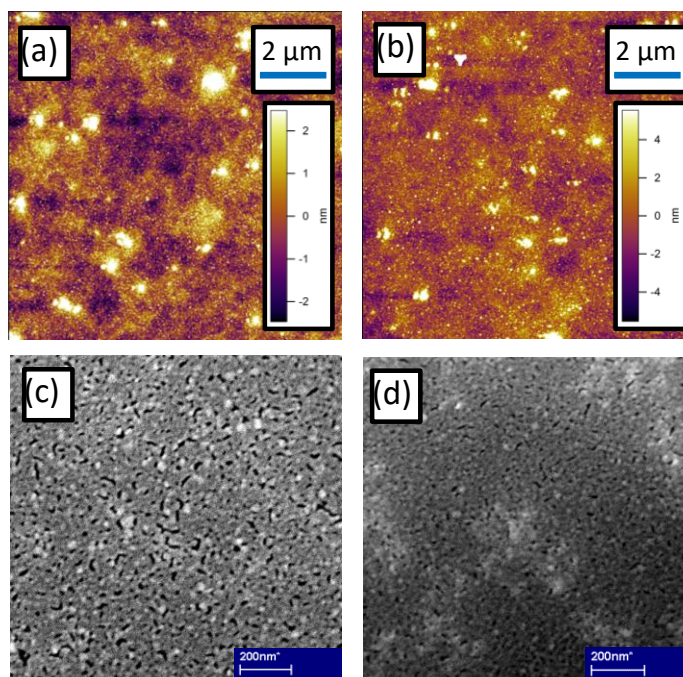


**Figure 5.30:** Morphology of layers in a PBDTTT-EFT:PC<sub>71</sub>BM OPV; H<sub>y</sub>MoO<sub>3-x</sub> layers measured with AFM for (a) 0.58:1 MPA:Mo doped and (b) un-doped films;; Morphology of Ag electrode measured with SEM for (c) 0.58:1 MPA:Mo doped and (d) un-doped films.

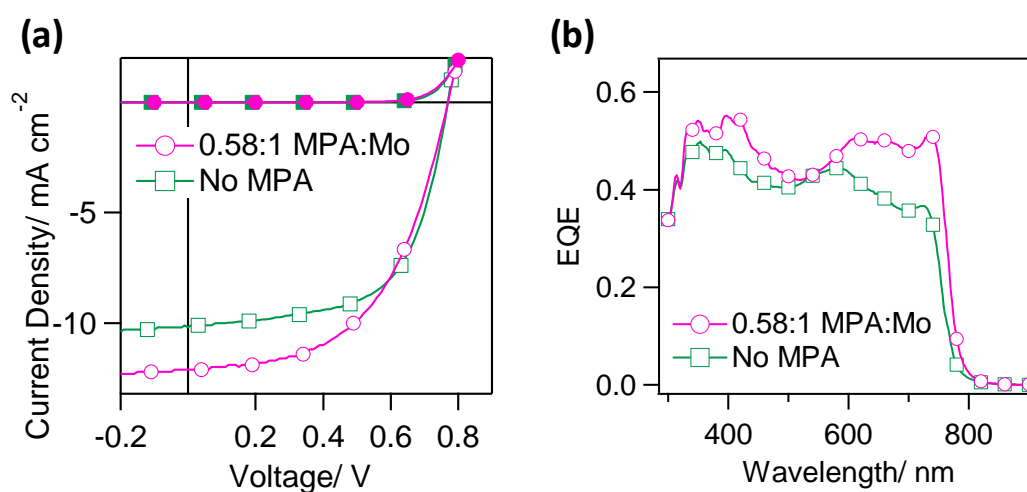


**Figure 5.31:** Characterisation of AlCuAl | PBDTTT-EFT:PC<sub>71</sub>BM | H<sub>y</sub>MoO<sub>3-x</sub> | Ag (8 nm) OPVs with and without an MPA doping of 0.58:1 MPA:Mo of (a) *JV* curves under illumination (empty markers) and in the dark (filled markers) and (b) EQE.

	$J_{sc}/\text{mA cm}^{-2}$	$V_{oc}/\text{V}$	$FF$	$PCE/\%$	$R_{series}/\Omega \text{ cm}^2$
No MPA	10.02 $\pm$ 0.39	0.77 $\pm$ 0.01	0.60 $\pm$ 0.02	4.64 $\pm$ 0.11	11.97 $\pm$ 1.13
With MPA	12.06 $\pm$ 0.39	0.76 $\pm$ 0.02	0.51 $\pm$ 0.03	4.71 $\pm$ 0.25	18.07 $\pm$ 2.80

**Table 5.7:** Key device parameters of Al | Cu | Al | PBDTTT-EFT:PC<sub>71</sub>BM | H<sub>y</sub>MoO<sub>3-x</sub> | Ag (8 nm) OPVs with and without an MPA doping of 0.58:1 MPA:Mo. Series resistance estimated from the gradient of the *JV* curve under open circuit.

However, due to the reduction in *FF* the overall improvement in PCE is small. The reduction in *FF* appears to be due to an increased series resistance in the devices, as estimated from the inverse of the gradient of the current-voltage characteristic at the open-circuit condition. The reasons for this increase in series resistance when using PBDTTT-EFT:PC<sub>71</sub>BM as the light harvesting layer are as yet not fully understood.

#### 5.4.5 Substitution of Ag with Cu

Finally, in order to reduce the materials cost of the Ag window electrode the possibility of substituting some of the Ag with another lower cost metal was explored. Cu has a bulk conductivity comparable to that of Ag, alloys readily with Ag and is also known to interact strongly with thiol moieties, making it an obvious choice as a lower cost substitute for Ag in this context.

A similar XPS experiment to that used to probe the interaction between Ag and H<sub>y</sub>MoO<sub>3-x</sub> was performed using Cu in place of Ag, the data for which is shown in Figure 5.32. As seen previously the evaporation of the metal results in a large increase in the thiolate character of the MPA species (Figure 5.32(a) & (b)) which is attributed to

binding with the incoming Cu. At the same time reduction of the underlying Mo film also occurs with the ratio of Mo oxidation states changing from 50% Mo<sup>+6</sup>: 50% Mo<sup>+5</sup> to 5% Mo<sup>+6</sup>: 56% Mo<sup>+5</sup>: 39% Mo<sup>+4</sup> (Figure 32(c) & (d)). In contrast to the case of Ag there is clear evidence for oxidation of Cu because there is a satellite peak at a binding energy of 944.9 eV (Figure 5.32(e)), which can be assigned to Cu<sup>2+</sup>.<sup>183</sup> Additionally, the Cu LMM Auger spectra shows a large change in the shape of the spectrum when the Cu film thickness is increased from ~1 nm to ~3 nm (Figure 5.32(f)).

For the thicker Cu film the Auger spectrum is consistent with that of bulk Cu<sup>0</sup> as previously reported by Platzman *et al.*,<sup>183</sup> whereas the thinner film has a large peak centred 570.6 eV which can again be assigned to Cu<sup>2+</sup>. It is however unclear as to whether the Cu<sup>2+</sup> signal is also due to the formation of CuO or an alloy of MoO<sub>x</sub> and Cu, since Greiner *et al.* have shown that a MoO<sub>x</sub>:Cu alloy can readily form and give rise to an Auger LMM spectrum similar to that in Figure 5.32(f) for the ~1 nm Cu film.<sup>89</sup> Upon doping the H<sub>y</sub>MoO<sub>3-x</sub> films with 0.86:1 MPA:Mo the oxidation state composition changes from 36% Mo<sup>+6</sup>: 64% Mo<sup>+5</sup> to 5% Mo<sup>+6</sup>: 38% Mo<sup>+5</sup>: 57% Mo<sup>+4</sup> after ~1 nm Cu deposition. By comparing the LMM Auger spectra for the MPA doped films to the undoped films two large differences are noticeable (Figure 32(f)). Firstly, the line shapes of the spectra are very different, with the MPA doped sample exhibiting a line shape much more similar to that of bulk Cu<sup>0</sup> than on the undoped H<sub>y</sub>MoO<sub>3-x</sub> film. Additionally, the intensity of the Cu signal is much larger when deposited on the MPA doped H<sub>y</sub>MoO<sub>3-x</sub> film.

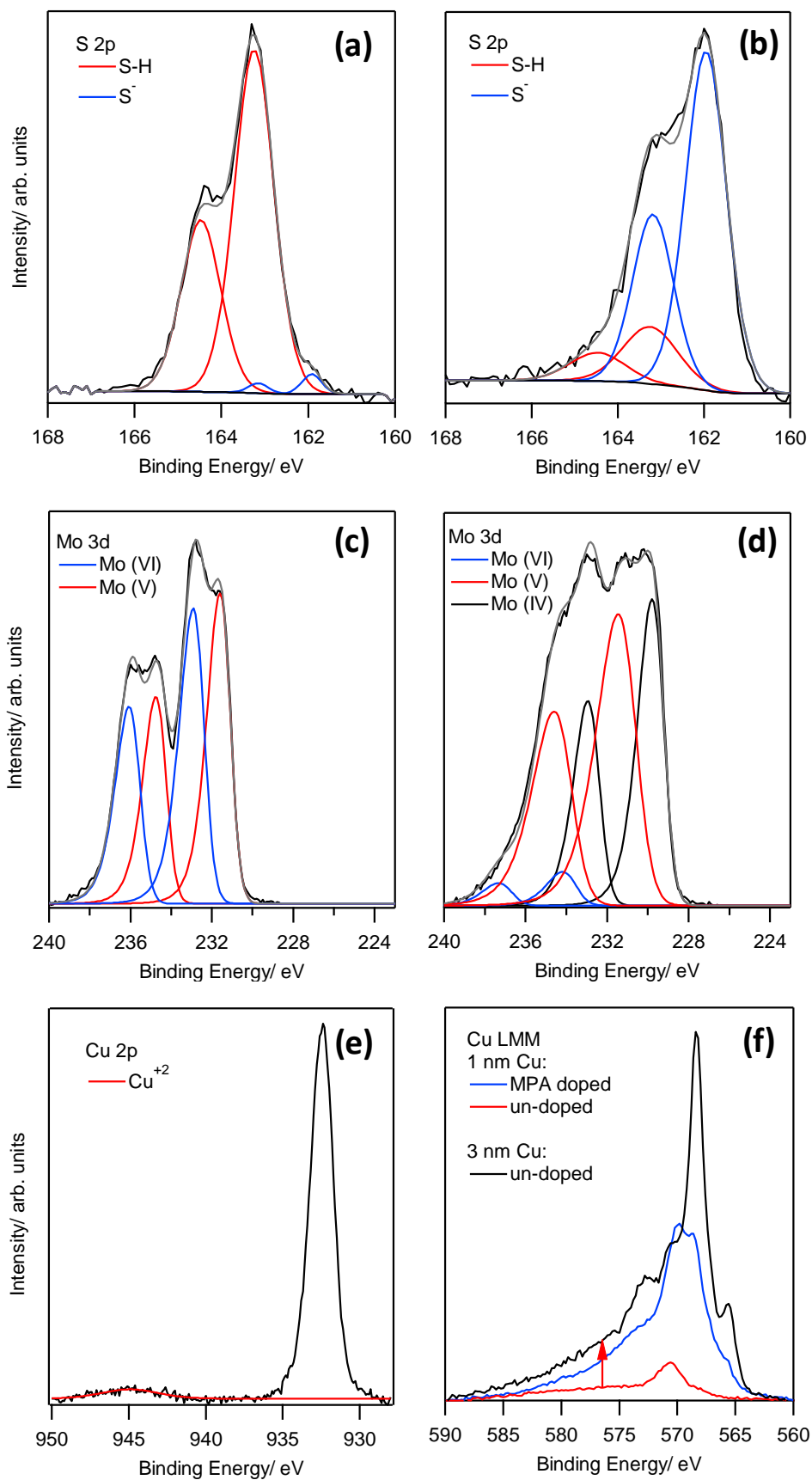


**Figure 5.32:** HRXPS spectra of (a)  $H_yMoO_{3-x}:MPA$  (1:0.86) films S 2p region before and (b) after deposition of  $\sim 1$  nm Cu, (c) un-doped  $H_yMoO_{3-x}$  Mo 3d region before and (d) after deposition of  $\sim 1$  nm Cu, (e) un-doped  $H_yMoO_{3-x}$  Cu 2p 3d region after  $\sim 1$  nm Cu deposition and (f) Cu LMM Auger spectra for a  $\sim 1$  nm or  $\sim 3$  nm Cu film evaporated on un-doped  $H_yMoO_{3-x}$  and  $H_yMoO_{3-x}:MPA$  (1:0.86) films. Thin black lines (counts) and thick dashed red lines (overall fit).

It should be noted that after  $\sim 3$  nm Cu deposition on the MPA doped film an identical line-shape to the non-doped  $\sim 3$  nm Cu sample was seen in the Auger spectra but at a greater intensity. Since identical Cu thickness was deposited on films with and without MPA this difference in intensity is tentatively ascribed to improved adhesion of Cu at the interface when MPA is present which would block the diffusion of Cu atoms into the bulk of the  $H_yMoO_{3-x}$  film and so hinder the formation of an alloy. Evidence for this is provided by the SEM images of the Cu electrode on  $H_yMoO_{3-x}$  (Figure 5.33) from which it was found that more compact Cu films were formed when the MPA is present.

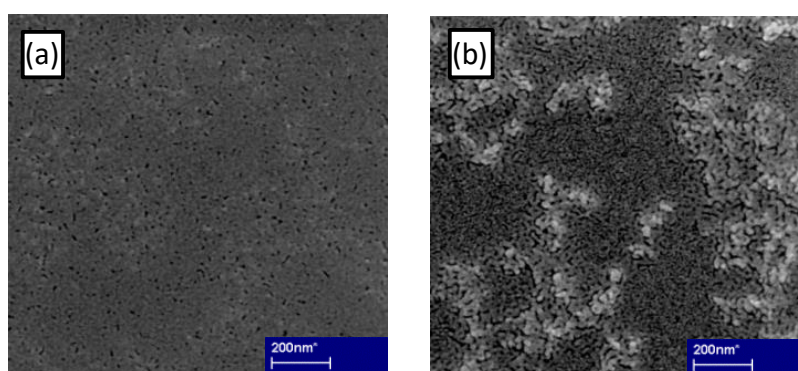


**Figure 5.33:** Morphology of Cu | Ag electrode measured with SEM for (a) 0.86:1 MPA:Mo doped and (b) un-doped  $H_yMoO_{3-x}$  films in a PTB7:PC<sub>71</sub>BM OPV.

Top-illuminated OPVs were fabricated with a bilayer Cu (4 nm) | Ag (4 nm) electrode which combines the higher transparency of Ag with the lowered cost of Cu.<sup>161</sup> The 4 nm Cu layer was deposited first to increase the stability of the OPV because Ag is more resistant to oxidation in air. OPVs were fabricated with the structure; Al | Cu | Al | PTB7:PC<sub>71</sub>BM | H<sub>y</sub>MoO<sub>3-x</sub>:MPA | Cu (4 nm) | Ag (4 nm) with and without MPA doping of the H<sub>y</sub>MoO<sub>3-x</sub> film (Figure 5.34). The optimised loading for the PTB7:PC<sub>71</sub>BM BHJ of 0.86:1 MPA:Mo, as shown in Figure 5.24(c), was used.

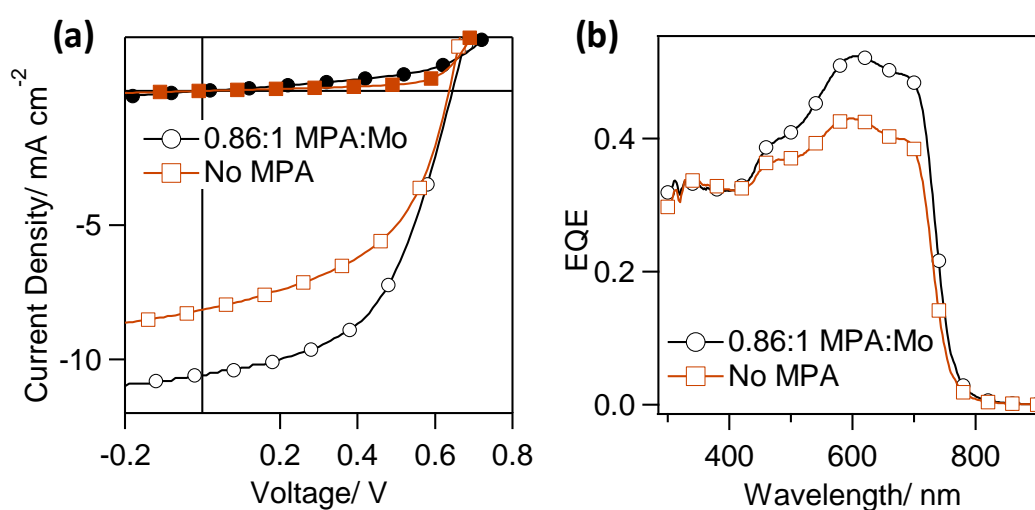


**Figure 5.34:** Characterisation of Al | Cu | Al | PTB7:PC<sub>71</sub>BM | H<sub>y</sub>MoO<sub>3-x</sub> | Cu (4 nm) | Ag (4 nm) OPVs with and without an MPA doping of 0.86:1 MPA:Mo of (a) *JV* curves under illumination (empty marker) and in the dark (filled markers); (b) EQE.

	$J_{sc}/\text{mA cm}^{-2}$	$V_{oc}/\text{V}$	$FF$	$PCE/\%$	$R_{series}/\Omega \text{cm}^2$
No MPA	$8.15 \pm 0.52$	$0.62 \pm 0.02$	$0.47 \pm 0.03$	$2.40 \pm 0.34$	$16.14 \pm 1.32$
With MPA	$10.30 \pm 0.37$	$0.61 \pm 0.02$	$0.48 \pm 0.04$	$3.06 \pm 0.37$	$16.46 \pm 1.79$

**Table 5.8:** Key device parameters of Al | Cu | Al | PTB7:PC<sub>71</sub>BM | H<sub>y</sub>MoO<sub>3-x</sub> | Cu (4 nm) | Ag (4 nm) OPVs with and without an MPA doping of 0.86:1 MPA:Mo. Series resistance estimated from the gradient of the *JV* curve under open circuit.

---

A similar effect to that seen previously occurs when using a Cu | Ag bilayer electrode in place of Ag; an increase in  $J_{sc}$  due to increased photo-conversion at longer wavelengths (Figure 5.34 & Table 5.8). This improvement is again consistent with the improvement in the top electrode morphology (Figure 5.33) and so can be attributed to a decreased plasmonic absorption and scattering of the electrode in the MPA doped device stack.

## 5.5 Conclusions

This chapter has discussed the development of a new solution processed layer for top-illuminated organic photovoltaics that combines the function of wide band-gap hole-extraction layer with the role of seed layer for the formation of robust 8 nm Ag window electrodes. The advantages of this hybrid electronic material are (i) that it does not add to the complexity of device fabrication, since oxide charge extractions layers are an essential component of high performance OPVs, (ii) it does not use costly materials, such as Au, (iii) and it is compatible with a large range of organic semiconductors, since it is processed from ethanol. We have shown that the key organic component, MPA, (i) binds to the oxide matrix and silver electrode, promoting silver film formation and robustness at low Ag thickness, (ii) reduces the contact resistance at the Ag |  $H_yMoO_{3-x}$  interface without significantly adversely affecting the optical properties, and (iii) improves the film forming properties on the surface of organic semiconductor films. Ag film electrodes with a thickness of 8 nm deposited onto this hybrid interlayer have a sheet resistance as low as 9.7 Ohms per square and mean transparency  $\sim 80\%$  over the wavelength range  $\lambda = 400\text{--}900$  nm, even without the aid of an anti-reflecting layer. OPVs made with the MPA doped  $H_yMoO_{3-x}$  film showed a significant improvement in *PCE* over the un-doped films due, in part, to the more compact window electrode.

---

Combined with a greatly improved stability toward nitrogen and air exposure these properties make these electrodes an excellent match to the needs of high performance top-illuminated OPVs.  $H_yMoO_{3-x}:MPA$  was found to bind strongly to Cu also and so preliminary experiments into fabricating a bilayer Cu | Ag window electrode in conjunction with  $H_yMoO_{3-x}:MPA$  were conducted. The low-cost of Cu combined with the high transparency and stability of Ag will lead to a cheaper high performance OPV.

---

## Chapter 6.

# A Nano-Structured Reflective Electrode for Top-Illuminated OPVs

### 6.1 Summary

This chapter reports preliminary work relating to the fabrication and testing of a new type of substrate electrode for top-illuminated OPVs, designed to increase the path length of light in the device by scattering reflected light not absorbed on the first pass back into the absorbing layer, without compromising device  $R_{\text{shunt}}$ . The electrode is based on an optically thin Au film with a random array of apertures with dimensions of 100-300 nm and a depth of 8-15 nm supported on a reflective Al/AIO<sub>x</sub> substrate modified with a molecular adhesive. Whilst this work is at an early stage of development, it is included in this thesis to document the considerable progress made towards the development of this model electrode and some preliminary investigations into its functionality in top-illuminated OPVs.

### 6.2 Introduction

As previously explained in Chapter 1 a constraint on the thickness of the photo-active layer in OPVs is the low electron and hole mobility in organic semiconductors. Therefore the thickness of this layer is often not sufficient to absorb all of the light incident on the OPV before it leaves the device after reflection from the back contact.<sup>249,250</sup> By nano-structuring the reflective electrode it is possible to scatter the light which is not absorbed on first pass through the photo-active layer,

such that its path length through the photoactive layer the second time around is longer than the first, as illustrated in Figure 6.1.

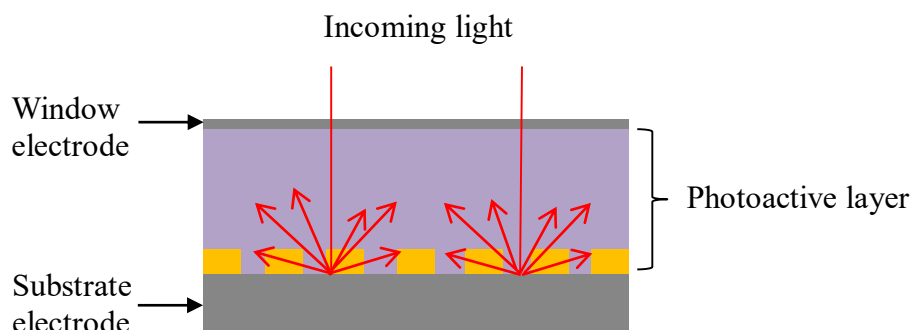


**Figure 6.1:** Schematic diagram showing the action of a nano-structures electrode as a light scattering element in a top-illuminated OPV.

The potential of this approach has been demonstrated in OPV device structures using metal nanoparticles with a diameter in the range of 60-100 nm by An *et al.*,<sup>104</sup> and also using metal films with an array of circular indentations of diameter 300 nm fabricated by nano-sphere lithography by Xu *et al.*<sup>226</sup> However, whilst such large features are necessary to efficiently scatter visible light, by introducing them in the form of particles there is a significant risk of compromising the  $R_{\text{shunt}}$  of the OPV, since these scattering elements are of a comparable thickness to the photo-active layer used in most high performance OPVs. By introducing shallow indentations into the film with lateral dimensions of the correct size to scatter light this problem is avoided, although the method proposed by Xu *et al.* is based on the use of nano-sphere lithography, which adds complexity to the device fabrication and would be very costly to scale to large areas. In both the aforementioned cases the improvement in device performance observed upon nano-structuring the back contact was attributed to a number of different effects including plasmonic absorption, light

---

scattering and increased contact area with the electrode. Since it is difficult to disentangle optical and electronic effects in the performance of an OPV device, the contribution from each of these could not be isolated.

Herein the fabrication of a Au electrode with a random dense array of apertures of the correct size to scatter visible light is described. The electrode is fabricated on a reflective Al/AIO<sub>x</sub> supporting substrate using a molecular adhesive layer of APTMS:MPTMS to enable control over film adhesion and morphology. Importantly the formation of the apertures requires no lithographic step, rather only simple annealing of the electrode, and the apertures formed have a very narrow depth distribution which helps to ensure minimal decreases in R<sub>shunt</sub>. Furthermore the large distribution of aperture size and shape should ensure broad-band light scattering which is important for PV applications, since PVs must ideally harvest light over a large range of wavelengths; 400-1100 nm. Au is used as the electrode material due to having a relatively high  $\Phi$  and good stability towards oxidation, which helps to simplify the interpretation of the results by removing complexity that arises from oxidation.

### 6.3 Experimental

Nano-structured reflective electrodes were fabricated using the 4 step process shown in Figure 6.2: (i) Evaporating Al (50 nm, 1 nm s<sup>-1</sup>) onto cleaned glass substrate followed by UV/O<sub>3</sub> treatment to create an AlO<sub>x</sub> film.; (ii) Deposition of a mixed APTMS:MPTMS monolayer from the vapour phase at ~50 mbar for 5 hours, followed by exposure to air for 3 hours, then a further 16 hours in APTMS:MPTMS vapour at ~50 mbar.; (iii) Thermal evaporation of a thin Au film (8 nm, 0.1 nm s<sup>-1</sup>);

(iv) Aperture formation by heating between 200-350°C for 5 minutes under N<sub>2</sub>. The methods used for OPV fabrication are given in Chapter 2 of this thesis.

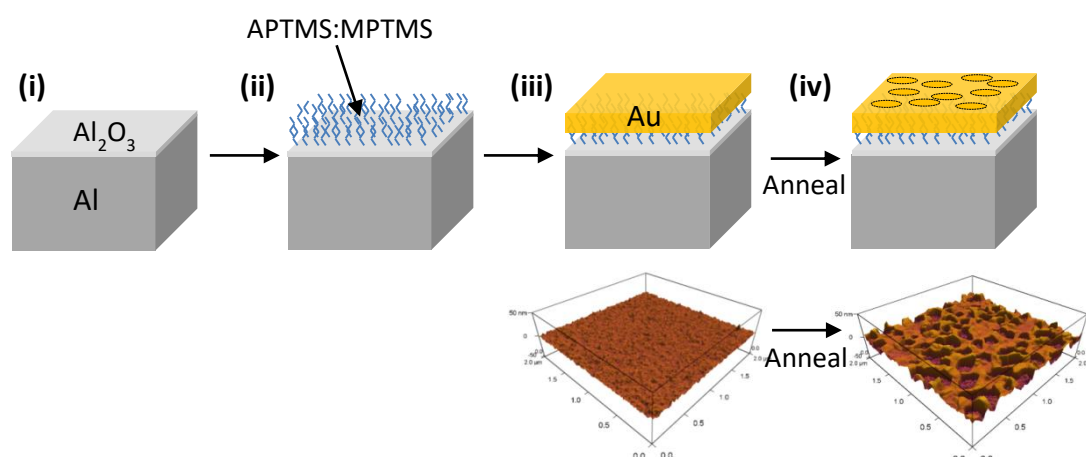


**Figure 6.2:** Electrode fabrication procedure: **(i)** Evaporation of Al onto cleaned glass substrate followed by UV/O<sub>3</sub> treatment to create an AlO<sub>x</sub>; **(ii)** Deposition of a mixed monolayer.; **(iii)** Evaporation of a thin Au film.; **(iv)** Aperture formation by annealing under N<sub>2</sub>. Morphology of the Au electrode pre and post annealing are included, measured using an AFM

#### 6.4 Results and Discussion

Apertures of different sizes and densities were formed in the Au film by thermal annealing at different temperatures between 200-350°C for 5 minutes as shown in Figure 6.3. As shown, both the size and density of the apertures is tuneable with increasing annealing temperature resulting in a higher density of larger apertures. Area analysis using the software WS×M<sup>251</sup> calculates the total area of apertures as 0.3% after 200°C; 3.3% after 250°C; 11.2% after 300°C and 37.7% after 350°C.

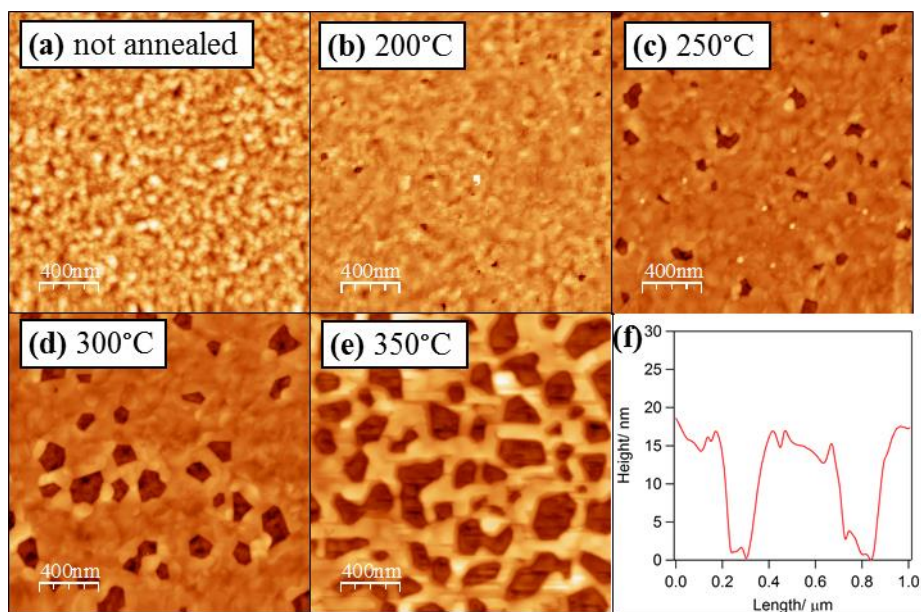


**Figure 6.3:** Morphology of glass | Al (50 nm) | APTMS:MPTMS | Au (8 nm) with (a) no heating, and after 5 minutes at (b) 200°C, (c) 250°C, (d) 300°C, and (e) 350°C collected via AFM. (f) A representative line scan taken from the image shown in (e).

Preliminary investigations were conducted in model OPV devices using electrodes annealed at 350°C for 5 minutes and the results are given in Figure 6.4 and Table 6.1. Surprisingly, introducing a high density of apertures into the nano-structured back electrode has only a very small effect on the performance of the device, as compared to identical devices using an electrode without apertures, with only a slight increase in  $J_{sc}$  (Table 6.1). This improvement is very small and cannot be conclusively stated to be due to light scattering, light trapping due to plasmon excitation occurring at electrode surface, or an effect brought about by a change in another of the electrodes properties.

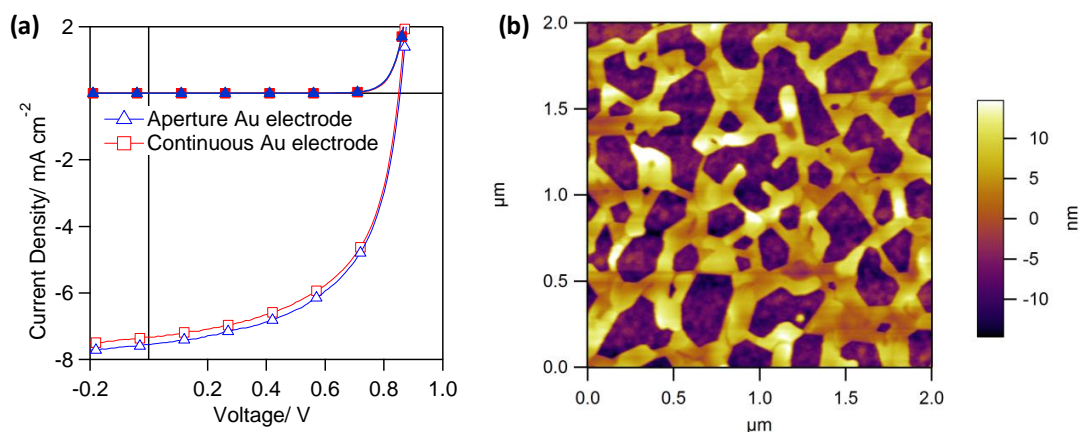


**Figure 6.4:** (a) Representative  $JV$  device characteristics of the structure Al (50 nm) | APTMS:MPTMS | Au (8 nm) | MoO<sub>3</sub> (5 nm) | PCDTBT:PC<sub>71</sub>BM | BCP (8 nm) | Al (1 nm) | Ag (14 nm) | MoO<sub>3</sub> (34 nm) with and without 38% aperture formation in the light (empty markers) and dark (filled markers). (b) Morphology of the annealed Au electrode collected with AFM.

	$J_{sc}/ \text{mA cm}^{-2}$	$V_{oc}/ \text{V}$	$FF$	$PCE/ \%$	$R_{series}/ \Omega \text{ cm}^2$
Ref	$7.33 \pm 0.37$	$0.85 \pm < 0.01$	$0.56 \pm 0.01$	$3.50 \pm 0.17$	$12.6 \pm 0.8$
Aperture	$7.50 \pm 0.29$	$0.86 \pm < 0.01$	$0.54 \pm 0.02$	$3.51 \pm 0.18$	$13.6 \pm 1.4$

**Table 6.1:** Key device data of the structure Al (50 nm) | APTMS:MPTMS | Au (8 nm) | MoO<sub>3</sub> (5 nm) | PCDTBT:PC<sub>71</sub>BM | BCP (8 nm) | Al (1 nm) | Ag (14 nm) | MoO<sub>3</sub> (34 nm) with and without aperture electrodes.

There is also a very slight decrease in  $FF$ , due to an increased  $R_{series}$ , when using the nano-structured electrode, which may result from an increase in the electrode sheet resistance due to either an increased path length or a scattering of the charge in the aperture electrode. However, it should be emphasised that the changes in  $FF$  and  $J_{sc}$

are very small, indeed within one standard deviation of each other, which is very surprising considering that roughly 30% of the electrode structure is absent compared to a flat homogenous electrode.

It is evident from the AFM images in Figure 6.3 that there is a large increase in the mean size of the Au crystallites upon annealing and so it is possible that this difference is what is causing the slight changes in device performance, since changes in crystallinity can change the energetics at the electrode – semiconductor interface. To investigate the effect of the increased grain size, electrodes were fabricated with varied crystallite sizes but without the formation of apertures. To achieve this, thicker (15 nm) Au electrodes are deposited on an APTMS:MPTMS monolayer directly on glass. A much shorter silane monolayer vapour time of 1 hour was used due to the stronger adhesion of the monolayer to glass than to  $\text{AlO}_x$  and the thicker film being more robust. These films were annealed at  $300^\circ\text{C}$  for 10 minutes in order to alter the grain size of the crystallites as illustrated in Figure 6.5.

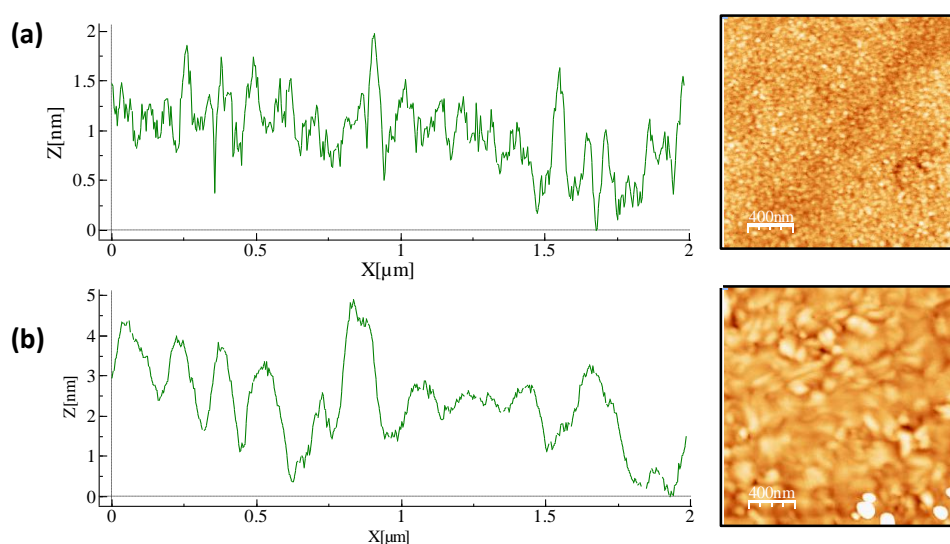


**Figure 6.5:** Morphology of Au electrodes with relevant line scans (a) pre and (b) post annealing at  $300^\circ\text{C}$  for 10 minutes.

The  $JV$  characteristics of devices using larger crystallite structures are shown in Figure 6.6 and Table 6.2. As can be seen the difference in electrode grain size has a very similar effect on the performance of the devices as seen with the aperture electrode. As with the aperture electrode there is a slight increase in the  $J_{sc}$ , although this effect is even smaller than previously seen so it arguably not significant. A decrease in  $FF$  is again seen upon annealing the electrode, but with a much more noticeable change to the  $R_{series}$  in this device set. Whilst this effect is again only small the similarity with the data in Table 6.1 lends credence to this being a real effect. The increase in crystallite size is therefore tentatively associated with the slight losses observed when using the aperture electrode (Figure 6.4).

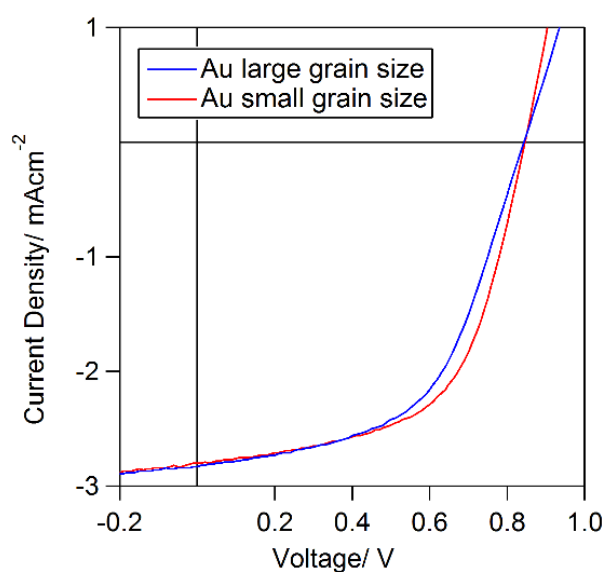


**Figure 6.6:** Representative  $JV$  device characteristics of the structure glass | APTMS:MPTMS | Au (15 nm) | MoO<sub>3</sub> (5 nm) | PCDTBT:PC<sub>71</sub>BM | BCP (8 nm) | Al (1 nm) | Ag (14 nm) | MoO<sub>3</sub> (34 nm) with and without annealed electrodes to induce a change in the grain size.

<b>Grain Size</b>	$J_{sc}/ \text{mA cm}^{-2}$	$V_{oc}/ \text{V}$	$FF$	$PCE/ \%$	$R_{series}/ \Omega \text{ cm}^2$
Small	$2.87 \pm 0.29$	$0.85 \pm < 0.01$	$0.58 \pm 0.03$	$1.40 \pm 0.08$	$57.2 \pm 8.6$
Large	$2.96 \pm 0.15$	$0.84 \pm < 0.01$	$0.56 \pm 0.02$	$1.39 \pm 0.18$	$72.7 \pm 17.6$

**Table 6.2:** *JV* device characteristics of the structure glass | APTMS:MPTMS | Au (15 nm) | MoO<sub>3</sub> (5 nm) | PCDTBT:PC<sub>71</sub>BM | BCP (8 nm) | Al (1 nm) | Ag (14 nm) | MoO<sub>3</sub> (34 nm) with and without annealed electrodes to induce a change in the grain size.

## 6.5 Conclusions

In summary the fabrication of a novel nano-structured reflective substrate electrode for top-illuminated OPVs has been described and demonstrated in model devices. Whilst no significant improvement in light harvesting has been observed in this limited device study, further work on this interesting electrode structure could lead to a scalable approach to increasing light harvesting in top-illuminated OPVs.

---

## Chapter 7.

### Future Outlook

In Chapter 3 a highly reflective, low work function metal electrode which offers high stability towards oxidation in air is described, that is based on the triple layer structure: Al (60 nm) | Cu (8 nm) | Al (0.8 nm). Potential areas for the further development of this electrode include: (i) An investigation into the reason for the increase in  $J_{sc}$  observed when fabricating OPV devices in the trilayer electrode as compared to bare Al, including the apparent increase seen in  $J_{sc}$  with oxidation. It is possible that this is due to a wetting phenomenon which may lead to a change in the composition or physical structure of the BHJ when deposited onto the oxide surface as compared to the bare metal. It could also be due to the dielectric properties of the ultra-thin oxide layer, which screen the image charge reducing recombination at the electrode. (ii) An extension of the stability study to include an investigation of effect of humidity and extended oxidation times. (iii) An investigation into the composition at each layer of the electrode to further elucidate the chemistry and structure possibly using dynamic secondary ion mass spectroscopy to depth profile the electrode.

In Chapter 4 the electrode developed in Chapter 3 is used to elucidate a new design rule for bulk-heterojunction OPVs. The key areas for further investigation on this topic are: (i) To expand the catalogue of semiconductors tested to include a larger selection of state-of-the-art polymers, such as PBDTTT-EFT.; (ii) To conduct a study aimed at investigating when and why the *push-back* effect occurs using varied organic semiconductors and substrate electrodes with a range of work functions.; (iii) To further validate the universality of the proposed design rule by

---

fabricating OPVs with varied hole-blocking layers, such as PFN and  $\text{TiO}_x$ , and using other low work function electrodes, such as Ca or Sm.

In Chapter 5 the synthesis of an organo-molybdenum bronze is described and used to enable the realisation of robust, low sheet resistance window electrodes with high far-field transparency. The key areas for further investigation of this hybrid charge extraction layer are: (i) The synthesis and comparison of analogous organo-doped metal oxide bronzes based on vanadium oxide and tungsten oxide material to identify the most promising for practical applications. (ii) An investigation into the efficacy of other organic dopants such as 3-aminopropionic acid, which may be more effective than MPA.

In Chapter 6 the results of a preliminary investigation into a nano-structured Au electrode at the reflective substrate are described. This electrode was developed to explore the potential for enhancement of  $J_{sc}$  in top-illuminated OPVs by increasing the path length of light in the device. Due to being at an early stage of research there are a number of potential avenues for further study, these include: (i) Applying the same fabrication process to other materials, e.g. Cu and Ag. (ii) Sensitising the electrode to increased plasmonic absorption through insertion of appropriate thin films. (iii) Fabricating aperture electrodes with varied monolayers and deposition conditions to achieve a more rapid fabrication route.

---

## References

- 1 International Energy Agency, 2015, 1–5.
- 2 C. Le Quéré, R. Moriarty, R. M. Andrew, J. G. Canadell, S. Sitch, J. I. Korsbakken, P. Friedlingstein, G. P. Peters, R. J. Andres, T. A. Boden, R. A. Houghton, J. I. House, R. F. Keeling, P. Tans, A. Arneeth, D. C. E. Bakker, L. Barbero, L. Bopp, J. Chang, F. Chevallier, L. P. Chini, P. Ciais, M. Fader, R. A. Feely, T. Gkritzalis, I. Harris, J. Hauck, T. Ilyina, A. K. Jain, E. Kato, V. Kitidis, K. Klein Goldewijk, C. Koven, P. Landschützer, S. K. Lauvset, N. Lefèvre, A. Lenton, I. D. Lima, N. Metzl, F. Millero, D. R. Munro, A. Murata, J. E. M. S. Nabel, S. Nakaoka, Y. Nojiri, K. O’Brien, A. Olsen, T. Ono, F. F. Pérez, B. Pfeil, D. Pierrot, B. Poulter, G. Rehder, C. Rödenbeck, S. Saito, U. Schuster, J. Schwinger, R. Séférian, T. Steinhoff, B. D. Stocker, A. J. Sutton, T. Takahashi, B. Tilbrook, I. T. Van Der Laan-Luijkx, G. R. Van Der Werf, S. Van Heuven, D. Vandemark, N. Viovy, A. Wiltshire, S. Zaehle and N. Zeng, *Earth Syst. Sci. Data*, 2015, **7**, 349–396.
- 3 T. F. Stocker, G.-K. Plattner, M. Tignor, S. K. Allen, J. Boschung, A. Nauels, Y. Xia, V. Bex, P. M. Midgley and (eds), *Summary for Policymakers. In: Climate Change 2013: The Physical Science Basis. Contribution of Working Group I to the Fifth Assessment Report of the Intergovernmental Panel on Climate Change*, Cambridge University Press, Cambridge, 2013.
- 4 P. Scapecchi, *The Health Costs of Inaction with Respect to Air Pollution*, 2008.
- 5 N. Butt, H. L. Beyer, J. R. Bennett, D. Biggs, R. Maggini, M. Mills, a. R. Renwick, L. M. Seabrook and H. P. Possingham, *Science*, 2013, **342**, 425–426.
- 6 C. J. Rhodes, *Sci. Prog.*, 2016, **99**, 97–104.
- 7 C. McGlade and P. Ekins, *Nature*, 2015, **517**, 187–190.
- 8 European Commission, *World Energy Technology Outlook - WETO H2*, 2006.
- 9 R. E. Smalley, *MRS Bull.*, 2005, **30**, 412–417.
- 10 S. Sorrell, J. Speirs, R. Bentley, A. Brandt and R. Miller, *Energy Policy*, 2010, **38**, 5290–5295.
- 11 D. Barlev, R. Vidu and P. Stroeve, *Sol. Energy Mater. Sol. Cells*, 2011, **95**, 2703–2725.
- 12 E. Kisel, A. Hamburg, M. Härm, A. Leppiman and M. Ots, *Energy Policy*, 2016, **95**, 1–9.
- 13 S. M. Shaahid and I. El-Amin, *Renew. Sustain. Energy Rev.*, 2009, **13**, 625–633.
- 14 W. R. Fahrner, *Amorphous Silicon / Crystalline Silicon Heterojunction Solar Cells*, Springer Berlin Heidelberg, Berlin, Heidelberg, 2013.
- 15 M. S. Friedolf, *IEEE Trans. Electron Devices*, 1976, **ED-23**, 640–643.
- 16 S. Xiao and S. Xu, *Crit. Rev. Solid State Mater. Sci.*, 2014, **39**, 277–317.
- 17 F. Machui, M. Hösel, N. Li, G. D. Spyropoulos, T. Ameri, R. R. Søndergaard, M. Jørgensen, A. Scheel, D. Gaiser, K. Kreul, D. Lenssen, M. Legros, N. Lemaitre, M. Vilkmann, M. Välimäki, S. Nordman, C. J. Brabec and F. C. Krebs, *Energy Environ. Sci.*,

- 
- 2014, **7**, 2792–2802.
- 18 C. W. Tang, *Appl. Phys. Lett.*, 1986, **48**, 183–185.
- 19 S. Morita, A. A. Zakhidov and K. Yoshino, *Solid State Commun.*, 1992, **82**, 249–252.
- 20 N. Sariciftci and L. Smilowitz, *Science.*, 1992, **258**, 1474–1476.
- 21 G. Yu, J. Gao, J. C. Hummelen, F. Wudl and A. J. Heeger, *Science.*, 1995, **270**, 1789–1791.
- 22 J. Zhao, Y. Li, G. Yang, K. Jiang, H. Lin, H. Ade, W. Ma and H. Yan, *Nat. Energy*, 2016, **1**, 15027.
- 23 M. A. Green, K. Emery, Y. Hishikawa, W. Warta and E. D. Dunlop, *Prog. Photovoltaics Res. Appl.*, 2015, **23**, 1–9.
- 24 M. Grätzel, *Acc. Chem. Res.*, 2009, **42**, 1788–1798.
- 25 J. Yan and B. R. Saunders, *RSC Adv.*, 2014, **4**, 43286–43314.
- 26 J. Du, Z. Du, J. Hu, Z. Pan, Q. Shen, J. Sun, D. Long, H. Dong, L. Sun, X. Zhong and L. Wan, *J. Am. Chem. Soc.*, 2016, **138**, 4201–4209.
- 27 M. Saliba, T. Matsui, J.-Y. Seo, K. Domanski, J.-P. Correa-Baena, M. K. Nazeeruddin, S. M. Zakeeruddin, W. Tress, A. Abate, A. Hagfeldt and M. Grätzel, *Energy Environ. Sci.*, 2016, **9**, 1989–1997.
- 28 D. Wang, M. Wright, N. K. Elumalai and A. Uddin, *Sol. Energy Mater. Sol. Cells*, 2016, **147**, 255–275.
- 29 B. Al-Rashdi, C. Somerfield and N. Hilal, *Sep. Purif. Rev.*, 2011, **40**, 209–259.
- 30 S.-S. Sun and L. R. Dalton, *Introduction to Organic Electronic and Optoelectronic Materials and Devices*, CRC Press, 2008.
- 31 S. J. Fonash, *Solar Cell Device Physics*, Elsevier, 2nd edn., 2010.
- 32 M. Hallermann, S. Haneder and E. Da Como, *Appl. Phys. Lett.*, 2008, **93**, 053307.
- 33 R. W. Strayer, W. Mackie and L. W. Swanson, *Surf. Sci.*, 1973, **34**, 225–248.
- 34 F. Deledalle, T. Kirchartz, M. S. Vezie, M. Campoy-Quiles, P. Shakya Tuladhar, J. Nelson and J. R. Durrant, *Phys. Rev. X*, 2015, **5**, 011032.
- 35 Q. Fu and T. Wagner, *Surf. Sci. Rep.*, 2007, **62**, 431–498.
- 36 O. V Mikhnenko, P. W. M. Blom and T. Nguyen, *Energy Environ. Sci.*, 2015, **8**, 1867–1888.
- 37 S. Dimitrov, B. Schroeder, C. Nielsen, H. Bronstein, Z. Fei, I. McCulloch, M. Heeney and J. Durrant, *Polymers.*, 2016, **8**, 14.
- 38 B. R. Patil, S. Shanmugam, J. P. Teunissen and Y. Galagan, *Org. Electron. physics, Mater. Appl.*, 2015, **21**, 40–46.
- 39 S. R. Forrest, *Nature*, 2004, **428**, 911–918.

- 
- 40 B. C. Thompson and J. M. J. Fréchet, *Angew. Chem. Int. Ed. Engl.*, 2008, **47**, 58–77.
- 41 A. J. Heeger, *Adv. Mater.*, 2014, **26**, 10–28.
- 42 G. Yu, J. Gao, J. C. Hummelen, F. Wudl and A. J. Heeger, *Science.*, 1995, **270**, 1789–1791.
- 43 S. Foster, F. Deledalle, A. Mitani, T. Kimura, K. B. Kim, T. Okachi, T. Kirchartz, J. Oguma, K. Miyake, J. R. Durrant, S. Doi and J. Nelson, *Adv. Energy Mater.*, 2014, **4**, 1–12.
- 44 G. Zhao, Y. He, Z. Xu, J. Hou, M. Zhang, J. Min, H. Y. Chen, M. Ye, Z. Hong, Y. Yang and Y. Li, *Adv. Funct. Mater.*, 2010, **20**, 1480–1487.
- 45 C. J. M. Emmott, J. a. Röhr, M. Campoy-Quiles, T. Kirchartz, A. Urbina, N. J. Ekins-Daukes and J. Nelson, *Energy Environ. Sci.*, 2015, **8**, 1317–1328.
- 46 M. M. Wienk, J. M. Kroon, W. J. H. Verhees, J. Knol, J. C. Hummelen, P. A. van Hal and R. A. J. Janssen, *Angew. Chemie Int. Ed.*, 2003, **42**, 3371–3375.
- 47 F. Zhang, Z. Zhuo, J. Zhang, X. Wang, X. Xu, Z. Wang, Y. Xin, J. Wang, J. Wang, W. Tang, Z. Xu and Y. Wang, *Sol. Energy Mater. Sol. Cells*, 2012, **97**, 71–77.
- 48 G. Zhao, Y. He, C. He, H. Fan, Y. Zhao and Y. Li, *Sol. Energy Mater. Sol. Cells*, 2011, **95**, 704–711.
- 49 C. Goh, R. J. Kline, M. D. McGehee, E. N. Kadnikova and J. M. J. Fréchet, *Appl. Phys. Lett.*, 2005, **86**, 1–3.
- 50 J. W. Kingsley, P. P. Marchisio, H. Yi, A. Iraqi, C. J. Kinane, S. Langridge, R. L. Thompson, A. J. Cadby, A. J. Pearson, D. G. Lidzey, R. a. L. Jones and A. J. Parnell, *Sci. Rep.*, 2014, **4**, 1–7.
- 51 C. Müller, E. Wang, L. M. Andersson, K. Tvingstedt, Y. Zhou, M. R. Andersson and O. Inganäs, *Adv. Funct. Mater.*, 2010, **20**, 2124–2131.
- 52 D. Chi, S. Qu, Z. Wang and J. Wang, *J. Mater. Chem. C*, 2014, **2**, 4383–4387.
- 53 W. Ma, C. Yang, X. Gong, K. Lee and A. J. Heeger, *Adv. Funct. Mater.*, 2005, **15**, 1617–1622.
- 54 Y. Kim, S. Cook, S. M. Tuladhar, S. A. Choulis, J. Nelson, J. R. Durrant, D. D. C. Bradley, M. Giles, I. McCulloch, C.-S. Ha and M. Ree, *Nat. Mater.*, 2006, **5**, 197–203.
- 55 N. Blouin, A. Michaud and M. Leclerc, *Adv. Mater.*, 2007, **19**, 2295–2300.
- 56 I. Olle, Z. Fengling and M. R. Andersson, *Acc. Chem. Res.*, 2009, **42**, 1731–1739.
- 57 H. Yi, S. Al-Faifi, A. Iraqi, D. C. Watters, J. Kingsley and D. G. Lidzey, *J. Mater. Chem.*, 2011, **21**, 13649–13656.
- 58 H. A. M. Van Mullekom, J. A. J. M. Vekemans, E. E. Havinga and E. W. Meijer, *Developments in the chemistry and band gap engineering of donor-acceptor substituted conjugated polymers*, 2001, vol. 32.
- 59 D. H. Wang, J. K. Kim, J. H. Seo, I. Park, B. H. Hong, J. H. Park and A. J. Heeger, *Angew.*

- Chemie - Int. Ed.*, 2013, **52**, 2874–2880.
- 60 S. Beaupré and M. Leclerc, *J. Mater. Chem. A*, 2013, **1**, 11097–11105.
- 61 Z. M. Beiley, E. T. Hoke, R. Noriega, J. Dacuña, G. F. Burkhard, J. A. Bartelt, A. Salleo, M. F. Toney and M. D. McGehee, *Adv. Energy Mater.*, 2011, **1**, 954–962.
- 62 L. Lu and L. Yu, *Adv. Mater.*, 2014, **26**, 4413–4430.
- 63 B. Ebenhoch, S. A. J. Thomson, K. Genevičius, G. Juška and I. D. W. Samuel, *Org. Electron.*, 2015, **22**, 62–68.
- 64 Y. M. Yang, W. Chen, L. Dou, W. Chang, H. Duan, B. Bob, G. Li and Y. M. Yang, *Nat. Photonics*, 2015, **9**, 190–198.
- 65 A. Foertig, J. Kniepert, M. Gluecker, T. Brenner, V. Dyakonov, D. Neher and C. Deibel, *Adv. Funct. Mater.*, 2014, **24**, 1306–1311.
- 66 S. J. Lou, J. M. Szarko, T. Xu, L. Yu, T. J. Marks and L. X. Chen, *J. Am. Chem. Soc.*, 2011, **133**, 20661–20663.
- 67 Y. W. Soon, H. Cho, J. Low, H. Bronstein, I. McCulloch and J. R. Durrant, *Chem. Commun.*, 2013, **49**, 1291–1293.
- 68 S. Zhang, L. Ye, W. Zhao, D. Liu, H. Yao and J. Hou, *Macromolecules*, 2014, **47**, 4653–4659.
- 69 Y. Zang, X. Gao, X. Lu, Q. Xin, J. Lin and J. Zhao, *Appl. Surf. Sci.*, 2016, **376**, 138–144.
- 70 W. Huang, E. Gann, L. Thomsen, C. Dong, Y. B. Cheng and C. R. McNeill, *Adv. Energy Mater.*, 2015, **5**, 1–11.
- 71 A. Soultati, A. M. Douvas, D. G. Georgiadou, L. C. Palilis, T. Bein, J. M. Feckl, S. Gardelis, M. Fakis, S. Kennou, P. Falaras, T. Stergiopoulos, N. a. Stathopoulos, D. Davazoglou, P. Argitis and M. Vasilopoulou, *Adv. Energy Mater.*, 2014, **4**, 1300896.
- 72 C. E. Petoukhoff, D. K. Vijapurapu and D. M. O'Carroll, *Sol. Energy Mater. Sol. Cells*, 2014, **120**, 572–583.
- 73 S. Wakim, S. Beaupré, N. Blouin, B.-R. Aich, S. Rodman, R. Gaudiana, Y. Tao and M. Leclerc, *J. Mater. Chem.*, 2009, **19**, 5351–5358.
- 74 L. K. Jagadamma, M. Abdelsamie, A. El Labban, E. Aresu, G. O. Ngongang Ndjawa, D. H. Anjum, D. Cha, P. M. Beaujuge and A. Amassian, *J. Mater. Chem. A*, 2014, **2**, 13321–13331.
- 75 H.-L. Yip, S. K. Hau, N. S. Baek, H. Ma and A. K.-Y. Jen, *Adv. Mater.*, 2008, **20**, 2376–2382.
- 76 G. Long, X. Wan, B. Kan, Z. Hu, X. Yang, Y. Zhang, M. Zhang, H. Wu, F. Huang, S. Su, Y. Cao and Y. Chen, *ChemSusChem*, 2014, **7**, 2358–2364.
- 77 P. Peumans and S. R. Forrest, *Appl. Phys. Lett.*, 2001, **79**, 126–128.
- 78 H.-W. Lin, S.-W. Chiu, L.-Y. Lin, Z.-Y. Hung, Y.-H. Chen, F. Lin and K.-T. Wong, *Adv. Mater.*, 2012, **24**, 2269–2272.

- 
- 79 Y.-E. Lee, S.-Y. Kim, W.-I. Jeong and J.-J. Kim, *Sol. Energy Mater. Sol. Cells*, 2013, **114**, 59–64.
- 80 J. Gilot, I. Barbu, M. M. Wienk and R. A. J. Janssen, *Appl. Phys. Lett.*, 2007, **91**, 113520.
- 81 A. Hadipour, D. Cheyng, P. Heremans and B. P. Rand, *Adv. Energy Mater.*, 2011, **1**, 930–935.
- 82 M. C. Barr, R. M. Howden, R. R. Lunt, V. Bulović and K. K. Gleason, *Adv. Energy Mater.*, 2012, **2**, 1404–1409.
- 83 Y. Shi, L. Tan, L. Chen and Y. Chen, *J. Mater. Chem. C*, 2014, **2**, 8054–8064.
- 84 S. Tokito, K. Noda and Y. Taga, *J. Phys. D: Appl. Phys.*, 1999, **29**, 2750–2753.
- 85 V. Shrotriya, G. Li, Y. Yao, C.-W. Chu and Y. Yang, *Appl. Phys. Lett.*, 2006, **88**, 073508.
- 86 J. Meyer, S. Hamwi, M. Kröger, W. Kowalsky, T. Riedl and A. Kahn, *Adv. Mater.*, 2012, **24**, 5408–5427.
- 87 M. T. Greiner, M. G. Helander, Z. B. Wang, W. M. Tang, J. Qiu and Z. H. Lu, *Appl. Phys. Lett.*, 2010, **96**, 3–6.
- 88 D. O. Scanlon, G. W. Watson, D. J. Payne, G. R. Atkinson, R. G. Egdell and D. S. L. Law, *J. Phys. Chem. C*, 2010, **114**, 4636–4645.
- 89 M. T. Greiner, L. Chai, M. G. Helander, W.-M. M. Tang and Z.-H. H. Lu, *Adv. Funct. Mater.*, 2013, **23**, 215–226.
- 90 J.-W. Kang, S.-P. Lee, D.-G. Kim, S. Lee, G.-H. Lee, J.-K. Kim, S.-Y. Park, J. H. Kim, H.-K. Kim and Y.-S. Jeong, *Electrochem. Solid-State Lett.*, 2009, **12**, 64–66.
- 91 D. B. Fraser and H. D. Cook, *J. Electrochem. Soc.*, 1972, **119**, 1368.
- 92 S. Kim and J.-L. Lee, *J. Photonics Energy*, 2012, **2**, 21215.
- 93 J. C. Bernède, L. Cattin, M. Morsli and Y. Berredjem, *Sol. Energy Mater. Sol. Cells*, 2008, **92**, 1508–1515.
- 94 F. Heinemeyer, D. Mader, D. Munster, T. Dullweber and R. Brendel, in *2nd Workshop on Metallization*, 2010, pp. 48–51.
- 95 E.-C. Chen, P.-T. Tsai, C.-Y. Tsai, J.-H. Chang, Z.-Y. Huang, H.-F. Meng, H.-M. Chen, H.-W. Lin, S.-F. Horng and H.-W. Zan, *Synth. Met.*, 2014, **187**, 172–177.
- 96 C.-F. Lin, S.-W. Liu, W.-F. Hsu, M. Zhang, T.-L. Chiu, Y. Wu and J.-H. Lee, *J. Phys. D: Appl. Phys.*, 2010, **43**, 395101.
- 97 M. Zhang, T.-L. Chiu, C.-F. Lin, J.-H. Lee, J.-K. Wang and Y. Wu, *Sol. Energy Mater. Sol. Cells*, 2011, **95**, 2606–2609.
- 98 T. Chiu, H. Mandal, M. Zhang, S. Yang and Y. Chuang, *Int. J. Photoenergy*, 2013, **2013**, 1–7.
- 99 B. Zimmermann, U. Würfel and M. Niggemann, *Sol. Energy Mater. Sol. Cells*, 2009,

- 93**, 491–496.
- 100 P. Kopola, B. Zimmermann, A. Filipovic, H. F. Schleiermacher, J. Greulich, S. Rousu, J. Hast, R. Myllylä and U. Würfel, *Sol. Energy Mater. Sol. Cells*, 2012, **107**, 252–258.
- 101 V. Kumar and H. Wang, *Sol. Energy Mater. Sol. Cells*, 2013, **113**, 179–185.
- 102 Y. Galagan, D. J. D. Moet, D. C. Hermes, P. W. M. Blom and R. Andriessen, *Org. Electron.*, 2012, **13**, 3310–3314.
- 103 C. J. An, C. Cho, J. K. Choi, J. M. Park, M. L. Jin, J. Y. Lee and H. T. Jung, *Small*, 2014, **10**, 1278–1283.
- 104 C. J. An, H.-W. Yoo, C. Cho, J.-M. Park, J. K. Choi, M. L. Jin, J.-Y. Lee and H.-T. Jung, *J. Mater. Chem. A*, 2014, **2**, 2915–2921.
- 105 J. Ham, W. J. Dong, J. Y. Park, C. J. Yoo, I. Lee and J.-L. Lee, *Adv. Mater.*, 2015, **27**, 4027–4033.
- 106 H. a Atwater and A. Polman, *Nat. Mater.*, 2010, **9**, 205–213.
- 107 P. R. West, S. Ishii, G. V. Naik, N. K. Emani, V. M. Shalaev and A. Boltasseva, *Laser Photon. Rev.*, 2010, **4**, 795–808.
- 108 S. L. Smitha, K. M. Nissamudeen, D. Philip and K. G. Gopchandran, *Spectrochim. Acta - Part A Mol. Biomol. Spectrosc.*, 2008, **71**, 186–190.
- 109 J. Xue, S. Uchida, B. P. Rand and S. R. Forrest, *Appl. Phys. Lett.*, 2004, **84**, 3013–3015.
- 110 Y. Long, B. Li, Y. Li, W. Zheng, Q. Wang and R. Su, *J. Mod. Opt.*, 2014, **61**, 943–953.
- 111 P. You, Z. Liu, Q. Tai, S. Liu and F. Yan, *Adv. Mater.*, 2015, 3632–3638.
- 112 Z. Liu, J. Li, Z.-H. Sun, G. Tai, S.-P. Lau and F. Yan, *ACS Nano*, 2012, **6**, 810–818.
- 113 P. Solar, Z. Li, S. a Kulkarni, P. P. Boix, E. Shi, A. Cao, K. Fu and S. K. Batabyal, *ACS Nano*, 2014, **8**, 6797–6804.
- 114 Y. Zhou, T. M. Khan, J.-C. C. Liu, C. Fuentes-Hernandez, J. W. Shim, E. Najafabadi, J. P. Youngblood, R. J. Moon and B. Kippelen, *Org. Electron.*, 2014, **15**, 661–666.
- 115 D. Gupta, M. M. Wienk and R. A. J. Janssen, *ACS Appl. Mater. Interfaces*, 2014, **6**, 13937–13944.
- 116 J. Krantz, T. Stubhan, M. Richter, S. Spallek, I. Litzov, G. J. Matt, E. Spiecker and C. J. Brabec, *Adv. Funct. Mater.*, 2013, **23**, 1711–1717.
- 117 L. Zuo, S. Zhang, H. Li and H. Chen, *Adv. Mater.*, 2015, 6983–6989.
- 118 J. Zou, H.-L. Yip, S. K. Hau and A. K.-Y. Jen, *Appl. Phys. Lett.*, 2010, **96**, 203301.
- 119 Y. M. Chang, C. P. Chen, J. M. Ding, C. Y. Leu, M. J. Lee and R. De Chen, *Sol. Energy Mater. Sol. Cells*, 2013, **109**, 91–96.
- 120 J. Nekarda, D. Reinwand, A. Grohe, P. Hartmann, R. Preu, R. Trassl and S. Wieder, in *Conference Record of the IEEE Photovoltaic Specialists Conference*, 2009, pp. 000892–000896.

- 
- 121 K. M. Gupta and N. Gupta, *Advanced Electrical and Electronics Materials*, John Wiley & Sons, Inc., Hoboken, NJ, USA, 2015.
- 122 D. W. Lynch and W. R. Hunter, in *Handbook of Optical Constants of Solids*, Elsevier, 1985, vol. 1, pp. 275–367.
- 123 S. Schubert, J. Meiss, L. Müller-Meskamp and K. Leo, *Adv. Energy Mater.*, 2013, **3**, 438–443.
- 124 Y. (Michael) Yang, Q. Chen, Y.-T. Hsieh, T.-B. Song, N. De Marco, H. Zhou and Y. Yang, *ACS Nano*, 2015, **9**, 7714–7721.
- 125 H. Kim, K. T. Lee, C. Zhao, L. J. Guo and J. Kanicki, *Org. Electron. physics, Mater. Appl.*, 2015, **20**, 103–111.
- 126 K. Jung, H.-J. Song, G. Lee, Y. Ko, K. Ahn, H. Choi, J. Y. Kim, K. Ha, J. Song, J.-K. Lee, C. Lee and M. Choi, *ACS Nano*, 2014, **8**, 2590–2601.
- 127 Y. Liu, C.-F. Guo, S. Huang, T. Sun, Y. Wang and Z. Ren, *J. Mater.*, 2015, **1**, 52–59.
- 128 J. Meiss, N. Allinger, M. K. Riede and K. Leo, *Appl. Phys. Lett.*, 2008, **93**, 103311.
- 129 S. Schubert, L. Müller-Meskamp and K. Leo, *Adv. Funct. Mater.*, 2014, **24**, 1–9.
- 130 H. M. Stec, R. J. Williams, T. S. Jones and R. a. Hatton, *Adv. Funct. Mater.*, 2011, **21**, 1709–1716.
- 131 M. Kawamura, Y. Ishizuka, S. Yoshida, Y. Abe and K. H. Kim, *Thin Solid Films*, 2013, **532**, 7–10.
- 132 H. M. Stec and R. a Hatton, *ACS Appl. Mater. Interfaces*, 2012, **4**, 6013–6020.
- 133 C. K. O’Sullivan and G. G. Guilbault, *Biosens. Bioelectron.*, 1999, **14**, 663–670.
- 134 J. Janata, *Principles of Chemical Sensors*, 2009.
- 135 C. Lu, *J. Appl. Phys.*, 1972, **43**, 4385.
- 136 A. Teichler, J. Perelaer and U. S. Schubert, *J. Mater. Chem. C*, 2013, **1**, 1910–1925.
- 137 A. McEvoy, T. Markvart and L. Castaner, *Practical Handbook of Photovoltaics*, Elsevier: Walham, 2012.
- 138 P. Van der Heide, in *X-Ray Photoelectron Spectroscopy*, John Wiley & Sons, Inc., Hoboken, NJ, USA, 2011, pp. 1–12.
- 139 E. Mateo-Mart and C.-M. Pradier, in *Intelligent and Biosensors*, InTech, 2010, pp. 323–344.
- 140 D. Cahen and A. Kahn, *Adv. Mater.*, 2003, **15**, 271–277.
- 141 J. S. Kim, B. Lägél, E. Moons, N. Johansson, I. D. Baikie, W. R. Salaneck, R. H. Friend and F. Cacialli, *Synth. Met.*, 2000, **111**, 311–314.
- 142 N. Hayashi, H. Ishii, Y. Ouchi and K. Seki, *J. Appl. Phys.*, 2002, **92**, 3784.
- 143 W. N. Hansen and G. J. Hansen, *Surf. Sci.*, 2001, **481**, 172–184.

- 
- 144 A. Vldar and M. Postek, *Microsc. Microanal.*, 2005, **11**, 764–765.
- 145 C. Kasl and M. J. R. Hoch, *Rev. Sci. Instrum.*, 2005, **76**, 1–5.
- 146 G. Dennler, M. C. Scharber and C. J. Brabec, *Adv. Mater.*, 2009, **21**, 1323–1338.
- 147 J. Grepstad, P. Gartland and B. Slagsvold, *Surf. Sci.*, 1976, **57**, 348–362.
- 148 A. W. Dweydari and C. H. B. Mee, *Phys. Status Solidi*, 1975, **27**, 223–230.
- 149 P. Sullivan, A. Duraud, L. Hancox, N. Beaumont, G. Mirri, J. H. R. Tucker, R. a. Hatton, M. Shipman and T. S. Jones, *Adv. Energy Mater.*, 2011, **1**, 352–355.
- 150 S. Foster, C. E. Finlayson, P. E. Keivanidis, Y.-S. Huang, I. Hwang, R. H. Friend, M. B. J. Otten, L.-P. Lu, E. Schwartz, R. J. M. Nolte and A. E. Rowan, *Macromolecules*, 2009, **42**, 2023–2030.
- 151 J. H. Park, T.-W. Lee, B.-D. Chin, D. H. Wang and O. O. Park, *Macromol. Rapid Commun.*, 2010, **31**, 2095–2108.
- 152 S. K. Hau, H.-L. Yip, N. S. Baek, J. Zou, K. O’Malley and A. K.-Y. Jen, *Appl. Phys. Lett.*, 2008, **92**, 253301.
- 153 J. C. Bernède, Y. Berredjem, L. Cattin and M. Morsli, *Appl. Phys. Lett.*, 2008, **92**, 083304.
- 154 J. Y. Kim, S. H. Kim, H.-H. Lee, K. Lee, W. Ma, X. Gong and a. J. Heeger, *Adv. Mater.*, 2006, **18**, 572–576.
- 155 T. Kuwabara, T. Nakayama, K. Uozumi, T. Yamaguchi and K. Takahashi, *Sol. Energy Mater. Sol. Cells*, 2008, **92**, 1476–1482.
- 156 K. Wefers and Alcoa Laboratories, *Oxides and Hydroxides of Aluminum*, 1987.
- 157 S.-H. Lee, J.-H. Kim, T.-H. Shim and J.-G. Park, *Electron. Mater. Lett.*, 2009, **5**, 47–50.
- 158 W.-J. Shin, J.-H. Kim, M.-C. Oh, J. C. Kim and T.-H. Yoon, in *Advanced LEDs for Solid State Lighting*, eds. C.-H. Hong, T. Taguchi, J. Han and L. Chen, 2006, vol. 6355, p. 635519.
- 159 A. Turak, *RSC Adv.*, 2013, **3**, 6188–6225.
- 160 M. Wang, F. Xie, J. Du, Q. Tang, S. Zheng, Q. Miao, J. Chen, N. Zhao and J. B. Xu, *Sol. Energy Mater. Sol. Cells*, 2011, **95**, 3303–3310.
- 161 U.S. Geological Survey, *Mineral Commodity Summaries*, 2014.
- 162 W. Li and D. Y. Li, *J. Chem. Phys.*, 2005, **122**, 064708.
- 163 T. Sakurai, S. Toyoshima, H. Kitazume, S. Masuda, H. Kato and K. Akimoto, *J. Appl. Phys.*, 2010, **107**, 043707.
- 164 O. S. Hutter, H. M. Stec and R. A. Hatton, *Adv. Mater.*, 2013, **25**, 284–288.
- 165 B. P. Rand, J. Xue, F. Yang and S. R. Forrest, *Appl. Phys. Lett.*, 2005, **87**, 233508.
- 166 M. Brumbach, D. Placencia and N. R. Armstrong, *J. Phys. Chem. C*, 2008, **112**, 3142–

- 3151.
- 167 H. Do Kim, H. Ohkita, H. Benten and S. Ito, *ACS Appl. Mater. Interfaces*, 2014, **6**, 17551–17555.
- 168 W. Lee, H. Choi, S. Hwang, J. Y. Kim and H. Y. Woo, *Chem. - A Eur. J.*, 2012, **18**, 2551–2558.
- 169 F. Zhang, W. Mammo, L. M. Andersson, S. Admassie, M. R. Andersson and O. Inganäs, *Adv. Mater.*, 2006, **18**, 2169–2173.
- 170 I. P. Lopéz, L. Cattin, D.-T. Nguyen, M. Morsli and J. C. Bernède, *Thin Solid Films*, 2012, **520**, 6419–6423.
- 171 R. J. Gutmann, T. Paul Chow, W. N. Gill, A. E. Kaloyeros, W. A. Lanford and S. P. Murarka, *MRS Proc.*, 1994, **337**, 41–57.
- 172 O. S. Hutter and R. A. Hatton, *Adv. Mater.*, 2015, **27**, 326–331.
- 173 J. Schmitz, J. Brillo, I. Egry and R. Schmid-Fetzer, *Int. J. Mater. Res.*, 2009, **100**, 1529–1535.
- 174 H. B. Michaelson, *J. Appl. Phys.*, 1977, **48**, 4729–4733.
- 175 A. Wagenpfahl, D. Rauh, M. Binder, C. Deibel and V. Dyakonov, *Phys. Rev. B*, 2010, **82**, 115306.
- 176 W. Tress, K. Leo and M. Riede, *Adv. Funct. Mater.*, 2011, **21**, 2140–2149.
- 177 A. Cerezo, A. K. Petford-Long, D. J. Larson, S. Pinitsoontorn and E. W. Singleton, *J. Mater. Sci.*, 2006, **41**, 7843–7852.
- 178 J. a. Assimos and D. Trivich, *Phys. Status Solidi*, 1974, **26**, 477–488.
- 179 W. A. Lanford, P. J. Ding, W. Wang, S. Hymes and S. P. Murarka, *Thin Solid Films*, 1995, **262**, 234–241.
- 180 W. Wang, W. A. Lanford and S. P. Murarka, *Appl. Phys. Lett.*, 1996, **68**, 1622–1624.
- 181 R. M. Cook, L.-J. Pegg, S. L. Kinnear, O. S. Hutter, R. J. H. Morris and R. A. Hatton, *Adv. Energy Mater.*, 2011, **1**, 440–447.
- 182 M. C. Biesinger, L. W. M. Lau, A. R. Gerson and R. S. C. Smart, *Appl. Surf. Sci.*, 2010, **257**, 887–898.
- 183 I. Platzman, R. Brenner, H. Haick and R. Tannenbaum, *J. Phys. Chem. C*, 2008, **112**, 1101–1108.
- 184 J. Ghijsen, L. Tjeng, J. van Elp, H. Eskes, J. Westerink, G. Sawatzky and M. Czyzyk, *Phys. Rev. B*, 1988, **38**, 11322–11330.
- 185 A. Baddorf and J. Wendelken, *Surf. Sci.*, 1991, **256**, 264–271.
- 186 G. Ertl, R. Hierl and H. Knözinger, *Appl. Surf. Sci.*, 1980, **5**, 49–64.
- 187 J. C. Klein, C. P. Li, D. M. Hercules and J. F. Black, *Appl. Spectrosc.*, 1984, **38**, 729–734.

- 
- 188 N. S. McIntyre and M. G. Cook, *Anal. Chem.*, 1975, **47**, 2208–2213.
- 189 B. Strohmeier, D. Levden, R. Field and D. Hercules, *J. Catal.*, 1985, **530**, 514–530.
- 190 J. A. Rotole, *Surf. Sci. Spectra*, 1998, **5**, 18–24.
- 191 J. A. Rotole, *Surf. Sci. Spectra*, 1998, **5**, 4–10.
- 192 A. C. Miller, *Surf. Sci. Spectra*, 1993, **2**, 55–60.
- 193 M. Chase, *NIST-JANAF thermochemical tables*, Washington, D.C. : American Chemical Society ; Woodbury, N.Y. : American Institute of Physics for the National Institute of Standards and Technology, ©1998., 4th edn., 1998.
- 194 C. J. Mulligan, M. Wilson, G. Bryant, B. Vaughan, X. Zhou, W. J. Belcher and P. C. Dastoor, *Sol. Energy Mater. Sol. Cells*, 2014, **120**, 9–17.
- 195 L.-M. Chen, Z. Xu, Z. Hong and Y. Yang, *J. Mater. Chem.*, 2010, **20**, 2575–2598.
- 196 H.-L. Yip and A. K.-Y. Jen, *Energy Environ. Sci.*, 2012, **5**, 5994–6011.
- 197 Y. Chen, Z. Hu, Z. Zhong, W. Shi, J. Peng, J. Wang and Y. Cao, *J. Phys. Chem. C*, 2014, **118**, 21819–21825.
- 198 G. Kim, J. Kong, J. Kim, H. Kang, H. Back, H. Kim and K. Lee, *Adv. Energy Mater.*, 2015, **5**, 1401298.
- 199 A. Hadipour, R. Müller and P. Heremans, *Org. Electron.*, 2013, **14**, 2379–2386.
- 200 S. Chambon, L. Derue, M. Lahaye, B. Pavageau, L. Hirsch and G. Wantz, *Materials.*, 2012, **5**, 2521–2536.
- 201 Q. Bao, S. Fabiano, M. Andersson, S. Braun, Z. Sun, X. Crispin, M. Berggren, X. Liu and M. Fahlman, *Adv. Funct. Mater.*, 2016, 1077–1084.
- 202 C. Tengstedt, W. Osikowicz, W. R. Salaneck, I. D. Parker, C. H. Hsu and M. Fahlman, *Appl. Phys. Lett.*, 2006, **88**, 1–3.
- 203 H. Ishii, K. Sugiyama, E. Ito and K. Seki, *Adv. Mater.*, 1999, **11**, 605–625.
- 204 M. S. Tyler, O. S. Hutter, D. M. Walker and D. R. Hatton, *ChemPhysChem*, 2015, **16**, 1203–1209.
- 205 B. Pradhan, S. Albrecht, B. Stiller and D. Neher, *Appl. Phys. A Mater. Sci. Process.*, 2014, **115**, 365–369.
- 206 L. Kronik, Y. Shapira and S. Yoram, *Surf. Sci. Rep.*, 1999, **37**, 1–206.
- 207 R. J. Davis, M. T. Lloyd, S. R. Ferreira, M. J. Bruzek, S. E. Watkins, L. Lindell, P. Sehati, M. Fahlman, J. E. Anthony and J. W. P. Hsu, *J. Mater. Chem.*, 2011, **21**, 1721–1729.
- 208 H. Ishii, N. Hayashi, E. Ito, Y. Washizu, K. Sugi, Y. Kimura, M. Niwano, Y. Ouchi and K. Seki, *Phys. status solidi*, 2004, **201**, 1075–1094.
- 209 S. R. Day, R. A. Hatton, M. A. Chesters and M. R. Willis, *Thin Solid Films*, 2002, **410**, 159–166.

- 
- 210 H. Ishii, H. Oji, E. Ito, N. Hayashi, D. Yoshimura and K. Seki, *J. Lumin.*, 2000, **87-89**, 61–65.
- 211 M. Iwamoto, A. Fukuda and E. Itoh, *J. Appl. Phys.*, 1994, **75**, 1607–1610.
- 212 M. S. Tyler, I. M. Nadeem and R. A. Hatton, *Mater. Horiz.*, 2016, **3**, 348–354.
- 213 Y. Tanaka, K. Kanai, Y. Ouchi and K. Seki, *Org. Electron. physics, Mater. Appl.*, 2009, **10**, 990–993.
- 214 H. Yanagi, T. Kuroda, K. B. Kim, Y. Toda, T. Kamiya and H. Hosono, *J. Mater. Chem.*, 2012, **22**, 4278–4281.
- 215 Y. Liang, Z. Xu, J. Xia, S. T. Tsai, Y. Wu, G. Li, C. Ray and L. Yu, *Adv. Mater.*, 2010, **22**, 135–138.
- 216 P. Cheng, Y. Li and X. Zhan, *Energy Environ. Sci.*, 2014, **7**, 2005–2011.
- 217 H. T. Nicolai, M. Kuik, G. a. H. Wetzelaer, B. de Boer, C. Campbell, C. Risko, J. L. Brédas and P. W. M. Blom, *Nat. Mater.*, 2012, **11**, 882–887.
- 218 E. J. Meijer, A. V. G. Mangnus, C. M. Hart, D. M. De Leeuw and T. M. Klapwijk, *Appl. Phys. Lett.*, 2001, **78**, 3902–3904.
- 219 W. C. Tsoi, S. J. Spencer, L. Yang, A. M. Ballantyne, P. G. Nicholson, A. Turnbull, A. G. Shard, C. E. Murphy, D. D. C. Bradley, J. Nelson and J. S. Kim, *Macromolecules*, 2011, **44**, 2944–2952.
- 220 M. C. Scharber, D. Mühlbacher, M. Koppe, P. Denk, C. Waldauf, A. J. Heeger and C. J. Brabec, *Adv. Mater.*, 2006, **18**, 789–794.
- 221 N. Koch, A. Vollmer, S. Duhm, Y. Sakamoto and T. Suzuki, *Adv. Mater.*, 2007, **19**, 112–116.
- 222 J. Niederhausen, P. Amsalem, J. Frisch, A. Wilke, A. Vollmer, R. Rieger, K. Müllen, J. P. Rabe and N. Koch, *Phys. Rev. B*, 2011, **84**, 165302.
- 223 E. Kawabe, H. Yamane, R. Sumii, K. Koizumi, Y. Ouchi, K. Seki and K. Kanai, *Org. Electron.*, 2008, **9**, 783–789.
- 224 W. Osikowicz, M. P. de Jong, S. Braun, C. Tengstedt, M. Fahlman and W. R. Salaneck, *Appl. Phys. Lett.*, 2006, **88**, 193504.
- 225 J. Huang, G. Li and Y. Yang, *Appl. Phys. Lett.*, 2005, **87**, 112105.
- 226 W.-F. Xu, M.-Y. Pan, P.-H. Fu, S.-W. Li, D.-W. Huang and P.-K. Wei, *J. Mater. Chem. C*, 2015, **3**, 9131–9136.
- 227 H. Jin, C. Tao, M. Velusamy, M. Aljada, Y. Zhang, M. Hamsch, P. L. Burn and P. Meredith, *Adv. Mater.*, 2012, **24**, 2572–2577.
- 228 Y. Galagan, A. Manor, R. Andriessen and E. a Katz, in *2012 38th IEEE Photovoltaic Specialists Conference (Pvsc)*, 2012, pp. 2750–2752.
- 229 N. Espinosa, F. O. Lenzmann, S. Ryley, D. Angmo, M. Hösel, R. R. Søndergaard, D. Huss, S. Däfinger, S. Grisch, J. M. Kroon, M. Jørgensen and F. C. Krebs, *J. Mater.*

- Chem. A*, 2013, **1**, 7037–7049.
- 230 H. Youn, H. J. Park and L. J. Guo, *Small*, 2015, **11**, 2228–2246.
- 231 F. Xie, W. C. H. Choy, C. Wang, X. Li, S. Zhang and J. Hou, *Adv. Mater.*, 2013, **25**, 2051–2055.
- 232 M. Vasilopoulou, A. Soultati, D. G. Georgiadou, T. Stergiopoulos, L. C. Palilis, S. Kennou, N. a. Stathopoulos, D. Davazoglou and P. Argitis, *J. Mater. Chem. A*, 2014, **2**, 1738–1749.
- 233 R. Steim, F. R. Kogler and C. J. Brabec, *J. Mater. Chem.*, 2010, **20**, 2499–2512.
- 234 K. Zilberberg, J. Meyer and T. Riedl, *J. Mater. Chem. C*, 2013, **1**, 4796–4815.
- 235 X. Li, F. Xie, S. Zhang, J. Hou and W. C. Choy, *Light Sci. Appl.*, 2015, **4**, e273.
- 236 X. Li, F. Xie, S. Zhang, J. Hou and W. C. H. Choy, *Adv. Funct. Mater.*, 2014, **24**, 7348–7356.
- 237 M. Vasilopoulou, A. M. Douvas, D. G. Georgiadou, L. C. Palilis, S. Kennou, L. Sygellou, A. Soultati, I. Kostis, G. Papadimitropoulos, D. Davazoglou and P. Argitis, *J. Am. Chem. Soc.*, 2012, **134**, 16178–16187.
- 238 Y. Kurusu, *Bull. Chem. Soc. Jpn.*, 1981, **54**, 293–294.
- 239 S. Ayyappan and C. N. R. Rao, *Mater. Res. Bull.*, 1995, **30**, 947–951.
- 240 J. Wang, J. Zhang, B. Meng, B. Zhang, Z. Xie and L. Wang, *ACS Appl. Mater. Interfaces*, 2015, **7**, 13590–13596.
- 241 T. H. Fleisch, *J. Chem. Phys.*, 1982, **76**, 780–786.
- 242 F. Bournel, C. Laffon, P. Parent and G. Tourillon, *Surf. Sci.*, 1996, **350**, 60–78.
- 243 L. Kanninen, N. Jokinen, H. Ali-Löytty, P. Jussila, K. Lahtonen, M. Hirsimäki, M. Valden, M. Kuzmin, R. Pärna and E. Nömmiste, *Surf. Sci.*, 2011, **605**, 1968–1978.
- 244 G. Gonella, O. Cavalleri, S. Terreni, D. Cvetko, L. Floreano, a. Morgante, M. Canepa and R. Rolandi, *Surf. Sci.*, 2004, **566-568**, 638–643.
- 245 E. Ito, H. Oji, N. Hayashi, H. Ishii, Y. Ouchi and K. Seki, *Appl. Surf. Sci.*, 2001, **175-176**, 407–411.
- 246 S. Braun, W. R. Salaneck and M. Fahlman, *Adv. Mater.*, 2009, **21**, 1450–1472.
- 247 A. M. Ferraria, A. P. Carapeto and A. M. Botelho Do Rego, *Vacuum*, 2012, **86**, 1988–1991.
- 248 K. Wojciechowski, M. Saliba, T. Leijtens, A. Abate and H. J. Snaith, *Energy Environ. Sci.*, 2014, **7**, 1142–1147.
- 249 S.-B. Rim, S. Zhao, S. R. Scully, M. D. McGehee and P. Peumans, *Appl. Phys. Lett.*, 2007, **91**, 243501.
- 250 D.-H. Ko, J. R. Tumbleston, A. Gadisa, M. Aryal, Y. Liu, R. Lopez and E. T. Samulski, *J. Mater. Chem.*, 2011, **21**, 16293.

- 
- 251 I. Horcas, R. Fernández, J. M. Gómez-Rodríguez, J. Colchero, J. Gómez-Herrero and A. M. Baro, *Rev. Sci. Instrum.*, 2007, **78**, 013705.